

1 A search for sparticles in zero lepton final states

2 Russell W. Smith

3 Submitted in partial fulfillment of the

4 requirements for the degree of

5 Doctor of Philosophy

6 in the Graduate School of Arts and Sciences

7 COLUMBIA UNIVERSITY

8 2016

9

© 2016

10

Russell W. Smith

11

All rights reserved

12

ABSTRACT

13

A search for sparticles in zero lepton final states

14

Russell W. Smith

15 TODO : Here's where your abstract will eventually go. The above text is all in the
16 center, but the abstract itself should be written as a regular paragraph on the page,
17 and it should not have indentation. Just replace this text.

Contents

19	Contents	i
20	1 Introduction	1
21	2 The Standard Model	5
22	2.1 Overview	5
23	2.2 Field Content	5
24	2.3 Deficiencies of the Standard Model	15
25	3 Supersymmetry	21
26	3.1 Supersymmetric theories : from space to superspace	21
27	3.2 Minimally Supersymmetric Standard Model	24
28	3.3 Phenomenology	30
29	3.4 How SUSY solves the problems with the SM	32
30	3.5 Conclusions	34
31	4 The Large Hadron Collider	37
32	4.1 Basics of Accelerator Physics	37
33	4.2 Accelerator Complex	40
34	4.3 Large Hadron Collider	41
35	4.4 Dataset Delivered by the LHC	43
36	5 The ATLAS detector	49

37	5.1	Magnets	50
38	5.2	Inner Detector	52
39	5.3	Calorimetry	56
40	5.4	Muon Spectrometer	60
41	5.5	Trigger System	65
42	6	Object Reconstruction	71
43	6.1	Primitive Object Reconstruction	71
44	6.2	Physics Object Reconstruction and Quality Identification	77
45	7	Recursive Jigsaw Reconstruction	103
46	7.1	Razor variables	103
47	7.2	Recursive Jigsaw Reconstruction	108
48	7.3	Variables used in the search for zero lepton SUSY	114
49	8	A search for supersymmetric particles in zero lepton final states with the Recursive Jigsaw Technique	121
50	8.1	Simulation samples	121
51	8.2	Event selection	123
52	8.3	Background estimation	130
54	9	Results	157
55	9.1	Signal region distributions	157
56	9.2	Systematic Uncertainties	160
57	9.3	Limits and Model-dependent Exclusions	162
58	Conclusion		169
59	9.4	New Section	169
60	Bibliography		171

61	Additional N-1 plots	185
62	Compressed region N-1 plots	185

Acknowledgements

Dedication

Introduction

67 Particle physics is a remarkably successful field of scientific inquiry. The ability to
 68 precisely predict the properties of a exceedingly wide range of physical phenomena,
 69 such as the description of the cosmic microwave background [1, 2], the understanding
 70 of the anomalous magnetic dipole moment of the electron [3, 4], and the measurement
 71 of the number of weakly-interacting neutrino flavors [5] is truly amazing.

72 The theory that has allowed this range of predictions is the *Standard Model*
 73 of particle physics (SM). The Standard Model combines the electroweak theory of
 74 Glashow, Weinberg, and Salam [6–8] with the theory of the strong interactions, as
 75 first envisioned by Gell-Mann and Zweig [9, 10]. This quantum field theory (QFT)
 76 contains a number of particles, whose interactions describe phenomena up to the TeV
 77 scale. These particles are manifestations of the fields of the Standard Model, after
 78 application of the Higgs Mechanism. The particle content of the SM consists only of
 79 six quarks, six leptons, four gauge bosons, and a scalar Higgs boson.

80 The Standard Model has some theoretical and experimental deficiencies. The SM
 81 contains 26 free parameters¹. We would like to understand these free parameters
 82 in terms of a more fundamental theory.

83 The major theoretical concern of the Standard Model, as it pertains to this thesis,
 84 is the *hierarchy problem* [11–15]. The light mass of the Higgs boson (125 GeV) should
 85 be quadratically dependent on the scale of UV physics, due to the quantum corrections

¹This is the Standard Model corrected to include neutrino masses. These parameters are the fermion masses (6 leptons, 6 quarks), CKM and PMNS mixing angles (8 angles, 2 CP-violating phases), W/Z/Higgs masses (3), the Higgs field expectation value, and the couplings of the strong, weak, and electromagnetic forces (3 α_{force}).

86 from high-energy physics processes. The most perplexing experimental issue is the
87 existence of *dark matter*, as demonstrated by galactic rotation curves [16–22]. This
88 data has shown that there exists additional matter which has not yet been seen
89 interacting with the particles of the Standard Model. There is no particle in the SM
90 which can act as a candidate for dark matter.

91 Both of these major issues, as well as numerous others, can be solved by the
92 introduction of *supersymmetry* (SUSY) [15, 23–35]. In supersymmetric theories, each
93 SM particles has a so-called *superpartner*, or sparticle partner, differing from given SM
94 particle by 1/2 in spin. These theories solve the hierarchy problem, since the quantum
95 corrections induced from the superpartners exactly cancel those induced by the SM
96 particles. In addition, these theories are usually constructed assuming *R*–parity,
97 which can be thought of as the “charge” of supersymmetry, with SM particles having
98 $R = 1$ and sparticles having $R = -1$. In collider experiments, since the incoming
99 SM particles have total $R = 1$, the resulting sparticles are produced in pairs. This
100 produces a rich phenomenology, which is characterized by significant hadronic activity
101 and large missing transverse energy (E_T^{miss}), which provide significant discrimination
102 against SM backgrounds [36].

103 Despite the power of searches for supersymmetry where E_T^{miss} is a primary
104 discriminating variable, there has been significant interest in the use of other variables
105 to discriminate against SM backgrounds. These include searches employing variables
106 such as α_T , $M_{T,2}$, and the razor variables (M_R, R^2) [37–47]. In this thesis, we
107 will present the first search for supersymmetry using the novel Recursive Jigsaw
108 Reconstruction (RJR) technique. RJR can be considered the conceptual successor
109 of the razor variables. We impose a particular final state “decay tree” on an events,
110 which roughly corresponds to a simplified Feynmann diagram in decays containing
111 weakly-interacting particles. We account for the missing degrees of freedom associated
112 with weakly-interacting particles by a series of simplifying assumptions, which allow

113 us to calculate our variables of interest at each step in the decay tree. This allows
114 an unprecedented understanding of the internal structure of the decay and additional
115 variables to reject Standard Model backgrounds.

116 This thesis describes a search for the superpartners of the gluon and quarks, the
117 gluino and squarks, in final states with zero leptons, with 13.3 fb^{-1} of data using
118 the ATLAS detector. We organize the thesis as follows. The theoretical foundations
119 of the Standard Model and supersymmetry are described in Chapters 2 and 3. The
120 Large Hadron Collider and the ATLAS detector are presented in Chapters 4 and 5.
121 The reconstruction of physics objects is presented in Chapter 6. Chapter 7 provides
122 a detailed description of Recursive Jigsaw Reconstruction and a description of the
123 variables used for the particular search presented in this thesis. Chapter 8 presents
124 the details of the analysis, including details of the dataset, object reconstruction,
125 and selections used. In Chapter 9, the final results are presented; since there is no
126 evidence for a supersymmetric signal in the analysis, we present the final exclusion
127 curves in simplified supersymmetric models.

*The Standard Model*130 **2.1 Overview**

131 The Standard Model (SM) is another name for a theory of the internal symmetry
 132 group $SU(3)_C \otimes SU(2)_L \otimes U(1)_Y$ and its associated set of parameters. The SM is the
 133 culmination of years of work in both theoretical and experimental particle physics. In
 134 this thesis, we take the view that theorists construct a model with the field content and
 135 symmetries as inputs, and write down the most general Lagrangian consistent with
 136 those symmetries. Assuming this model is compatible with nature (in particular, the
 137 predictions of the model are consistent with previous experiments), experimentalists
 138 are responsible for testing the parameters by measurements.

139 Additional theoretical background is in ?? . The philosophy and notations are
 140 inspired by [48, 49].

141 **2.2 Field Content**

The Standard Model field content is

$$\begin{aligned} \text{Fermions} &: Q_L(3, 2)_{+1/3}, U_R(3, 1)_{+4/3}, D_R(3, 1)_{-2/3}, L_L(1, 2)_{-1}, E_R(1, 1)_{-2} \\ \text{Scalar (Higgs)} &: \phi(1, 2)_{+1} \\ \text{Vector Fields} &: G^\mu(8, 1)_0, W^\mu(1, 3)_0, B^\mu(1, 1)_0 \end{aligned} \tag{2.1}$$

142 where the $(A, B)_Y$ notation represents the irreducible representation under $SU(3)$
 143 and $SU(2)$, with Y being the electroweak hypercharge. Each of these fermion fields

144 has an additional index, representing the three generation of fermions.

145 We observed that Q_L, U_R , and D_R are triplets under $SU(3)_C$; these are the *quark*
146 fields. The *color* group, $SU(3)_C$ is mediated by the *gluon* field $G^\mu(8, 1)_0$, which has
147 8 degrees of freedom. The fermion fields $L_L(1, 2)_{-1}$ and $E_R(1, 1)_{-2}$ are singlets under
148 $SU(3)_C$; we call them the *lepton* fields.

149 Next, we note the “left-handed” (“right-handed”) fermion fields, denoted by $L(R)$
150 subscript, The left-handed fields form doublets under $SU(2)_L$. These are mediated
151 by the three degrees of freedom of the “W” fields $W^\mu(1, 3)_0$. These fields only act
152 on the left-handed particles of the Standard Model. This is the reflection of the
153 “chirality” of the Standard Model The left-handed and right-handed particles are
154 treated differently by the electroweak forces. The right-handed fields, U_R, D_R , and
155 E_R , are singlets under $SU(2)_L$.

156 The $U(1)_Y$ symmetry is associated to the $B^\mu(1, 1)_0$ boson with one degree of
157 freedom. The charge Y is known as the electroweak hypercharge.

158 To better understand the phenomenology of the Standard Model, let us investigate
159 each of the *sectors* of the Standard Model separately.

160 Electroweak sector

The electroweak sector refers to the $SU(2)_L \otimes U(1)_Y$ portion of the Standard Model gauge group. Following our philosophy of writing all gauge-invariant and renormalizable terms, the electroweak Lagrangian can be written as

$$\mathcal{L} = W_a^{\mu\nu} W_{\mu\nu}^a + B^{\mu\nu} B_{\mu\nu} + (D^\mu \phi)^\dagger D_\mu \phi - \mu^2 \phi^\dagger \phi - \lambda (\phi^\dagger \phi)^2. \quad (2.2)$$

where $W_a^{\mu\nu}$ are the three ($a = 1, 2, 3$) gauge bosons associated to the $SU(2)_L$ gauge group, $B^{\mu\nu}$ is the one gauge boson of the $U(1)_Y$ gauge group, and ϕ is the complex Higgs multiplet. The covariant derivative D^μ is given by

$$D^\mu = \partial^\mu + \frac{ig}{2} W_a^\mu \sigma_a + \frac{ig'}{2} B^\mu \quad (2.3)$$

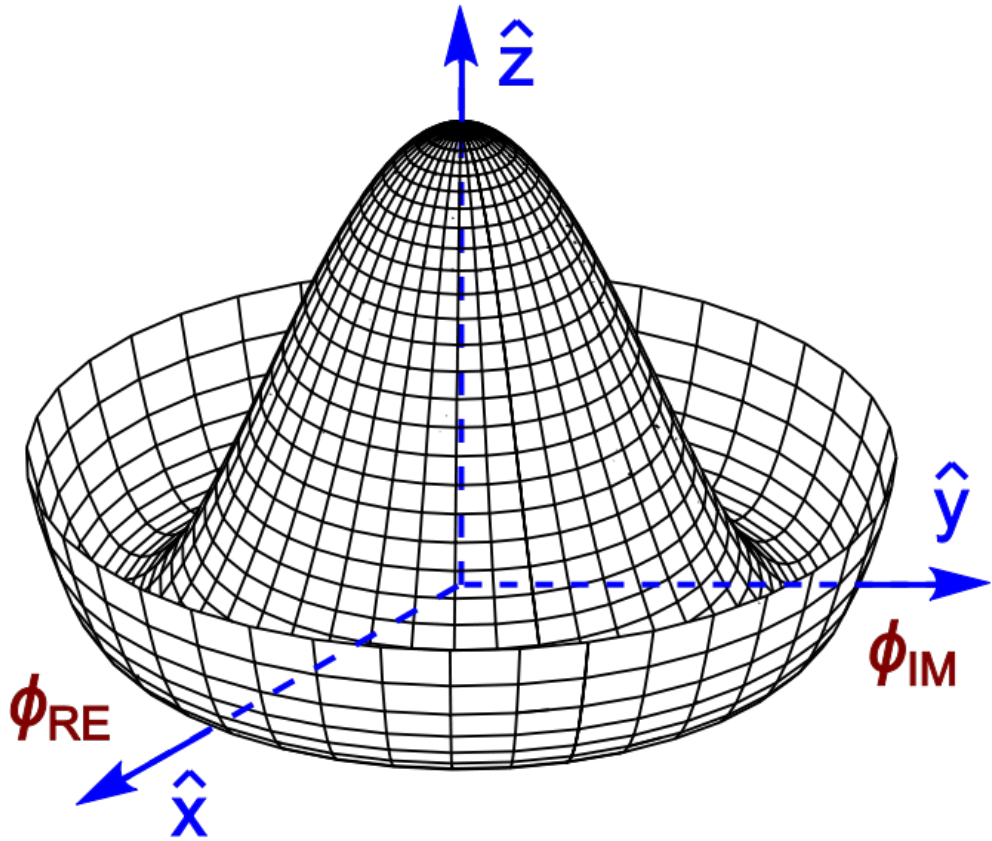


Figure 2.1: Sombrero potential

where $i\sigma_a$ are the Pauli matrices times the imaginary constant, which are the generators for $SU(2)_L$, and g and g' are the $SU(2)_L$ and $U(1)_Y$ coupling constants, respectively. The field strength tensors $W_a^{\mu\nu}$ and $B^{\mu\nu}$ are given by the commutator of the covariant derivative associated to each field

$$B^{\mu\nu} = \partial^\mu B^\nu - \partial^\nu B^\mu \quad (2.4)$$

$$W_a^{\mu\nu} = \partial^\mu W_a^\nu - \partial^\nu W_a^\mu - g\epsilon_{abc}W_a^\mu W_b^\nu, \quad i = 1, 2, 3$$

161

162 The terms in the Lagrangian Eq. (2.2) proportional to μ^2 and λ make up the
 163 “Higgs potential” [50]. As normal (see Appendix ??), we restrict $\lambda > 0$ to guarantee
 164 our potential is bounded from below, and we also require $\mu^2 < 0$, which gives us the
 165 standard “sombrero” potential shown in Fig. 2.1.

This potential has infinitely many minima at $\langle \phi \rangle = \sqrt{2m/\lambda}$. The ground state is *spontaneously* broken by the choice of ground state, which induces a vacuum expectation value (VEV). Without loss of generality, we can choose the Higgs field ϕ to point in the real direction, and write the Higgs field ϕ in the following form :

$$\phi = \frac{1}{\sqrt{2}} \exp\left(\frac{i}{v} \sigma_a \theta_a\right) \begin{pmatrix} 0 \\ v + h(x) \end{pmatrix}. \quad (2.5)$$

We choose a gauge to rotate away the dependence on θ_a , such that we can write simply

$$\phi = \frac{1}{\sqrt{2}} \begin{pmatrix} 0 \\ v + h(x) \end{pmatrix}. \quad (2.6)$$

Now, we can see how the masses of the vector bosons are generated from the application of the Higgs mechanism. We plug Eq. Eq. (2.6) back into the electroweak Lagrangian, and only showing the relevant mass terms in the vacuum state where $h(x) = 0$ see that (dropping the Lorentz indices) :

$$\begin{aligned} \mathcal{L}_M &= \frac{1}{8} \left| \begin{pmatrix} gW_3 + g'B & g(W_1 - iW_2) \\ g(W_1 + iW_2) & -gW_3 + g'B \end{pmatrix} \begin{pmatrix} 0 \\ v \end{pmatrix} \right|^2 \\ &= \frac{g^2 v^2}{8} \left[W_1^2 + W_2^2 + \left(\frac{g'}{g} B - W_3 \right)^2 \right] \end{aligned} \quad (2.7)$$

Defining the *Weinberg* angle $\tan(\theta_W) = g'/g$ and the following *physical* fields :

$$W^\pm = \frac{1}{\sqrt{2}} (W_1 \mp iW_2) \quad (2.8)$$

$$Z^0 = \cos \theta_W W_3 - \sin \theta_W B$$

$$A^0 = \sin \theta_W W_3 + \cos \theta_W B$$

we can write the piece of the Lagrangian associated to the vector boson masses as

$$\mathcal{L}_{MV} = \frac{1}{4} g^2 v^2 W^+ W^- + \frac{1}{8} (g^2 + g'^2) v^2 Z^0 Z^0. \quad (2.9)$$

and we have the following values of the masses for the vector bosons :

$$\begin{aligned} m_W^2 &= \frac{1}{4}v^2g^2 \\ m_Z^2 &= \frac{1}{4}v^2(g^2 + g'^2) \\ m_A^2 &= 0 \end{aligned} \tag{2.10}$$

We thus see how the Higgs mechanism gives rise to the masses of the W^\pm and Z boson in the Standard Model. As expected, the mass of the photon is zero. The $SU(2)_L \otimes U(1)_Y$ symmetry of the initially massless $W_{1,2,3}$ and B fields is broken to the $U(1)_{EM}$. Of the four degrees of freedom in the complex Higgs doublet, three are “eaten” when we give mass to the W^\pm and Z_0 , while the other degree of freedom is the Higgs particle, as discovered in 2012 by the ATLAS and CMS collaborations [51, 52].

173 Quantum Chromodynamics

Quantum chromodynamics (or the theory of the *strong* force) characterizes the behavior of *colored* particles, collectively known as *partons*. The partons of the Standard Model are the (fermionic) quarks, and the (bosonic) gluons. The strong force is governed by $SU(3)_C$, an unbroken symmetry in the Standard Model, which implies the gluon remains massless. Defining the covariant derivative for QCD as

$$D^\mu = \partial^\mu + ig_s G_a^\mu L_a, a = 1, \dots, 8 \tag{2.11}$$

where L_a are the generators of $SU(3)_C$, and g_s is the coupling constant of the strong force. The QCD Lagrangian then is given by

$$\mathcal{L}_{\text{QCD}} = i\bar{\psi}_f D_\mu \gamma^\mu \psi_f - \frac{1}{4} G_{a,\mu\nu} G_a^{\mu\nu} \tag{2.12}$$

where the summation over f is for quarks *families*, and $G_a^{\mu\nu}$ is the gluon field strength tensor, given by

$$G_a^{\mu\nu} = \partial^\mu G_a^\nu - \partial^\nu G_a^\mu - g_s f^{abc} G_b^\mu G_c^\nu, a, b, c = 1, \dots, 8 \tag{2.13}$$

174 where f^{abc} are the structure constants of $SU(3)_C$, which are analogous to ϵ_{abc} for
175 $SU(2)_L$. The kinetic term for the quarks is contained in the standard ∂_μ term, while
176 the field strength term contains the interactions between the quarks and gluons, as
177 well as the gluon self-interactions.

178 Written down in this simple form, the QCD Lagrangian does not seem much
179 different from the QED Lagrangian, with the proper adjustments for the different
180 group structures. The gluon is massless, like the photon, so one could naïvely expect
181 an infinite range force, and it pays to understand why this is not the case. The
182 reason for this fundamental difference is the gluon self-interactions arising in the
183 field strength tensor term of the Lagrangian. This leads to the phenomena of *color*
184 *confinement*, which describes how one only observes color-neutral particles alone in
185 nature. In contrast to the electromagnetic force, particles which interact via the
186 strong force experience a *greater* force as the distance between the particles increases.
187 At long distances, the potential is given by $V(r) = -kr$. At some point, it is more
188 energetically favorable to create additional partons out of the vacuum than continue
189 pulling apart the existing partons, and the colored particles undergo *fragmentation*.
190 This leads to *hadronization*. Bare quarks and gluons are actually observed as sprays
191 of hadrons (primarily kaons and pions). These sprays are known as *jets*, which are
192 what are observed by experiments.

193 It is important to recognize the importance of understanding these QCD inter-
194 actions in high-energy hadron colliders such as the LHC. Since protons are hadrons,
195 proton-proton collisions such as those produced by the LHC are primarily governed
196 by the processes of QCD. In particular, by far the most frequent process observed in
197 LHC experiments is dijet production from gluon-gluon interactions, as can be seen
198 (Fig. 2.2). These gluons that interact are part of the *sea* particles inside the proton; the
199 simple $p = uud$ model does not apply. The main *valence* uud quarks are constantly
200 interacting via gluons, which can themselves radiate gluons or split into quarks, and

Standard Model Production Cross Section Measurements

Status: August 2016

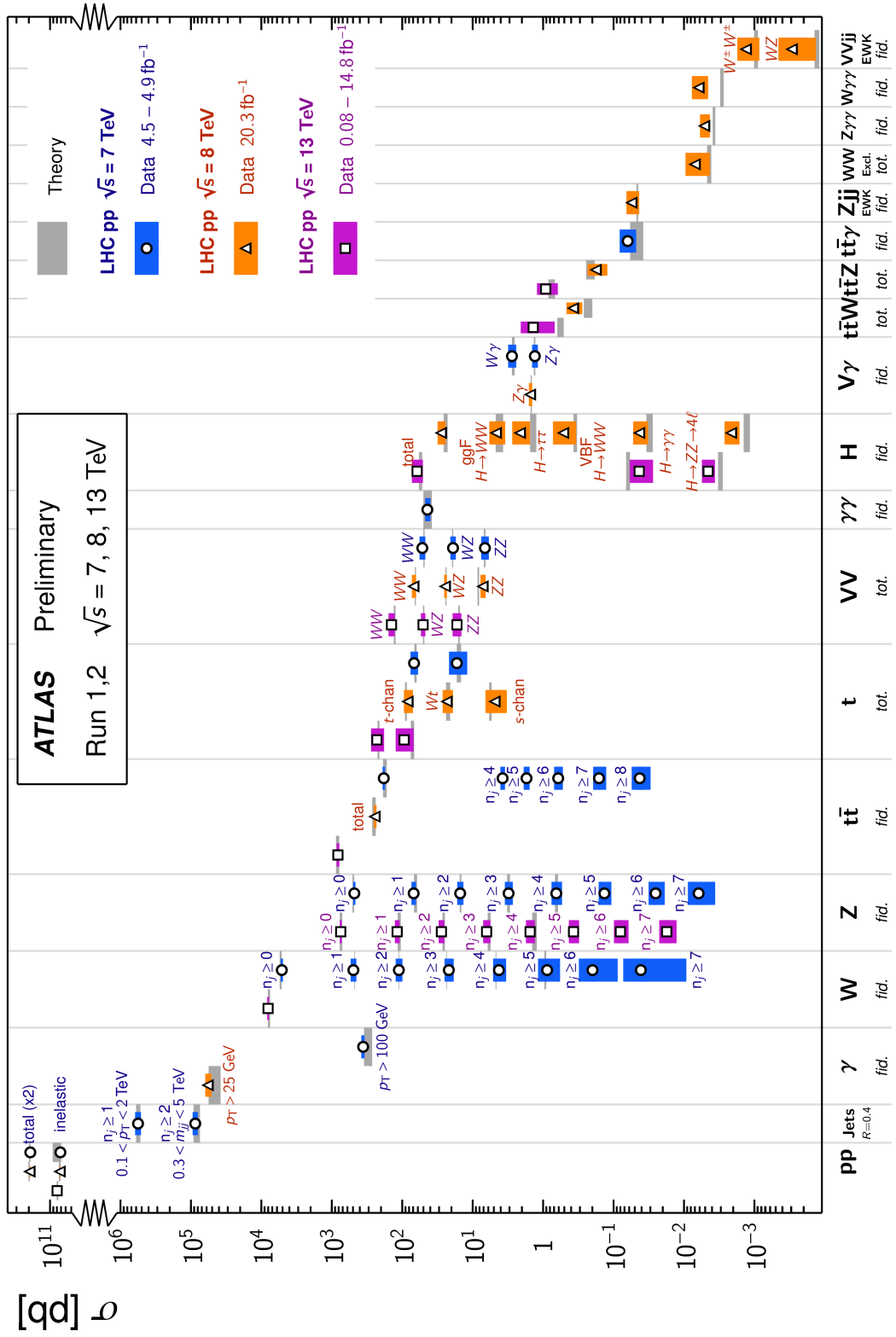


Figure 2.2: Cross-sections of various Standard Model processes

so on. A more useful understanding is given by the colloquially-known *bag* model [53, 54], where the proton is seen as a “bag” of (in principle) infinitely many partons, each with energy $E < \sqrt{s} = 6.5$ TeV. One then collides this (proton) bag with another, and views the products of this very complicated collision, where calculations include many loops in nonperturbative QCD calculations.

Fortunately, we are generally saved by the QCD factorization theorems [55]. This allows one to understand the hard (i.e. short distance or high energy) $2 \rightarrow 2$ parton process using the tools of perturbative QCD, while making series of approximations known as a *parton shower* model to understand the additional corrections from nonperturbative QCD. We will discuss the reconstruction of jets by experiments in Ch. 6.

Fermions

We will now look more closely at the fermions in the Standard Model [56].

As noted earlier in Sec. 2.2, the fermions of the Standard Model can be first distinguished between those that interact via the strong force (quarks) and those which do not (leptons).

There are six leptons in the Standard Model, which can be placed into three *generations*.

$$\begin{pmatrix} e \\ \nu_e \end{pmatrix}, \begin{pmatrix} \mu \\ \nu_\mu \end{pmatrix}, \begin{pmatrix} \tau \\ \nu_\tau \end{pmatrix} \quad (2.14)$$

There is the electron (e), muon (μ), and tau (τ), each of which has an associated neutrino (ν_e, ν_μ, ν_τ). Each of the so-called charged (“electron-like”) leptons has electromagnetic charge -1 , while the neutrinos all have $q_{EM} = 0$.

Often in an experimental context, lepton is used to denote the stable electron and metastable muon, due to their striking experimental signatures. Taus are often treated separately, due to their much shorter lifetime of $\tau_\tau \sim 10^{-13}s$. These decay

223 through hadrons or the other leptons, so often physics analyses at the LHC treat
224 them as jets or leptons, as will be done in this thesis.

225 As the neutrinos are electrically neutral, nearly massless, and only interact via the
226 weak force, it is quite difficult to observe them directly. Since LHC experiments rely
227 overwhelmingly on electromagnetic interactions to observe particles, the presence of
228 neutrinos is not observed directly. Neutrinos are instead observed by the conservation
229 of four-momentum in the plane transverse to the proton-proton collisions, known as
230 *missing transverse energy*.

There are six quarks in the Standard Model : up, down, charm, strange, top, and bottom. Quarks are similar organized into three generations :

$$\begin{pmatrix} u \\ d \end{pmatrix}, \begin{pmatrix} c \\ s \end{pmatrix}, \begin{pmatrix} t \\ b \end{pmatrix} \quad (2.15)$$

231 where we speak of “up-like” quarks and “down-like” quarks.

232 Each up-like quark has charge $q_{up} = 2/3$, while the down-like quarks have $q_{down} =$
233 $-1/3$. At the high energies of the LHC, one often makes the distinction between
234 the light quarks (u, d, c, s), the bottom quark, and top quark. In general, due to
235 the hadronization process described above, the light quarks, with masses $m_q < \sim$
236 1.5 GeV are indistinguishable by LHC experiments. Their hadronic decay products
237 generally have long lifetimes and they are reconstructed as jets.¹. The bottom quark
238 hadronizes primarily through the B -mesons, which generally travels a short distance
239 before decaying to other hadrons. This allows one to distinguish decays via b -quarks
240 from other jets. This procedure is known as *b-tagging* and will be discussed more in
241 Ch.Ch. 5.

242 Due to its large mass, the top quark decays before it can hadronize. There are
243 no bound states associated to the top quark. The top is of particular interest at

¹In some contexts, charm quarks are also treated as a separate category, although it is quite difficult to distinguish charm quarks from the other light quarks at high energy colliders.

Standard Model Interactions (Forces Mediated by Gauge Bosons)



Figure 2.3: The interactions of the Standard Model

- 244 the LHC; it has a striking signature through its most common decay mode $t \rightarrow Wb$.
 245 Decays via tops, especially $t\bar{t}$ are frequently an important signal decay mode, or an
 246 important background process.

247 **Interactions in the Standard Model**

- 248 We briefly overview the entirety of the fundamental interactions of the Standard
 249 Model. These can also be found in Fig. 2.3.

250 The electromagnetic force, mediated by the photon, interacts with via a three-

251 point coupling all charged particles in the Standard Model. The photon thus interacts
252 with all the quarks, the charged leptons, and the charged W^\pm bosons.

253 The weak force is mediated by three particles : the W^\pm and the Z^0 . The Z^0 can
254 interacts with all fermions via a three-point coupling. A real Z_0 can thus decay to
255 a fermion-antifermion pair of all SM fermions except the top quark, due to its large
256 mass. The W^\pm has two important three-point interactions with fermions. First, the
257 W^\pm can interact with an up-like quark and a down-like quark; an important example
258 in LHC experiments is $t \rightarrow Wb$ The coupling constants for these interactions are
259 encoded in the unitary matrix known as the Cabibbo–Kobayashi–Maskawa (CKM)
260 matrix [57, 58], and are generally known as flavor-changing interactions. Secondly,
261 the W^\pm interacts with a charged lepton and its corresponding neutrino. In this case,
262 the unitary matrix that corresponds to CKM matrix for quarks is the identity matrix,
263 which forbids (fundamental) vertices such as $\mu \rightarrow We$. For leptons, instead this is
264 a two-step process : $\mu \rightarrow \nu_m u W \rightarrow \nu_m u \bar{\nu}_e e$. Finally, there are the self-interactions
265 of the weak gauge bosons. There is a three-point and four-point interaction. All
266 combinations are allowed which conserve electric charge.

267 The strong force is mediated by the gluon, which as discussed above also carries
268 the strong color charge. There is the fundamental three-point interaction, where a
269 quark radiates a gluon. Additionally, there are the three-point and four-point gluon-
270 only interactions.

271 2.3 Deficiencies of the Standard Model

272 The Standard Model has been enormously successful. This relatively simple theory is
273 capable of explaining a very wide range of phenomenom, which ultimately break down
274 to combinations of nine diagrams shown in Fig. 2.3 at tree level. Unfortunately, there
275 are some unexplained problems with the Standard Model. We cannot go through all

m_e	Electron mass	511 keV
m_μ	Muon mass	105.7 MeV
m_τ	Tau mass	1.78 GeV
m_u	Up quark mass	1.9 MeV ($m_{\bar{MS}} = 2\text{GeV}$)
m_d	Down quark mass	4.4 MeV ($m_{\bar{MS}} = 2\text{GeV}$)
m_s	Strange quark mass	87 MeV ($m_{\bar{MS}} = 2\text{GeV}$)
m_c	Charm quark mass	1.32 GeV ($m_{\bar{MS}} = m_c$)
m_b	Bottom quark mass	4.24 GeV ($m_{\bar{MS}} = m_b$)
m_t	Top quark mass	172.7 GeV (on-shell renormalization)
θ_{12} CKM	12-mixing angle	13.1°
θ_{23} CKM	23-mixing angle	2.4°
θ_{13} CKM	13-mixing angle	0.2°
δ CKM	CP-violating Phase	0.995
g'	U(1) gauge coupling	0.357 ($m_{\bar{MS}} = m_Z$)
g	SU(2) gauge coupling	0.652 ($m_{\bar{MS}} = m_Z$)
g_s	SU(3) gauge coupling	1.221 ($m_{\bar{MS}} = m_Z$)
θ_{QCD}	QCD vacuum angle	~0
VEV	Higgs vacuum expectation value	246 GeV
m_H	Higgs mass	125 GeV

Table 2.1: Parameters of the Standard Model. For values dependent on the renormalization scheme, we use a combination of the on-shell normalization scheme [59–62] and modified minimal subtraction scheme with $m_{\bar{MS}}$ as indicated in the table [63]

276 of the potential issues in this thesis, but we will motivate the primary issues which
 277 naturally lead one to *supersymmetry*, as we will see in Ch. 3.

The Standard Model has many free parameters, shown in Tab. 2.1. In general, we prefer models with less free parameters. A great example of this fact, and the primary experimental evidence for EWSB, is the relationship between the couplings of the weak force and the masses of the gauge bosons of the weak force :

$$\rho \equiv \frac{m_W^2}{m_Z^2 \cos^2 \theta_W} \stackrel{?}{=} 1 \quad (2.16)$$

278 where ? indicates that this is a testable prediction of the Standard Model (in
 279 particular, that the gauge bosons gain mass through EWSB). This relationship has
 280 been measured within experimental and theoretical predictions. We would like to
 281 produce additional such relationships, which would exist if the Standard Model is a

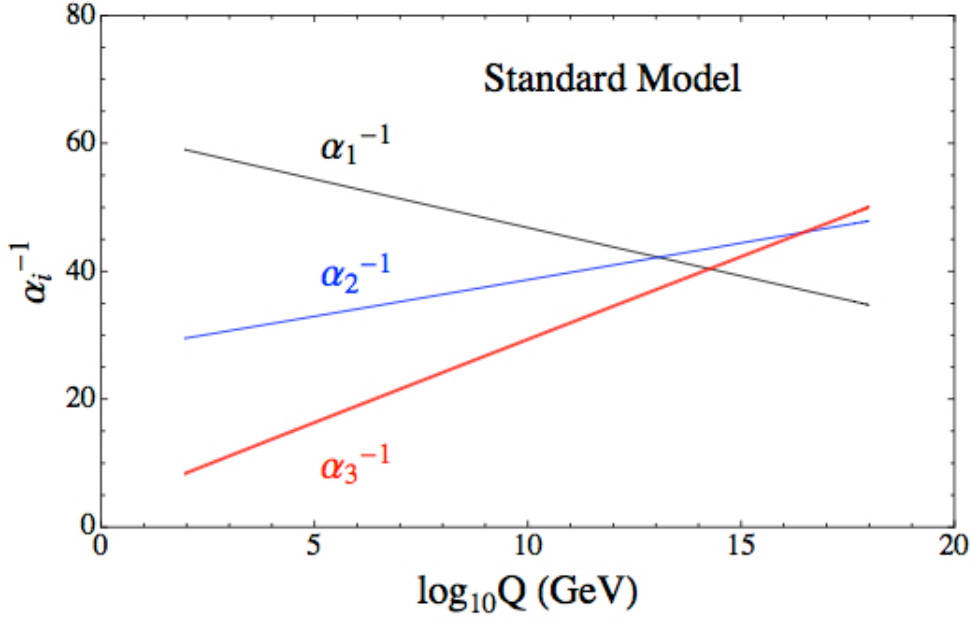


Figure 2.4: The running of Standard Model gauge couplings. The Standard Model couplings do not unify at high energies, which indicates it cannot completely describe nature through the Planck scale.

282 low-energy approximation of some other theory.

283 An additional issue is the lack of *gauge coupling unification*. The couplings of
 284 any quantum field theory “run” as a function of the distance scales (or inversely,
 285 energy scales) of the theory. The idea is closely related to the unification of the
 286 electromagnetic and weak forces at the so-called *electroweak scale* of $O(100$ GeV).
 287 One would hope this behavior was repeated between the electroweak forces and the
 288 strong force at some suitable energy scale. The Standard Model does not exhibit this
 289 behavior, as we can see in Fig. 2.4.

But, the most significant problem with the Standard Model is the *hierarchy problem*. In its most straightforward incarnation, the Higgs scalar field is subject to quantum corrections through loop diagrams, as shown in Fig. 2.5. For demonstration, we use the contributions from the top quark, since the top quark has the largest Higgs Yukawa coupling due to its large mass. In general, we should expect these corrections to quadratically depend on the scale of the ultraviolet physics, Λ . Briefly assume

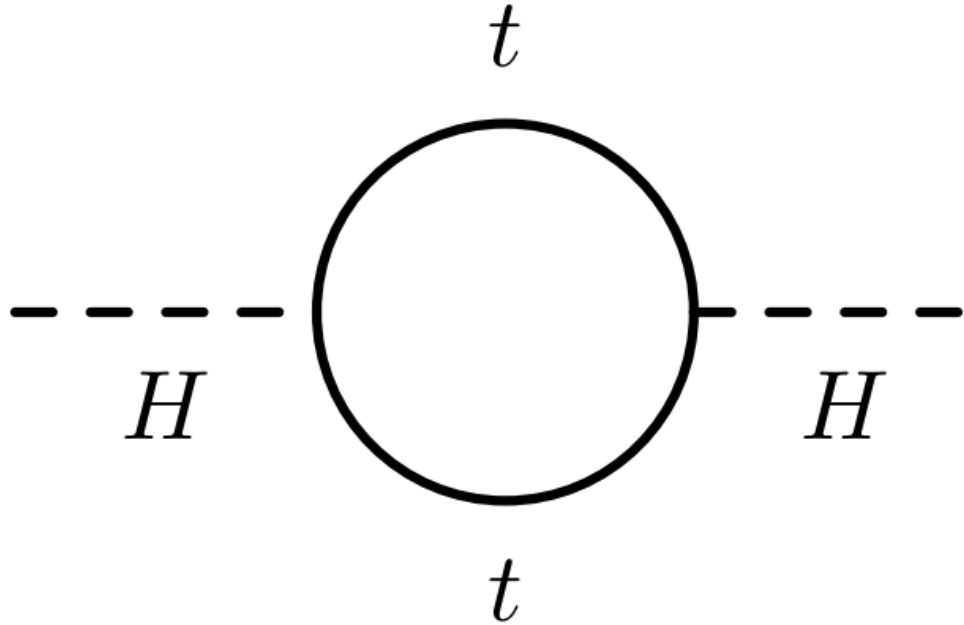


Figure 2.5: The dominant quantum loop correction to the Higgs mass in the Standard Model.

there is no new physics before the Planck scale of gravity, $\Lambda_{\text{Planck}} = 10^{19}$ GeV. In this case, we expect the corrections to the Higgs mass to be

$$\delta m_H^2 \approx \left(\frac{m_t}{8\pi^2 \langle \phi \rangle_{VEV}} \right)^2 \Lambda_{\text{Planck}}^2. \quad (2.17)$$

290 To achieve the miraculous cancellation required to get the observed Higgs mass of
 291 125 GeV, one needs to then set the bare Higgs mass m_0 , our input to the Standard
 292 Model Lagrangian, itself to a *precise* value $\sim 10^{19}$ GeV. This extraordinary level of
 293 parameter finetuning is quite undesirable, and within the framework of the Standard
 294 Model alone, there is little that can be done to alleviate this issue.

295 An additional concern, of a different nature, is the lack of a *dark matter* candidate
 296 in the Standard Model. Dark matter was discovered by observing galactic rotation
 297 curves, which showed that much of the matter that interacts gravitationally is invisible
 298 to our (electromagnetic) telescopes [16–22]. The postulation of the existence of dark
 299 matter, which interacts at least through gravity, allows one to understand these galactic

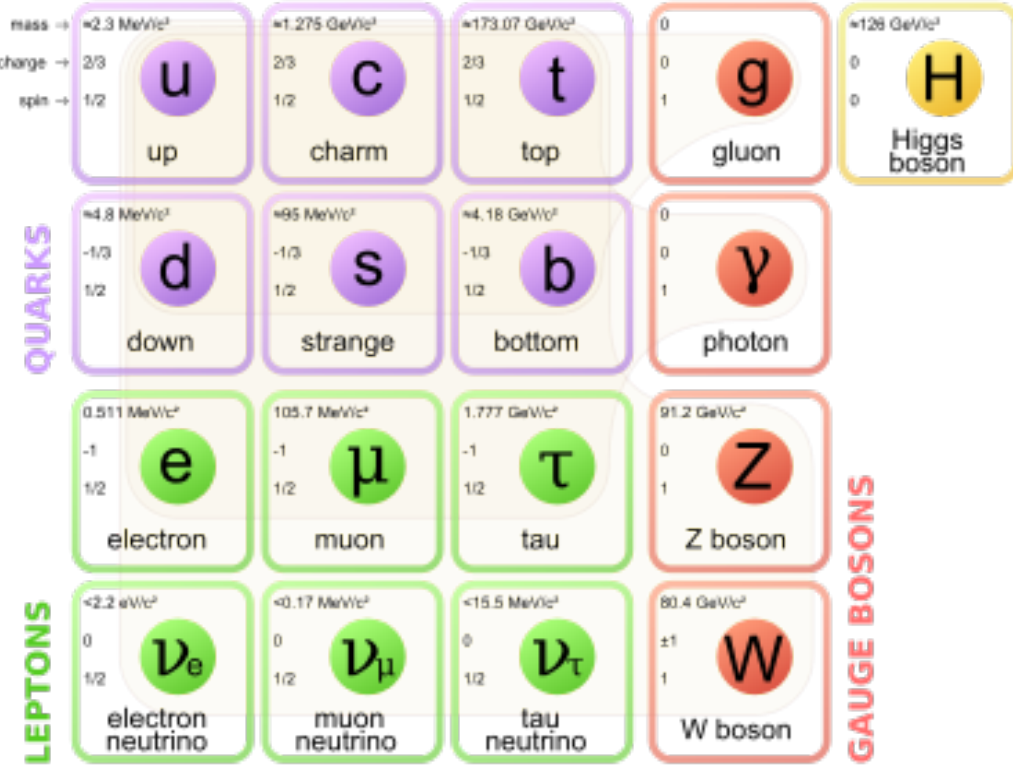


Figure 2.6: Particles of the Standard Model

300 rotation curves. Unfortunately, no particle in the Standard Model could possibly be
 301 the dark matter particle. The only candidate truly worth another look is the neutrino,
 302 but it has been shown that the neutrino content of the universe is simply too small
 303 to explain the galactic rotation curves [22, 64]. The experimental evidence from
 304 the galactic rotations curves thus show there *must* be additional physics beyond the
 305 Standard Model, which is yet to be understood.

306 In the next chapter, we will see how these problems can be alleviated by the theory
 307 of supersymmetry.

Supersymmetry

310 This chapter will introduce supersymmetry (SUSY) [15, 23–35]. We will begin
 311 by introducing the concept of a *superspace*, and discuss some general ingredients of
 312 supersymmetric theories. This will include a discussion of how the problems with the
 313 Standard Model described in Ch. 2 are naturally fixed by these theories.

314 The next step is to discuss the particle content of the *Minimally Supersymmetric*
 315 *Standard Model* (MSSM). As its name implies, this theory contains the minimal
 316 additional particle content to make Standard Model supersymmetric. We then discuss
 317 the important phenomenological consequences of this theory, especially as it would
 318 be observed in experiments at the LHC.

319 **3.1 Supersymmetric theories : from space to
 320 superspace**

321 **Coleman-Mandula “no-go” theorem**

322 We begin the theoretical motivation for supersymmetry by citing the “no-go” theorem
 323 of Coleman and Mandula [65]. This theorem forbids *spin-charge unification*. It
 324 states that all quantum field theories which contain nontrivial interactions must be
 325 a direct product of the Poincaré group of Lorentz symmetries, the internal product
 326 of gauge symmetries, and the discrete symmetries of parity, charge conjugation,
 327 and time reversal. The assumptions which go into building the Coleman-Mandula

theorem are quite restrictive, but there is solution, which has become known as *supersymmetry* [26, 66]. In particular, we must introduce a *spinorial* group generator Q . Alternatively, and equivalently, this can be viewed as the addition of anti-commuting coordinates. Space plus these new anti-commuting coordinates is then called *superspace* [67]. We will not investigate this view in detail, but it is also a quite intuitive and beautiful way to construct supersymmetry [15].

334 Supersymmetry transformations

A *supersymmetric* transformation Q transforms a bosonic state into a fermionic state, and vice versa :

$$Q |\text{Fermion}\rangle = |\text{Boson}\rangle \quad (3.1)$$

$$Q |\text{Boson}\rangle = |\text{Fermion}\rangle \quad (3.2)$$

To ensure this relation holds, Q must be an anticommuting spinor. Additionally, since spinors are inherently complex, Q^\dagger must also be a generator of the supersymmetry transformation. Since Q and Q^\dagger are spinor objects (with $s = 1/2$), we can see that supersymmetry must be a spacetime symmetry. The Haag-Lopuszanski-Sohnius extension [66] of the Coleman-Mandula theorem [65] is quite restrictive about the forms of such a symmetry. Here, we simply write the (anti-) commutation relations [15] :

$$Q_\alpha, Q_{\dot{\alpha}}^\dagger = -2\sigma_{\alpha\dot{\alpha}\mu} P_\mu \quad (3.3)$$

$$Q_\alpha, Q_{\dot{\beta}} = Q_{\dot{\alpha}}^\dagger, Q_{\dot{\beta}}^\dagger = 0 \quad (3.4)$$

$$[P^\mu, Q_\alpha] = [P^\mu, Q_{\dot{\alpha}}^\dagger] = 0 \quad (3.5)$$

335 Supermultiplets

In a supersymmetric theory, we organize single-particle states into irreducible representations of the supersymmetric algebra which are known as *supermultiplets*.

338 Each supermultiplet contains a fermion state $|F\rangle$ and a boson state $|B\rangle$. These two
339 states are known as *superpartners*. These are related by some combination of
340 Q and Q^\dagger , up to a spacetime transformation. Q and Q^\dagger commute with the mass-
341 squared operator $-P^2$ and the operators corresponding to the gauge transformations
342 [15]: in particular, the gauge interactions of the Standard Model. In an unbroken
343 supersymmetric theory, this means the states $|F\rangle$ and $|B\rangle$ have exactly the same mass,
344 electromagnetic charge, electroweak isospin, and color charges. One can also prove
345 [15] that each supermultiplet contains the exact same number of bosonic (n_B) and
346 fermion (n_F) degrees of freedom. We now explore the possible types of supermultiples
347 one can find in a renormalizable supersymmetric theory.

348 Since each supermultiplet must contain a fermion state, the simplest type of
349 supermultiplet contains a single Weyl fermion state ($n_F = 2$) which is paired with
350 $n_B = 2$ scalar bosonic degrees of freedom. This is most conveniently constructed
351 as single complex scalar field. We call this construction a *scalar supermultiplet* or
352 *chiral supermultiplet*. The second name is indicative, as only chiral supermultiplets
353 can contain fermions whose right-handed and left-handed components transform
354 differently under the gauge interactions (as of course happens in the Standard Model).

355 The second type of supermultiplet we construct is known as a *gauge supermul-*
356 *tiplet*. We take a spin-1 gauge boson (which must be massless due to the gauge
357 symmetry, so $n_B = 2$) and pair this with a single massless Weyl spinor¹. The gauge
358 bosons transform as the adjoint representation of their respective gauge groups
359 Their fermionic partners, which are known as gauginos, must also. In particular,
360 the left-handed and right-handed components of the gaugino fermions have the same
361 gauge transformation properties.

362 Excluding gravity, this is the entire list of supermultiplets which can participate
363 in renormalizable interactions in what is known as $N = 1$ supersymmetry. This

¹Choosing an $s = 3/2$ massless fermion leads to nonrenormalizable interactions.

means there is only one copy of the supersymmetry generators Q and Q^\dagger . This is essentially the only “easy” phenomenological choice, since it is the only option in four dimensions which allows for the chiral fermions and parity violations to be built into the Standard Model. We will not look further into $N > 1$ supersymmetry in this thesis.

The primary goal, after understanding the possible structures of the multiplets above, is to fit the Standard Model particles into a multiplet, and therefore make predictions about their supersymmetric partners. We explore this in the next section.

3.2 Minimally Supersymmetric Standard Model

To construct what is known as the MSSM [15, 68–71], we need a few ingredients and assumptions. First, we match the Standard Model particles with their corresponding superpartners of the MSSM. We will also introduce the naming of the superpartners (also known as *sparticles*). We discuss a very common additional restraint imposed on the MSSM, known as R –parity. We also discuss the concept of soft supersymmetry breaking and how it manifests itself in the MSSM.

Chiral supermultiplets

The first thing we deduce is directly from Sec. 3.1. The bosonic superpartners associated to the quarks and leptons *must* be spin 0, since the quarks and leptons must be arranged in a chiral supermultiplet. This is essential, since the chiral supermultiplet is the only one which can distinguish between the left-handed and right-handed components of the Standard Model particles. The superpartners of the quarks and leptons are known as *squarks* and *sleptons*, or *sfermions* in aggregate. (for “scalar quarks”, “scalar leptons”, and “scalar fermion”). The “s-” prefix can also be added to the individual quarks i.e. *selectron*, *sneutrino*, and *stop*. The notation

388 is to add a \sim over the corresponding Standard Model particle i.e. \tilde{e} , the selectron is
 389 the superpartner of the electron. The two-component Weyl spinors of the Standard
 390 Model must each have their own (complex scalar) partner i.e. e_L, e_R have two distinct
 391 partners : \tilde{e}_L, \tilde{e}_R . As noted above, the gauge interactions of any of the sfermions are
 392 identical to those of their Standard Model partners.

Due to the scalar nature of the Higgs, it must obviously lie in a chiral supermultiplet. To avoid gauge anomalies and ensure the correct Yukawa couplings to the quarks and leptons [15], we must add additional Higgs bosons to any supersymmetric theory. In the MSSM, we have two chiral supermultiplets. The SM (SUSY) parts of the multiplets are denoted $H_u(\tilde{H}_u)$ and $H_d(\tilde{H}_d)$. Writing out H_u and H_d explicitly:

$$H_u = \begin{pmatrix} H_u^+ \\ H_u^0 \end{pmatrix} \quad (3.6)$$

$$H_d = \begin{pmatrix} H_d^0 \\ H_d^- \end{pmatrix} \quad (3.7)$$

393 we see that H_u looks very similar to the SM Higgs with $Y = 1$, and H_d is symmetric
 394 with $+ \rightarrow -$ and $Y = -1$. The SM Higgs boson, h_0 , is a linear superposition of the
 395 neutral components of these two doublets. The SUSY parts of the Higgs multiplets,
 396 \tilde{H}_u and \tilde{H}_d , are each left-handed Weyl spinors. For generic spin-1/2 sparticles, we
 397 add the “-ino” suffix. We then call the partners of the two Higgs collectively the
 398 *Higgsinos*.

399 Gauge supermultiplets

400 The superpartners of the gauge bosons must all be in gauge supermultiplets since
 401 they contain a spin-1 particle. Collectively, we refer to the superpartners of the
 402 gauge bosons as the gauginos.

403 The first gauge supermultiplet contains the gluon, and its superpartner, which is
 404 known as the *gluino*, denoted \tilde{g} . The gluon is of course the SM mediator of $SU(3)_C$

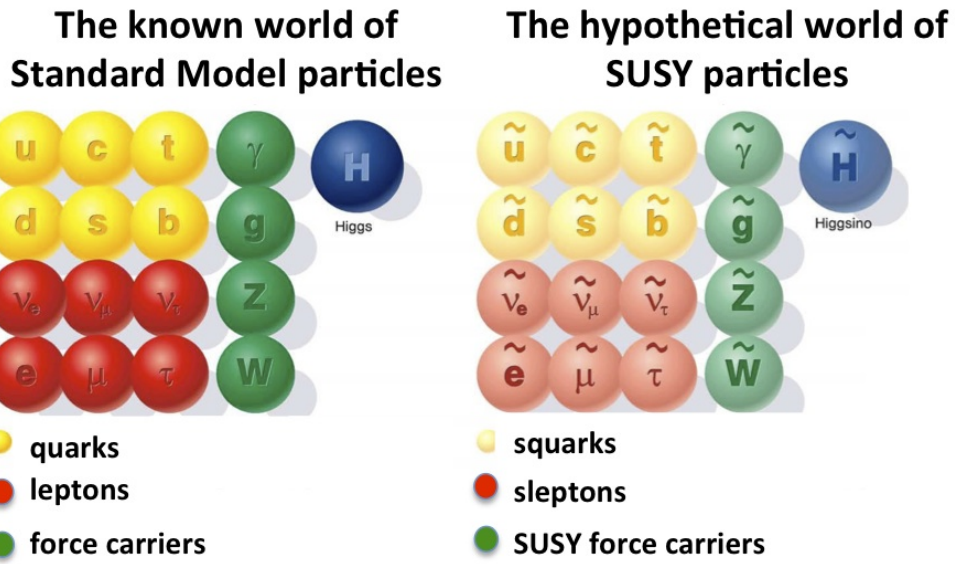


Figure 3.1: Particles of the MSSM

405 The gluino is also a colored particle, subject to $SU(3)_C$. From the SM before EWSB,
 406 we have the four gauge bosons of the electroweak symmetry group $SU(2)_L \otimes U(1)_Y$:
 407 $W^{1,2,3}$ and B^0 . The superpartners of these particles are thus the *winos* $\tilde{W}^{1,2,3}$ and
 408 *bino* \tilde{B}^0 , where each is placed in another gauge supermultiplet with its corresponding
 409 SM particle. After EWSB, without breaking supersymmetry, we would also have the
 410 zino \tilde{Z}^0 and photino $\tilde{\gamma}$.

411 The entire particle content of the MSSM can be seen in Fig. 3.1.

412 At this point, it's important to take a step back. Where are these particles?
 413 As stated above, supersymmetric theories require that the masses and all quantum
 414 numbers of the SM particle and its corresponding sparticle are the same. Of course,
 415 we have not observed a selectron, squark, or wino. The answer, as it often is, is that
 416 supersymmetry is *broken* by the vacuum state of nature [15].



Figure 3.2: This Feynmann diagram shows how proton decay is induced in the MSSM, if one does not impose R -parity.

417 **R -parity**

This section is a quick aside to the general story. R – parity refers to an additional discrete symmetry which is often imposed on supersymmetric models. For a given particle state, we define

$$418 \quad R = (-1)^{3(B-L)+2s} \quad (3.8)$$

418 where B, L is the baryon (lepton) number and s is the spin. The imposition of
 419 this symmetry forbids certain terms from the MSSM Lagrangian that would violate
 420 baryon and/or lepton number. This is required in order to prevent proton decay, as
 421 shown in Fig. 3.2². .

422 In supersymmetric models, this is a \mathbb{Z}_2 symmetry, where SM particles have $R = 1$
 423 and sparticles have $R = -1$. We will take R – parity as part of the definition of
 424 the MSSM. We will discuss later the *drastic* consequences of this symmetry on SUSY
 425 phenomenology

426 **Soft supersymmetry breaking**

The fundamental idea of *soft* supersymmetry breaking [15, 34, 35, 72, 73] is that we would like to break supersymmetry without reintroducing the quadratic divergences

²Proton decay can actually be prevented by allowing only one of the four potential R-parity violating terms to survive.

we discussed at the end of Chapter Ch. 2. We write the Lagrangian in a form :

$$\mathcal{L}_{\text{MSSM}} = \mathcal{L}_{\text{SUSY}} + \mathcal{L}_{\text{soft}} \quad (3.9)$$

427 In this sense, the symmetry breaking is “soft”, since we have separated out the
 428 completely symmetric terms from those soft terms which will not allow the quadratic
 429 divergences to the Higgs mass.

430 The explicitly allowed terms in the soft-breaking Lagrangian are [35]:

431 • Mass terms for the scalar components of the chiral supermultipletss

432 • Mass terms for the Weyl spinor components of the gauge supermultipletss

433 • Trilinear couplings of scalar components of chiral supermultiplets

In particular, using the field content described above for the MSSM, the softly-broken portion of the MSSM Lagrangian can be written

$$\mathcal{L}_{\text{soft}} = -\frac{1}{2} \left(M_3 \tilde{g} \tilde{g} + M_2 \tilde{W} \tilde{W} + M_1 \tilde{B} \tilde{B} + c.c. \right) \quad (3.10)$$

$$- \left(\tilde{u} a_u \tilde{Q} H_u - \tilde{d} a_d \tilde{Q} H_d - \tilde{e} a_e \tilde{L} H_d + c.c. \right) \quad (3.11)$$

$$- \tilde{Q}^\dagger m_Q^2 \tilde{Q} - \tilde{L}^\dagger m_L^2 \tilde{L} - \tilde{u} m_u^2 \tilde{u}^\dagger - \tilde{d} m_d^2 \tilde{d}^\dagger - \tilde{e} m_e^2 \tilde{e}^\dagger \quad (3.12)$$

$$- m_{H_u}^2 H_u^* H_u - m_{H_d}^2 H_d^* H_d - (b H_u H_d + cc). \quad (3.13)$$

434 where we have introduced the following notations :

435 1. M_3, M_2, M_1 are the gluino, wino, and bino masses.

436 2. a_u, a_d, a_e are complex 3×3 matrices in family space.

437 3. $m_Q^2, m_u^2, m_d^2, m_L^2, m_e^2$ are hermitian 3×3 matrices in family space.

438 4. $m_{H_u}^2, m_{H_d}^2, b$ are the SUSY-breaking contributions to the Higgs potential.

439 We have written matrix terms without any sort of additional notational decoration
 440 to indicate their matrix nature, and we now show why. The first term Item 1 is the
 441 set of mass terms for the gluino, wino, and bino. The second term Item 2, containing
 442 a_u, a_d, a_e , has strong constraints from experiments [74, 75]. We will assume that
 443 each $a_i, i = u, d, e$ is proportional to the Yukawa coupling matrix : $a_i = A_{i0}y_i$. The
 444 third term Item 3 can be similarly constrained by experiments [68, 75–82]. We will
 445 assume the elements of the fourth term Item 4 contributing to the Higgs potential as
 446 well as all of the Item 1 terms must be real, which limits the possible CP-violating
 447 interactions to those of the Standard Model. We thus only consider flavor-blind,
 448 CP-conserving interactions within the MSSM.

The important mixing for mass and gauge interaction eigenstates in the MSSM occurs within electroweak sector, in a process akin to EWSB in the Standard Model. The neutral portions of the Higgsinos doublets and the neutral gauginos ($\tilde{H}_u^0, \tilde{H}_d^0, \tilde{B}^0, \tilde{W}^0$) of the gauge interaction basis mix to form what are known as the *neutralinos* of mass basis :

$$M_{\tilde{\chi}} = \begin{pmatrix} M_1 & 0 & -c_\beta s_W m_Z & s_\beta s_W m_Z \\ 0 & M_2 & c_\beta c_W m_Z & -s_\beta c_W m_Z \\ -c_\beta s_W m_Z & c_\beta c_W m_Z & 0 & -\mu \\ s_\beta s_W m_Z & -s_\beta c_W m_Z & -\mu & 0 \end{pmatrix} \quad (3.14)$$

449 where $s(c)$ are the sine and cosine of angles related to EWSB, which introduced
 450 masses to the gauginos and higgsinos. Diagonalization of this matrix gives the four
 451 neutralino mass states, listed without loss of generality in order of increasing mass :
 452 $\tilde{\chi}_{1,2,3,4}^0$.

453 The neutralinos, especially the lightest neutralino $\tilde{\chi}_1^0$, are important ingredients
 454 in SUSY phenomenology.

455 The same process can be done for the electrically charged gauginos with
 456 the charged portions of the Higgsino doublets along with the charged winos

457 $(\tilde{H}_u^+, \tilde{H}_d^+, \tilde{W}^+, \tilde{W}^-)$. This leads to the *charginos*, again in order of increasing mass :
458 $\tilde{\chi}_{1,2}^\pm$.

459

3.3 Phenomenology

460 We are finally at the point where we can discuss the phenomenology of the MSSM,
461 in particular as it manifests itself at the energy scales of the LHC.

462 As noted above in Sec. 3.2, the assumption of R -parity has important conse-
463 quences for MSSM phenomenology. The SM particles have $R = 1$, while the sparticles
464 all have $R = -1$. Simply, this is the “charge” of supersymmetry. Since the particles
465 of LHC collisions (pp) have total incoming $R = 1$, we must expect that all sparticles
466 will be produced in *pairs*. An additional consequence of this symmetry is the fact
467 that the lightest supersymmetric particle (LSP) is *stable*. Off each branch of the
468 Feynmann diagram shown in Fig. 3.3, we have $R = -1$, and this can only decay to
469 another sparticle and a SM particle. Once we reach the lightest sparticle in the decay,
470 it is absolutely stable. This leads to the common signature E_T^{miss} for a generic SUSY
471 signal.

472 For this thesis, we will be presenting an inclusive search for squarks and gluinos
473 with zero leptons in the final state. This is a very interesting decay channel, due to
474 the high cross-sections of $\tilde{g}\tilde{g}$ and $\tilde{q}\tilde{q}$ decays, as can be seen in Sec. 3.3 [83].

475 This is a direct consequence of the fact that these are the colored particles of the
476 MSSM. Since the sparticles interact with the gauge groups of the SM in the same way
477 as their SM partners, the colored sparticles, the squarks and gluinos, are produced
478 and decay as governed by the color group $SU(3)_C$ with the strong coupling g_S . Gluino
479 pair production is particularly copious, due to color factor corresponding to the color
480 octet of $SU(3)_C$.

481 In the case of squark pair production, the most common decay mode of the squark

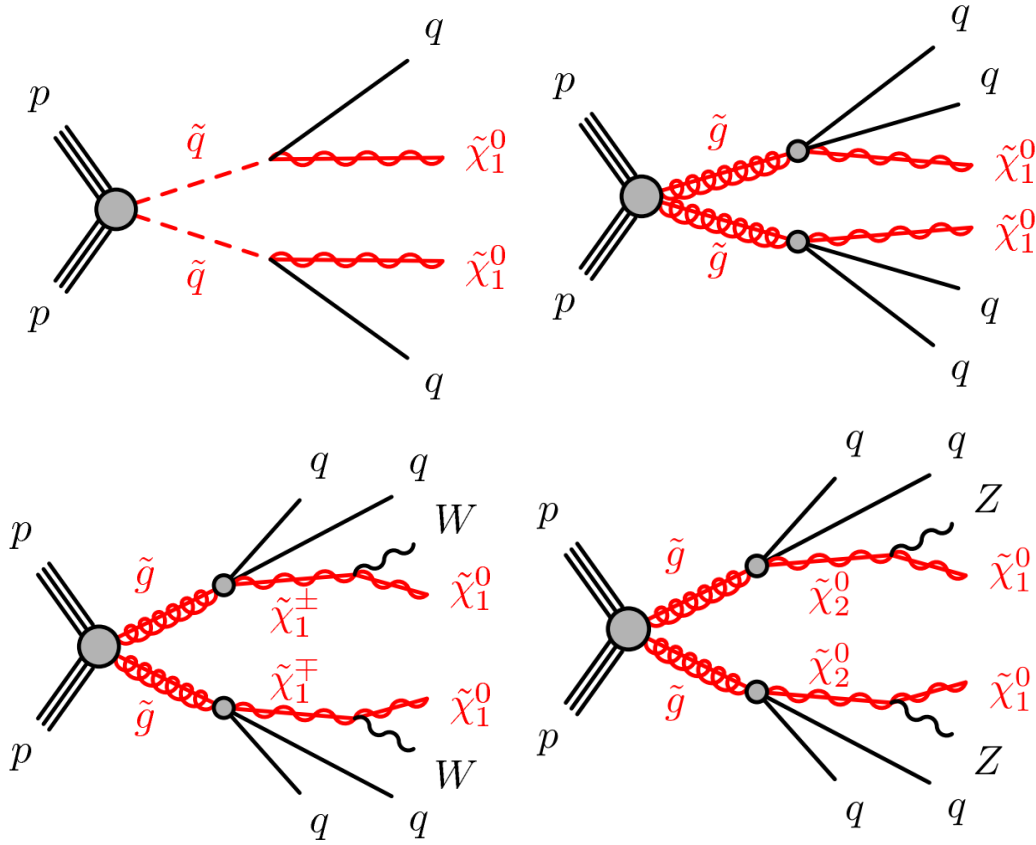


Figure 3.3: SUSY signals considered in this thesis

in the MSSM is a decay directly to the LSP plus a single SM quark [15]. This means the basic search strategy for squark pair production is two jets from the final state quarks, plus missing transverse energy from the LSPs.

For gluino pair production, the most common decay is $\tilde{g} \rightarrow g\tilde{q}$, due to the large g_S coupling. The squark then decays as listed above. In this case, we generically search for four jets and missing transverse energy from the LSPs.

In the context of experimental searches for SUSY, we often consider *simplified models*. These models make certain assumptions which allow easy comparisons of results by theorists and experimentalists. In the context of this thesis, the simplified models will make assumptions about the branching ratios described in the preceding paragraphs. In particular, we will often choose a model where the decay of interest occurs with 100% branching ratio. This is entirely for ease of interpretation, but it is

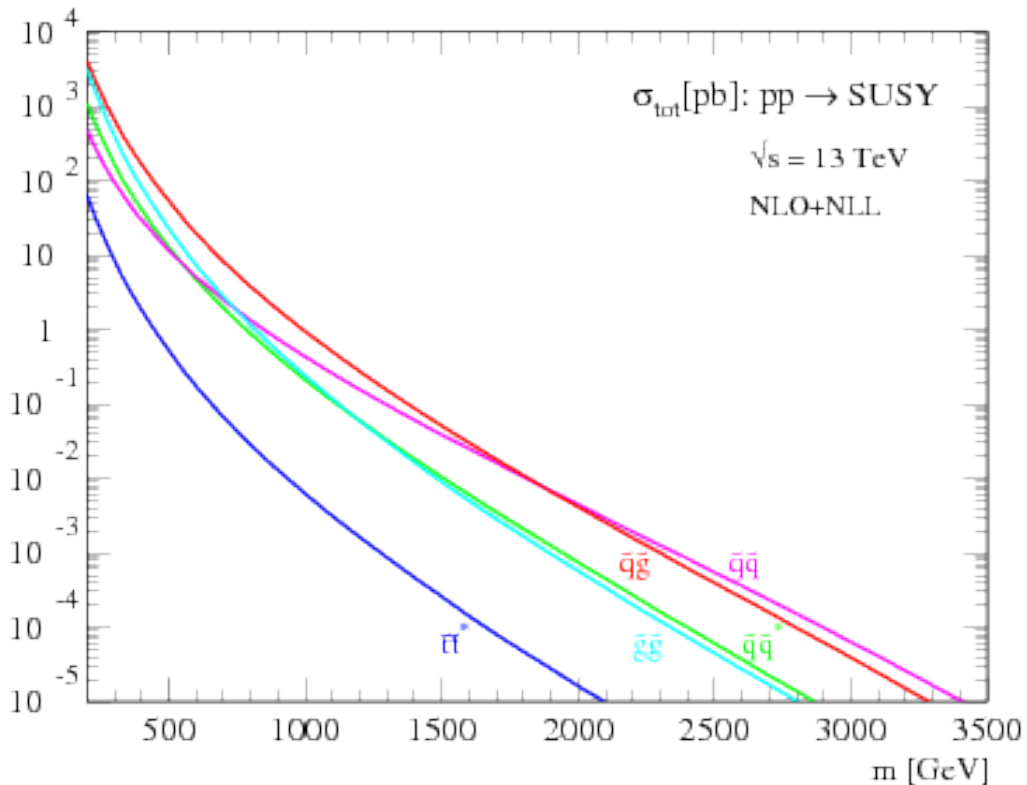


Figure 3.4: SUSY production cross-sections as a function of sparticle mass at $\sqrt{s} = 13$ TeV.

494 important to recognize that these are more a useful comparison tool, especially with
 495 for setting limits, than a strict statement about the potential masses of sought-after
 496 beyond the Standard Model particle.

497 3.4 How SUSY solves the problems with the SM

498 We now return to the issues with the Standard Model as described in Ch. 2 to see
 499 how these issues are solved by supersymmetry.

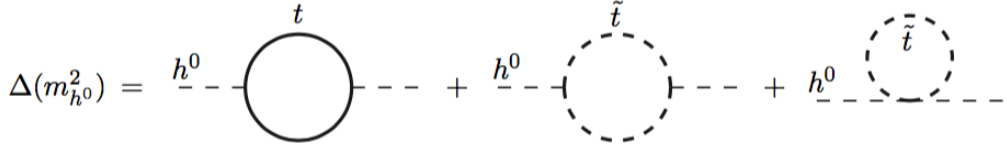


Figure 3.5: Loop diagrams correct the Higgs mass in the MSSM

500 Quadratic divergences to the Higgs mass

The quadratic divergences induced by the loop corrections to the Higgs mass, for example from the top Yukawa coupling, goes as

$$\delta m_H^2 \approx \left(\frac{m_t}{8\pi^2 \langle \phi \rangle_{VEV}} \right)^2 \Lambda_{Planck}^2. \quad (3.15)$$

501 The miraculous thing about SUSY is each of these terms *automatically* comes with
 502 a term which exactly cancels this contribution [15]. The fermions and bosons
 503 have opposite signs in this loop diagram to all orders in perturbation theory, which
 504 completely solves the hierarchy problem. This is the strongest motived reason for
 505 supersymmetry.

506 Gauge coupling unification

507 An additional motivation for supersymmetry is seen by the gauge coupling unification
 508 high scales. In the Standard Model, as we saw the gauge couplings fail to unify at
 509 high energies. In the MSSM and many other forms of supersymmetry, the gauge
 510 couplings unify at high energy, as can be seen in Fig. 3.6. This provides additional
 511 aesthetic motivation for supersymmetric theories.

512 Dark matter

513 As we discussed previously, the lack of any dark matter candidate in the Standard
 514 Model naturally leads to beyond the Standard Model theories. In the Standard Model,
 515 there is a natural dark matter candidate in the lightest supersymmetric particle [15]

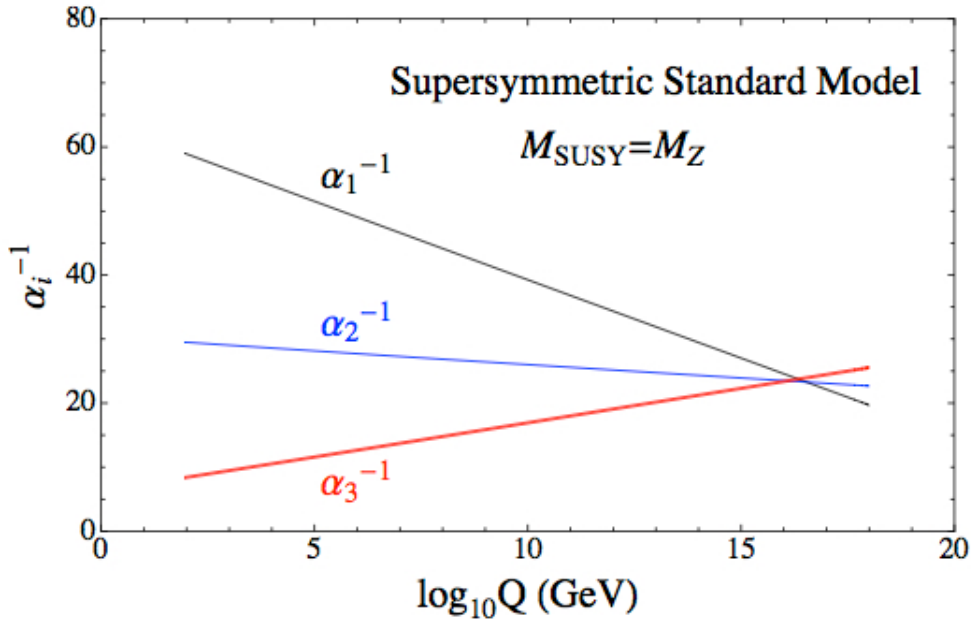


Figure 3.6: The running of Standard Model gauge couplings: compare to Fig. 2.4. The MSSM gauge couplings nearly intersect at high energies.

516 The LSP would in dark matter experiments be called a *weakly-interacting massive*
 517 *particle* (WIMP), which is a type of cold dark matter [22, 84]. These WIMPS would
 518 only interact through the weak force and gravity, which is exactly as a model like
 519 the MSSM predicts for the neutralino. In Fig. 3.7, we can see the current WIMP
 520 exclusions for a given mass. The range of allowed masses which have not been
 521 excluded for LSPs and WIMPs have significant overlap. This provides additional
 522 motivation outside of the context of theoretical details.

523 3.5 Conclusions

524 Supersymmetry is the most well-motivated theory for physics beyond the Standard
 525 Model. It provides a solution to the hierarchy problem, leads to gauge coupling
 526 unification, and provides a dark matter candidate consistent with galactic rotation
 527 curves. As noted in this chapter, due to the LSPs in the final state, most SUSY



Figure 3.7: WIMP exclusions from direct dark matter detection experiments.

528 searches require a significant amount of missing transverse energy in combination
 529 with jets of high transverse momentum. However, there is some opportunity to do
 530 better than this, especially in final states where one has two weakly-interacting LSPs
 531 on opposite sides of some potentially complicated decay tree. We will see how this is
 532 done in Ch. 7.

The Large Hadron Collider

535 The Large Hadron Collider (LHC) produces high-energy protons which collide at the
 536 center of multiple large experiments at CERN on the outskirts of Geneva, Switzerland
 537 [85]. The LHC produces the highest energy collisions in the world, with a design
 538 center-of-mass energy of $\sqrt{s} = 14$ TeV, which allows the experiments to investigate
 539 physics at higher energies than previous colliders. This chapter will summarize the
 540 basics of accelerator physics, especially with regards to discovering physics beyond
 541 the Standard Model. We will describe the CERN accelerator complex and the LHC.

542 **4.1 Basics of Accelerator Physics**

543 This section follows closely the presentation of [86].

Simple particle accelerators simply rely on the acceleration of charged particles in a static electric field. Given a field of strength E , charge q , and mass m , this is simply

$$a = \frac{qE}{m}. \quad (4.1)$$

544 For a given particle with a given mass and charge, this is limited by the static electric
 545 field which can be produced, which in turn is limited by electrical breakdown at high
 546 voltages.

547 There are two complementary solutions to this issue. First, we use the *radio*
 548 *frequency acceleration* technique. We call the devices used for this *RF cavities*. The
 549 cavities produce a time-varied electric field, which oscillate such that the charged

550 particles passing through it are accelerated towards the design energy of the RF
 551 cavity. This oscillation forces the particles into *bunches*, since particles which are
 552 slightly off the central energy induced by the RF cavity are accelerated towards the
 553 design energy.

Second, one bends the particles in a magnetic field, which allows them to pass through the same RF cavity over and over. This second process is often limited by *synchrotron radiation*, which describes the radiation produced when a charged particle is accelerated. The power radiated is

$$P \sim \frac{1}{r^2} \left(E/m \right)^4 \quad (4.2)$$

554 where r is the radius of curvature and E, m is the energy (mass) of the charged
 555 particle. Given an energy which can be produced by a given set of RF cavities (which
 556 is *not* limited by the mass of the particle), one then has two options to increase the
 557 actual collision energy : increase the radius of curvature or use a heavier particle.
 558 Practically speaking, the easiest options for particles in a collider are protons and
 559 electrons, since they are copiously produced in nature and do not decay¹. Given the
 560 dependence on mass, we can see why protons are used to reach the highest energies.
 561 The tradeoff for this is that protons are not point particles, and we thus we don't
 562 know the exact incoming four-vectors of the protons. This is a reflection of the “bag
 563 model” discussed in Ch. 2, where each proton is actually a bag of incoming quarks
 564 and gluons, which individually contribute to the total proton energy.

The particle *beam* refers to the bunches combined. An important property of a beam of a particular energy E , moving in uniform magnetic field B , containing particles of momentum p is the *beam rigidity* :

$$R \equiv rB = p/c. \quad (4.3)$$

¹Muon colliders are a potential future option at high energies, since the relativistic γ factor gives them a relatively long lifetime in the lab frame.

565 The linear relation between r and p , or alternatively B and p have important
 566 consequences for LHC physics. For hadron colliders, this is the limiting factor on
 567 going to higher energy scales; one needs a proportionally larger magnetic field to
 568 keep the beam accelerating in a circle.

569 Besides the rigidity of the beam, the most important quantities to characterize
 570 a beam are known as the (normalized) *emittance* ϵ_N and the *betatron function* β .
 571 These quantities determine the transverse size σ of a relativistic beam $v \leq c$ beam :
 572 $\sigma^2 = \beta^* \epsilon_N / \gamma_{\text{rel}}$, where β^* is the value of the betatron function at the collision point
 573 and γ_{rel} is the Lorentz factor.

These quantities determine the *instantaneous luminosity* L of a collider, which combined with the cross-section σ of a particular physics process, give the rate of the physics process :

$$R = L\sigma. \quad (4.4)$$

The instantaneous luminosity L is given by :

$$L = \frac{f_{\text{rev}} N_b^2 F}{4\pi\sigma^2} = \frac{f_{\text{rev}} n N_b^2 \gamma_{\text{rel}} F}{4\pi\beta^* \epsilon_N}. \quad (4.5)$$

574 Here we have introduced the frequency of revolutions f_{rev} , the number of bunches n ,
 575 the number of protons per bunch N_b^2 , and a geometric factor F related to the crossing
 576 angle of the beams.

The *integrated luminosity* $\int L dt$ gives the total number of a particular physics process P , with cross-section σ_P .

$$N_P = \sigma_P \int L dt. \quad (4.6)$$

577 Due to this simple relation, one can also quantify the “amount of data delivered” by
 578 a collider simply by $\int L dt$.



Figure 4.1: The CERN accelerator complex. Copyright CERN.

4.2 Accelerator Complex

The Large Hadron Collider is the last accelerator in a chain of accelerators which together form the CERN accelerator complex, shown in Fig. 4.1. The protons begin their journey to annihilation in a hydrogen source, where they are subsequently ionized. The first acceleration occurs in the Linac 2, a linear accelerator composed of RF cavities. The protons leave the Linac 2 at an energy of 50 MeV and enter the Proton Synchrotron Booster (PSB). The PSB contains four superimposed rings, which accelerate the protons to 1.4 GeV. The protons are then injected into the Proton Synchrotron (PS). This synchrotron increases the energy up to 25 GeV. After leaving the PS, the protons enter the Super Proton Synchrotron (SPS). This is the last step before entering the LHC ring, and the protons are accelerated to 450 GeV. From the SPS, the protons are injected into the beam pipes of the LHC. The process

591 to fill the LHC rings with proton bunches from start to finish typically takes about
592 four minutes.

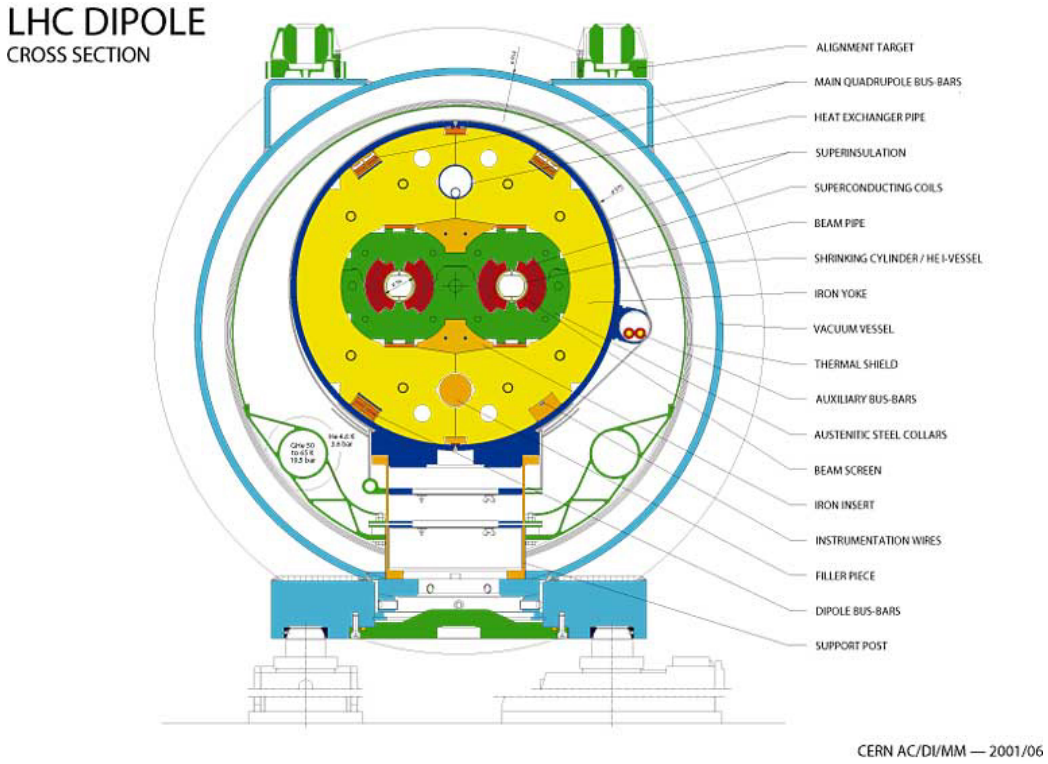
593 **4.3 Large Hadron Collider**

The Large Hadron Collider is the final step in the CERN accelerator complex, and produces the collisions analyzed in this thesis. From the point of view of experimentalists on the general-purpose ATLAS and CMS experiments, the main goal of the LHC is to deliver collisions at the highest possible energy, with the highest possible instantaneous luminosity. The LHC was installed in the existing 27 km tunnel used by the Large Electron Positron (LEP) collider [87]. This allowed the existing accelerator complex at CERN, described in the previous section, to be used as the injection system to prepare the protons up to 450 GeV. Many aspects of the LHC design were decided by this very constraint, and specified the options allowed to increase the energy or luminosity. In particular, the radius of the tunnel was already specified. From Eq.Eq. (4.3), this implies the momentum (or energy) of the beam is entirely determined by the magnetic field. Given the 27 km circumference of the LEP tunnel, one can calculate the required magnetic field to reach the 7 TeV per proton design energy of the LHC :

$$r = C/2\pi = 4.3 \text{ km} \quad (4.7)$$

$$\rightarrow B = \frac{p}{rc} = 5 \text{ T} \quad (4.8)$$

594 In fact, the LHC consists of eight 528 m straight portions consisting of RF cavities,
595 used to accelerate the particles, and 8 circular portions which bend the protons
596 around the LHC ring. These circular portions actually have a slightly smaller radius
597 of curvature $r = 2804$ m, and require $B = 8.33$ T. To produce this large field,
598 superconducting magnets are used.



CERN AC/DI/MM — 2001/06

Figure 4.2: Schematic of an LHC dipole magnet. Copyright CERN.

599 Magnets

600 There are many magnets used by the LHC machine, but the most important are
 601 the 1232 dipole magnets. A schematic is shown in Fig. Fig. 4.2 and a photograph is
 602 present in Fig. 4.3.

603 The magnets are made of Niobium and Titanium. The maximum field strength is
 604 10 T when cooled to 1.9 Kelvin. The magnets are cooled by superfluid helium, which
 605 is supplied by a large cryogenic system. Due to heating between the eight helium
 606 refrigerators and the beampipe, the helium is cooled in the refrigerators to 1.8 K.

607 A failure in the cooling system can cause what is known as a *quench*. If the
 608 temperature goes above the critical superconducting temperature, the metal loses its
 609 superconducting properties, which leads to a large resistance in the metal. This leads
 610 to rapid temperature increases, and can cause extensive damages if not controlled.

611 The dipole magnets are 16.5 meters long with a diameter of 0.57 meters. There

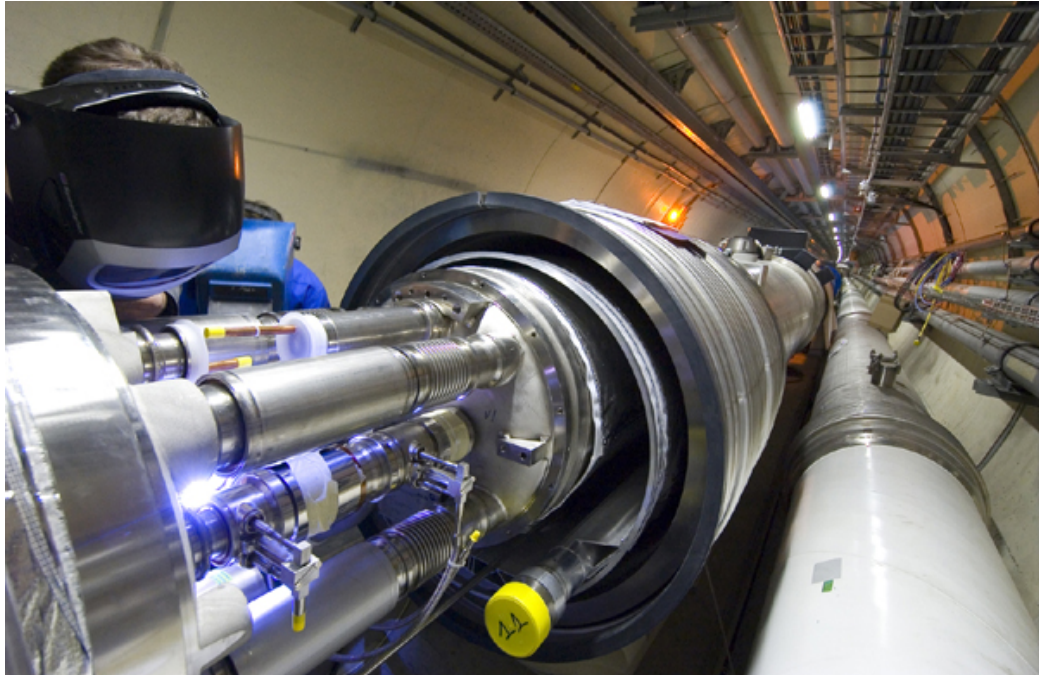


Figure 4.3: Photograph of a technician connecting an LHC dipole magnet. Copyright CERN.

612 are two individual beam pipes inside each magnet, which allows the dipoles to house
613 the beams travelling in both directions around the LHC ring. They curve slightly,
614 at an angle of 5.1 mrad, which carefully matches the curvature of the ring. The
615 beampipes inside of the magnets are held in high vacuum to avoid stray interactions
616 with the beam.

617 4.4 Dataset Delivered by the LHC

618 In this thesis, we analyze the data delivered by the LHC to ATLAS in the 2015 and
619 2016 datasets. The beam parameters relevant to this dataset are available in Tab. 4.1.
620

621 The peak instantaneous luminosity delivered in 2015 (2016) was $L =$
622 $5.2(11) \text{ cm}^{-2}\text{s}^{-1} \times 10^{33}$. One can note that the instantaneous luminosity delivered in
623 the 2016 dataset exceeds the design luminosity of the LHC. The total integrated

Parameter	Injection	Extraction
Energy (GeV)	450	7000
Rigidity (T-m)	3.8	23353
Bunch spacing (ns)	25	25
Design Luminosity ($\text{cm}^{-2}\text{s}^{-1} \times 10^3$)	-	1.0
Bunches per proton beam	2808	2808
Protons per bunch	1.15 e11	1.15 e11
Beam lifetime (hr)	-	10
Normalized Emittance ϵ_N (mm μrad)	3.3	3.75
Betatron function at collision point β^* (cm)	-	55

Table 4.1: Beam parameters of the Large Hadron Collider.

624 luminosity delivered was 13.3 fb^{-1} . In Fig. 4.4, we display the integrated luminosity
 625 per day for 2015 and 2016.

626 Pileup

627 *Pileup* is the term for the additional proton-proton interactions which occur during
 628 each bunch crossing of the LHC. At the beginning of the LHC physics program, there
 629 had not been a collider which averaged more than a single interaction per bunch
 630 crossing. In the LHC, each bunch crossing (or *event*) generally contains multiple
 631 proton-proton interactions. An simulated event with many *vertices* can be seen in
 632 Fig. 4.5. The so-called *primary vertex* (or *hard scatter vertex*) refers to the vertex
 633 which has the highest Σp_T^2 The summation occurs over the *tracks* in the detector,
 634 which we will describe later [ATL-INDET-PUB-2009-001]. We then distinguish
 635 between *in-time* pileup and *out-of-time* pileup. In-time pileup refers to the additional
 636 proton-proton interactions which occur in the event. Out-of-time pileup refers to
 637 effects related to proton-proton interactions previous bunch crossings.

638 We quantify in-time pileup by the number of “primary”² vertices in a particular
 639 event. To quantify the out-of-time pileup, we use the average number of interactions

²The primary vertex is as defined above, but we unfortunately use the same name here.

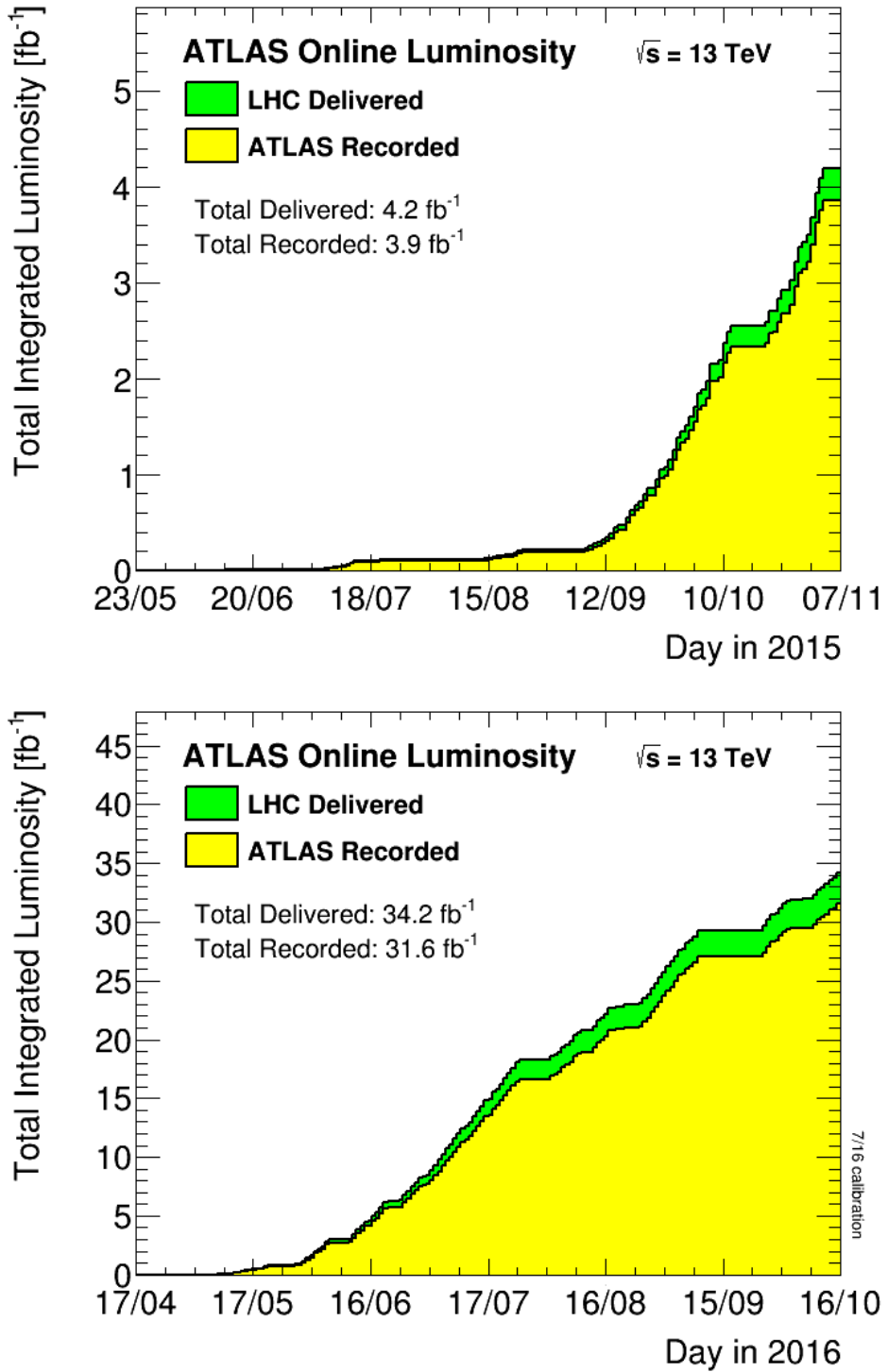


Figure 4.4: Integrated Luminosity delivered by the LHC and collected by ATLAS in the 2015 and 2016 datasets.

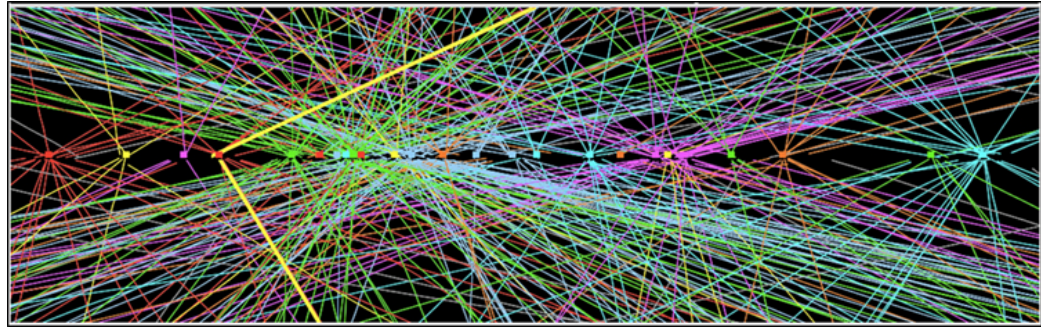


Figure 4.5: Simulated event with many pileup vertices.

640 per bunch crossing $\langle \mu \rangle$. In Fig. 4.6, we show the distribution of μ for the dataset
641 used in this thesis.



Figure 4.6: Mean number of interactions per bunch crossing in the 2015 and 2016 datasets.

The ATLAS detector

644 The dataset analyzed in this thesis was taken by the ATLAS detector [88], which
 645 is located at the “Point 1” cavern of the LHC, just across the street from the main
 646 CERN campus. The much-maligned acronym stands for *A Toroidal LHC ApparatuS*.
 647 ATLAS is a massive cylindrical detector, with a radius of 12.5 m and a length of
 648 44 m, with nearly hermitic coverage around the collision point. Each of the many
 649 subdetectors plays a role in measuring the energy, momentum, and type of the particles
 650 produced in collisions delivered by the LHC. These subdetectors are immersed in
 651 a hybrid solenoid-toroid magnet system which allows for precise measurements of
 652 particle momenta. The central solenoid magnet contains a magnetic field of 2 T. A
 653 schematic of the detector is shown in Fig. 5.1.

654 The *inner detector* (ID) lies closest to the collision point, and contains three
 655 separate subdetectors. It provides pseudorapidity¹ coverage of $|\eta| < 2.5$ for charged
 656 particles. The tracks reconstructed from the inner detector hits are used to
 657 reconstruct the primary vertices and to determine the momemta of charged particles.
 658 The ATLAS *calorimeter* consists of two subdetectors, known as the *electromagnetic*
 659 and *hadronic* calorimeters. These detectors stop particles and measure their energy

¹ATLAS uses a right-handed Cartesian coordinate system. The origin is defined by the nominal beam interaction point. The positive- z direction is defined by the incoming beam travelling counterclockwise around the LHC. The positive- x direction points towards the center of the LHC ring from the origin, and the positive- y direction points upwards towards the sky. For particles of transverse (in the $x - y$ plane) momentum $p_T = \sqrt{p_x^2 + p_y^2}$ and energy E , it is generally most convenient fully describe this particle’s kinematics as measured by the detector in the (p_T, ϕ, η, E) basis. The angle $\phi = \arctan(p_y/p_x)$ is the standard azimuthal angle, and $\eta = \ln \tan(\theta/2)$ is known as the pseudorapidity, and defined based on the standard polar angle $\theta = \arccos(p_z/p_T)$. For locations of detector elements, both (r, ϕ, η) and (z, ϕ, η) can be useful.



Figure 5.1: The ATLAS detector. Copyright CERN.

660 deposition. The calorimeters provide coverage out to pseudorapidity of $|\eta| < 4.9$. The
 661 muon spectrometer is aptly named, as it measures muons, which are the only particles
 662 which generally reach the outer portions of the detector. In this region, we have the
 663 large tracking systems of the muon spectrometer, which provide precise measurements
 664 of muon momenta. The muon spectrometer has pseudorapidity coverage of $|\eta| < 2.7$.

665 5.1 Magnets

666 ATLAS contains multiple magnetic systems. Primarily, we are concerned with the
 667 solenoid, used by the inner detector, and the toroids located outside of the ATLAS
 668 calorimeter. A schematic is shown in Fig. 5.2. These magnetic fields are used to bend
 669 charged particles, which subsequently allows one to measure their momentum.

670 The ATLAS central solenoid is a 2.3 m diameter, 5.3 m long solenoid at the center
 671 of the ATLAS detector. It produces a uniform magnetic field of 2 T. An important
 672 design constraint for the central solenoid was the decision to place it in between

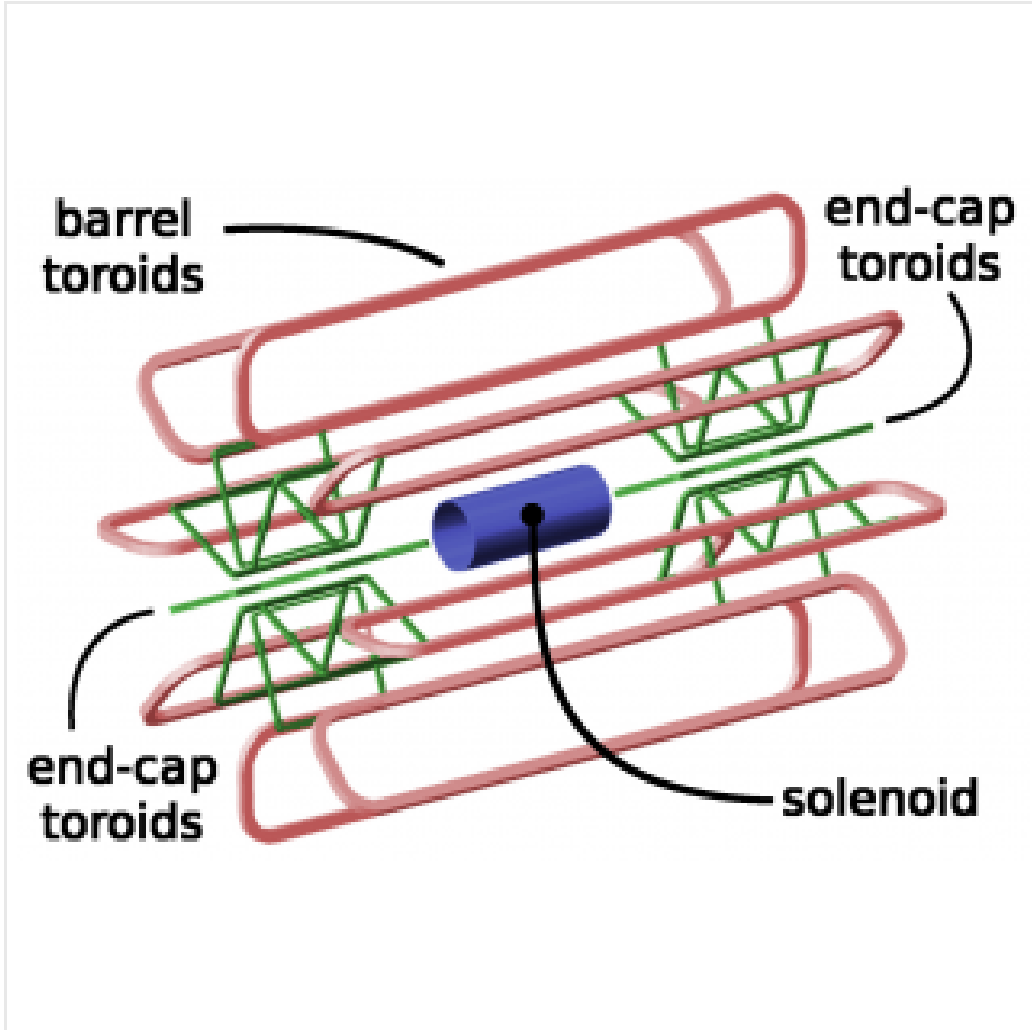


Figure 5.2: The ATLAS magnet system. Copyright CERN.

673 the inner detector and the calorimeters. To avoid excessive energy deposition which
674 could affect calorimeter measurements, the central solenoid must be as transparent
675 as possible².

676 The toroid system consists of eight air-core superconducting barrel loops, which
677 give ATLAS its distinctive shape. There are also two endcap air-core magnets. These
678 produce a magnetic field in a region of approximately 26 m in length and 10 m of
679 radius. The magnetic field in this region is non-uniform.

²This is also one of the biggest functional differences between ATLAS and CMS In CMS, the solenoid is outside of the calorimeters.



Figure 5.3: The ATLAS inner detector. Copyright CERN.

680 5.2 Inner Detector

681 The ATLAS inner detector consists of three separate tracking detectors, which are
 682 known as, in order of increasing distance from the interaction point, the Pixel
 683 Detector, Semiconductor Tracker (SCT), and the Transition Radiation Tracker
 684 (TRT). When charged particles pass through these tracking layers, they produce
 685 *hits*, which using the known 2 T magnetic field, allows the reconstruction of *tracks*.
 686 Tracks are used as inputs for reconstruction of many higher-level physics objects,
 687 such as electrons, muons, photons, and E_T^{miss} . Accurate track reconstruction is thus
 688 crucial for precise measurements of charged particles.

689 Pixel Detector

690 The ATLAS pixel detector consists four layers of silicon “pixels” [89]. This refers
 691 to the segmentation of the active medium into pixels, which provide precise 3D hit
 692 locations. The layers are known as the “Insertable” B-Layer (IBL), the B-Layer (or

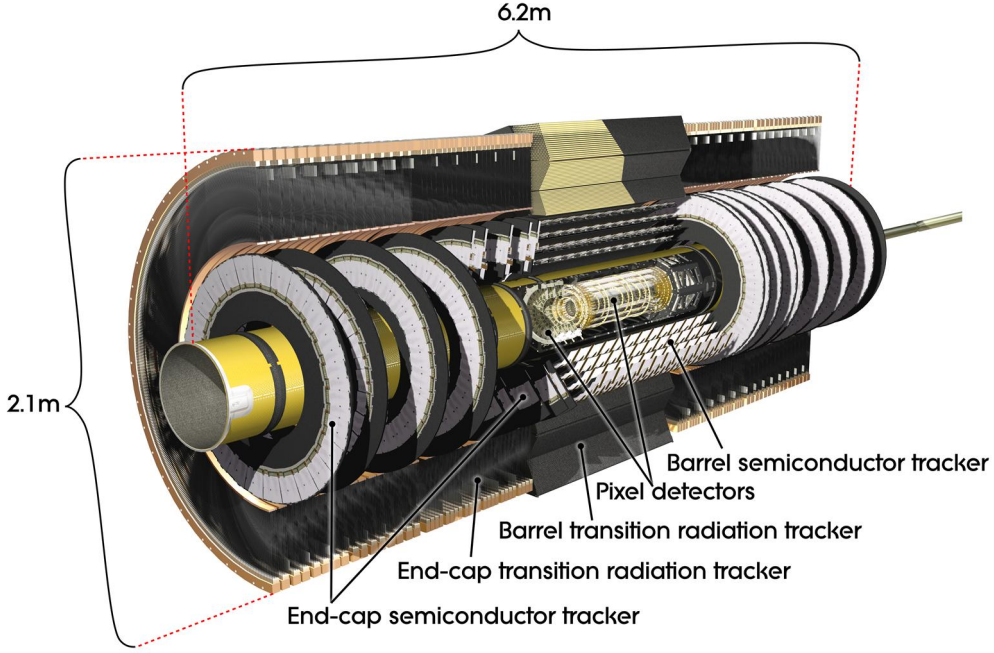


Figure 5.4: The ATLAS pixel detector. Copyright CERN.

693 Layer-0), Layer-1, and Layer-2, in order of increasing distance from the interaction
 694 point. These layers are close to the interaction point, and therefore experience
 695 significant radiation exposure.

696 Layer-1, Layer-2, and Layer-3 were installed with the initial construction of
 697 ATLAS. They contain front-end integrated electronics (FEI3s) bump-bonded to 1744
 698 silicon modules. Each module is $250 \mu\text{m}$ in thickness and contains 47232 pixels.
 699 These pixels have planar sizes of $50 \times 400 \mu\text{m}^2$ or $50 \times 600 \mu\text{m}^2$, to provide highly
 700 accurate location information. The FEI3s are mounted on long rectangular structures
 701 known as staves, which encircle the beam pipe. A small tilt to each stave allows full
 702 coverage in ϕ . These layers are at radii of 50.5 mm, 88.5 mm, and 122.5 mm from
 703 the interaction point.

704 The IBL was added to ATLAS after Run1 in 2012 at a radius of 33 mm from the
 705 interaction point [90]. The IBL was required to preserve the integrity of the pixel
 706 detector as radiation damage leads to inoperative pixels in the other layers. The IBL

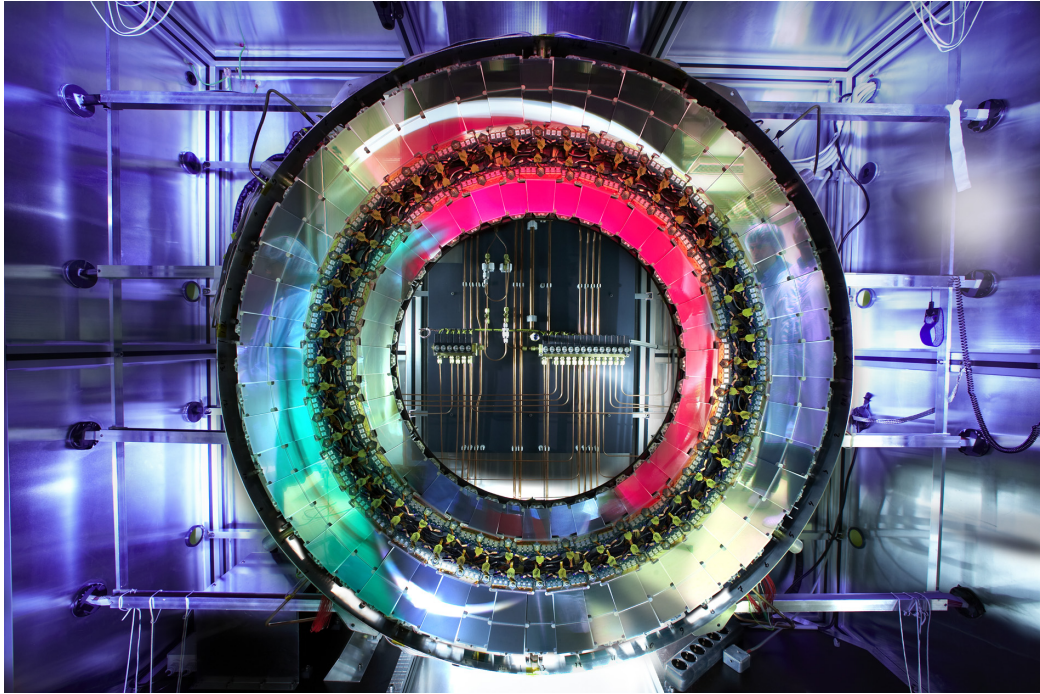


Figure 5.5: A ring of the Semiconductor Tracker. Copyright CERN.

707 consists of 448 FEI4 chips, arranged onto 14 staves. Each FEI4 has 26880 pixels, of
708 planar size $50 \times 250 \mu\text{m}$. This smaller granularity was required due to the smaller
709 distance to the interaction point.

710 In total, a charged particle passing through the inner detector would expect to
711 leave four hits in the pixel detector.

712 Semiconductor Tracker

713 The SCT is a silicon strip detector directly beyond Layer-2 of the pixel detector [91].
714 The dual-sensors of the SCT contain 2×768 individual strips. Each strip has area
715 6.4 cm^2 . The SCT dual-sensor is double-layered, at a relative angle of 40 mrad.
716 Together, these layers provide the necessary 3D information for track reconstruction.
717 There are four of these double-layers, at radii of 284 mm, 355 mm, 427 mm, and 498
718 mm. These double-layers provide hits comparable to those of the pixel detector. The
719 SCT provides an four additional hits to reconstruct tracks for each charged particle.

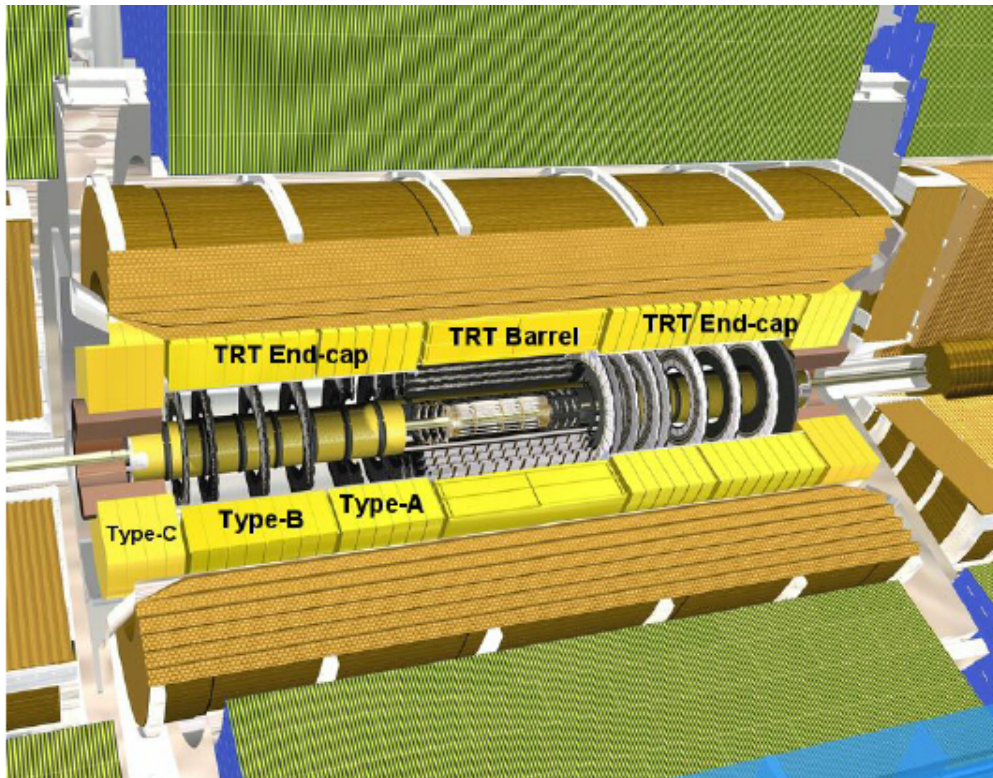


Figure 5.6: A schematic of the Transition Radiation Tracker. Copyright CERN.

720 Transition Radiation Tracker

721 The Transition Radiation Tracker is the next detector radially outward from the SCT.
722 It contains straw drift tubes. Each tube contains a tungsten gold-plated wire of $32 \mu\text{m}$
723 diameter held under high voltage (-1530 V) with the edge of the Kapton-aluminum
724 tube. They are filled with a gas mixture of primarily xenon that is ionized when
725 a charged particle passes through the tube. The ions are collected by the “drift”
726 due to the voltage inside the tubes, which is read out by the electronics. Due to
727 the dielectric difference between the gas and tubes, transition radiation is induced.
728 This is important for distinguishing electrons from their predominant background of
729 minimum ionizing particles. Generally, electrons have a much larger Lorentz factor
730 than minimum ionizing particles, which leads to additional transition radiation. This
731 is used to discriminate electrons from background in electron reconstruction.

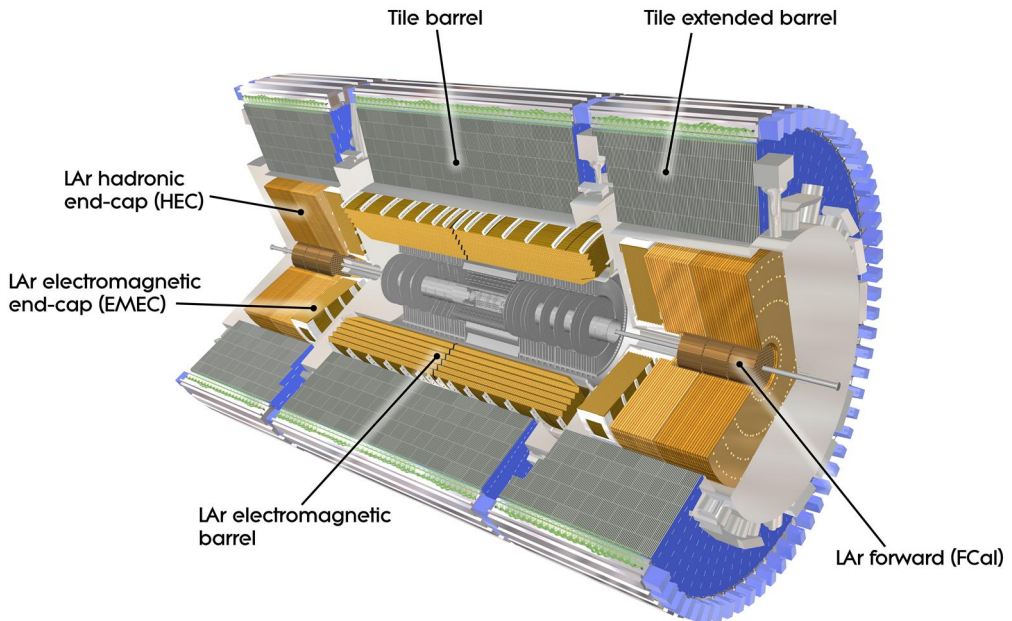


Figure 5.7: The ATLAS calorimeter. Copyright CERN.

⁷³² 5.3 Calorimetry

⁷³³ The calorimetry of the ATLAS detector also includes multiple subdetectors which
⁷³⁴ allow precise measurements of the electrons, photons, and hadrons produced in
⁷³⁵ collisions delivered by the LHC. Calorimeters work by stopping particles in their
⁷³⁶ material and measuring the energy deposition. This energy is deposited as a
⁷³⁷ cascade of particles induce from interactions with the detector material known as
⁷³⁸ *showers*. ATLAS uses *sampling* calorimeters, alternating a dense absorbing material
⁷³⁹ to induce showers with an active layer to measure energy depositions by the induced
⁷⁴⁰ showers. Since some energy is deposited into the absorption layers as well, the energy
⁷⁴¹ depositions must be properly calibrated for the detector.

⁷⁴² Electromagnetic objects (electrons and photons) and hadrons have different
⁷⁴³ interaction properties. We use different types of calorimeters to accurately measure
⁷⁴⁴ these classes of objects, which we call *electromagnetic* and *hadronic* calorimeters.
⁷⁴⁵ ATLAS contains multiple separate calorimeters : the liquid argon (LAr) electro-

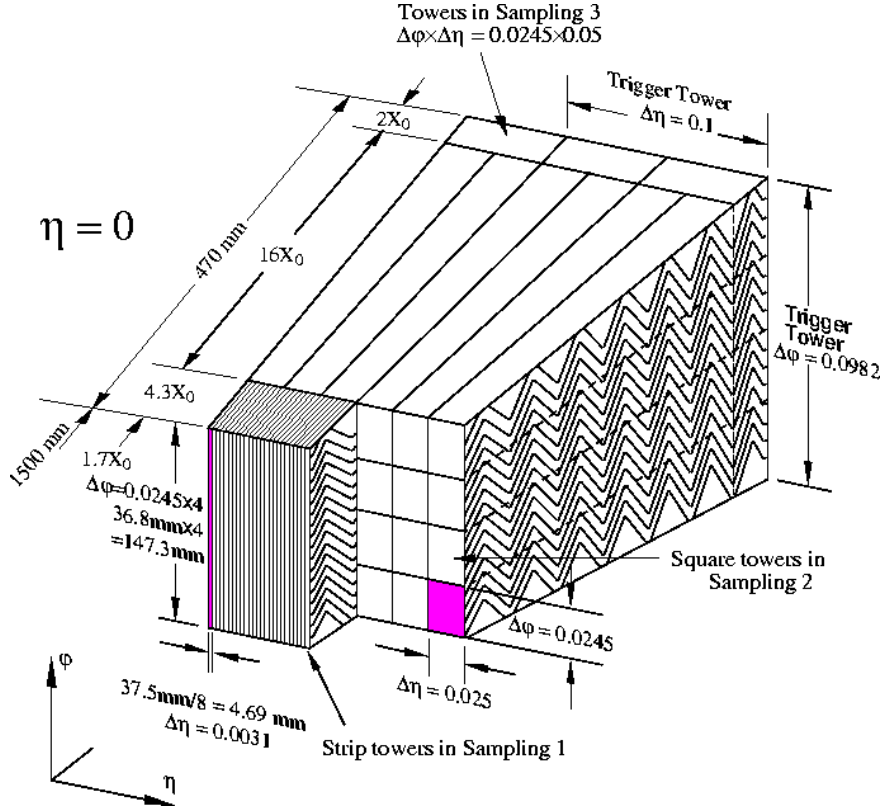


Figure 5.8: A schematic of a subsection of the barrel LAr electromagnetic calorimeter.
Copyright CERN.

746 magnetic barrel calorimeter, the Tile barrel hadronic calorimeter, the LAr endcap
 747 electromagnetic calorimeter, the LAr endcap hadronic calorimeter, and the LAr
 748 Forward Calorimeter (FCal). Combined, these provide full coverage in ϕ up to
 749 $|\eta| < 4.9$. They are shown in Fig. 5.7.

750 Electromagnetic Calorimeters

751 The electromagnetic calorimeters of the ATLAS detector consist of the barrel and
 752 endcap LAr calorimeters. These are arranged into an “accordion” shape, shown
 753 in Fig. 5.8, which allows full coverage in ϕ and significant coverage in η while
 754 still allowing support structures for detector operation. The accordion is made of
 755 layers with liquid argon (active detection material) and lead (absorber) to induce
 756 electromagnetic showers. The LAr EM calorimeters are each more than 20 radiation

757 lengths deep, which provides the high stopping power necessary to properly measure
758 the electromagnetic showers.

759 The barrel component of the LAr EM calorimeter extends from the center of the
760 detector out to $|\eta| < 1.475$. The calorimeter has a presampler, which measures the
761 energy of any EM shower induced before the calorimeter. This has segmentation of
762 $\Delta\eta = 0.025, \Delta\phi = .01$. There are three “standard” layers in the barrel, which have
763 decreasing segmentation into calorimeter *cells* as one travels radially outward from
764 the interaction point. The first layer has segmentation of $\Delta\eta = 0.003, \Delta\phi = .1,$
765 and is quite thin with a depth of 4 radiation lengths. It provides precise η and
766 ϕ measurements for incoming EM objects. The second layer is the deepest at 16
767 radiation lengths, with a segmentation of $\Delta\eta = 0.025, \Delta\phi = 0.025$. It is primarily
768 responsible for stopping the incoming EM particles, which dictates its large relative
769 thickness, and measures most of the energy of the incoming particles. The third layer
770 is only 2 radiation lengths deep, with a rough segmentation of $\Delta\eta = 0.05, \Delta\phi = .025$.
771 The deposition in this layer is primarily used to distinguish hadrons interacting
772 electromagnetically and entering the hadronic calorimeter from the strictly EM
773 objects which are stopped in the second layer.

774 The barrel EM calorimeter has a similar overall structure, but extends from $1.4 <$
775 $|\eta| < 3.2$. The η segmentation is smaller in the endcap than the barrel, while the
776 ϕ segmentation is the same. In total, the EM calorimeters contain about 190000
777 individual calorimeter cells.

778 Hadronic Calorimeters

779 The hadronic calorimetry of ATLAS sits directly outside the EM calorimetry. It
780 contains three subdetectors : the barrel Tile calorimeter, the endcap LAr calorimeter,
781 and the Forward LAr Calorimeter. Similar to the EM calorimeters, these are
782 sampling calorimeters that alternate steel (dense material) with an active layer



Figure 5.9: A schematic of Tile hadronic calorimeter. Copyright CERN.

783 (plastic scintillator).

784 The barrel Tile calorimeter extends out to $|\eta| < 1.7$. It has three layers, which
 785 combined give about 10 interaction lengths to provide excellent stopping power for
 786 hadrons. This is critical to avoid excess *punchthrough* to the muon spectrometer
 787 beyond the hadronic calorimeters. The first layer has a depth of 1.5 interaction
 788 lengths. The second layer is again the thickest at a depth of 4.1 interaction lengths.
 789 Most of the energy of incoming particles is deposited in the second layer. Both
 790 the first and second layer have segmentation of $\Delta\eta = 0.1, \Delta\phi = 0.1$. Generally,
 791 one does not need as fine granularity in the hadronic calorimeter, since the energy
 792 depositions in the hadronic calorimeters will be summed into the composite objects as
 793 jets. The third layer has a thickness of 1.8 interaction lengths, with a segmentation of
 794 $\Delta\eta = 0.2, \Delta\phi = 0.1$. The use of multiple layers gives information about the induced
 795 hadronic shower as it propagates through the detector material.

796 The endcap LAr hadronic calorimeter is a sampling calorimeter which covers the

797 region $1.5 < |\eta| < 3.2$. Liquid argon is the active material and it uses a copper
798 absorber. Unlike the other sampling calorimeters in ATLAS, it does not use the
799 accordion shape. Instead, it is a flat detector perpendicular to the interaction point.
800 The segmentation varies with η , ranging from cells of size $\Delta\eta = 0.1, \Delta\phi = 0.1$ in the
801 center region to $\Delta\eta = 0.2, \Delta\phi = 0.2$ in the forward region.

802 The forward LAr calorimeter is the last subdetector of the ATLAS calorimetry.
803 Of those subdetectors which are used for standard reconstruction techniques, the
804 FCal sits at the most extreme values of $3.1 < |\eta| < 4.9$. The FCal itself is made of
805 three subdetectors: the electromagnetic FCal1 and hadronic FCal2 and FCal3. The
806 absorber in FCal1 is copper, with a liquid argon active medium. FCal2 and FCal3
807 also use a liquid argon active medium, with a tungsten absorber.

808 5.4 Muon Spectrometer

809 The muon spectrometer sits outside the hadronic calorimetry, with pseudorapidity
810 coverage out to $|\eta| < 2.7$. The MS is a huge detector, with some detector elements
811 existing as far as 11 m in radius from the interaction point. This system is used
812 almost exclusively to measure the momenta of muons. These systems provide a
813 rough measurement, which is used in triggering (described in Sec. 5.5), and a precise
814 measurement to be used in offline event reconstruction. The MS produces tracks in a
815 similar way to the ID. The hits in each subdetector are recorded and then tracks are
816 produced from these hits. Muon spectrometer tracks are largely independent of the
817 ID tracks due to the independent solenoidal and toroidal magnet systems used in the
818 ID and MS respectively. The MS consists of four separate subdetectors: the barrel
819 region is covered by the Resistive Plate Chambers (RPCs) and Monitored Drift Tubes
820 (MDTs) while the endcaps are covered by MDTs, Thin Gap Chambers (TGCs), and
821 Cathode Strip Chambers (CSCs).

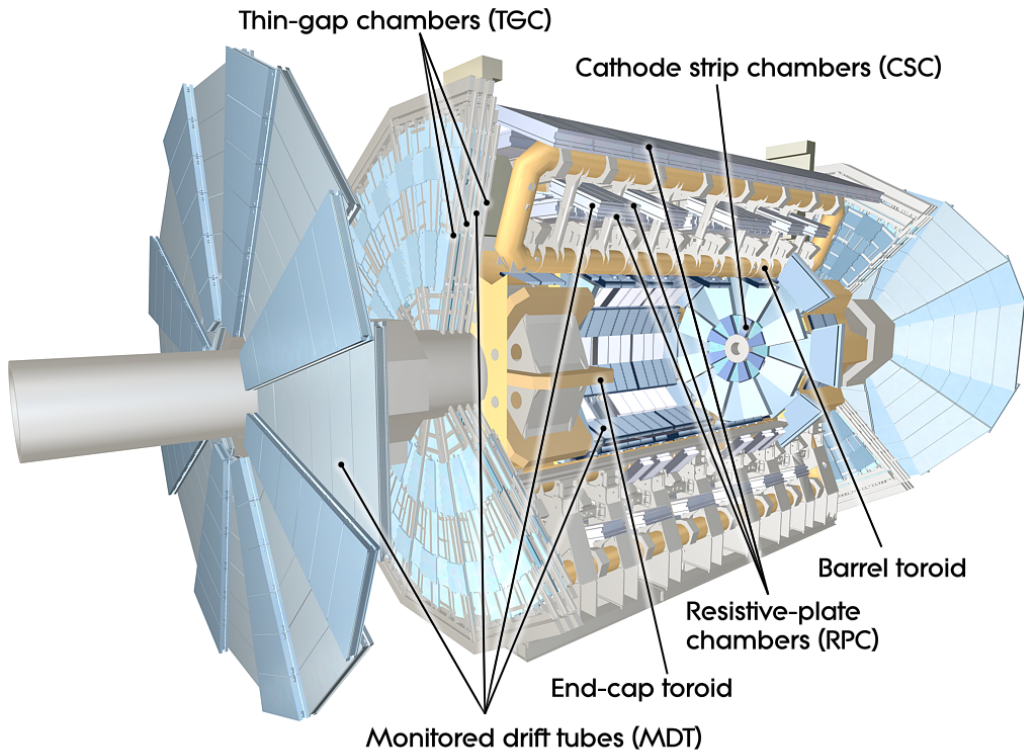


Figure 5.10: The ATLAS muon spectrometer. Copyright CERN.

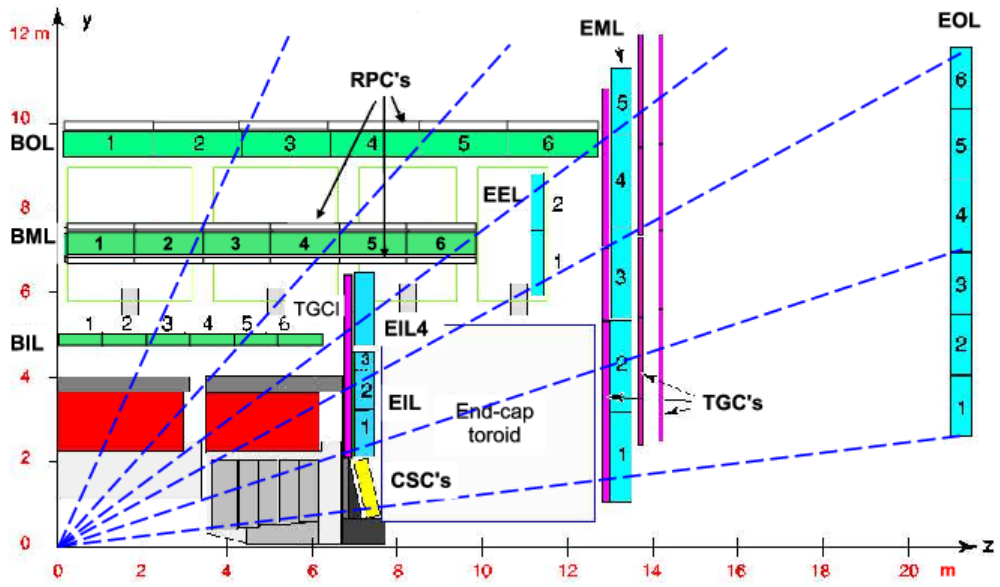


Figure 5.11: A schematic in z/η showing the location of the subdetectors of the muon spectrometer. Copyright CERN.

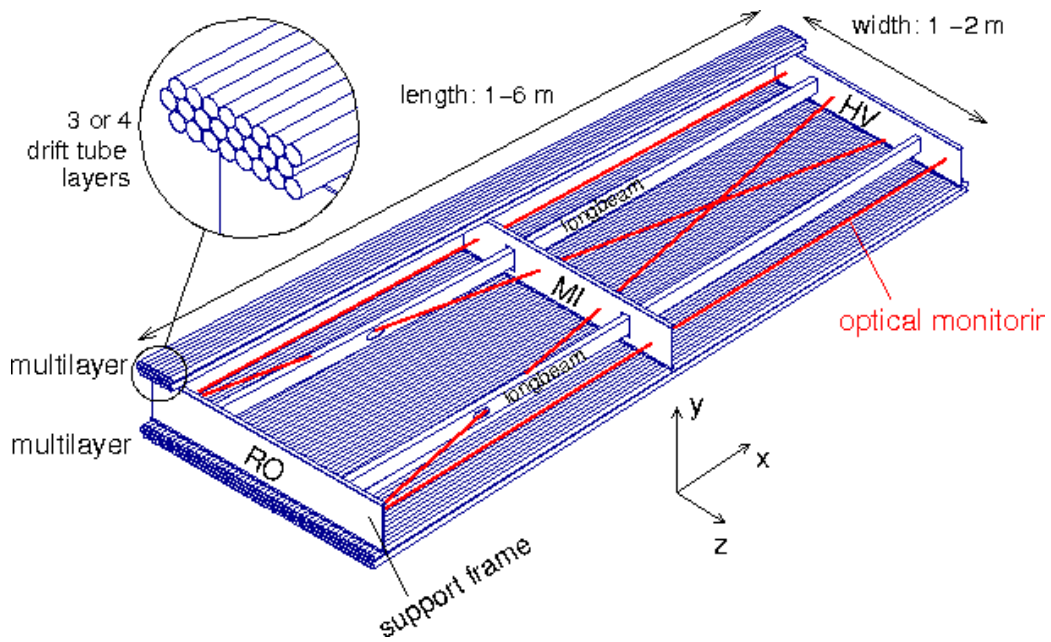


Figure 5.12: Schematic of a Muon Drift Tube chamber. Copyright CERN.

822 Monitored Drift Tubes

823 The MDT system is the largest individual subdetector of the MS. MDTs provide
824 precision measurements of muon momenta as well as fast measurements used for
825 triggering. There are 1088 MDT chambers providing coverage out to pseudorapidity

826 $|\eta| < 2.7$. Each consists of an aluminum tube containing an argon-CO₂ gas mixture.
827 In the center of each tube there 50 μm diameter tungsten-rhenium wire at a voltage of
828 3080 V. A muon entering the tube will induce ionization in the gas, which will “drift”
829 towards the wire due to the voltage. One measures this ionization as a current in the
830 wire. The current comes with a time measurement related to how long it takes the
831 ionization to drift to the wire.

832 These tubes are layered in a pattern shown in Fig. 5.12. Combining the
833 measurements from the tubes in each layer gives good position resolution. The
834 system consists of three subsystems of these layers, at 5 m, 7 m, and 9 m from the
835 interaction point. The innermost layer is directly outside the hadronic calorimeter.
836 The combination of these three measurements gives precise momenta measurements
837 for muons.

838 Resistive Plate Chambers

839 The RPC system is alternated with the MDT system in the barrel. The first two layers
840 of RPC detectors surround the second MDT layer while the third is outside the final
841 MDT layer. The RPC system covers pseudorapidity $|\eta| < 1.05$. Each RPC consists
842 of two parallel plates at a distance of 2 mm surrounding a C₂H₂F₄ mixture. The
843 electric field between these plates is 4.9k kV/mm. Just as in the MDTs, an incoming
844 muon ionizes the gas, and the deposited ionization is collected by the detector (in this
845 case on the plates). It is quite fast, but with a relatively poor spatial resolution of
846 1 cm. Still, it can provide reasonable ϕ resolution due to its large distance from the
847 interaction point. This is most useful in triggering, where the timing requirements
848 are quite severe. The RPCs also complement the MDTs by providing a measurement
849 of the non-bending coordinate.



Figure 5.13: Photo of the installation of Cathode Strip Chambers and Monitored Drift Tubes. Copyright CERN.

850 **Cathode Strip Chambers**

851 The CSCs are used in place of MDTs in the first layer of the endcaps. This region,
852 at $2.0 < |\eta| < 2.7$, has higher particle multiplicity at close distance to the interaction
853 point from low-energy photons and neutrons. The MDTs are not equip to deal with
854 the high particle rate in this region, so the CSCs were designed to deal with this
855 deficiency.

856 Each CSC consists multiwire proportional chambers, oriented radially outward
857 from the interaction point. These chambers overlap partially in ϕ . The wires contain
858 a gas mixture of argon and CO₂, which is ionized when muons enter. The detectors
859 operate with a voltage of 1900 V, with much lower drift times than the MDTs. They
860 provide less hits than MDTs, but their lower drift times lower uptime and reduce the
861 amount of detector overload.

862 The CSCs are arranged into four planes on the wheels of the muon spectrometer,
863 as seen in Fig. Fig. 5.13. There are 32 CSCs in total, with 16 on each side of the
864 detector in η .

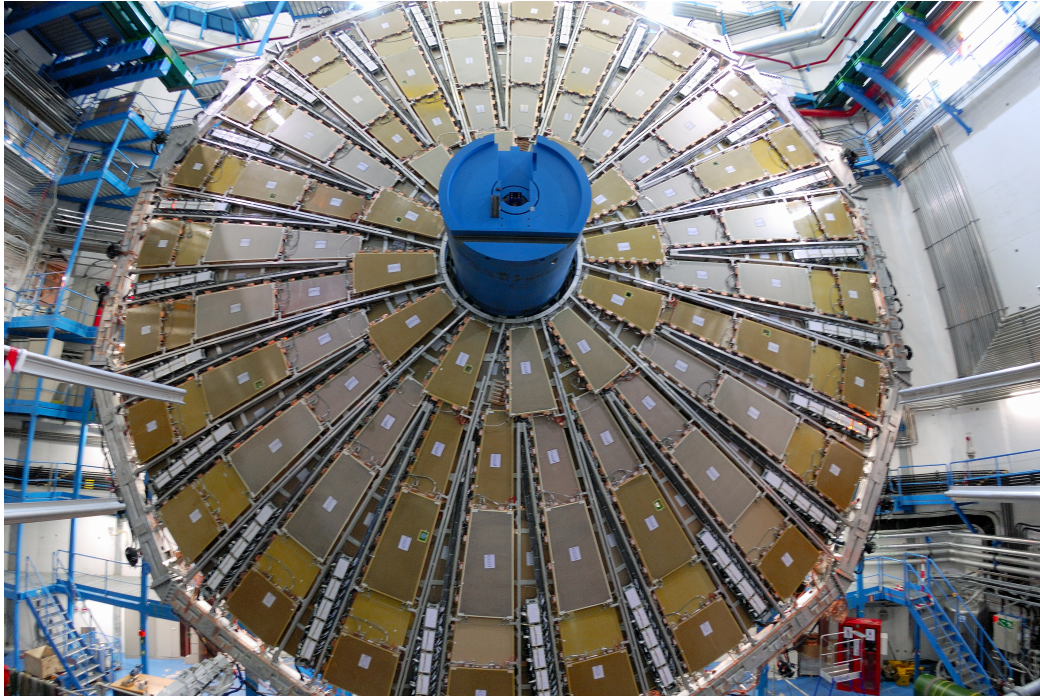


Figure 5.14: Photo of a muon Big Wheel, consisting of Thin Gap Chambers.
Copyright CERN.

865 **Thin Gap Chambers**

866 The TGCs serve the purpose of the RPCs in the endcap at pseudorapidity of $1.05 <$
867 $|\eta| < 2.4$, by providing fast measurements used for triggering. They are multiwire
868 proportional chambers similar to the CSCs. The fast readouts necessary for triggering
869 are provided by a high electric field and a small wire-to-wire distance of 1.8 mm.
870 These detectors provide both η and ϕ information, allowing the trigger to use as
871 much information as possible when selecting events.

872 **5.5 Trigger System**

873 The data rate delivered by the LHC is staggering [92]. In the 2016 dataset, the
874 collision rate was 40 MHz, meaning a *bunch spacing* of 25 ns. In each of the event,
875 there are many proton-proton collisions. Most of the collisions are uninteresting,
876 such as elastic scattering of protons, or even inelastic scattering leading to low-energy

877 dijet events. These low-energy events have have been studied in detail in previous
878 experiments.

879 Even if one is genuinely interested in these events, it's *impossible* to save all of
880 the information available in each event. If all events were written "to tape" (as the
881 jargon goes), ATLAS would store terabytes of data per second. We are limited to only
882 about 1000 Hz readout by computing processing time and storage space. We thus
883 implement a *trigger* which provides fast inspection of events to drastically reduce
884 the data rate from the 40 MHz provided by the LHC to the 1000 Hz we can write to
885 tape for further analysis.

886 The ATLAS trigger system consists of a two-level trigger, known as the Level-
887 1 trigger (L1 trigger) and the High-Level Trigger (HLT)³. Trigger selections are
888 organized into *trigger chains*, where events passing a particular L1 trigger are passed
889 to a corresponding HLT trigger. For example, one would require a particular high- p_T
890 muon at L1, with additional quality requirements at HLT. One can also use HLT
891 triggers as prerequisites for each other, as is done in some triggers requiring both jets
892 and E_T^{miss} .

893 **Level-1 Trigger**

894 The L1 trigger is hardware-based, and provides the very fast rejection needed to
895 quickly select events of interest. The L1 trigger uses only what is known as *prompt*
896 data to quickly identify interesting events. Only the calorimeters and the triggering
897 detectors (RPCs and TGCs) of the MS are fast enough to be considered at L1,
898 since the tracking reconstruction algorithms used by the ID and the more precise
899 MS detectors are very slow. This allows quick identification of events with the

³In Run1, ATLAS ran with a three-level trigger system. The L1 was essentially as today. The HLT consisted of two separate systems known as the L2 trigger and the Event Filter (EF). This was changed to the simpler system used today during the shutdown between Run1 and Run2.

900 most interesting physical objects: large missing transverse momentum and high- p_T
901 electrons, muons, and jets.

902 L1 trigger processing is done locally. This means that events are selected without
903 considering the entire available event. Energy deposits over some threshold are
904 reconstructed as *regions of interest* (RoIs). These RoIs are then compared using
905 pattern recognition hardware to “expected” patterns for the given RoIs. Events with
906 RoIs matching these expected patterns are then handed to the HLT through the
907 Central Trigger Processor. This step lowers the data rate down to about 75 kHz.

908 **High-Level Trigger**

909 After passing the L1 trigger, events are passed to the HLT, which takes the incoming
910 data rate from \sim 75 kHz down to the \sim 1 kHz that can be written to tape. The HLT
911 performs much like a simplified offline reconstruction, using many common quality
912 and analysis cuts to eliminate uninteresting events. This is done by using computing
913 farms located close to the detector, which process events in parallel. Individually,
914 each event which enters the computing farms takes about 4 seconds to reconstruct.
915 However, some events take significantly longer to reconstruct, which necessitates
916 careful monitoring of the HLT to ensure smooth operation.

917 HLT triggers are targeted to a particular physics process, such as a E_T^{miss} trigger,
918 single muon trigger, or multijet trigger. The collection of all triggers is known as
919 the trigger *menu*. Since many low-energy particles are produced in collisions, it is
920 necessary to set a *trigger threshold* on the object of interest. Due to the changing
921 luminosity conditions of the LHC, these thresholds change constantly. The most
922 common strategy is to increase the trigger thresholds with increasing instantaneous
923 luminosity. This allows an approximately constant number of events to be written
924 for further analysis. Triggers which have rates higher than those designated by the
925 menu are *prescaled*. A prescaled trigger only records every n th event which passes

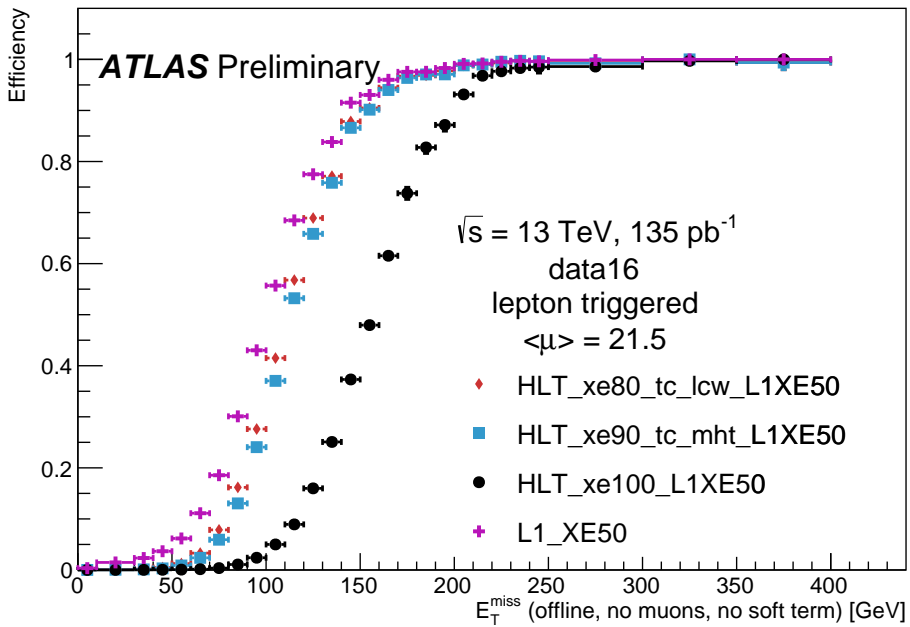


Figure 5.15: Turn-on curves for the E_T^{miss} triggers used in this thesis.

the trigger requirements, where n is the prescale value. Inne wishes to investigate all data events passing some set of analysis cuts, so often one uses the “lowest threshold unprescaled trigger”. *Turn-on curves* allow one to select the needed offline analysis cut to ensure the trigger is fully efficient. An example turn-on curve for the E_T^{miss} triggers used in the signal region of this analysis is shown in Fig. 5.15.

The full set of the lowest threshold unprescaled triggers considered here can be found in Tab. 5.1. These are the lowest unprescaled triggers associated to the SUSY signal models and Standard Model backgrounds considered in this thesis. More information can be found in [92].

Physics Object	Trigger	p_T Threshold (GeV)	Level-1 Seed	Requirements	Rate (Hz)
2015 Data					
E_T^{miss}	HLT_xe70	70	L1_XE50	-	60
Muon	HLT_mu24_loose	24	L1_MU15	isolated, loose	130
Muon	HLT_mu50	50	L1_MU15	-	30
Electron	HLT_e24_lhmedium_iloose	24	L1_EM20VH	medium OR isolated, loose	140
Electron	HLT_e60_lhmedium	60	L1_EM20VH	medium	10
Electron	HLT_e120_lhloose	120	L1_EM20VH	loose	<10
Photon	HLT_g120_loose	120	L1_EM20VH	loose	20
2016 Data					
E_T^{miss}	HLT_xe100_mht_L1XE50	100	L1_XE50	-	180
Muon	HLT_mu24_ivarmedium	24	L1_MU20	medium	120
Muon	HLT_mu50	50	L1_MU20	-	40
Electron	HLT_e24_lhtight_nod0	24	L1_EM22VHI	tight with no d_0 OR loose	110
Electron	HLT_e60_lhmedium_nod0	60	L1_EM22VHI	medium with no d_0	10
Electron	HLT_e140_lhloose_nod0	140	L1_EM22VHI	loose with no d_0	<10
Photon	HLT_g140_loose	140	L1_EM22VHI	loose	20

Table 5.1: High-Level Triggers used in this thesis. Descriptions of loose, medium, tight, and isolated can be found in [92]. The d_0 cut refers to a quality cut on the vertex position, which was removed from many triggers in 2016 to increase sensitivity to displaced vertex signals. For most triggers, the increased thresholds in 2016 compared to 2016 were designed to keep the rate approximately equal.

Object Reconstruction

937 This chapter describes the reconstruction algorithms used within ATLAS. We will
938 make the distinction between the “primitive” objects which are reconstructed from
939 the detector signals from the “composite” physics objects we use in measurements
940 and searches for new physics.

941 6.1 Primitive Object Reconstruction

942 The primitive objects reconstructed by ATLAS are *tracks* and (calorimeter) *clusters*.
943 These are reconstructed directly from tracking hits and calorimeter energy deposits
944 into cells. Tracks can be further divided into inner detector and muon spectrom-
945 eter tracks. Calorimeter clusters can be divided into sliding-window clusters and
946 topological clusters (topoclusters).

947 Inner Detector Tracks

948 Inner detector tracks are reconstructed from hits in the inner detector [93, 94] These
949 hits indicate that a charged particle has passed through the detector material. Due
950 to the 2 T solenoid in the inner detector, the hits associated with any individual
951 particle will be curved. The amount of curvature determines the momentum of the
952 particle. In any given event, there are upwards of 10^4 hits, making it impossible to do
953 any sort of combinatorics to reconstruct tracks. There are two algorithms used by
954 ATLAS track reconstruction, known as *inside-out* and *outside-in*.

955 ATLAS first employs the inside-out algorithm. One assumes the track begins
956 at the interaction point. Moving out from the interaction point, one creates track
957 seeds. Track seeds are proto-tracks constructed from three hits. These hits can be
958 distributed as three pixel hits, two pixel hits and one SCT hit, or three SCT hits.
959 One extrapolates the track and uses a combinatorial Kalman filter [93], which adds
960 the rest of the pixel and SCT hits to the seeds. This is done seed by seed, so it
961 avoids the combinatorial complexity involved with checking all hits with all seeds.
962 At this point, the algorithm applies an additional filter to avoid ambiguities from
963 nearby tracks. The TRT hits are added to the seeds using the same method. After
964 this procedure, all hits are associated to a track.

965 The next step is to determine the correct kinematics of the track. This is
966 done by applying a fitting algorithm which outputs the best-fit track parameters
967 by minimizing the track distance from hits, weighted by each hit's resolution. These
968 parameters are $(d_0, z_0, \eta, \phi, q/p)$ where d_0 (z_0) is the transverse (longitudinal) impact
969 parameter and q/p is the charge over the track momenta. This set of parameters
970 uniquely defines the measurement of the trajectory of the charged particle associated
971 to the track. An illustration of a track with these parameters is shown in Fig. 6.1.

972 The other track reconstruction algorithm is the outside-in algorithm. As the
973 name implies, we start from the outside of the inner detector, in the TRT, and
974 extend the tracks in toward the interaction point. One begins by seeding from
975 TRT hits, and extending the track back towards the center of the detector. The
976 same fitting procedure is used as in the inside-out algorithm to find the optimal
977 track parameters. This algorithm is particularly important for finding tracks which
978 originate from interactions with the detector material, especially the SCT. For tracks
979 from primary vertices, this often finds the same tracks as the inside-out algorithm,
980 providing an important check on the consistency of the tracking procedure.

981 In the high luminosity environment of the LHC, even the tracks reconstructed

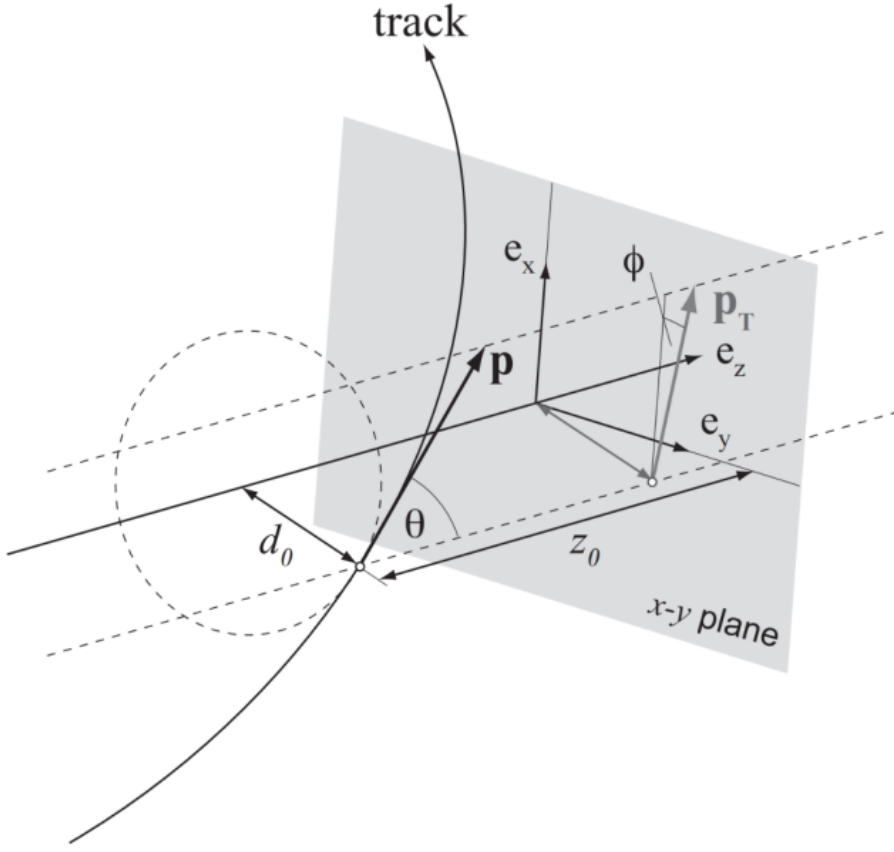
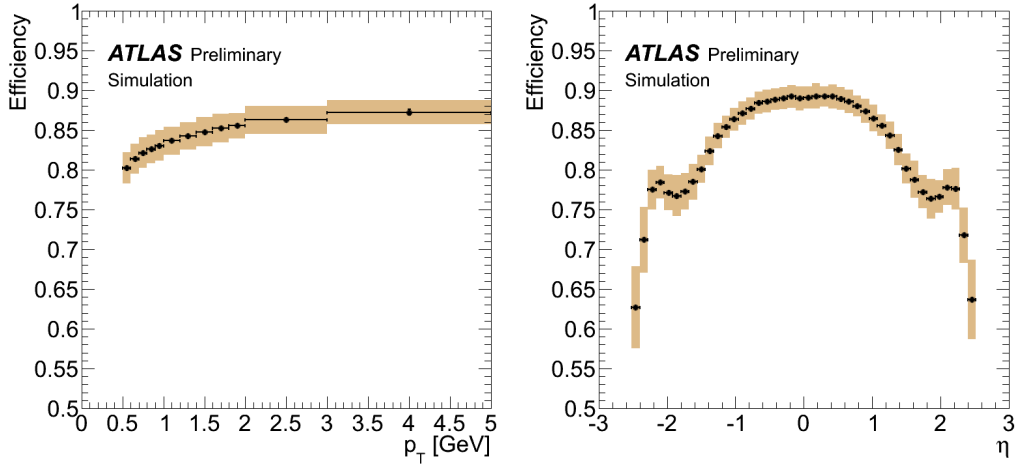


Figure 6.1: The parameters associated to a track.

from precision detectors such as those of ATLAS inner detector can sometimes lead to fake tracks from simple combinatoric chance. Several quality checks are imposed after track fitting which reduce this background. Seven silicon (pixel + SCT) hits are required for all tracks. No more than two *holes* are allowed in the pixel detector. Holes are expected measurements from the track that are missing in the pixel detector. Finally, tracks with poor fit quality, as measured by χ^2/ndf , are also rejected. Due to the high quality of the silicon measurements in the pixel detector and SCT, these requirements give good track reconstruction efficiency, as seen in Fig. 6.2 for simulated events [95].



(a) Track reconstruction as a function of p_T . (b) Track reconstruction as a function of η .

Figure 6.2: Track reconstruction efficiency as a function of track p_T and η . The efficiency is defined as the number of reconstructed tracks divided by the number of generate charged particles.

991 Sliding-window clusters

992 The sliding-window algorithm is a way to combine calorimeter cells into composite
 993 objects (clusters) to be used as inputs for other algorithms [96]. Sliding-window
 994 clusters are the primary inputs to electron and photon reconstruction, as described
 995 below. The electromagnetic calorimeter has high granularity, with a cell size of
 996 $(\eta, \phi) = (.025, .025)$ in the coarsest second layer throughout most of the calorimeter.
 997 The “window” consists of 3 by 5 cells in the (η, ϕ) space. All layers are added on
 998 this same 2D space. One translates this window over the space and seeds a cluster
 999 whenever the energy sum of the cells is maximized. If the seed energy is greater
 1000 than 2.5 GeV, this seed is called a sliding-window cluster. This choice was motivated
 1001 to optimize the reconstruction efficiency of proto-electrons and proto-photons while
 1002 rejecting fakes from electronic noise and additional particles from pileup vertices.

1003 **Topological clusters**

1004 Topoclusters are the output of the algorithm used within ATLAS to combine
1005 hadronic and electromagnetic calorimeter cells in a way which extracts signal from
1006 a background of significant electronic noise [97]. They are the primary input to the
1007 algorithms which reconstruct jets.

1008 Topological clusters are reconstructed from calorimeter cells in the following way.
1009 First, one maps all cells onto a single $\eta - \phi$ plane so one can speak of *neighboring*
1010 cells. Two cells are considered neighboring if they are in the same layer and directly
1011 adjacent, or if they are in adjacent layers and overlap in $\eta - \phi$ space. The *significance*
1012 ξ_{cell} of a cell during a given event is

$$\xi_{\text{cell}} = \frac{E_{\text{cell}}}{\sigma_{\text{noise},\text{cell}}} \quad (6.1)$$

1013 where $\sigma_{\text{noise},\text{cell}}$ is measured for each cell in ATLAS and E_{cell} measures the current
1014 energy level of the cell. One thinks of this as the measurement of the energy *over*
1015 *threshold* for the cell.

1016 Topocluster *seeds* are defined as calorimeter cells which have a significance $\xi_{\text{cell}} >$
1017 4. These are the inputs to the algorithm. One iteratively tests all cells adjacent
1018 to these seeds for $\xi_{\text{cell}} > 2$. Each cells passing this selection is then added to the
1019 topocluster, and the procedure is repeated. When the algorithm reaches the point
1020 where there are no additional adjacent cells with $\xi_{\text{cell}} > 2$, every positive-energy cell
1021 adjacent to the current proto-cluster is added. The collection of summed cells is a
1022 topocluster. An example of this procedure for a simulation dijet event is shown in
1023 Fig. 6.3.

1024 There are two calibrations used for clusters [98]. These are known as the
1025 electromagnetic (EM) scale [99] and the local cluster weighting (LCW) scale [97].
1026 The EM scale is the energy read directly out of the calorimeters as described. This
1027 scale is appropriate for electromagnetic processes. The LCW scale applies additional

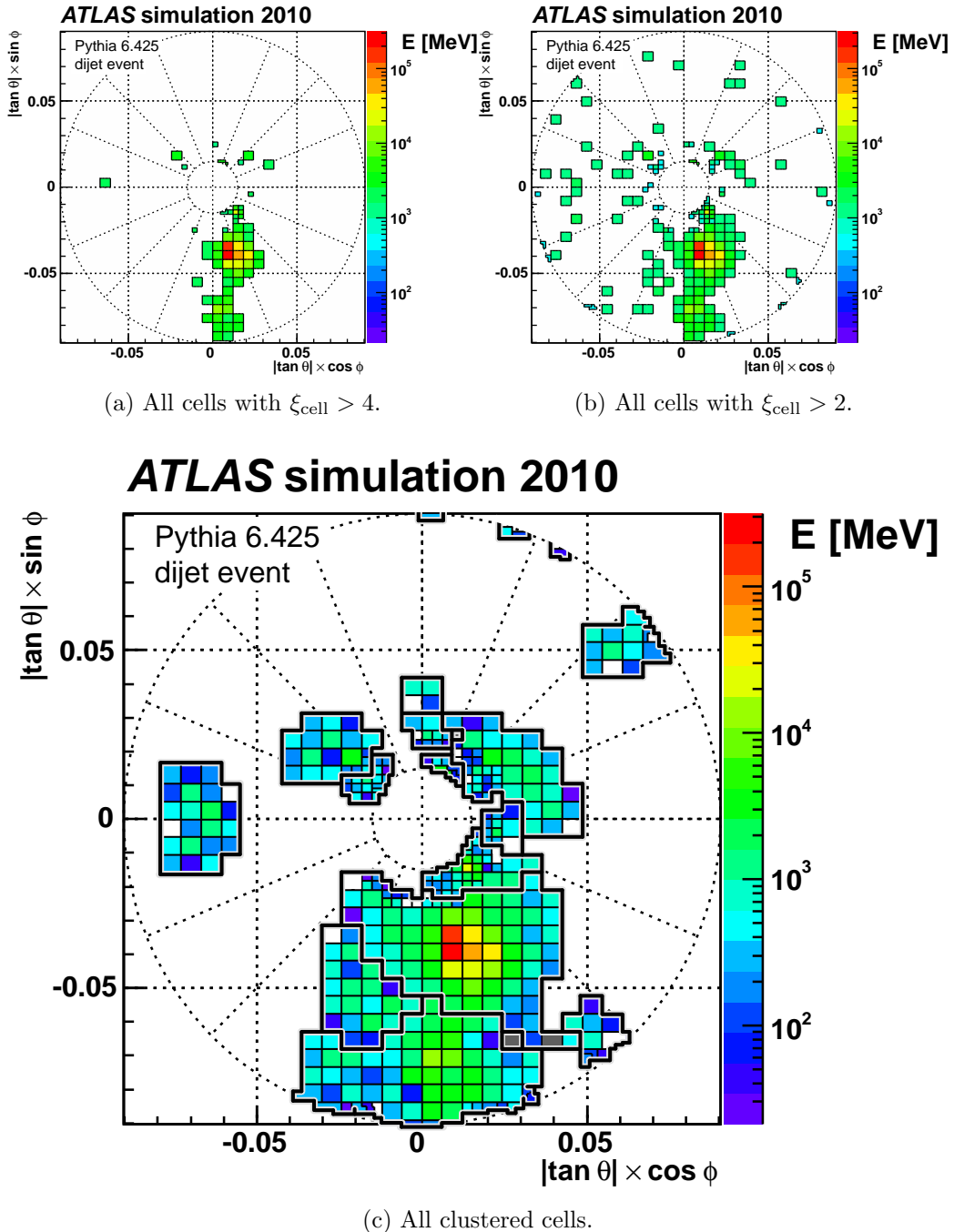


Figure 6.3: Example of topoclustering on a simulated dijet event.

1028 scaling to the clusters based on the shower development. The cluster energy can be
1029 corrected for calorimeter noncompensation and the differences in the hadronic and
1030 electromagnetic calorimeters’ responses. This scale provides additional corrections
1031 that improve the accuracy of hadronic energy measurements. This thesis only uses
1032 the EM scale corrections. LCW scaling requires additional measurements that only
1033 became available with additional data. Due to the jet calibration procedure that
1034 we will describe below, it is also a relatively complicated procedure to rederive the
1035 “correct” jet energy.

1036 Muon Spectrometer Tracks

1037 Muon spectrometer tracks are fit using the same algorithms as the ID tracks, but
1038 different subdetectors. The tracks are seeded by hits in the MDTs or CSCs. After
1039 seeding in the MDTs and CSCs, the hits from all subsystems are refit as the final
1040 MS track. These tracks are used as inputs to the muon reconstruction, as we will see
1041 below.

1042 6.2 Physics Object Reconstruction and Quality

1043 Identification

1044 There are essentially six objects used in ATLAS searches for new physics: electrons,
1045 photons, muons, τ -jets, jets, and E_T^{miss} . The reconstruction of these objects is
1046 described here. In this thesis, τ lepton jets are not treated differently from other
1047 hadronic jets, and we will not consider their reconstruction algorithms. A very
1048 convenient summary plot is shown in Fig. 6.4.

1049 One often wishes to understand “how certain” we are that a particular object
1050 is truly the underlying physics object. In ATLAS, we often generically consider, in

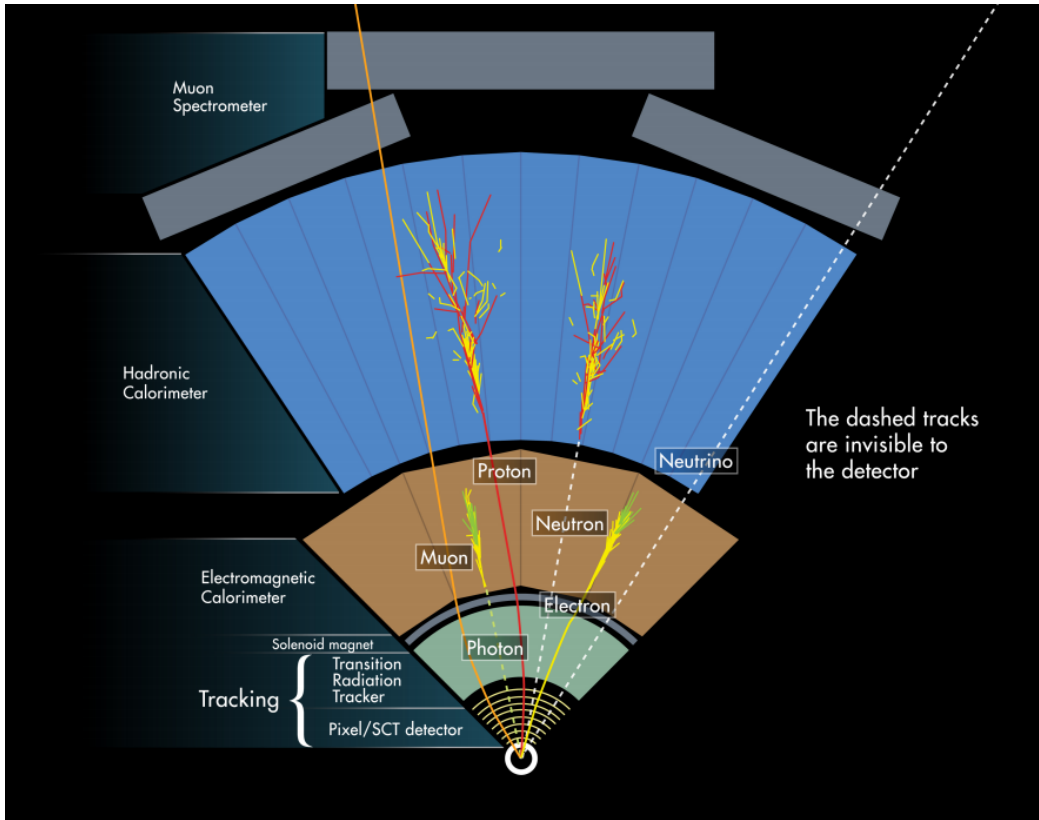


Figure 6.4: The interactions of particles with the ATLAS detector. Solid lines indicate the particle is interacting with the detector, while dashed lines are shown where the particle does not interact.

1051 order, *very loose*, *loose*, *medium*, and *tight* objects¹. These are ordered in terms of
 1052 decreasing object efficiency, or equivalently, decreasing numbers of fake objects. We
 1053 will also describe briefly the classification of objects into these categories.

1054 In this thesis, since we present a search for new physics in a zero lepton final state,
 1055 we will provide additional details about jet and E_T^{miss} reconstruction.

¹ These are not all used for all objects, but it's conceptually useful to think of these different categories.

1056 **Electrons and Photons**

1057 **Reconstruction**

1058 The reconstruction of electrons and photons (often for brevity called “electromagnetic
1059 objects”) is very similar [96, 100, 101]. This is because the reconstruction begins
1060 with the energy deposit in the calorimeter in the form of an electromagnetic shower.
1061 For any incoming e/γ , many more electrons and photons are produced in the shower.
1062 The measurement in the calorimeter is similar for these two objects.

1063 One begins the reconstruction of electromagnetic objects from the sliding-window
1064 clusters reconstructed from the EM calorimeter. These $E > 2.5$ GeV clusters the
1065 the primary seed for electrons and photons. One then looks for all ID tracks within
1066 $\Delta R < 0.3$, where $\Delta R = \sqrt{\Delta\eta^2 + \Delta\phi^2}$. We “match” the track and cluster if they are
1067 within $\Delta\phi < 0.2$ in the direction of track curvature, or $\Delta\phi < 0.05$ in the direction
1068 opposite the track curvature. Those track-cluster seeds with tracks pointing to the
1069 primary vertex are reconstructed as electrons.

1070 For photons, we have two options to consider, known as *converted* and *unconverted*
1071 photons. Due to the high energy of the LHC collisions, typical photons have energy
1072 $>\sim 1$ GeV. At this scale, photons interact almost exclusively via pair-production
1073 in the presence of the detector material, as shown in Fig. 6.5 [56]. If the track-
1074 cluster seed has a track which does not point at the primary vertex, we reconstruct
1075 this object as a converted photon. This happens since the photon travels a distance
1076 before decay into two electrons, and see the tracks coming from this secondary vertex.
1077 Those clusters which do not have any associated tracks are then reconstruced as an
1078 unconverted photon.

1079 The final step in electromagnetic object reconstruction is the final energy value.
1080 This process is different between electrons and photons due to their differing
1081 signatures in the EM calorimeter. In the barrel, electrons energies are assigned as

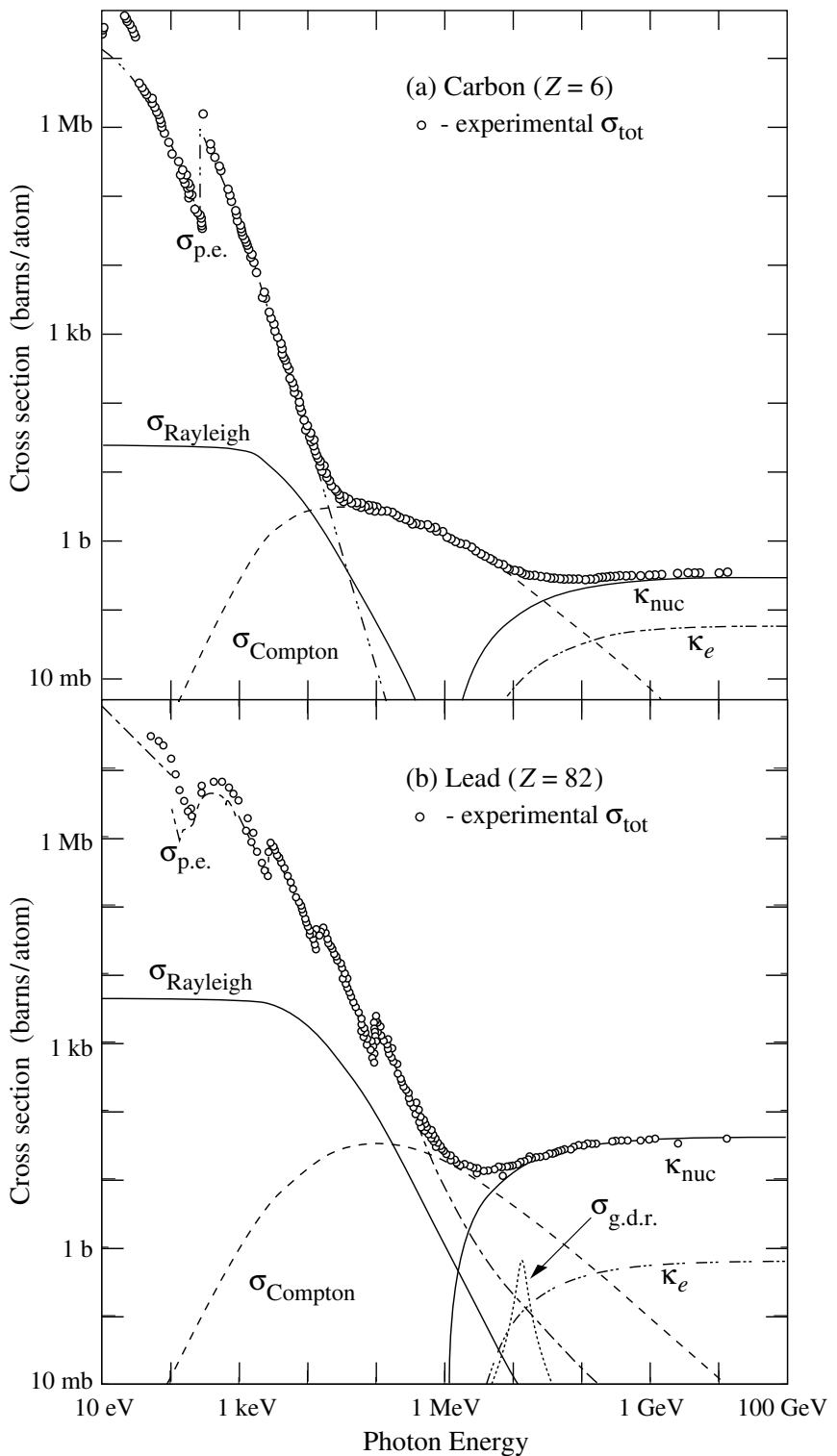


Figure 6.5: Photon total cross sections as a function of energy in carbon and lead, showing the contributions of different processes [56].

1082 the sum of the 3 clusters in η and 7 clusters in ϕ to account for the electron curving
1083 in the ϕ direction. Barrel photons are assigned the energy sum of (3, 5) clusters in
1084 (η, ϕ) space. In the endcap, the effect of the magnetic field on the electrons is smaller,
1085 and there is a coarser granularity. Both objects sum the (5, 5) clusters for their final
1086 energy value.

1087 Quality Identification

1088 Electrons have a number of important backgrounds which can give fakes. Fake
1089 electrons come primarily from secondary vertices in hadron decays or misidentified
1090 hadronic jets. To reduce these backgrounds, quality requirements are imposed on
1091 electron candidates. Loose electrons have requirements imposed on the shower
1092 shapes in the electromagnetic calorimeter and on the quality of the associated ID
1093 track. There is also a requirement that there is a small energy deposition in the
1094 hadronic calorimeter behind the electron, to avoid jets being misidentified as electrons
1095 (low hadronic leakage). Medium and tight electrons have increasingly stronger
1096 requirements on these variables, and additional requirements on the isolation (as
1097 measured by ΔR) and matching of the ID track momentum and the calorimeter
1098 energy deposit.

1099 Photons are relatively straightforward to measure, since there are few background
1100 processes [102]. The primary is pion decays to two photons, which can cause a jet
1101 to be misidentified as photon. Loose photons have requirements on the shower shape
1102 and hadronic leakage. Tight photons have tighter shower shape cuts, especially on
1103 the high granularity first layer of the EM calorimeter. The efficiency for unconverted
1104 tight photons as a function of p_T is shown in

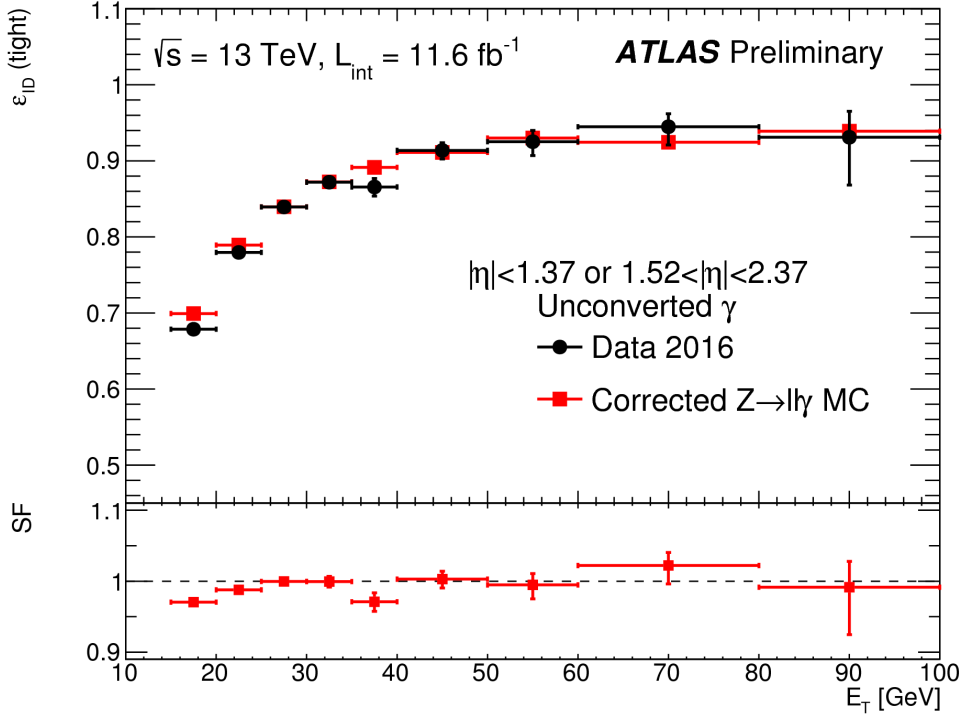


Figure 6.6: Unconverted photon efficiency as measured in [102].

1105 Muons

1106 Reconstruction

1107 Muons are reconstructed using measurements from all levels of the ATLAS detec-
 1108 tor [103]. They leave a ID track, a small, characteristic deposition in the EM calorime-
 1109 ter, and then a track in the muon spectrometer. The primary reconstruction technique
 1110 produces a so-called *combined* muon. “Combined” means using a combination of the
 1111 ID and MS tracks to produce the final reconstructed muon kinematics. This is done
 1112 by refitting the hits associated to both tracks, and using this refit track for the muon
 1113 kinematics.

1114 Quality Identification

Several additional criteria are used to assure muon measurements are free of significant background contributions, especially from pion and kaon decays to muons.

Muons produced via these decay processes are often characterized by a “kink”. Candidate muons with a poor fit quality, characterized by $\chi^2/\text{n.d.f.}$, are thus rejected. Additionally, the absolute difference in momentum measurements between the ID and MS provide another handle, since the other decay products from hadron decays carry away some amount of the initial hadron momentum. This is measured by

$$\rho' = \frac{|p_T^{\text{ID}} - p_T^{\text{MS}}|}{p_T^{\text{Combined}}}. \quad (6.2)$$

Additionally, there is a requirement on the q/p significance, defined as

$$S_{q/p} = \frac{|(q/p)^{\text{ID}} - (q/p)^{\text{MS}}|}{\sqrt{\sigma_{\text{ID}}^2 + \sigma_{\text{MS}}^2}}. \quad (6.3)$$

1115 The $\sigma_{\text{ID,MS}}$ in the denominator of Eq. Eq. (6.3) are the uncertainties on the corre-
 1116 sponding quantity from the numerator. Finally, cuts are placed on the number of
 1117 hits in the various detector elements.

1118 Subsequently tighter cuts on these variables allow one to define the different muon
 1119 identification criteria. Loose muons have the highest reconstruction efficiency, but
 1120 the highest number of fake muons, since there are no requirements on the number
 1121 of subdetector hits and the loosest requirements on the suite of quality variables.
 1122 Medium muons consist of Loose muons with tighter cuts on the quality variables.
 1123 They also require more than three MDT hits in at least two MDT layers. These are
 1124 the default used by ATLAS analyses. Tight muons have stronger cuts than those of
 1125 the medium selection, and reducing the reconstruction efficiency. The reconstruction
 1126 efficiency as a function of p_T can be seen for Medium muons in Fig. 6.7.

1127 Jets

1128 Jets are composite objects corresponding to many physical particles [56, 104, 105]
 1129 This is a striking difference from the earlier particles. Fortunately, we normally (and
 1130 in this thesis) only need information about the original particle produced in the

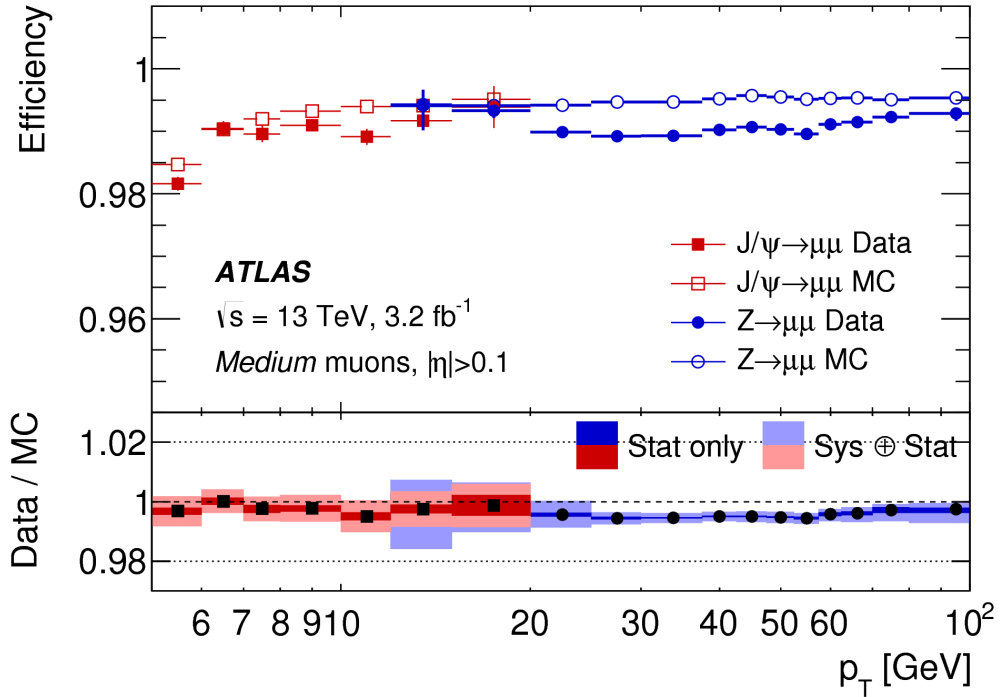


Figure 6.7: Medium muon efficiency as measured in [103].

1131 primary collision. In the SM, this corresponds to quarks and gluons. Due to the
 1132 hadronization process, free quarks and gluons spontaneously hadronize and produce
 1133 a hadronic shower, which we call a jet. These showers can be measured by the EM
 1134 and hadronic calorimeters, and the charged portions can be measured in the ID. The
 1135 first step is to combine these measurements into a composite object representing the
 1136 underlying physical parton. This is done via jet algorithms.

1137 Jet Algorithms

1138 It might seem straightforward to combine the underlying physical particles into a
 1139 jet. There are three important characteristics required for any jet reconstruction
 1140 algorithm to be used by ATLAS.

- 1141 • Collinear safety - if any particle with four-vector p is replaced by two particles
 1142 of p_1, p_2 with $p = p_1 + p_2$, the subsequent jet should not change

1143 • Radiative (infrared) safety - if any particle with four-vector p radiates a particle
1144 of energy $\alpha \rightarrow 0$, the subsequent jet should not change

1145 • Fast - the jet algorithm should be “fast enough” to be useable by ATLAS
1146 computing resources

1147 The first two requirements can be seen in terms of requirements on soft gluon emission.
1148 Since partons emit arbitrarily soft gluons freely, one should expect the algorithms
1149 to not be affected by this emission. The final requirement is of course a practical
1150 limitation.

The algorithms in use by ATLAS (and CMS) which satisfies these requirements are collectively known as the k_T algorithms [106–108]. These algorithms iteratively combine the “closest” objects, defined using the following distance measures :

$$d_{ij} = \min(k_{T,i}^{2p}, k_{T,j}^{2p}) \frac{\Delta_{ij}^2}{R^2} \quad (6.4)$$
$$d_{iB} = k_{Ti}^{2p}$$

1151 In Eq.Eq. (6.4), $k_{T,i}$ is the transverse momentum of i -th jet *constituent* and Δ_{ij} is
1152 the angular distance ΔR between the constituents. Both R and p are adjustable
1153 parameters: R is known as the (jet) *cone size* and p regulates the power of the energy
1154 versus the geometrical scales. The algorithm sequence, for a given set of objects i
1155 with four-vector k :

1156 1. Find the minimum distance in the set of all d_{ij} and d_{iB} .

1157 2. If the distance is one of the d_{ij} , combine the input pair of object i, j and return
1158 to (1). If the distance is one of the d_{iB} , remove the object from the list, call it
1159 a jet, and return to (1).

1160 This process ends when all objects i have been added to a jet.

1161 Any choice of (p, R) has requirements of collinear and radiative safety. In essence,
1162 the choice is then to optimize based on speed and the potential for new physics

1163 discoveries. In ATLAS, we make the choice of $p = -1$ which is also known as the
1164 *anti- k_T* algorithm. The choice of $R = 0.4$ is used for the distance parameter of the
1165 jets.

1166 The primary “nice” quality of this algorithm can be seen with the following
1167 example. Consider three inputs to an anti- k_T algorithm, all with $\eta = 0$:

- 1168 • Object 1 : $(p_T, \phi) = (30 \text{ GeV}, 0)$
- 1169 • Object 2 : $(p_T, \phi) = (20 \text{ GeV}, -0.2)$
- 1170 • Object 3 : $(p_T, \phi) = (10 \text{ GeV}, 0.2)$
- 1171 • Object 4 : $(p_T, \phi) = (1 \text{ GeV}, 0.5)$

1172 In the case shown, it seems natural to first combine the “bigger” objects 1 and 2.
1173 These then pick up the extra small object 3, and object 4 is not included in the jet.
1174 This is what is done by the anti- k_T algorithm. The (normal) k_T algorithm with $p = 1$
1175 instead combines the smallest objects, 3 and 4, first. Object 1 and 2 combine to form
1176 their own jet, instead of these jets picking up object 3. This behavior is not ideal due
1177 to effects from pileup, as we will see in the next section.

1178 Jet Reconstruction

1179 In ATLAS, jets are reconstructed using multiple different objects as inputs, including
1180 tracks, “truth” objects, calorimeter clusters, and *particle flow objects* (PFOs).
1181 For physics analyses, ATLAS primarily uses jets reconstructed from calorimeter
1182 clusters, but we will describe the others here, as they are often used for systematic
1183 uncertainties.

1184 Calorimeter jets are reconstructed using topoclusters with the anti- k_T algorithm
1185 with $R = 0.4$. The jet reconstruction algorithm is run on the collection of all
1186 topoclusters reconstructed as in Sec. 6.1. Both EM and LCW scale clusters are

1187 used in the ATLAS reconstruction software and produce two sets of jets for analysis.
1188 As stated above, this thesis presents an analysis using jets reconstructed using EM
1189 scale clusters, which we refer to as *EM jets*.

1190 Tracks can be used as inputs to jet reconstruction algorithms. Jets reconstructed
1191 from tracks are known as *track jets*. Since the ID tracks do not measure neutral
1192 objects, these jets underestimate the true jet energy. However, these are still useful
1193 for checks and derivations of systematic uncertainties.

1194 *Truth* jets are reconstructed from *truth* particles. In this case, truth is jargon
1195 for simulation. In simulation, the actual simulated particles are available and used
1196 as inputs to the jet reconstruction algorithms. Similarly to track jets, these are not
1197 useful in and of themselves, but are used in conjunction with studies of reconstructed
1198 jets.

1199 The last object used as inputs to jet reconstruction algorithms are *particle flow*
1200 *objects* (PFOs). These are used extensively as the primary input to jet particle
1201 reconstruction algorithms by the CMS collaboration [109]. Particle flow objects are
1202 reconstructed by associating tracks and clusters through a combination of angular
1203 distance measures and detector response measurements to create a composite object
1204 which contains information from both the ID and the calorimeters. For calorimeter
1205 clusters which do not have any associated ID track, the cluster is simply the PFO.
1206 The natural association between tracks and clusters provides easy pileup subtraction
1207 since tracks are easily associated to the primary vertex. As pileup has increased, the
1208 utility of using PFOs as inputs to jet reconstruction has increased as well.

1209 Jet Calibration

1210 Jets as described in the last section are still *uncalibrated*. Even correcting the cluster
1211 energies using the LCW does not fully correct the jet energy, due to particles losing
1212 energy in the calorimeters. This is corrected using the *jet energy scale* (JES). The

1213 JES is a series of calibrations which on average restore the correct truth jet energy
1214 for a given reconstructed jet. The steps to derive the JES are described in Fig. 6.8
1215 and described here.

1216 The first step is the origin correction. This adjusts the jet to point at the
1217 primary vertex. Next, is the jet-area based pileup correction. This step subtracts
1218 the “average” pileup as measured by the energy density ρ outside of the jets and
1219 assumes this is a good approximation for the pileup inside the jet. One removes
1220 energy $\Delta E = \rho \times A_{\text{jet}}$ in this step. The residual pileup correction applies a final offset
1221 correction by parametrizing the change in jet energy as a function of the number of
1222 primary vertices N_{PV} and the average number of interactions μ . More details can be
1223 found in [105].

1224 The next step is the most important single correction, known as the AbsoluteE-
1225 taJES. Due to the use of noncompensation and sampling calorimeters in ATLAS,
1226 the measured energy of a jet is a fraction of the true energy of the outgoing parton.
1227 Additionally, due to the use of different technologies and calorimeters throughout the
1228 detector, there are directional biases induced by these effects. The correction bins a
1229 multiplicative factor in p_{T} and η which scales the reconstructed jets to corresponding
1230 truth jet p_{T} . This step does not entirely correct the jets, since it is entirely a
1231 simulation-based approach.

1232 The final steps are known as the global sequential calibration (GSC) and the
1233 residual in-situ calibration. The GSC uses information about the jet showering shape
1234 to apply additional corrections based on the expected shape of gluon or quark jets.
1235 The final step is the residual in-situ calibration, which is only applied to data. This
1236 step uses well-measured objects recoiling off a jet to provide a final correction to the
1237 jets in data. In the low p_{T} region ($20 \text{ GeV} \lesssim p_{T,\text{jet}} \lesssim 200 \text{ GeV}$), $Z \rightarrow ll$ events are
1238 used as a reference object. In the p_{T} region ($100 \text{ GeV} \lesssim p_{T,\text{jet}} \lesssim 600 \text{ GeV}$), the reference
1239 object is a photon, while in the high p_{T} region ($p_{T,\text{jet}} \gtrsim 200 \text{ GeV}$), the high p_{T} jet is

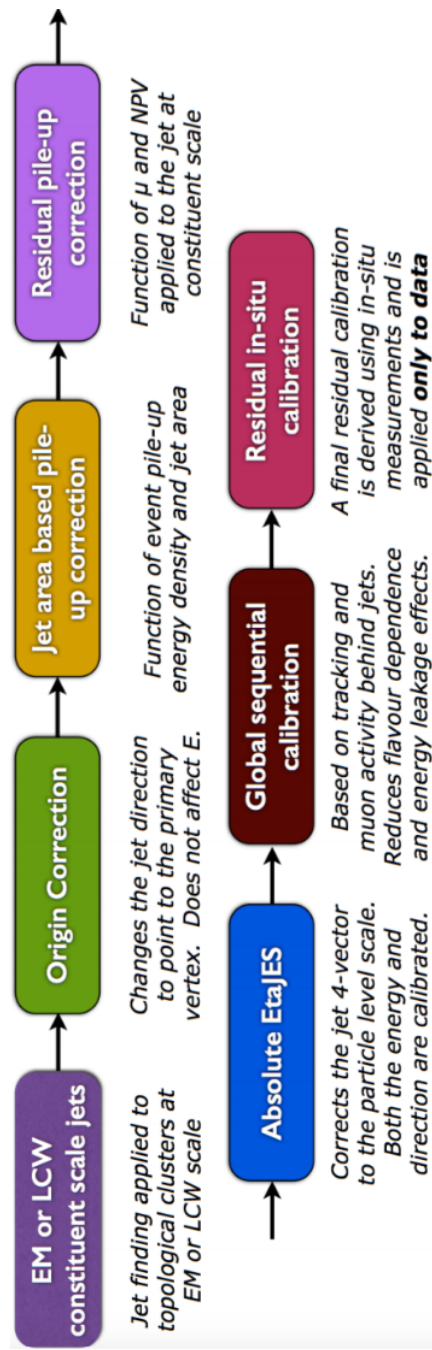


Figure 6.8: The steps used by ATLAS to calibrate jets

1240 compared to multiple smaller p_T jets. The reference object is the group of multijets.
 1241 After the application of the residual in-situ calibration, the data and MC scales are
 1242 identical up to corresponding uncertainties. The combined JES uncertainty as a
 1243 function of p_T is shown in Fig. 6.9.

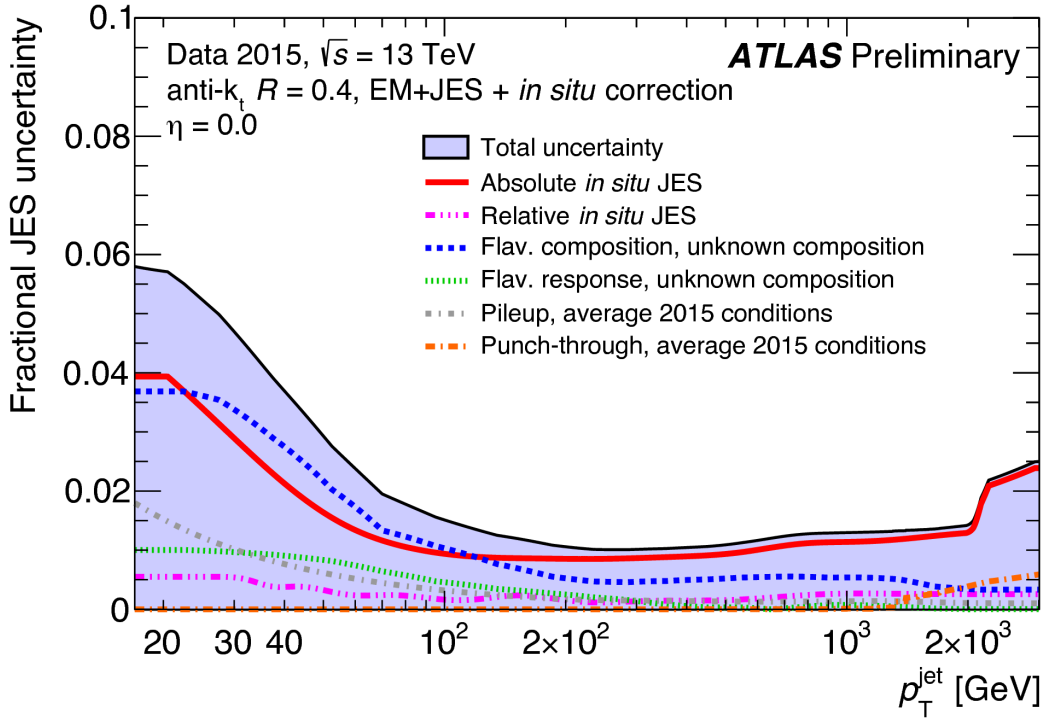


Figure 6.9: Combined jet energy scale uncertainty as a function of p_T at $\eta = 0$.

1244 Jet Vertex Tagger

1245 The *jet vertex tagger* (JVT) technique is used to separate pileup jets from those
 1246 associated to the hard primary vertex [110]. The technique for doing so first involves
 1247 *ghost association* [111]. Ghost association runs the anti- k_T jet clustering algorithm
 1248 on a combined collection of the topoclusters and tracks. The tracks *only* momenta
 1249 are set to zero², with only the directional information included. As discussed above,
 1250 the anti- k_T algorithm is “big to small”; tracks are associated to the “biggest” jet
 1251 near them in (η, ϕ) . This method uniquely associates each track to a jet, without
 1252 changing the final jet kinematics.

1253 The JVT technique uses a combination of track variables to determine the
 1254 likelihood that the jet originated at the primary vertex. For jets which have associated
 1255 tracks from ghost association, this value ranges from 0 (likely pileup jet) to 1 (likely

²Not exactly zero, since zero momentum tracks wouldn’t have a well-defined (η, ϕ) coordinate, but set to a value obeying $p_{T,track} << 400$ MeV = $p_{track,min}$. This is the minimum momentum for a track to reach the ATLAS inner detector.

1256 hard scatter jet). Jets without associated tracks are assigned $\text{JVT} = -.1$. The
1257 working point of $\text{JVT} > .59$ is used for jets in this thesis.

1258 **B-jets**

1259 Jets originating from bottom quarks (b-jets) can be *tagged* by the ATLAS detec-
1260 tor [112, 113]. B-hadrons, which have a comparatively long lifetime compared
1261 to hadrons consisting of lighter quarks, can travel a macroscopic distance inside
1262 the ATLAS detector. The high-precision tracking detectors identify the secondary
1263 vertices from these decays and the jet matched to that vertex is called a *b-jet*. The
1264 MV2c10 algorithm [112, 113], based on boosted decision trees, identifies these jets
1265 using a combination of variables sensitive to the difference between light-quark and
1266 b-quark jets. The efficiency of this tagger is 77%, with a rejection factor of 134 for
1267 light-quarks and 6 for charm jets.

1268 **Missing Transverse Momentum**

1269 Missing transverse momentum $E_{\text{T}}^{\text{miss}}$ [114] is a key observable in searches for new
1270 physics, especially in SUSY searches [115, 116]. However, $E_{\text{T}}^{\text{miss}}$ is not a uniquely
1271 defined object when considered from the detector perspective (as compared to the
1272 Feynammn diagram), and it is useful to understand the choices that affect the
1273 performance of this observable in searches for new physics.

1274 **$E_{\text{T}}^{\text{miss}}$ Definitions**

Hard objects refers to all physical objects as defined in the previous sections. The
 $E_{\text{T}}^{\text{miss}}$ reconstruction procedure uses these hard objects and the *soft term* to provide
a value and direction of the missing transverse momentum. The $E_{x(y)}^{\text{miss}}$ components

are calculated as:

$$E_{x(y)}^{\text{miss}} = E_{x(y)}^{\text{miss, } e} + E_{x(y)}^{\text{miss, } \gamma} + E_{x(y)}^{\text{miss, jets}} + E_{x(y)}^{\text{miss, } \mu} + E_{x(y)}^{\text{miss, soft}}, \quad (6.5)$$

1275 where each value $E_{x(y)}^{\text{miss, } i}$ is the negative vectorial sum of the calibrated objects defined
1276 in the previous sections.

1277 For purposes of E_T^{miss} reconstruction, we must assign an *overlap removal* ordering.
1278 This is to avoid double counting of the underlying primitive objects (clusters and
1279 tracks) which are inputs to the reconstruction of the physics objects. We resolve this
1280 in the following order : electrons, photons , jets and muons. This is motivated by the
1281 performance of the reconstruction of these objects in the calorimeters.

1282 The soft term $E_{x(y)}^{\text{miss, soft}}$ contains all of the primitive objects which are not
1283 associated to any of the reconstructed physics objects. we need to choose which
1284 primitive object to use. The primary choices which have been used within ATLAS
1285 are the *calorimeter-based soft term* (CST) and the *track-based soft term* (TST) [114].
1286 Based on the soft term choice, we then call E_T^{miss} built with a CST (TST) soft term
1287 simply CST (TST) E_T^{miss} . An additional option, which will be important as pileup
1288 continues to increase, is particle flow E_T^{miss} (PFlow E_T^{miss}).

1289 The CST E_T^{miss} was used for much of the early ATLAS data-taking. CST E_T^{miss}
1290 is built from the calibrated hard objects, combined with the calorimeter clusters
1291 which are *not* assigned to any of those hard objects. In the absence of pileup, it
1292 provides the best answer for the “true” E_T^{miss} in a given event, due to the impressive
1293 hermiticity of the calorimeters. Unfortunately, the calorimeters do not know from
1294 where their energy deposition came, and thus CST is susceptible to drastically reduced
1295 performance with increasing pileup.

1296 TST E_T^{miss} is the standard for ATLAS searches as currently performed by ATLAS.
1297 TST E_T^{miss} is reconstructed using the calibrated hard objects and a soft term from
1298 the tracks which are not assigned to any of those hard objects. In particular, due
1299 to the track-vertex association efficiency, one chooses tracks which only come from

1300 the primary vertex. This reduces the pileup contributions to the E_T^{miss} measurement.
1301 However, since the ID tracking system is unable to detect neutral objects, the TST
1302 E_T^{miss} is “wrong”. In most searches for new physics, the soft E_T^{miss} is generally a small
1303 fraction of the total E_T^{miss} , and thus this bias is not particularly hurtful.

1304 PFlow E_T^{miss} uses the PFOs described above to build the E_T^{miss} . The PFOs which
1305 are assigned to hard objects are calibrated, and the PFOs which are not assigned
1306 to any hard object are added to the soft term. In this context, it is convenient to
1307 distinguish between “charged” and “neutral” PFOs. Charged PFOs can be seen as
1308 a topocluster which has an associated track, while neutral PFOs do not. A charged
1309 PFO is essentially a topocluster which is matched with the primary vertex. The
1310 neutral PFOs have the same status as the original topoclusters. Thus a “full” PFlow
1311 E_T^{miss} should have performance somewhere between TST E_T^{miss} and CST E_T^{miss} ³. A
1312 *charged* PFlow E_T^{miss} should be the same as TST.

1313 Measuring E_T^{miss} Performance : event selection

1314 The question is now straightforward: how do we compare these different algorithms?
1315 We compare these algorithms in $Z \rightarrow \ell\ell + \text{jets}$ and $W \rightarrow \ell\nu + \text{jets}$ events. Due to
1316 the presence of leptons, these events are well-measured “standard candles”. Here
1317 we present the results in early 2015 data with $Z \rightarrow \mu\mu$ and $W \rightarrow e\nu$ events, as
1318 shown in [117, 118]. This result was important to assure the integrity of the E_T^{miss}
1319 measurements at the higher energy and pileup environment of Run-2.

1320 The $Z \rightarrow \ell\ell$ selection is used to measure the intrinsic E_T^{miss} resolution of the
1321 detector. Neutrinos only occur in these events from heavy-flavor decays inside of jets,
1322 and thus $Z \rightarrow \ell\ell$ events have very low E_T^{miss} . This provides an ideal event topology
1323 to understand the modelling of E_T^{miss} mismeasurement. Candidate $Z \rightarrow \mu\mu$ events
1324 are first required to pass a muon or electron trigger, as described in Tab. 5.1. Offline,

³Naively, due to approximate isospin symmetry, about 2/3 of the hadrons will be charged and 1/3 will be neutral.

1325 the selection of $Z \rightarrow \mu\mu$ events requires exactly two medium muons. The muons are
 1326 required to have opposite charge and $p_T > 25$ GeV, and mass of the dimuon system
 1327 is required to be consistent with the Z mass $|m_l - m_Z| < 25$ GeV.

$W \rightarrow \ell\nu$ events are an important topology to evaluate the E_T^{miss} modelling in events with real E_T^{miss} . This E_T^{miss} is from the neutrino, which is not detected. The E_T^{miss} in these events has a characteristic distribution with a peak at $\frac{1}{2}m_W$. The selection of $W \rightarrow e\nu$ events begins with the selection of exactly one electron of medium quality. A selection on TST $E_T^{\text{miss}} > 25$ GeV drastically reduces the background from multijet events where the jet fakes an electron. The transverse mass is used to select the $W \rightarrow e\nu$ events :

$$m_T = \sqrt{2p_T^\ell E_T^{\text{miss}}(1 - \cos \Delta\phi)}, \quad (6.6)$$

1328 where $\Delta\phi$ is the difference in the ϕ between the E_T^{miss} and the electron. m_T is required
 1329 to be greater than 50 GeV.

1330 There are two main ingredients to investigate : the E_T^{miss} resolution and the E_T^{miss}
 1331 scale.

1332 Measuring E_T^{miss} Performance in early 2015 data : metrics

1333 To compare these algorithms we use the E_T^{miss} resolution, E_T^{miss} scale, and linearity.
 1334 Representative distributions of TST E_x^{miss} , E_y^{miss} , and E_T^{miss} from early 2015 datataking are shown in Fig. 6.10.

The E_T^{miss} resolution is an important variable due to the fact that the bulk of the distributions associated to $E_{x(y)}^{\text{miss}}$ are Gaussian distributed [Aad2012]. However, to properly measure the tails of this distribution, especially when considering non-calorimeter based soft terms, it is important to use the root-mean square as the proper measure of the resolution. This is strictly larger than resolution as measured using a fit to a Gaussian, due to the long tails from i.e. track mismeasurements. The resolution is measured with respect to two separate variables : $\sum E_T$ and N_{PV} . $\sum E_T$

is an important measure of the “total event activity”. It is defined as

$$\sum E_T = \sum p_T^e + \sum p_T^\gamma + \sum p_T^\tau + \sum p_T^{\text{jets}} + \sum p_T^\mu + \sum p_T^{\text{soft}}. \quad (6.7)$$

1336 The measurement as a function of N_{PV} is useful to understand the degradation of
 1337 E_T^{miss} performance with increasing pileup. Fig. 6.11 shows the TST E_T^{miss} resolution
 1338 in the early 2015 data compared with simulation. The degradation of the TST E_T^{miss}
 1339 performance is shown as a function of pileup N_{PV} and total event activity $\sum E_T$. We
 1340 see that the degradation is significant as a function of these variables, but simulation
 1341 describes the data well.

Another important performance metric is the E_T^{miss} scale. This indicates how well we measure the magnitude of the E_T^{miss} , as CST E_T^{miss} contains additional particles from pileup, while soft neutral particles⁴ are ignored by TST E_T^{miss} . To determine this in data, we again use $Z \rightarrow \mu\mu$ events, where the $Z \rightarrow \mu\mu$ system is treated as a well-measured reference object. The component of E_T^{miss} which is in the same direction as the reconstructed $Z \rightarrow \mu\mu$ system is sensitive to potential biases in the detector response. The unit vector \mathbf{A}_Z of the Z system is defined as

$$\mathbf{A}_Z = \frac{\vec{p}_T^{\ell^+} + \vec{p}_T^{\ell^-}}{|\vec{p}_T^{\ell^+} + \vec{p}_T^{\ell^-}|}, \quad (6.8)$$

1342 where $\vec{p}_T^{\ell^+}$ and $\vec{p}_T^{\ell^-}$ are the transverse momenta of the leptons from the Z boson
 1343 decay. The relevant scale metric is the mean value of the \vec{E}_T^{miss} projected onto \mathbf{A}_Z :
 1344 $\langle \vec{E}_T^{\text{miss}} \cdot \mathbf{A}_Z \rangle$. In Fig. 6.12, the scale is shown for the early 2015 dataset. The negative
 1345 bias, which is maximized at about 5 GeV, is a reflection of two separate effects. The
 1346 soft neutral particles are missed by the tracking system, and thus ignored in TST
 1347 E_T^{miss} . Missed particles due to the limited ID acceptance can also affect the scale.

For events with real E_T^{miss} , one can also look at the *linearity* in simulation. This

⁴“Soft” here means those particles which are not hard enough to be reconstructed as their own particle, using the reconstruction algorithms above.

is defined as

$$\text{linearity} = \langle \frac{E_T^{\text{miss}} - E_T^{\text{miss,Truth}}}{E_T^{\text{miss,Truth}}} \rangle. \quad (6.9)$$

1348 $E_T^{\text{miss,Truth}}$ refers to “truth” particles as defined before, or the magnitude of the vector
1349 sum of all noninteracting particles. The linearity is expected to be zero if the E_T^{miss}
1350 is reconstructed at the correct scale.

1351 Particle Flow Performance

1352 As described above, the resolution, scale, and linearity are metrics to understand the
1353 performance of the different E_T^{miss} algorithms. In this section, we present comparisons
1354 of the different algorithms, including particle flow, in simulation and using a data
1355 sample from 2015 of 80 pb^{-1} . In these plots, “MET_PFlow-TST” refers to charged
1356 PFlow E_T^{miss} , while the other algorithms are as described above.

1357 Figs. 6.14 and 6.15 show the resolution and scale in simulated $Z \rightarrow \mu\mu$ events.
1358 The resolution curves follow the expected behavior discussed before. Due to the high
1359 pileup in 2015 run conditions, the CST E_T^{miss} resolution is poor, and further degrades
1360 with increasing pileup and event activity. The “regular” PFlow E_T^{miss} shows reduces
1361 pileup and event activity dependence as compared to the CST. PFlow E_T^{miss} can be
1362 seen as a hybrid of TST E_T^{miss} and CST E_T^{miss} . The charged PFOs ($\sim 2/3$) are pileup
1363 suppressed, while the neutral PFOs (or topoclusters) are not. Both charged PFlow
1364 and TST E_T^{miss} show only a small residual dependence on N_{PV} and $\sum E_T$, since they
1365 have fully pileup suppressed inputs through track associations.

1366 The scale plots are shown for $Z+\text{jets}$ events and Z events with no jets. For the
1367 nonsuppressed CST, the scale continues to worsen with increasing p_T^Z . The standard
1368 PFlow algorithm performs the second worst in the region of high p_T^Z , but is the best at
1369 low p_T^Z . We note the improved scale of the charged PFlow E_T^{miss} compared to the TST
1370 E_T^{miss} . Considering the resolution is essentially identical, the PFlow algorithm is better
1371 picking up the contributions from additional neutral particles. In events with no jets,

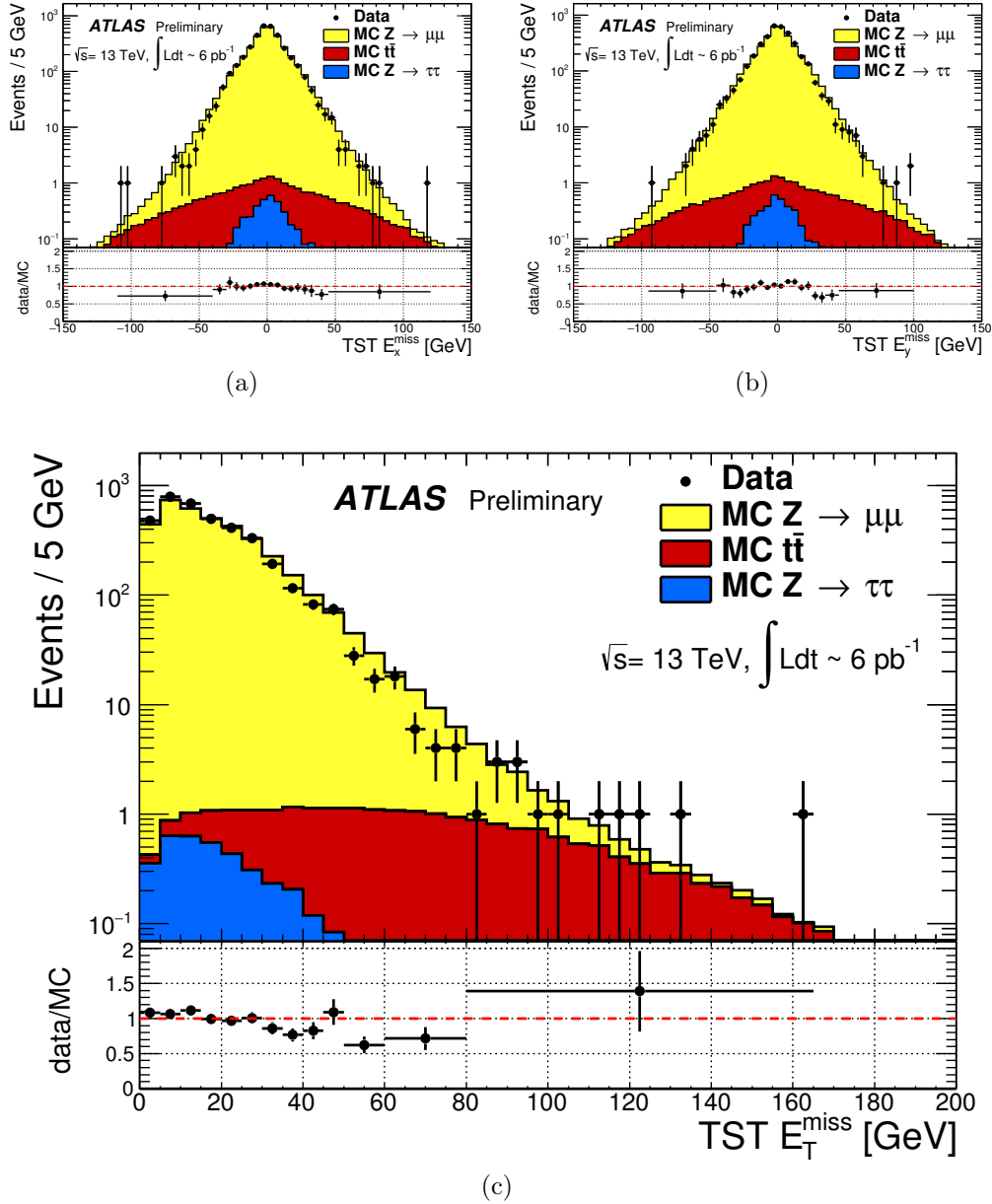


Figure 6.10: TST E_x^{miss} , E_y^{miss} , and E_T^{miss} distributions of early $\sqrt{s} = 13 \text{ TeV}$ data compared with simulation after the $Z \rightarrow \mu\mu$ selection. The data sample consists of 6 pb^{-1} .

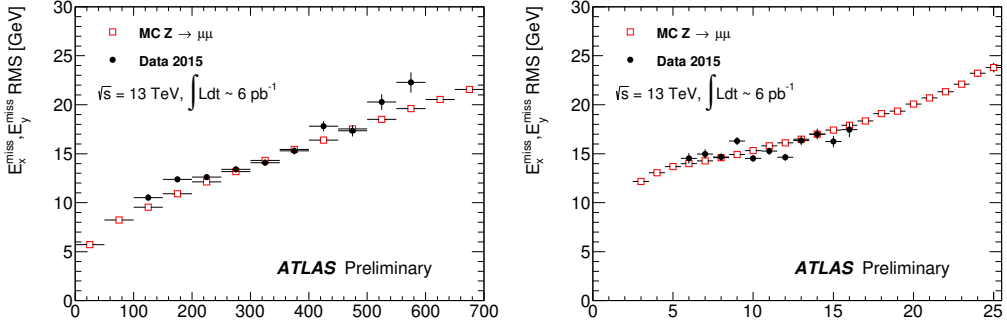


Figure 6.11: Resolution of TST E_T^{miss} of early $\sqrt{s} = 13$ TeV data compared with simulation after the $Z \rightarrow \mu\mu$ selection. The data sample consists of 6 pb^{-1} .

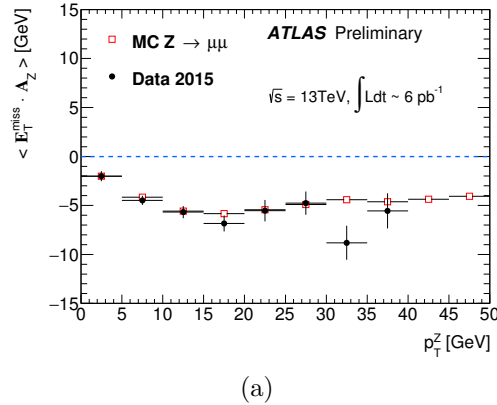


Figure 6.12: Scale of TST E_T^{miss} of early $\sqrt{s} = 13$ TeV data compared with simulation after the $Z \rightarrow \mu\mu$ selection. The data sample consists of 6 pb^{-1} .

1372 the soft term is essentially the only indication of the E_T^{miss} mismeasurement, since
 1373 the muons will be well-measured. In this case, the pileup effects cancel, on average,
 1374 due to the $U(1)_\phi$ symmetry of the ATLAS detector, and CST performs rather well
 1375 compared to the more complicated track-based algorithms. The full PFlow algorithm
 1376 performs best, since it provides a small amount of pileup suppression on the neutral
 1377 components from CST.

1378 The resolution and linearity are shown in simulated $W \rightarrow e\nu$ events in Fig. 6.13.
 1379 The resolution in $W \rightarrow e\nu$ events shows a similar qualitative behavior to $Z \rightarrow$
 1380 $\mu\mu$ events. The CST E_T^{miss} has the worst performance, with charged PFlow E_T^{miss}

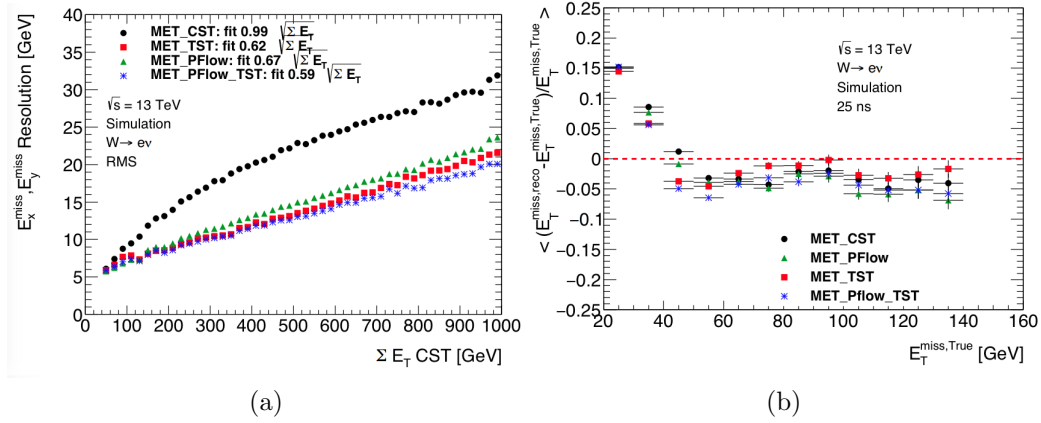


Figure 6.13: Comparison of $E_{\text{T}}^{\text{miss}}$ resolution and linearity using different $E_{\text{T}}^{\text{miss}}$ algorithms with simulated $W \rightarrow e\nu$ events.

1381 performing best. The surprise here is the scale associated to TST $E_{\text{T}}^{\text{miss}}$ has the
 1382 strongest performance throughout the space parameterized by $E_{\text{T}}^{\text{miss,Truth}}$, except for
 1383 one bin at $40 \text{ GeV} < E_{\text{T}}^{\text{miss,Truth}} < 50 \text{ GeV}$. The scale in these events is best measured
 1384 using a track-based soft term.

1385 The resolution also investigated in real data passing the $Z \rightarrow \mu\mu$ selection
 1386 described above. A comparison of the $E_{\text{T}}^{\text{miss}}$ between real data and simulation for
 1387 each algorithm is presented in Fig. 6.16. The resolution as a function of $\sum E_{\text{T}}$ and
 1388 N_{PV} is shown in Fig. 6.17 for this dataset. Overall, the real dataset shows the
 1389 same general features as the simulation dataset in terms of algorithm performance.
 1390 However, the performance of all algorithms seems to be significantly worse in data.
 1391 This is likely due to simplifications made in the simulation: soft interactions which
 1392 are not simulated have a significant effect on an event level variable such as the $E_{\text{T}}^{\text{miss}}$
 1393 resolution.

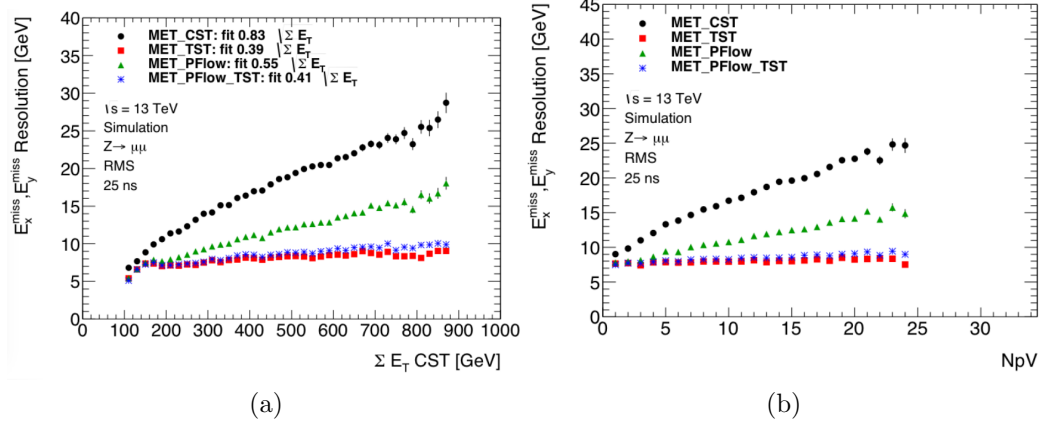


Figure 6.14: Comparison of E_T^{miss} resolution using different E_T^{miss} algorithms with simulated $Z \rightarrow \mu\mu$ events.

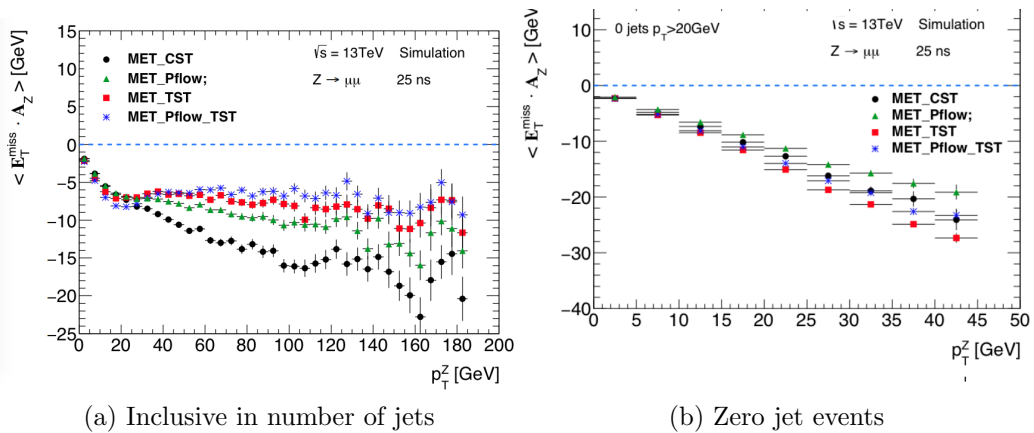


Figure 6.15: Comparison of E_T^{miss} scale using different E_T^{miss} algorithms with simulated $Z \rightarrow \mu\mu$ events.

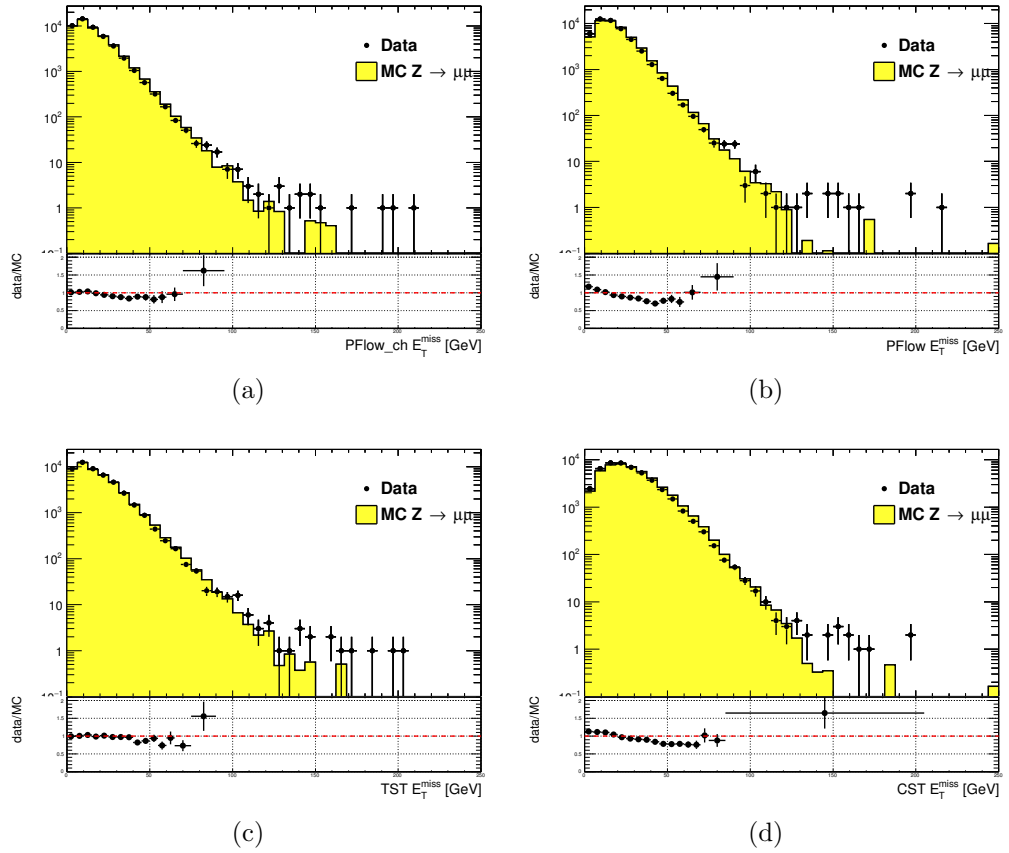


Figure 6.16: Comparison of E_T^{miss} distributions using different E_T^{miss} algorithms with a data sample of 80 pb^{-1} after the $Z \rightarrow \mu\mu$ selection

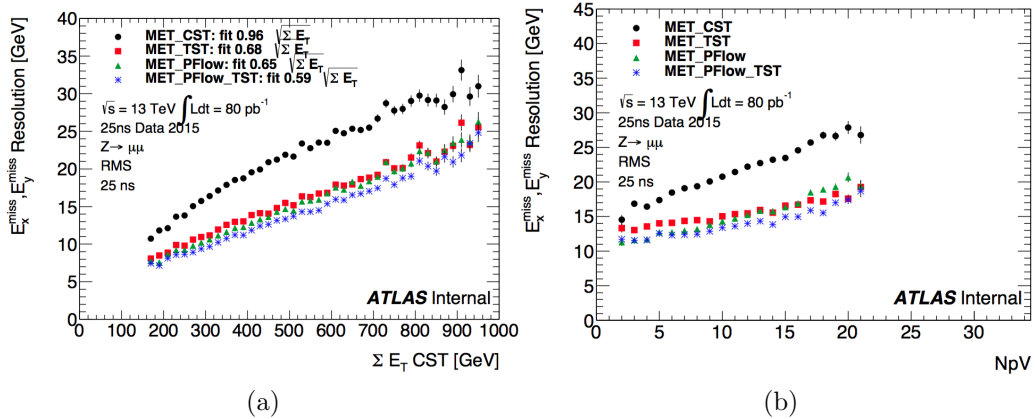


Figure 6.17: Comparison of E_T^{miss} resolution using different E_T^{miss} algorithms with a data sample of 80 pb^{-1} after the $Z \rightarrow \mu\mu$ selection

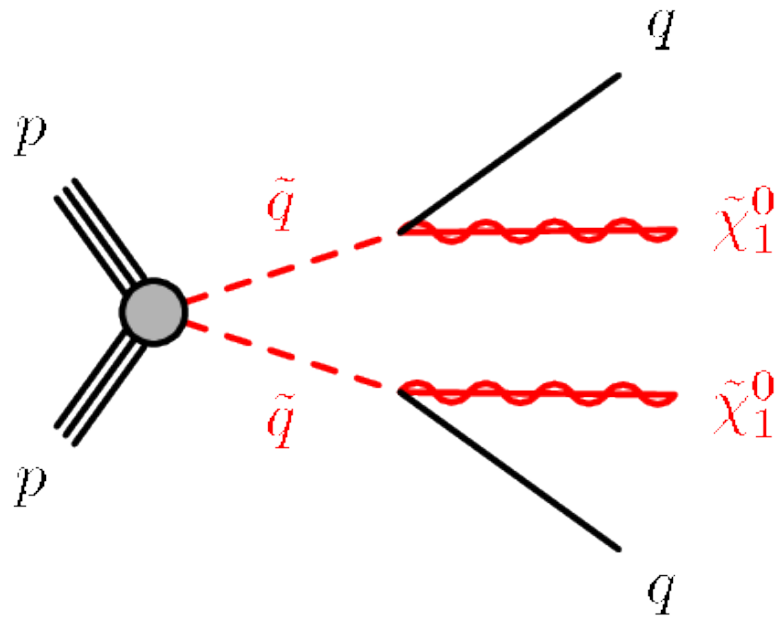
Recursive Jigsaw Reconstruction

1396 *Recursive Jigsaw Reconstruction* (RJR) [119, 120] is a novel algorithm used for
 1397 the analysis presented in this thesis. RJR is the conceptual successor to the razor
 1398 technique [121, 122], which has been used successfully in many new physics searches
 1399 [37, 38, 40, 41, 47, 123]. In this chapter, we will first present the razor technique,
 1400 and describe the razor variables. We will then present the RJR algorithm. After the
 1401 description of the algorithm, we will describe the precise RJR variables used in the
 1402 analysis.

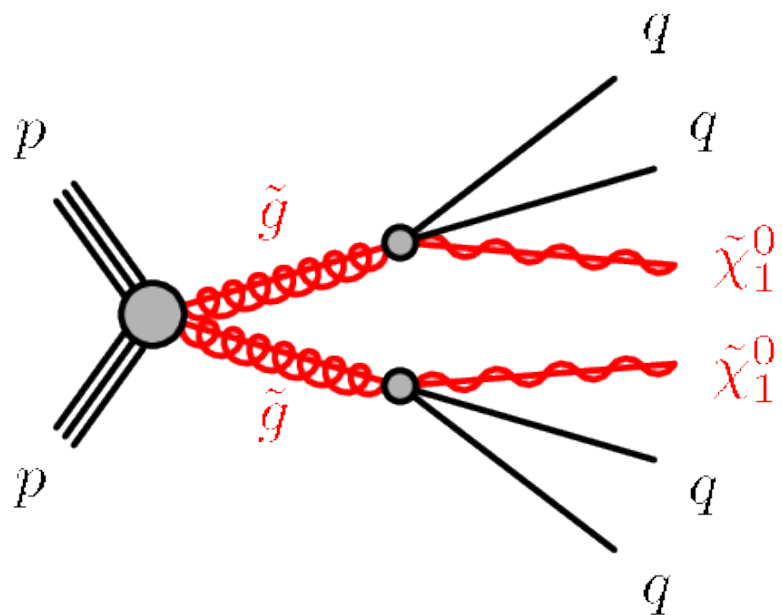
1403 **7.1 Razor variables**1404 **Motivation**

1405 We consider SUSY models where gluinos and squarks are pair-produced. Pair-
 1406 production is a consequence of the R -parity imposed in many SUSY models. R -parity
 1407 violation is highly constrained by limits on proton decay [15], and is often assumed
 1408 in SUSY model building. The Feynman diagrams considered are shown in Fig. 7.1.

1409 The consequences of this \mathbb{Z}_2 symmetry are drastic [15]. To understand the
 1410 utility of the razor variables, the stability of the lightest supersymmetric particle
 1411 is important. In many SUSY models, including the ones considered in this thesis,
 1412 this is the lightest neutralino $\tilde{\chi}_1^0$. This means that on either side of a SUSY decay
 1413 process, where we begin with sparticle pair production, we have a final state particle
 1414 which is not detected. Generically, this leads to E_T^{miss} . Selections based on E_T^{miss} are



(a) Squark pair production



(b) Gluino pair production

Figure 7.1: Feynman diagrams for the SUSY signals considered in this thesis

1415 very good at reducing backgrounds, for example from QCD processes.

1416 However, there are limitations to searches based on E_T^{miss} . Due to jet mismeasurements, instrumental failures, finite detector acceptance, nongaussian tails in the detector response, and production of neutrinos inside of jets, there are many sources of “fake” E_T^{miss} which does not correspond to a Standard Model neutrino or new physics object such as an LSP. An additional limitation is the complete lack of longitudinal information. As events from QCD backgrounds tend to have higher boosts along the z -direction, this neglects an important discriminator for use in searches for SUSY. Finally, E_T^{miss} is only one object, which is a measurement for *two* separate LSPs. If one could factorize this information somehow, this would provide additional information to potentially discriminate against backgrounds. The *razor variables* (M_{Δ}^R, R^2) are more robust than E_T^{miss} -based variables against sources of fake E_T^{miss} as well as providing additional longitudinal information which can be used to discriminate against backgrounds [121, 122].

1429 Derivation of the razor variables

1430 To derive the razor variables (M_{Δ}^R, R^2), we start with a generic situation of the pair
1431 production of heavy sparticles with mass m_{Heavy} .¹ Each sparticle decays to a number
1432 of observable objects (in this thesis, jets), and an unobservable $\tilde{\chi}_1^0$ of mass $m_{\tilde{\chi}_1^0}$. We
1433 will combine all of the jets into a *megajet*; this process will be described below. We
1434 begin by analyzing the decay in the “rough-approximation”, or in modern parlance,
1435 *razor frame* (R -frame). This is the frame where the sparticle is at rest. Note that
1436 by construction, there are two razor frames corresponding to each sparticle. The
1437 complete set of frames considered in the case of the razor variables is shown in Fig. 7.2.

1438

¹The razor variables have undergone confusing notational changes over the years. We will be self-consistent, but the notation used here may be different from references.

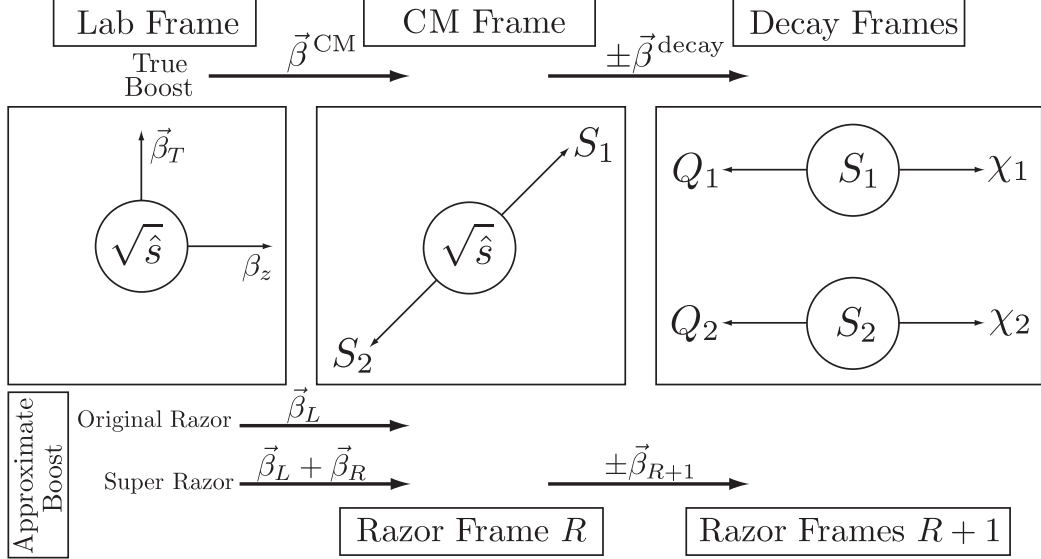


Figure 7.2: Frames considered when applying the razor technique, from [122].

In the R -frame, the decay is straightforward to analyze. Each megajet has energy E_1^R, E_2^R in the frame of its parent sparticle, and we define a characteristic mass M_R :

$$E_1^R = E_2^R = \frac{m_{\text{Heavy}}^2 - m_{\tilde{\chi}_1^0}^2}{2m_{\text{Heavy}}} \quad (7.1)$$

$$M_R = 2 \times E_1^R = 2 \times E_2^R = \frac{m_{\text{Heavy}}^2 - m_{\tilde{\chi}_1^0}^2}{m_{\text{Heavy}}}. \quad (7.2)$$

For cases where $m_{\text{Heavy}} \gg m_{\tilde{\chi}_1^0}$, M_R is an estimator of m_{Heavy} . This scenario happens in the SM, such as in $t\bar{t}$ and WW events, where the $\tilde{\chi}_1^0$ is instead a neutrino.

The question now is how to use this simple derivation in the lab frame, where we actually conduct our measurements. There are two related issues: how to combine the jets into the megajets, and how to “transform” (or *boost*) to the R -frame.

To construct the megajets, the procedure is the following. For a given set of jets $j_i, i = 0, \dots, n_{\text{jet}}$, we construct *all* combinations of their four-momenta such that there is at least one jet inside each megajet. Among this set of possible megajets $\{J_{1,2}\}$, we make the following unique choice for the megajets. We minimize the following quantity:

$$m_{J_1}^2 + m_{J_2}^2. \quad (7.3)$$

1444 In modern parlance, this is known as a *jigsaw*. This is a *choice*. It may have nice
 1445 physical qualities or satisfy some convenient intuition about the events, but as we
 1446 will see later, other choices are possible.

We now describe how we translate our megajet kinematics, measured in the lab frame, to the R -frame. This is a two-step procedure. We perform two *boosts*: a longitudinal boost β_L and a transverse boost β_T . Schematically,

$$J_1^R \xrightarrow{\beta_T} J_1^{CM} \xrightarrow{\beta_L} J_1^{\text{lab}} \quad (7.4)$$

$$J_2^R \xrightarrow{-\beta_T} J_2^{CM} \xrightarrow{\beta_L} J_2^{\text{lab}} \quad (7.5)$$

(7.6)

1447 The $J_{1,2}^{\text{lab}}$ correspond directly to those in the megajet construction. We drop the
 1448 “lab” designation for the rest of the discussion. The question is how to compute the
 1449 magnitudes of these boosts, given the missing degrees of freedom.

For the transverse boost β_T , recall the two megajets have equal energies in their R -frame by construction. This constraint can be reexpressed as a constraint on the magnitude of this boost, in terms of the boost velocity β_L and corresponding Lorentz factor γ_L :

$$\beta_T = \frac{\gamma_L(E_1 - E_2) - \gamma_L\beta_L(p_{1,z} - p_{2,z})}{\hat{\beta}_T \cdot (p_{1,T} + p_{2,T})} \quad (7.7)$$

where we have denoted the lab frame four-vectors as $p_i = (E_i, \vec{p}_{i,T}, p_z)$. We now make the *choice* for the direction of the transverse boost $\hat{\beta}_T$:

$$\hat{\beta}_T = \frac{\vec{p}_{1,T} + \vec{p}_{2,T}}{|\vec{p}_{1,T} + \vec{p}_{2,T}|}. \quad (7.8)$$

1450 This choice forces the denominator of Eq. (7.7) to unity, and corresponds to aligning
 1451 the transverse boost direction with the sum of the two megajets transverse directions.

For the longitudinal boost, we choose $\vec{\beta}_L$ along the z -direction, with magnitude:

$$\beta_L = \frac{p_{1,z} + p_{2,z}}{E_1 + E_2}. \quad (7.9)$$

1452 Viewed in terms of the original parton-parton interactions, this is the choice which
 1453 “on average” gives $p_{z,\text{CM}} = 0$, as we would expect. This well-motivated choice due to
 1454 the total z symmetry.

We now have intuitive guesses for both boosts, which allow us write our original characteristic mass M_R in terms of the lab frame variables, by application of these two Lorentz boosts to the energies of Eq. (7.1):

$$M_R^2 \xrightarrow{\beta_T} M_{R,\text{CM}}^2 \xrightarrow{\beta_L} M_{R,\text{lab}}^2 = (E_1 + E_2)^2 - (p_{1,z} + p_{2,z})^2. \quad (7.10)$$

Finally, we define an additional mass variable, which include the missing transverse energy E_T^{miss} . Importantly, note that we did not use the E_T^{miss} in the definition of M_R , which depends only on the energies of the megajets. Backgrounds with no invisible particles (such as multijet events) must have J_1 and J_2 back to back. Thus, we define the transverse mass:

$$(M_R^T)^2 = \frac{1}{2} \left[E_T^{\text{miss}}(p_{1,T} + p_{2,T}) - \vec{E}_T^{\text{miss}} \cdot (\vec{p}_{1,T} + \vec{p}_{2,T}) \right]. \quad (7.11)$$

Generally, we have $M_R^T < M_R$, so we define a dimensionless ratio (“the razor”):

$$R^2 = \left(\frac{M_R^T}{M_R} \right)^2. \quad (7.12)$$

1455 For signal events, we expect R to peak around $R \sim 1/4$, while backgrounds without
 1456 real E_T^{miss} are expected to have $R \sim 0$.

1457 7.2 Recursive Jigsaw Reconstruction

1458 Recursive Jigsaw Reconstruction is an algorithm allowing the imposition of a decay
 1459 tree interpretation of a particular event [119, 120]. The idea is to construct the
 1460 underlying kinematic variables (the masses and decay angles) on an event-by-event
 1461 level. This is done “recursively” through a decay tree which corresponds, sometimes
 1462 approximately, to the Feynmann diagram for the signal process of interest. After

1463 each step of the recursive procedure, the objects are “placed” into one bucket (or
1464 branch) of the decay tree, and the process is repeated on each frame we have imposed.
1465 The imposition of these decay trees is done by a *jigsaw* rule: a procedure to resolve
1466 combinatoric or kinematic ambiguities while traversing the decay tree. This procedure
1467 is performed by the `RestFrames` software packages [124]

1468 In events where all objects are fully reconstructed, this is straightforward, and
1469 of course has been used for many years in particle physics experiments. Events
1470 which contain E_T^{miss} are more difficult, due to the loss of information: the potential
1471 for multiple mismeasured or simply unmeasureable objects, such as neutrinos or the
1472 LSP in SUSY searches. There can also be combinatoric ambiguities in deciding how
1473 to group objects of the same type. Specifically here, we will be concerned with the
1474 jigsaw rule to associate jets to a particular branch of a decay tree. The jigsaw rules
1475 we impose will remove these ambiguities. First, we will describe the decay trees used
1476 in this thesis, and then describe the jigsaw rules we will use. Finally, we will describe
1477 the variables used in the all-hadronic SUSY search presented in this thesis.

1478 Decay Trees

1479 The decay trees imposed in this thesis are shown in Fig. 7.3. Leaving temporarily the
1480 question of “how” we apply the jigsaw rules, let us compare these trees to the signal
1481 processes of interest. In particular, we want to compare the Feynman diagrams of
1482 Fig. 7.1 with the decay trees of Fig. 7.3. The decay tree in Fig. 7.4(a) corresponds
1483 exactly to that expected from squark pair production, and matches closely with the
1484 principles of the razor approach. We first apply a jigsaw rule, indicated by a line, to
1485 the kinematics of the objects in the *lab* frame. This outputs the kinematics of our
1486 event in the *parent-parent (PP)* frame, or in the razor terminology, the CM frame.
1487 That is, the kinematics of this frame are an estimator for the kinematics in the center
1488 of mass frame of the CM of pass of the squark pair production system. We apply

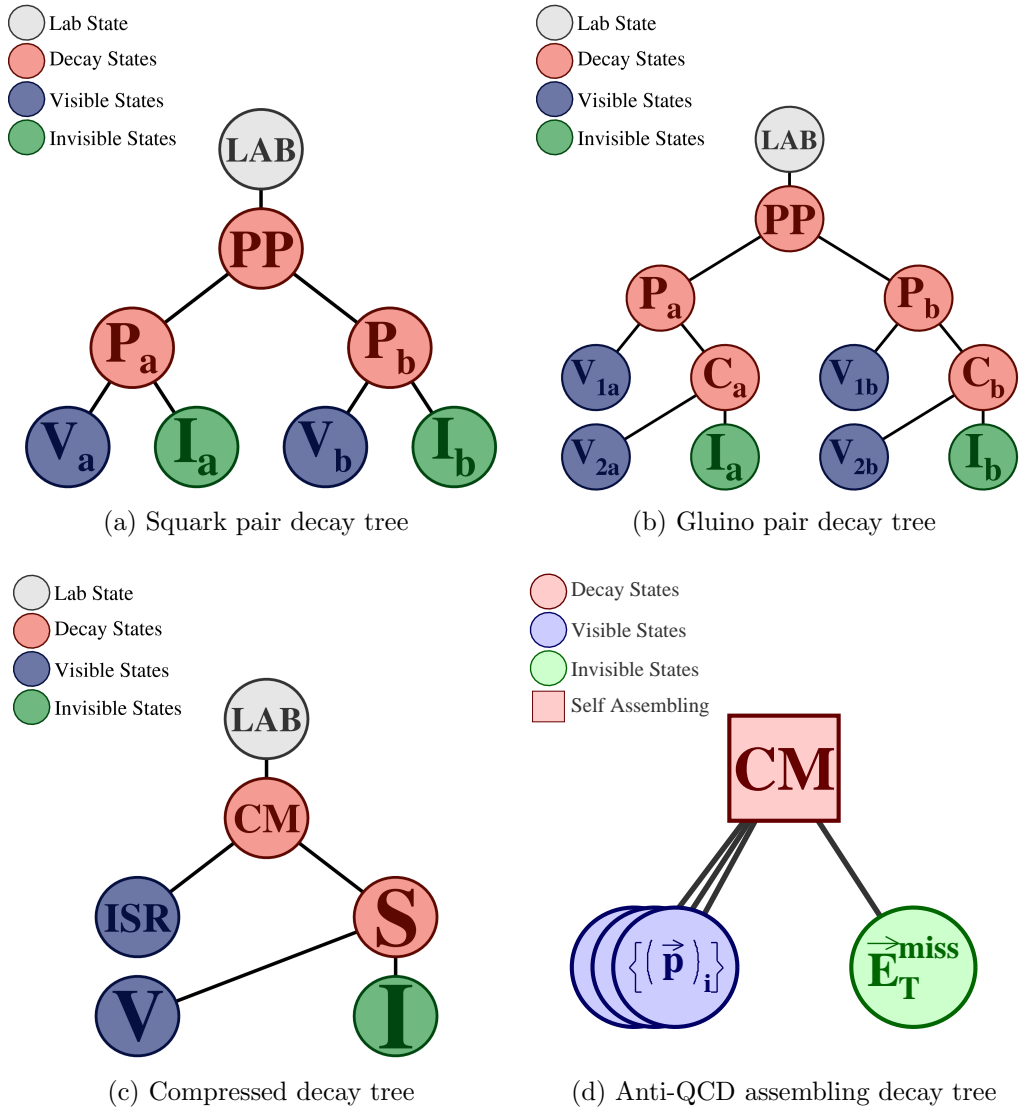


Figure 7.3: RJR decay trees

1489 another jigsaw, which splits the objects in the PP frame into two new frames, known
 1490 as the P_a and P_b systems. These are equivalent to the razor frames, and represent
 1491 proxy frames where each squark is at rest. In P_a (P_b), the decay is symmetric between
 1492 the visible V_a (V_b) objects and the invisible system I_a (I_b). To generate the estimator
 1493 of the kinematics of the V_a , V_b , I_a , and I_b systems in the P_a and P_b systems, we apply
 1494 another jigsaw rule to split the total E_T^{miss} between P_a and P_b . For the case of squark
 1495 pair production, this is the expected decay tree, and we stop the recursive calculation

1496 at that level.

1497 In the case of gluino pair production, we expect two additional jets, and we can
1498 perform an additional boost in each of P_a and P_b , to what we call the C_a and C_b
1499 frames. The decay tree is shown in Fig. 7.4(b). In this case we apply a jigsaw at the
1500 level of P_a (P_b) which separates a single visible object V_{1a} (V_{2a}) from the child frame
1501 C_a (C_b). This child frame represents the hypothesized squark after the decay $\tilde{g} \rightarrow g\tilde{q}$,
1502 which then decays as in the squark case.

The third decay tree used in this thesis is the *compressed* decay tree. Compressed refers to signal models which have a small splitting between the mass of the proposed sparticle and the $\tilde{\chi}_1^0$. The sparticle decay products in compressed models (i.e. the jets and E_T^{miss}) do not generally have large scale [119]. Instead, the strategy is generally to look for a large-scale initial state radiation (ISR) jet which is recoiling off the pair-produced sparticles. In the case where the LSPs receive no momentum from the sparticle decays, the following approximation holds:

$$E_T^{\text{miss}} \sim -p_T^{\text{ISR}} \times \frac{m_{\tilde{\chi}_1^0}}{m_{\text{sparticle}}} \quad (7.13)$$

1503 where p_T^{ISR} is the transverse momentum associated to the entire ISR system.

1504 RJR offers a natural and straightforward way to exploit this feature in events
1505 containing ISR. One imposes the simple decay tree in Fig. 7.4(c) with associated
1506 jigsaw rules. With suitable jigsaw rules, this decay tree “picks out” the large p_T ISR
1507 jet, recoiling off the E_T^{miss} and additional radiation from the sparticle decays. This
1508 provides a convenient set of variables to understand compressed scenarios.

1509 There is one other decay tree, shown in Fig. 7.4(d). This is special, as it is only
1510 used for the purpose of QCD rejection, and does not directly map to a sparticle decay
1511 chain. Due to the large production cross-sections of QCD events, even very rare large
1512 jet mismeasurements can lead to significant E_T^{miss} which can enter the signal region.
1513 To reduce these backgrounds, one usually rejects events which contain jets which are

1514 “too close” by some distance metric to the E_T^{miss} in the event. Generally, in the past,
1515 the distance metric has been defined as simply the angular distance ΔR .

1516 The *self-assembling tree* can be seen as defining a distance metric which depends
1517 on the magnitudes of the E_T^{miss} and jets rather than simply their distance in angular
1518 space. Depending on the exact kinematics, the one or two closest jets are found, and
1519 label the E_T^{miss} *siblings*.

1520 In this section, we have seen how one imposes particular decay trees on an event
1521 to produce a basis of kinematic variables in the approximated frames relevant to
1522 the hypothesized sparticle decay chain. This explains why we call this procedure
1523 “recursive”: the procedure can be iterated through as many steps of a decay tree as
1524 necessary, and each application of a jigsaw rule is dependent on the variables produced
1525 in the last step. The question is: *what are these jigsaw rules?*.

1526 Jigsaw Rules

1527 Jigsaw rules are the fundamental step that allow the recursive definitions of the
1528 variables of interest. The rules we imposed must fully define kinematic variables
1529 at each step in a decay tree. The only possible solution to fully define the event
1530 kinematics in terms of the frames of the hypothesized decays is the imposition of
1531 external constraints to eliminate additional degrees of freedom. In principle, these
1532 need not have any particular physical motivation. Instead, the jigsaw rules are a
1533 way to resolve the mathematical ambiguities to fully reconstruct the full decay chain
1534 kinematics. However, most practical jigsaw rules also have some reasonable physical
1535 motivation, which we will also elucidate.

1536 In the original razor point of view, some jigsaw rules can be seen as the definitions
1537 of the boosts which relate the different frames of interest, while other rules allow one
1538 to combine multiple objects and place them into a particular hemisphere (previously
1539 megajet). These are the two forms of jigsaw rules: combinatoric and kinematic. As

1540 we have stressed before, the jigsaw rules are a *choice*: as long as a particular jigsaw
1541 rule allows the definition of variables at each step in a decay tree, it is “as valid” as
1542 any other rule.

Practically speaking, we use only a small subset of possible jigsaw rules. The combinatoric jigsaw rule has already been introduced as megajet construction above. The minimization of

$$m_{J_1}^2 + m_{J_2}^2. \quad (7.14)$$

1543 is a jigsaw rule to deal with the combinatoric ambiguity implicit in which jets go in
1544 which hemisphere. This is the jigsaw rule used in the decay trees when going from
1545 one frame to two frames such as $PP \rightarrow P_a, P_b$.

1546 We will use three other jigsaw rules, which are all kinematic jigsaw rules. One has
1547 already been used in the razor technique. The minimization of β_L will be used as the
1548 jigsaw rule in the first step of each decay tree: the lab frame to the PP/CM frame.
1549 This is equivalent to the imposition of longitudinal boost invariance, as we expect on
1550 average $p_{z,PP,\text{CM}} = 0$. One defines a unique longitudinal boost by imposition of this
1551 external constraint.

1552 The final two jigsaw rules used in this thesis was not used in the razor technique.
1553 We describe them here.

The first kinematic ambiguity is the total mass of the invisible system M_I . We guess this to be:

$$M_I^2 = M_V^2 - 4M_{V_a}M_{V_b}. \quad (7.15)$$

1554 As we stated above, there is no need to “justify” the jigsaw rules, as they are in some
1555 ways a mathematical trick to fully resolve the event kinematics. The symmetry of
1556 the production mechanism, where we have two decay products V_i and I_i produced
1557 from the decay of the same heavy sparticle, is explicit with this jigsaw choice.

1558 The final jigsaw rule is used to resolve the “amount” of E_T^{miss} that “belongs” to
1559 each hemisphere, and therefore how to impose the transverse boost onto each of i.e.
1560 P_a and P_b from PP . Equivalently, it can be seen as the resolution of the kinematics of
1561 the I_a and I_b objects in the squark and gluino pair production decay trees. Recall that
1562 at this point, we have already approximated the boost of the PP frame. The choice we
1563 use is to minimize the masses P_a and P_b , while simultaneously constraining $P_a = P_b$.
1564 As is the case in the last step, there is a straightforward physical interpretation of this
1565 choice. In the signal models we are considering, P_a and P_b are the estimated frames
1566 of the squark or gluino pair-produced as a heavy resonance. We then of course expect
1567 $M_{P_a} = M_{P_b}$.

1568 The imposition of the decay trees, with ambiguities resolved through the jigsaw
1569 rules, give a full set of boosts relating the frames of each decay tree. In each frame,
1570 we have estimates for the frame mass and decay angles, which can be used in searches
1571 for new physics. In the next section, we describe the variables that are used in this
1572 thesis in more details.

1573 **7.3 Variables used in the search for zero lepton**

1574 **SUSY**

1575 We describe here the variables used in the RJR search described in [120]. These
1576 were reconstructed using the RJR algorithm as just described, using the RestFrames
1577 packages [124]. In these frames, the momenta of all objects placed into that branch
1578 of the decay tree are available (after application of the approximated boost), and in
1579 principle we can calculate any variable of interest such as invariant masses or the
1580 angles between these objects. The truly useful set of variables are highly dependent
1581 on the signal process, and we leave their discussion to the subsequent sections. It is
1582 useful to understand the philosophy employed in the construction of these variables.

1583 In general, we can split variables useful for searches for new physics into two
1584 categories: *scaleful* and *scaleless* variables. In this search, we will use a set of scaleful
1585 variables called the H variables. The scaleless variables will consist of ratios and
1586 angles. In general, we want to restrict the number of scaleful cuts we apply, for two
1587 reasons. Different scaleful variables are often highly correlated, and this of course
1588 limits the utility of additional cuts. Additionally, selections based on many scaleful
1589 variables often overoptimize for particular signal model of interest, especially as
1590 related to the mass difference chosen between the sparticle and the LSP. To avoid
1591 this, each decay tree will only use two scale variables, one which quantifies the overall
1592 mass scale of the event, and another which acts as a measure of the event balance.

1593 **Squark and gluino variables**

1594 Taking our general philosophy to a particular case, we here describe the variables
1595 used by the squark and gluino searches. We have a suite of scale variables which we
1596 will call the H variables, and a suite of angles and ratios.

1597 As we have described above, the RJR algorithm gives us access to the masses
1598 of each frame of interest. It may seem natural that these variables would be the
1599 most useful for discrimination of the signal from background processes. However, these
1600 masses, such as the invariant mass of the PP system M_{PP} , can be significantly
1601 affected by the additional jets in the events. In backgrounds with significant jet
1602 activity such as $Z + \text{jets}$ and $W + \text{jetsevents}$, these masses can have large values which
1603 complicate discrimination from the signal processes. Instead, we use the H variables,
1604 as they show resilience to this effect, and provide stronger discrimination from the SM
1605 backgrounds. They take their name from the commonly used variable H_T , which is the
1606 scalar sum of the visible momentum. From the RJR technique, we can evaluate these
1607 variables in the non-lab frame and include longitudinal information. They are also
1608 constructed with *aggregate* momenta using a similar mass minimization procedure

1609 as we have already described.

We label these variables as $H_{n,m}^F$. They are evaluated in the frame F , where $F \in \{\text{lab}, PP, P_a, P_b\}$. When the discussion applies to both P_a and P_b , we will write P_i . The subscripts n and m denote the number of visible and invisible vectors considered, respectively. When there are more vectors available than n or m , we add up vectors using the hemisphere (megajet) jigsaw rule until there are n (m) objects².

In the opposite case, where n or m is greater than the number of available objects, one simply considers the available objects. The $H_{n,m}^F$ variables are then defined as

$$H_{n,m}^F = \sum_i^n |\vec{p}_{\text{vis},i}^F| + \sum_j^m |\vec{p}_{\text{inv},i}^F|. \quad (7.16)$$

It may not be clear that these variables encode independent information. Fundamentally, this is just an expression of the triangle inequality $\sum |\vec{p}| \geq |\sum \vec{p}|$. One can also define purely transverse of these variables, which we will denote $H_{T,n,m}^F$. Including this view, it is easy to see how the H variables are extensions of the normal H_T variables, as

$$H_T = H_{T,\infty,0}^{\text{lab}}. \quad (7.17)$$

1610 Although the H variables are interesting in their own right, the true power of
1611 the RJR technique comes from the construction of scaleless variables. The scaleless
1612 ratios and angles are in fact measured in the “right” frame, where right here means
1613 an approximation of the correct frame. This provides a less correlated set of variables
1614 than those measured in the lab frame, due to the corrections to the disparticle or
1615 sparticle system boosts from the RJR technique.

1616 To search for noncompressed squark pair production, we use the following set of
1617 RJR variables:

²Recall that these vectors are constructed by the imposition of the decay tree with the relevant jigsaw rules.

- 1618 • $H_{1,1}^{PP}$ - scale variable useful for discrimination against QCD backgrounds and
 1619 used in a similar way to E_T^{miss}

- 1620 • $H_{T,2,1}^{PP}$ - scale variable providing information on the overall mass scale of the
 1621 event for squark pair production. We will often call this the *full* scale variable.

- 1622 • $H_{T,1,1}^{PP}/H_{2,1}^{PP}$ - ratio used to prevent imbalanced events where the scale variable
 1623 is dominated by one high p_T jet or high E_T^{miss}

- 1624 • $p_{PP,z}^{\text{LAB}}/(p_{PP,z}^{\text{LAB}} + H_{T,2,1}^{PP})$ - ratio which prevents significant boosts in the z -direction.
 1625 $p_{PP,z}^{\text{LAB}}$ is a measure of the total boost of the PP system from the lab frame

- 1626 • $p_{T,j2}^{PP}/H_{T,2,1}^{PP}$ - ratio to force the second leading jet in the PP frame to carry a
 1627 significant portion of the total scalar sum of the total momenta in that frame.
 1628 This requirement is another balance requirement, on the total p_T of that second
 1629 jet in the PP frame.

1630 First, we note that there is an implicit requirement that each hemisphere has at least
 1631 one jet (to even reconstruct the P_a and P_b frames), thus we implicitly require two
 1632 or more jets, as we expect for squark pair production. The other important thing
 1633 to note is that all of the ratios use the full scale variable as the denominator. This
 1634 is sensible, as we expect all of these effects to be scaled with the full scale variable
 1635 $H_{T,2,1}^{PP}$. We will see a similar behavior for the gluino regions, with a new full scale
 1636 variable.

1637 To search for noncompressed gluino pair production, we use the following set of
 1638 RJR variables: Due to the increased complexity of the event topology with four jets,
 1639 there are additional handles we can exploit:

- 1640 • $H_{1,1}^{PP}$ - same as squark pair production variable

- 1641 • $H_{T,4,1}^{PP}$ - scale variable providing information on the overall mass scale of the
 1642 event for gluino pair production. As before, we often call this the *full* scale

1643 variable. Since this variable allows the jets to be separated in the PP frame, it
1644 is more appropriate for gluino pair production.

1645 • $H_{T,1,1}^{PP}/H_{4,1}^{PP}$ - ratio used to prevent imbalanced events where the scale variable
1646 is dominated by one high p_T jet or high E_T^{miss}

1647 • $H_{T,4,1}^{PP}/H_{4,1}^{PP}$ - ratio used to measure the fraction of the total scalar sum of the
1648 momentum in the transverse plane. Decay products from gluino pair production
1649 are expected to be fairly central

1650 • $p_{PP,z}^{\text{LAB}}/(p_{PP,z}^{\text{LAB}} + H_{T,4,1}^{PP})$ - ratio to used to prevent significant boosts in the
1651 z -direction

1652 • $\min(p_{T,j2_i}^{PP}/H_{T,2,1_i}^{PP})$ - ratio to require the second leading jet in *both* squark-like
1653 hemispheres C_a and C_b to contain a significant portion of *that frame's* momenta.
1654 This is similar to the $p_{T,j2}^{PP}/H_{T,2,1}^{PP}$ squark decay tree discriminator, but applied
1655 to both hemispheres C_a and C_b .

1656 • $\max(H_{1,0}^{P_i}/H_{2,0}^{P_i})$ - ratio requiring one jet in each of the P_i not encompass too
1657 much of the total momentum available in that frame. This ratio is generally a
1658 very loose cut.

1659 Compressed variables

1660 As we saw above, the decay tree imposed for compressed spectra is simpler. We do
1661 not attempt to fully reconstruct the details of the system recoiling off the ISR system,
1662 but use a straightforward set of variables in this case. One additional simplification
1663 is that all variables are force to be transverse in this case, by simply excluding the
1664 η/z information of the objects as inputs to the RJR reconstruction. We still use the
1665 philosophy of limiting our scaleful variables to just two. The compressed scenario
1666 uses the following set of RJR variables:

- 1667 • $p_{T,S}^{\text{ISR}}$ - scale variable that is the magnitude of the total transverse momenta of all
 1668 jets associated to the ISR system, as evaluated in the CM frame

- 1669 • $R_{\text{ISR}} \equiv p_I^{\hat{\text{CM}}} \cdot p_{T,S}^{\hat{\text{CM}}} / p_{T,S}^{\text{CM}}$ - this ratio is our measurement for the ratio of the LSP
 1670 mass to the compressed sparticle mass. In compressed cases, this should be
 1671 large, as this estimates the amount of the total $\text{CM} \rightarrow S$ boost carried by the
 1672 invisible system.

- 1673 • $M_{T,S}$ - the transverse mass of the S system

- 1674 • N_{jet}^V - the number of jets associated to the visible system V

- 1675 • $\Delta\phi_{\text{ISR},I}$ - the opening angle between the ISR system and the invisible system
 1676 measured in the lab frame. As the invisible system is expected to carry much
 1677 of the total S system momentum, this should be large, as we expect the ISR
 1678 system to recoil directly opposite the I system in that case.

1679 Anti-QCD variables

1680 For the self-assembling tree, we contruct two variables, which we combine to form a
 1681 single variable which rejects QCD events. In this case, we use the mass minimzation
 1682 jigsaw, with a fully transverse version of the event (i.e. we set all jet z/η components
 1683 to 0). This jigsaw defines the distance metric, and provides us with one or two jets
 1684 known as the $E_{\text{T}}^{\text{miss}}$ siblings. We define \vec{p}_{sib} as the sum of these jets, and define the
 1685 following quantities.

We calculate a ratio observable which examines the relative magnitude of the sibling vector \vec{p}_{sib} and $E_{\text{T}}^{\text{miss}}$, and an angle relating \vec{p}_{sib} and $E_{\text{T}}^{\text{miss}}$:

$$R(\vec{p}_{\text{sib}}, E_{\text{T}}^{\text{miss}}) \equiv \frac{\vec{p}_{\text{sib}} \cdot \hat{E}_{\text{T}}^{\text{miss}}}{\vec{p}_{\text{sib}} \cdot \hat{E}_{\text{T}}^{\text{miss}} + |\vec{E}_{\text{T}}^{\text{miss}}|} \quad (7.18)$$

$$\cos \theta(\vec{p}_{\text{sib}}, E_{\text{T}}^{\text{miss}}) \equiv \frac{(\vec{p}_{\text{sib}} + \vec{E}_{\text{T}}^{\text{miss}}) \cdot \vec{p}_{\text{sib}} + \hat{E}_{\text{T}}^{\text{miss}}}{|\vec{p}_{\text{sib}}| + E_{\text{T}}^{\text{miss}}} \quad (7.19)$$

These observables are highly correlated, but taking the following fractional difference provides strong discrimination between SUSY signal and QCD background events:

$$\Delta_{\text{QCD}} \equiv \frac{1 + \cos \theta(\vec{p}_{\text{sib}}, E_{\text{T}}^{\text{miss}}) - 2R(\vec{p}_{\text{sib}}, E_{\text{T}}^{\text{miss}})}{1 + \cos \theta(\vec{p}_{\text{sib}}, E_{\text{T}}^{\text{miss}}) + 2R(\vec{p}_{\text{sib}}, E_{\text{T}}^{\text{miss}})}. \quad (7.20)$$

1686 We will use this variable in the next chapter.

ADD CON₆₈₇
CLUSIONS



1689 *A search for supersymmetric particles in zero lepton final
 1690 states with the Recursive Jigsaw Technique*

1691 This section presents the details of the first search employing RJR variables as
 1692 discriminating variables, as described in [120]. We will describe the simulation
 1693 samples used, and then define the selections where we search for new SUSY
 1694 phenomena, which we call the *signal regions* (SRs) Afterwards, we describe the
 1695 background estimation techniques used in the analysis. Finally, we discuss the
 1696 treatment of systematic uncertainties, and how we combine them using a likelihood
 1697 method [125].

1698 **8.1 Simulation samples**

1699 We discussed the collision data sample provided by the LHC for the analysis in this
 1700 thesis. We analyze a dataset of 13.3 fb^{-1} of collision data, at $\sqrt{s} = 13 \text{ TeV}$. To select
 1701 events in data, we use the trigger system as previously discussed, and use the lowest
 1702 unprescaled trigger which is available for a particular Standard Model background.
 1703 We now discuss the simulation samples used for this search.

1704 Simulated data is fundamentally important to the ATLAS physics program.
 1705 Calibrations, measurements, and searches use Monte Carlo (MC) simulations to
 1706 compare with collision data. In this thesis, MC samples are used to optimize the
 1707 signal region selections, assist in background estimation, and assess the sensitivity to
 1708 specific SUSY signal models. The details of Monte Carlo production, accuracy, and

1709 utility are far beyond the scope of this thesis, but we provide a short description here.

1710 The first step is MC *generation*. A program is run which does a matrix-element
1711 calculation which produces a set of outgoing particles from the parton interactions.
1712 The output particles are *interfaced* [126] with the parton decays, showering, and
1713 hadronization processes. This can be done by the same program or another tool
1714 altogether. This produces a set of *truth* particles with their corresponding kinematics.

Physics process	Generator	Alternative generator	Cross-section normalization	PDF set	Parton shower	Tune
$W(\rightarrow \ell\nu) + \text{jets}$	SHERPA 2.2.0	MADGRAPH	NNLO	NNPDF3.0NNLO	SHERPA	SHERPA default
$Z/\gamma^*(\rightarrow \ell\bar{\ell}) + \text{jets}$	SHERPA 2.2.0	MADGRAPH	NNLO	NNPDF3.0NNLO	SHERPA	SHERPA default
$\gamma + \text{jets}$	SHERPA 2.1.1	-	LO	CT10	SHERPA	SHERPA default
$t\bar{t}$	Powheg-Box v2	Mc@NLO	NNLO+NNLL	CT10	PYTHIA 6.428	PERUGIA2012
Single top (Wt -channel)	Powheg-Box v2	Mc@NLO	NNLO+NNLL	CT10	PYTHIA 6.428	PERUGIA2012
Single top (s -channel)	Powheg-Box v2	Mc@NLO	NLO	CT10	PYTHIA 6.428	PERUGIA2012
Single top (t -channel)	Powheg-Box v1	Mc@NLO	NLO	CT10f4	PYTHIA 6.428	PERUGIA2012
$t\bar{t} + W/Z/WW$	MG5_aMC@NLO 2.2.3	-	NLO	NNPDF2.3LO	PYTHIA 8.186	A14
WW, WZ, ZZ	SHERPA 2.1.1	-	NLO	CT10	SHERPA	SHERPA default
Multijet	PYTHIA 8.186	-	LO	NNPDF2.3LO	PYTHIA 8.186	A14

Table 8.1: The Standard Model background Monte Carlo simulation samples used in this thesis. The generators, the order in α_s of cross-section calculations used for yield normalization, PDF sets, parton showers and tunes used for the underlying event are shown. Alternative generators are only used for the major backgrounds.

1715 For each major background, we employ a baseline sample and alternative sample,
1716 which we will use later to derive uncertainties on the theoretical cross-sections. The
1717 choice of generators for each background is itself a quite broad topic, which we avoid
1718 discussing here. A summary of the generators used is shown in tab. 8.1. In this thesis,
1719 we will use SHERPA [127] to generate boson events: $Z \rightarrow \ell\ell$, $W \rightarrow \ell\nu$, diboson, and
1720 photon events. These are interfaced with the SHERPA’s parton showering model
1721 [128]. The alternative samples for $Z \rightarrow \ell\ell$ and $W \rightarrow \ell\nu$ decays are generated
1722 with MADGRAPH [129] interfaced with PYTHIA8 [130]. Single top and $t\bar{t}$ events are
1723 generated with POWHEGBox [131] interfaced with itself and the alternative samples
1724 are generated with Mc@NLO [132] interfaced with HERWIG++ [133] QCD events
1725 are generated with PYTHIA8 [130]. Events with $t\bar{t}$ in association with a gauge boson
1726 are generated in MG5_aMC@NLO 2.2.3 [132] interfaced with PYTHIA8 [130].

1727 After generation of the truth level particles using the various generators interfaced

1728 with their parton showering models, we perform *simulation*. The detector response
1729 to the truth particles is simulated, and simulated hits are produced. This procedure
1730 ensures “as close as possible” treatment of simulation and collision data. In ATLAS,
1731 this is done using the GEANT4 toolkit [134]. This toolkit outputs simulated detector
1732 signals, on which we run the exact same reconstruction algorithms as described in
1733 the previous chapters. This allows us to produce output simulation datasets for each
1734 of the backgrounds in the analysis.

1735 8.2 Event selection

1736 This section describes the selection of the signal region events. We begin by describing
1737 the *preselection*, which is used to remove problematic events and reduce the dataset
1738 to a manageable size. We then describe the signal region strategy, and present the
1739 signal regions used in the analysis.

1740 Preselection

1741 The preselection is used to reduce the dataset to that of interest in this thesis. The
1742 preselection cuts are shown in Tab. 8.2. This selection is also used for the samples
1743 used for background estimation, except for the lepton veto.

1744 The cuts [1] and [4] are a set of cleaning cuts to remove problematic events.
1745 The *Good Runs List* is a centrally-maintained list of data runs which have been
1746 determined to be “good for physics”. This determination is made by analysis of the
1747 various subdetectors, and monitoring of their status. Event cleaning is used to veto
1748 events which could be affected by noncollision background, noise bursts, or cosmic
1749 rays.

1750 We require the lowest unprescaled E_T^{miss} trigger for the data run of interest, as
1751 described previously, in cut [2]. The lepton veto is applied in cut [5]. These two cuts

1752 are only used for the signal region selection.

1753 The rest of the preselection is used for the signal region and control regions used
1754 for background estimation. These cuts on scaleful variables used by previous searches
1755 are mostly used for the reduction of the dataset to a manageable size. Signal models
1756 with sensitivity to lower values of these scaleful variables have been ruled out by
1757 previous searches [135]. The final cut is on m_{eff} , which is the scalar sum of all jets
1758 and E_T^{miss} . This is the final discriminating variable used in the complementary search
1759 to this thesis, which is also presented in [120].

Cut	Description	
1	Good Runs List	Veto events with intolerable detector errors
2	Trigger	HLT_xe70 (2015), HLT_xe80_tclcw_L1XE50, or HLT_xe100_mht_L1XE50 (2016)
3	Event cleaning	Veto for noncollision background, noise bursts, and cosmic rays
4	Lepton veto	No leptons with $p_T > 10$ GeV after overlap removal
5	E_T^{miss} [GeV] >	250
6	$p_T(j_1)$ [GeV] >	200
7	$p_T(j_2)$ [GeV] >	50
8	m_{eff} [GeV] >	800

Table 8.2: Preselection for the various event topologies used in the analysis.

1760 Signal regions

1761 We define a set of signal regions using the RJR variables previously described.
1762 These signal regions are split into three general categories: squark pair production
1763 SRs, gluino pair production SRs, and compressed production SRs. Within these
1764 general SRs, we have a set of signal regions targetting different mass splittings of the
1765 sparticle and LSP.

1766 A schematic of this strategy is shown in Fig. 8.1. This type of plane is how most
1767 (R -parity conserving) SUSY searches are organized in both ATLAS and CMS. The

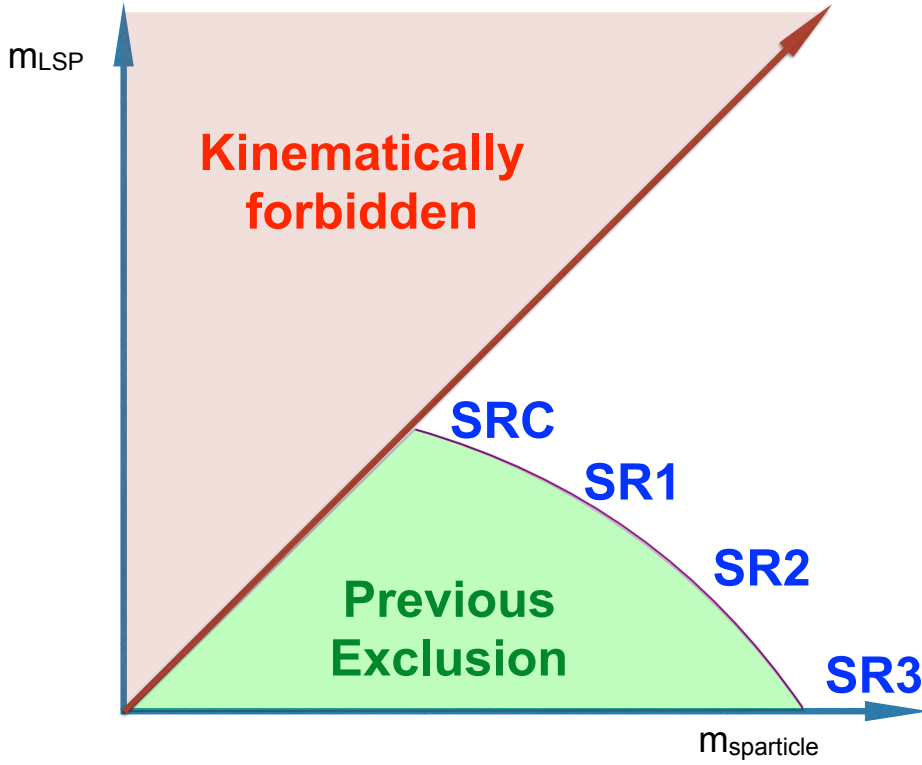


Figure 8.1: Schematic leading the development of the SUSY signal regions in this thesis. A variant of this schematic is used for most SUSY searches on ATLAS and CMS.

1768 horizontal axis is the mass of the sparticle considered. In the case of this thesis,
 1769 this will be the squark or gluino mass. On the horizontal axis, we place the LSP mass.
 1770 These are the two free parameters of the simplified models considered here. Our
 1771 search occurs in this two-parameter space. Each signal region targets some portion
 1772 of this plane. As shown in the figure, a new iteration of a search will use a set of
 1773 signal regions which have sensitivity just beyond those of the previous exclusions.
 1774 The choice of how many signal regions to use to fully cover this plane is in many
 1775 ways a matter of judgment, as it is important to avoid over or under/over-fitting
 1776 to the signal models of interest. To take the extreme example, one signal region
 1777 will obscure the different phenomena in signal events with large versus small mass
 1778 splittings, leading to underfitting. Binning as finely as possible¹ leads to overfitting
 1779 due to the fluctuations present in the signal and background events passing the various

1780 selections selection. In this thesis, we use six squark signal regions, six gluino signal
1781 regions, and five compressed regions.

1782 The full table defining all signal regions is shown in Tab. 8.3. In all cases, the
1783 signal region selections contain a combination of scaleful and scaleless cuts. Emphasis
1784 on cuts on scaleful variables provide stronger sensitivity to larger mass splittings,
1785 while additional sensitivity to smaller mass splittings is found using stronger cuts
1786 on scaleless variables. One envisions walking from SR1 (with tight scaleless cuts
1787 and loose scaleful cuts) in Fig. 8.1 towards SR3 by loosening the scaleless cuts and
1788 tightening the scaleful cuts. We will see this strategy at work in each set of signal
1789 regions.

1790 We have already described the useful variables in the previous chapter. The
1791 question is how to choose the optimal cuts for a given set of signal models, which are
1792 grouped in the mass splitting space. This was done by a brute force scan over the
1793 cut values, using a guess of integrated luminosity with a fixed systematic uncertainty
1794 scenario; the value of the systematic uncertainty is motivated by that from previous
1795 analyses. We choose the lowest cut value that maximizes the Z_{Bi} , as described in
1796 [136]. This figure of merit gives conservative estimates, as compared to i.e. S/\sqrt{B} .
1797 A figure showing an example of this selection tuning procedure is shown in Fig. 8.2.

1798 The compressed selections are split into five regions (SRC1-5), and due to the
1799 simplified nature of the compressed decay tree, has sensitivity in both the gluino
1800 and squark planes. The compressed regions target mass splittings with $m_{\text{sparticle}} -$
1801 $m_{\text{LSP}} \tilde{<} 200$ GeV. For the compressed region, $M_{T,S}$ is the primary scaleful variable.
1802 We can see the general strategy of lowering increasing scale cuts while decreasing the
1803 scaleless cuts here. SRC1 targets the most compressed scenarios, with mass splittings
1804 of less than 25 GeV, and has the loosest $M_{T,S}$ cut coupled with the tightest R_{ISR} and

¹This can be defined as having a signal region for each simulated signal sample, which for this analysis is ~ 100 .

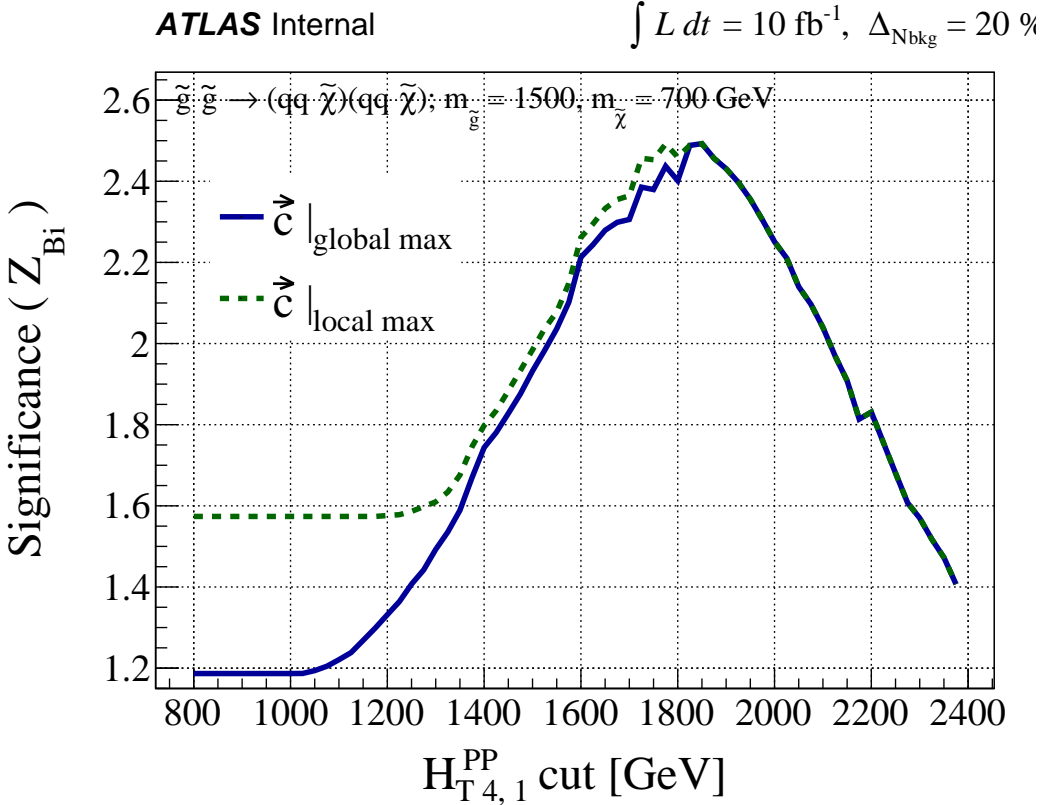


Figure 8.2: Optimization of the $H_{T,4,1}^{PP}$ cut for a gluino signal model with $(m_{\tilde{g}}, m_{\tilde{\chi}_1^0}) = (1500, 700)$ GeV assuming 10 fb^{-1} and an uncertainty of 20% on the background estimate.

1805 $\Delta\phi_{ISR,I}$ cuts. SRC4 and SRC5 target mass splittings of ~ 200 GeV, and are coupled
 1806 with the loosest scaleless cuts on R_{ISR} and $\Delta\phi_{ISR,I}$. We also note that SRC4 and
 1807 SRC5 have differing cuts on N_{jet}^V , since these SRs are closest to the noncompressed
 1808 regions, and can be seen as the “crossover” where the differences between squark and
 1809 gluino production begins to become manifest.

1810 The squark regions (for noncompressed spectra) are organized into six signal
 1811 regions. These are labeled by a numeral 1-3 and letter a/b. SRs sharing a common
 1812 numeral i.e. SRS1a and SRS1b share a common set of scaleless cuts, while differing in
 1813 the main scale variable $H_{T,2,1}^{PP}$. The two SRs for each set of scaleless cuts, only differing
 1814 in the main scale variable, can be seen in a naïve way as providing sensitivity to a

1815 range of luminosity scenarios². As before, we see that the scaleless cuts are loosened
1816 as we tighten the scaleful cuts, as we move across the table from SRS1a to SRS3b.
1817 This provides strong sensitivity to signal models with intermediate mass splittings with
1818 SRS1a to large mass splittings with SR3b.

1819 The gluino signal regions are organized entirely analogously to the squark signal
1820 regions. There are six gluino signal regions, again labeled via a numeral 1-3 and letter
1821 a/b. Those SRs sharing a common numeral have a common set of scaleless cuts, but
1822 differ in their main scale variable $H_{T,4,1}^{PP}$. The SRs follow scaleless vs scaleful strategy,
1823 with SRG1 having the loosest scaleful cut cuts coupled with the strongest scaleless
1824 cuts, and the converse being true in SRG3. As in the squark case, this strategy
1825 provides strong expected sensitivity throughout the gluino-LSP plane.

²These SRs were defined before the entire collision dataset was produced, and thus needed to be robust in cases where the LHC provided significantly different than expected performance.

Targeted signal	$\tilde{s}\tilde{s}, \tilde{s} \rightarrow q\tilde{\chi}_1^0$									
Requirement	Signal Region									
	RJR-S1		RJR-S2		RJR-S3					
$H_{1,1}^{PP}/H_{2,1}^{PP} \geq$	0.6		0.55		0.5					
$H_{1,1}^{PP}/H_{2,1}^{PP} \leq$	0.95		0.96		0.98					
$p_{PP, z}/(p_{PP, z}^{lab} + H_{T, 2,1}^{PP}) \leq$	0.5		0.55		0.6					
$p_{j2, T}^{PP}/H_{T, 2,1}^{PP} \geq$	0.16		0.15		0.13					
$\Delta_{QCD} >$	0.001									
	RJR-S1a	RJR-S1b	RJR-S2a	RJR-S2b	RJR-S3a	RJR-S3b				
$H_{T, 2,1}^{PP}$ [GeV] >	1000	1200	1400	1600	1800	2000				
$H_{1,1}^{PP}$ [GeV] >	1000		1400		1600					
Targeted signal	$\tilde{g}\tilde{g}, \tilde{g} \rightarrow q\bar{q}\tilde{\chi}_1^0$									
Requirement	Signal Region									
	RJR-G1		RJR-G2		RJR-G3					
$H_{1,1}^{PP}/H_{4,1}^{PP} \geq$	0.35		0.25		0.2					
$H_{T, 4,1}^{PP}/H_{4,1}^{PP} \geq$	0.8		0.75		0.65					
$p_{PP, z}/(p_{PP, z}^{lab} + H_{T, 4,1}^{PP}) \leq$	0.5		0.55		0.6					
$\min(p_{j2, T, i}^{PP}/H_{T, 2,1}^{PP}) \geq$	0.12		0.1		0.08					
$\max(H_{1,0}^{Pi}/H_{2,0}^{Pi}) \leq$	0.95		0.97		0.98					
$ \frac{2}{3}\Delta\phi_{V,P}^{PP} - \frac{1}{3}\cos\theta_p \leq$	0.5		—		—					
$\Delta_{QCD} >$	0									
	RJR-G1a	RJR-G1b	RJR-G2a	RJR-G2b	RJR-G3a	RJR-G3b				
$H_{T, 4,1}^{PP}$ [GeV] >	1000	1200	1500	1900	2300	2700				
$H_{1,1}^{PP}$ [GeV] >	600		800		900					
Targeted signal	compressed spectra in $\tilde{s}\tilde{s}$ ($\tilde{s} \rightarrow q\tilde{\chi}_1^0$); $\tilde{g}\tilde{g}$ ($\tilde{g} \rightarrow q\bar{q}\tilde{\chi}_1^0$)									
Requirement	Signal Region									
	RJR-C1	RJR-C2₁₂₉	RJR-C3	RJR-C4	RJR-C5					
$R_{ISR} \geq$	0.9	0.85	0.8	0.75	0.70					
$\Delta\phi_{ISR, I} >$	3.1	3.07	2.95	2.95	2.95					

Targeted signal	compressed spectra in $\tilde{s}\tilde{s}$ ($\tilde{s} \rightarrow q\tilde{\chi}_1^0$); $\tilde{g}\tilde{g}$ ($\tilde{g} \rightarrow q\bar{q}\tilde{\chi}_1^0$)				
Requirement	Signal Region				
	RJR-C1	RJR-C2₁₂₉	RJR-C3	RJR-C4	RJR-C5
$R_{ISR} \geq$	0.9	0.85	0.8	0.75	0.70
$\Delta\phi_{ISR, I} >$	3.1	3.07	2.95	2.95	2.95

1826 8.3 Background estimation

1827 We describe here the method of background estimation. In this thesis, we detail what
 1828 is colloquially called a “cut-and-count” analysis. This is in contrast to a “shape fit”
 1829 analysis, where one needs to consider the details of the variable distribution shapes.
 1830 Instead, we must ensure the overall normalization of the Standard Model backgrounds
 1831 are correct in the regions of phase space considered in the analysis. In order to
 1832 do this, we define a set of *control regions* which are free of SUSY contamination
 1833 based on the previously excluded analysis. We compare the number of events present
 1834 in the control regions in simulation with that in data to define a *transfer factor*
 1835 (TF). We extrapolate the number of expected events from each background using
 1836 this transfer factor to translate from the , which provides our final estimate of the
 1837 SM background in the corresponding signal region. To be explicit, each signal region
 1838 SR has a corresponding set of control regions.

More precisely, for a given signal region, we are attempting to estimate the value $N_{\text{SR}}^{\text{data}}$ for a given background. This value is estimated using the following equation:

$$N_{\text{SR}}^{\text{data,est}} = N_{\text{CR}}^{\text{data,obs}} \times \text{TF}_{\text{CR}} \equiv N_{\text{CR}}^{\text{data,obs}} \times \left(\frac{N_{\text{SR}}^{\text{MC}}}{N_{\text{CR}}^{\text{MC}}} \right) \quad (8.1)$$

1839 where the transfer factor TF is taken directly from MC. The two ingredients to our
 1840 estimation of $N_{\text{SR}}^{\text{data,obs}}$ is thus $N_{\text{CR}}^{\text{data,obs}}$ and the transfer factor taken from MC.

The transfer factor method is potentially more straightforward written in the following way:

$$N_{\text{SR}}^{\text{data,est}} = N_{\text{SR}}^{\text{MC}} \times \left(\frac{N_{\text{CR}}^{\text{data,obs}}}{N_{\text{CR}}^{\text{MC}}} \right) \equiv N_{\text{SR}}^{\text{MC}} \times \mu_{\text{CR}}. \quad (8.2)$$

1841 In this form, the correction to the overall normalization is explicit. The ratio $\frac{N_{\text{CR}}^{\text{data,obs}}}{N_{\text{CR}}^{\text{MC}}}$
 1842 which we call μ informs us how to scale $N_{\text{SR}}^{\text{MC}}$ in order to get the right overall
 1843 normalization. The assumption made with this method is that the overall shape of
 1844 the distribution should not change “that much” as one extrapolates to the signal
 1845 region.

1846 The CR definitions are motivated and designed according to two (generally
1847 competing) requirements:

- 1848 1. Statistical uncertainties due to low CR statistics
1849 2. Systematic uncertainties related to the extrapolation from the CR to the SR.

1850 This motivates the desire to make the control regions as similar as possible
1851 to the signal regions without risking signal contamination while ensuring high
1852 purity in the targeted SM background.

1853 In principle, one can also apply data-driven corrections to the TF obtained for each
1854 CR.

1855 In order to validate the transfer factors obtained from MC, we also develop a series
1856 of *validation regions* (VRs). These regions are generally designed to be “in between”
1857 the control region and signal region selections in phase space, and thus provide a
1858 check on the extrapolation from the control regions into the signal regions. Despite
1859 their closeness in phase space to the signal regions, they are also designed to have
1860 low signal contamination.

1861 In practice, we perform this estimation procedure simultaneously across all
1862 control regions; we describe this later. We only note this here since we can also
1863 apply Eq.Eq. (8.1) to measure the contamination of a control region with another
1864 background as well. This procedure accounts for the correlations between regions due
1865 to correlated systematic uncertainties. We next describe the control region selection
1866 for the major SM backgrounds for the analysis.

1867 **Control Regions**

1868 The primary backgrounds of note in this analysis are $Z + \text{jets}$, $W + \text{jets}$, $t\bar{t}$, and QCD
1869 events. There is also a minor background from diboson events which is taken directly
1870 from MC with an uncertainty of 50%. We describe the strategy to estimate these

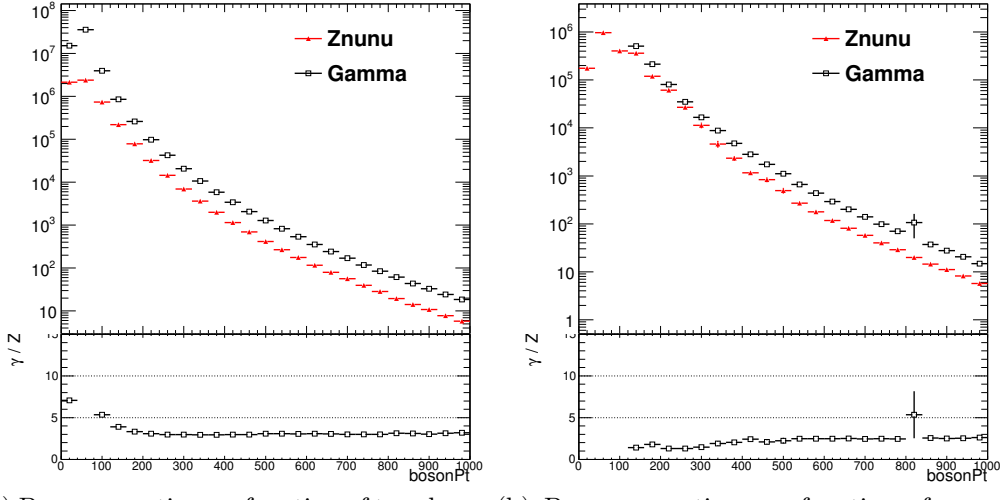
1871 various backgrounds here. A summary table is shown in Tab. 8.4. All distributions
 1872 shown in this section use the scaling factors μ from the background fits, which we
 1873 describe later.

CR	SM background	CR process	CR event selection
Meff/RJR-CR γ	$Z(\rightarrow \nu\bar{\nu}) + \text{jets}$	$\gamma + \text{jets}$	Isolated photon
Meff/RJR-CRQ	Multi-jet	Multi-jet	$\Delta_{\text{QCD}} < 0$ reversed requirement on $H_{1,1}^{PP}$ (RJR-S/G) or $R_{\text{ISR}} < 0.5$ (RJR-C)
Meff/RJR-CRW	$W(\rightarrow \ell\nu) + \text{jets}$	$W(\rightarrow \ell\nu) + \text{jets}$	$30 \text{ GeV} < m_T(\ell, E_T^{\text{miss}}) < 100 \text{ GeV}$, b -veto
Meff/RJR-CRT	$t\bar{t}(\text{+EW})$ and single top	$t\bar{t} \rightarrow b\bar{b}qq'\ell\nu$	$30 \text{ GeV} < m_T(\ell, E_T^{\text{miss}}) < 100 \text{ GeV}$, b -tag

Table 8.4: Control regions used in this thesis.

1874 Events with a Z boson decaying to neutrinos in association with jets are the
 1875 primary irreducible background in the analysis. These events have true E_T^{miss} from
 1876 the decaying neutrinos, and can have significant values of the scaleful variables of
 1877 interest. Naively, one might expect us to use $Z \rightarrow \ell\ell$ as the control process of interest,
 1878 as $Z \rightarrow \ell\ell$ events are quite well-measured. Unfortunately, the $Z \rightarrow \ell\ell$ branching ratio
 1879 is about half of from $Z \rightarrow \nu\nu$, which necessitates loosening the control region selection
 1880 significantly. This leads to unacceptably large systematic uncertainties in the transfer
 1881 factor.

1882 Instead, photon events are used as the control region for the $Z \rightarrow \nu\nu$ events. We
 1883 label this photon control region as CRY. The photon is required to have $p_T > 150 \text{ GeV}$
 1884 to ensure the trigger is fully efficient. The kinematic properties of photon events
 1885 strongly resemble those of Z events when the boson p_T is significantly above the
 1886 mass of the Z boson. In this regime, the neutral bosons are both scaleless, and can
 1887 be treated interchangeably, up to the differences in coupling strengths. Additionally,



(a) Boson p_T ratio as a function of true boson p_T
(b) Boson p_T ratio as a function of reconstructed boson p_T

Figure 8.3

the cross-section for $\gamma + \text{jets}$ events is significantly larger than $Z + \text{jets}$ events above the Z mass. These features are shown in Fig. 8.3 in simulated $Z \rightarrow \nu\nu$ truth and reconstructed events. The reconstructed $Z \rightarrow \nu\nu$ events define the boson p_T as simply the E_T^{miss} . In truth events, one clearly sees the effect of the Z mass below ~ 100 GeV, with a flattening of the ratio above ~ 300 GeV. In reconstructed events, the effects are less clear at low boson p_T , primarily due to cut sculpting from i.e. the trigger requirement on photon events, which necessitates a higher p_T cut on photon events for the trigger to remain fully efficient. Still, it is clear that the ratio flattens out at high boson p_T , and we are justified in the use of CRY to model the $Z + \text{jets}$ background.

The CRY kinematic selection is slightly looser in the scaleful variables for the noncompressed regions to provide sufficient control region statistics. This is chosen to be $H_{1,1}^{PP} > 900$ GeV ($H_{1,1}^{PP} > 550$ GeV) for the squark (gluino) regions to minimize the corresponding statistical and systematic uncertainties.

One additional correction scale factor is applied to $\gamma + \text{jets}$ events before calculating the transfer factors. This is known as the κ method, which is used to determine the disagreement arising from the use of a LO generator for photon events vs. a NLO

1904 generator for Z +jets events, which can reduce the theoretical uncertainties from
 1905 this disagreement. One can see this as a measurement of the k-factor for the LO
 1906 γ +jets sample. This is effectively done with an auxiliary CRZ region, defined using
 1907 two leptons with an invariant mass close with 25 GeV of the Z mass. The correction
 1908 factor derived for this purpose is $\kappa = 1.39 \pm 0.05$.

1909 Distributions of CRY in squark, gluino, and compressed regions are shown in
 1910 Figs. 8.4 to 8.6. One can see the quite high purity of CRY in photon events from
 1911 these plots.

Event with a W boson decaying leptonically via $W \rightarrow \ell\nu$ can also enter the signal region. In this case, we use leptonically to include all leptons (e, μ, τ). The W +jets events passing the event selection either have a hadronically-decaying τ , with a neutrino supplying E_T^{miss} , or the case where a muon or electron is misidentified as a jet or missed completely due to the limited detector acceptance. To model this background, we use a sample of one-lepton events with a veto on b-jets, which we label CRW. The lepton is required to have $p_T > 27$ GeV to guarantee a fully efficient trigger. We then treat this single lepton as a jet for purposes of the RJR variable calculations. We apply a kinematic selection on the transverse mass:

$$m_T = \sqrt{2p_{T,\ell}E_T^{\text{miss}}(1 - \cos\phi_e - E_\phi^{\text{miss}})}, \quad (8.3)$$

1912 around the W mass: $30 \text{ GeV} < m_T < 100 \text{ GeV}$. Checks in simulation shows that
 1913 these requirements give a sample of high purity $W \rightarrow \ell\nu$ background. Due to low
 1914 statistics using the kinematic cuts imposed in the signal regions, the control region
 1915 kinematic cuts are slightly loosened with respect to the signal region cuts. We use
 1916 the loosest cut in any signal region as the control region selection for all signal
 1917 regions. More clearly, the control region selection corresponding to each signal region
 1918 is the *same*. As discussed above, this leads to a tolerable increase in the systematic
 1919 uncertainty from the extrapolation from the CR to the SR when compared to the
 1920 resulting statistical uncertainty.

1921 Distributions of CRW in squark, gluino, and compressed regions are shown in
1922 Figs. 8.7 to 8.9. There is high purity in W +jets events in the control region
1923 corresponding to all signal regions.

1924 Top events are also an important background, for the same reasons as the
1925 W +jets background, due to the dominant top decay channel of $t \rightarrow Wb$. For a
1926 top event to be selected by the analysis criteria, as in the case of W +jets, we expect
1927 a W to decay via a τ lepton which decays hadronically or one a muon or electron to
1928 be misidentified as a jet or be outside the detector acceptance. We are not so worried
1929 about hadronic or all dileptonic tops: hadronic $t\bar{t}$ events generally have low E_T^{miss}
1930 (and $H_{1,1}^{PP}$) so they will not pass the kinematic cuts, while dileptonic $t\bar{t}$ events have a
1931 lower cross-section and good reconstruction efficiency from the two leptons. We are
1932 thus primarily concerned with semileptonic $t\bar{t}$ events with E_T^{miss} from the neutrino.
1933 To model this background, we use the same selection as the W selection, but require
1934 that one of the jets chosen by the analysis has at least one b -tag. This selection has
1935 quite high purity, as we expect the $t\bar{t}$ background to have two b -jets. Thus with
1936 the 70% b -tagging efficiency working point used in this analysis, ignoring (small)
1937 correlations between the two b -tags, we expect to tag one of the b -jets greater than
1938 90% of the time. As with CRW, we need to loosen the cuts applied to CRT with
1939 respect to the signal region in order to gain sufficient expected data statistics. We
1940 use exactly the same scheme; the CRT corresponding to each SR is identical, due to
1941 using the loosest set of cuts among the SRs. This comes at the cost of an increased
1942 systematic uncertainty for this extrapolation, but it was determined that this tradeoff
1943 resulted in the lowest overall uncertainty.

1944 Distributions of CRT in squark, gluino, and compressed regions are shown
1945 in Figs. 8.10 to 8.12. There is high purity in top events in the control region
1946 corresponding to all signal regions.

1947 The final important background is the QCD background. As briefly discussed in

1948 the previous chapter, QCD backgrounds are difficult, for a few reasons we describe
1949 here. The large cross-section for QCD events means that even very rare extreme
1950 mismeasurements can be seen in our signal regions. However, as these events are
1951 very rare, one requires extreme confidence in the tails of the distributions to use
1952 simulation as an input for background estimation. To avoid this, the strategy in
1953 these cases is to apply a strong enough cut to expect *zero* QCD events in the signal
1954 regions to avoid this issue. To produce a sample enriched in QCD, which we call CRQ,
1955 we reverse the Δ_{QCD} and $H_{1,1}^{PP}$ cuts. This analysis uses the jet smearing method, as
1956 described in [137]. This is a data-driven method which applies a resolution function
1957 to well-measured QCD events, which also an estimate of the impact of the jet energy
1958 mismeasurement on $E_{\text{T}}^{\text{miss}}$ and subsequently the RJR variables.

1959 Distributions of CRQ in squark, gluino, and compressed regions are shown
1960 in Figs. 8.13 to 8.15. There is high purity in top events in the control region
1961 corresponding to all signal regions.

1962 The final background of note in this background is the diboson background. This
1963 background is estimated directly from simulation. Due to the low cross-section of
1964 electroweak processes, this background is not significant in the signal regions. We
1965 assign a large ad-hoc 50% systematic on the cross-section, and do not attempt to
1966 define a control region for this background.

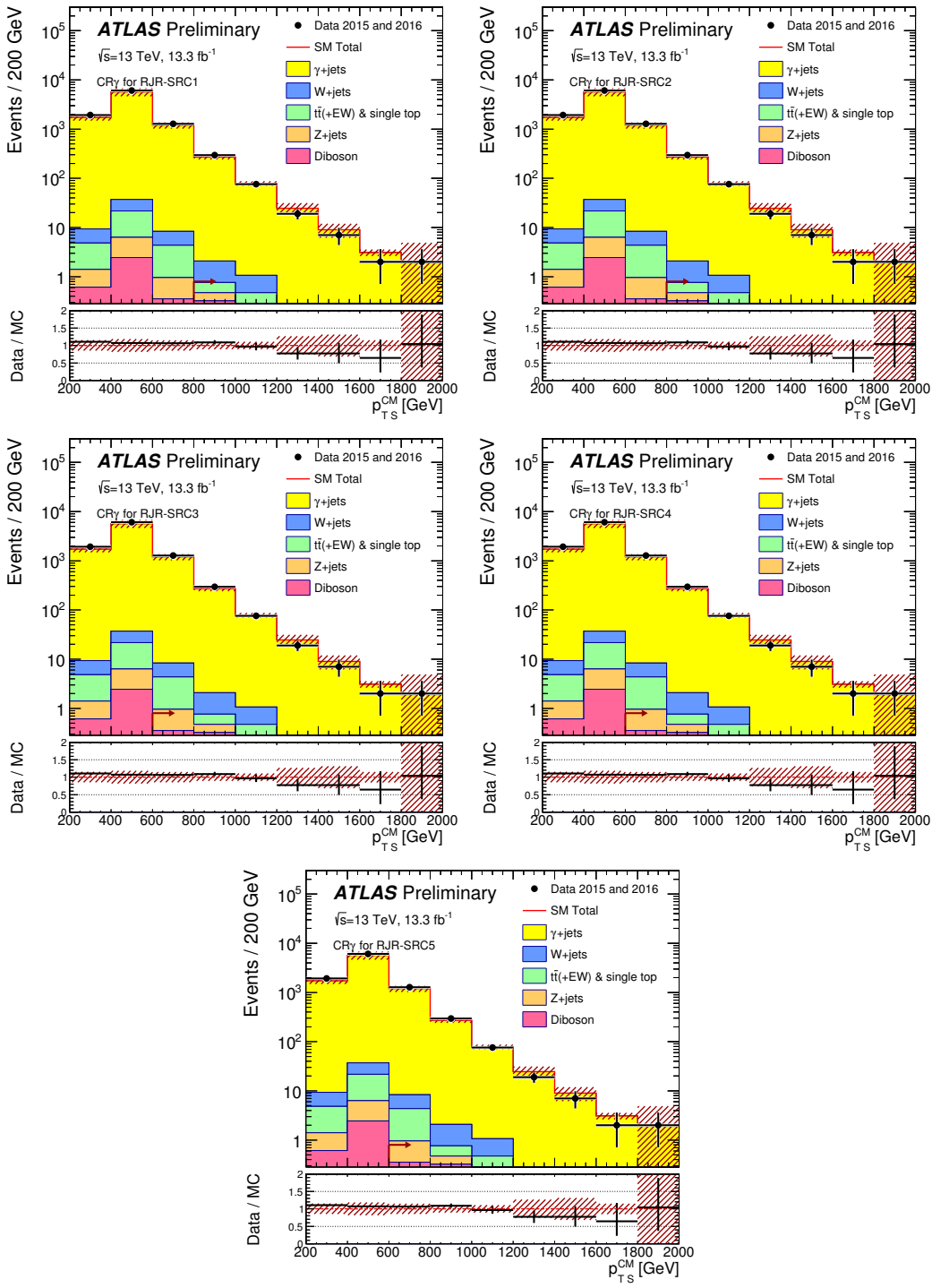


Figure 8.4: Scale variable distributions for the compressed CRY regions.

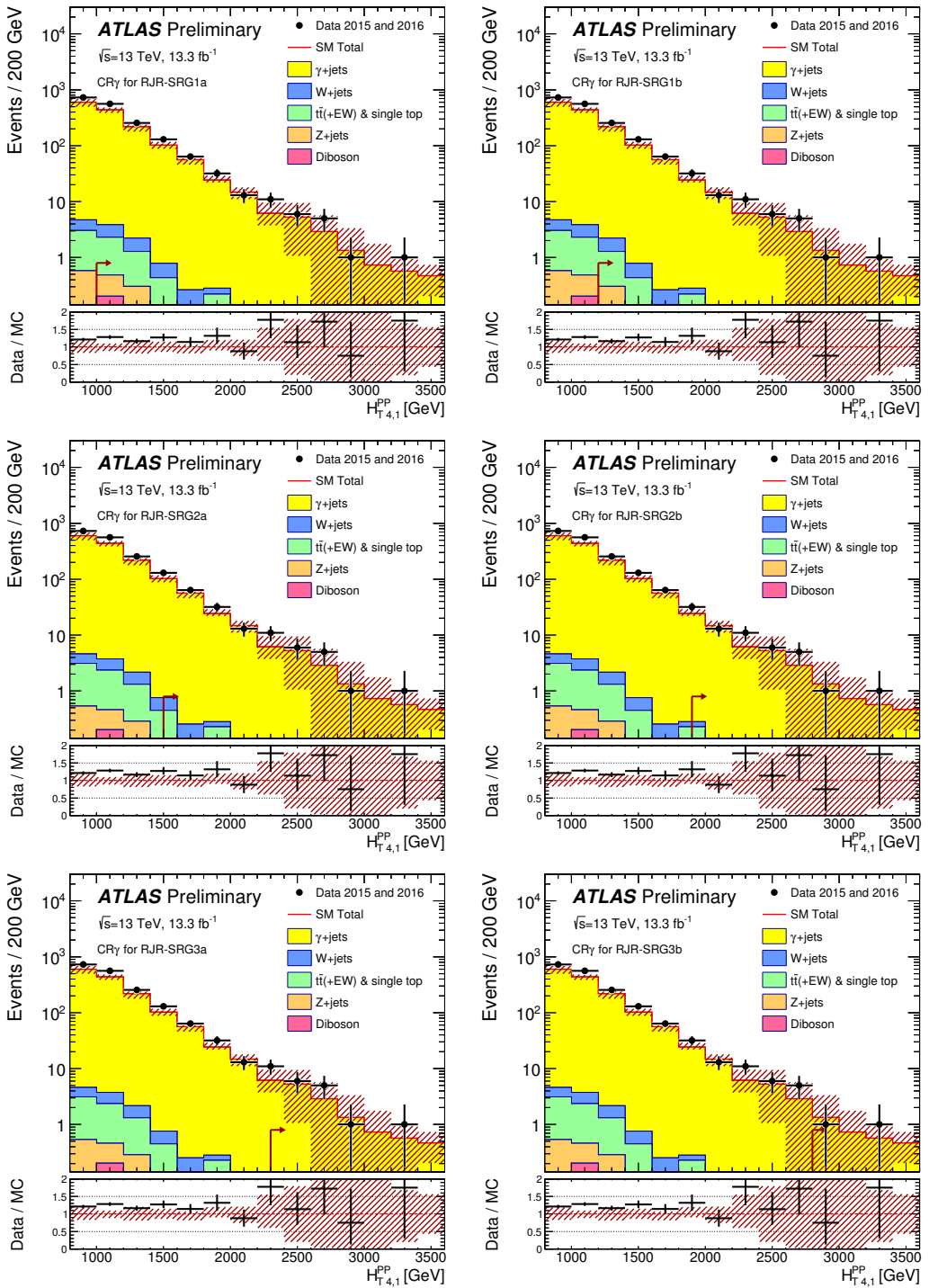


Figure 8.5: Scale variable distributions for the gluino CRY regions.

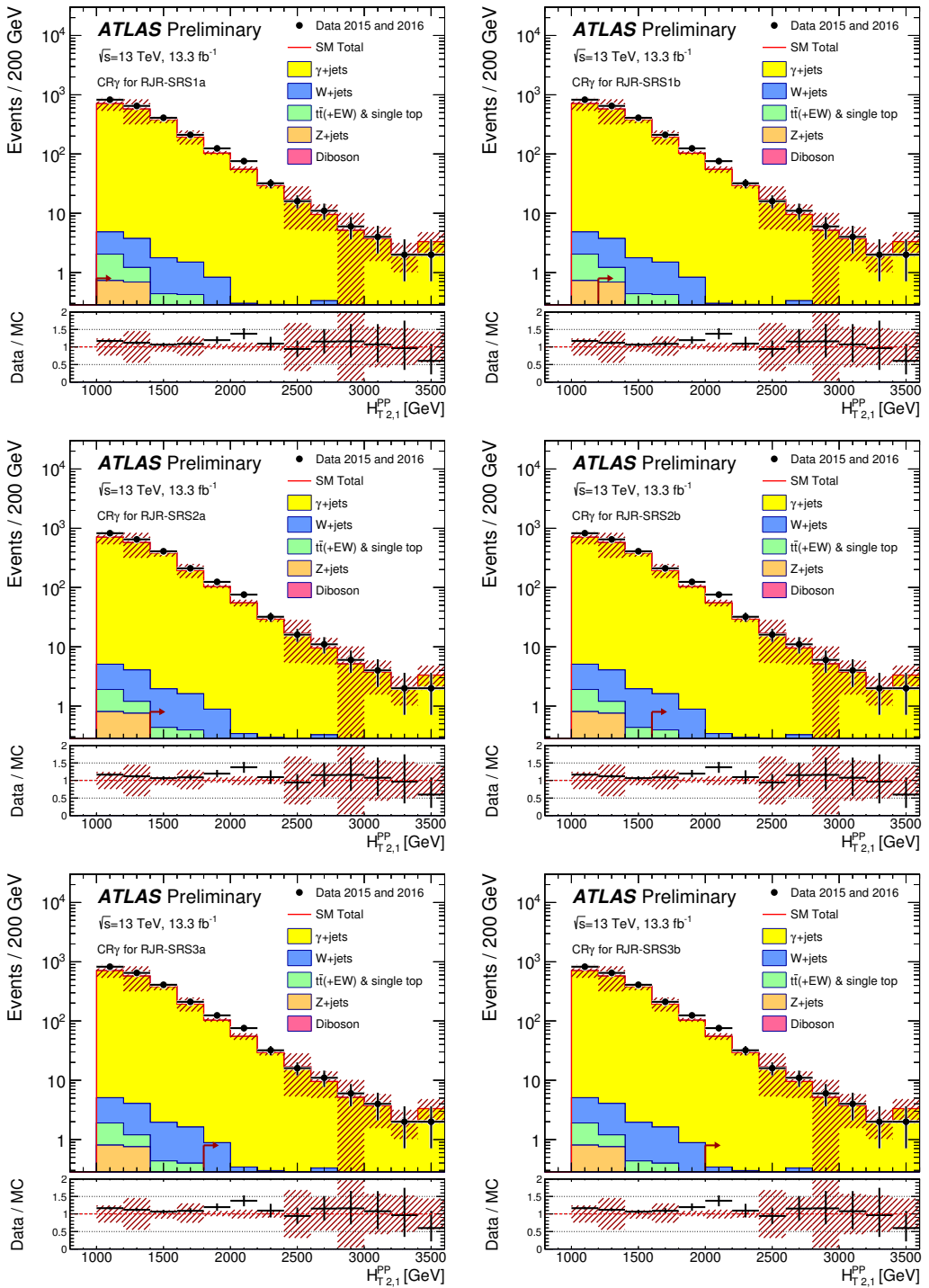


Figure 8.6: Scale variable distributions for the squark CRY regions.

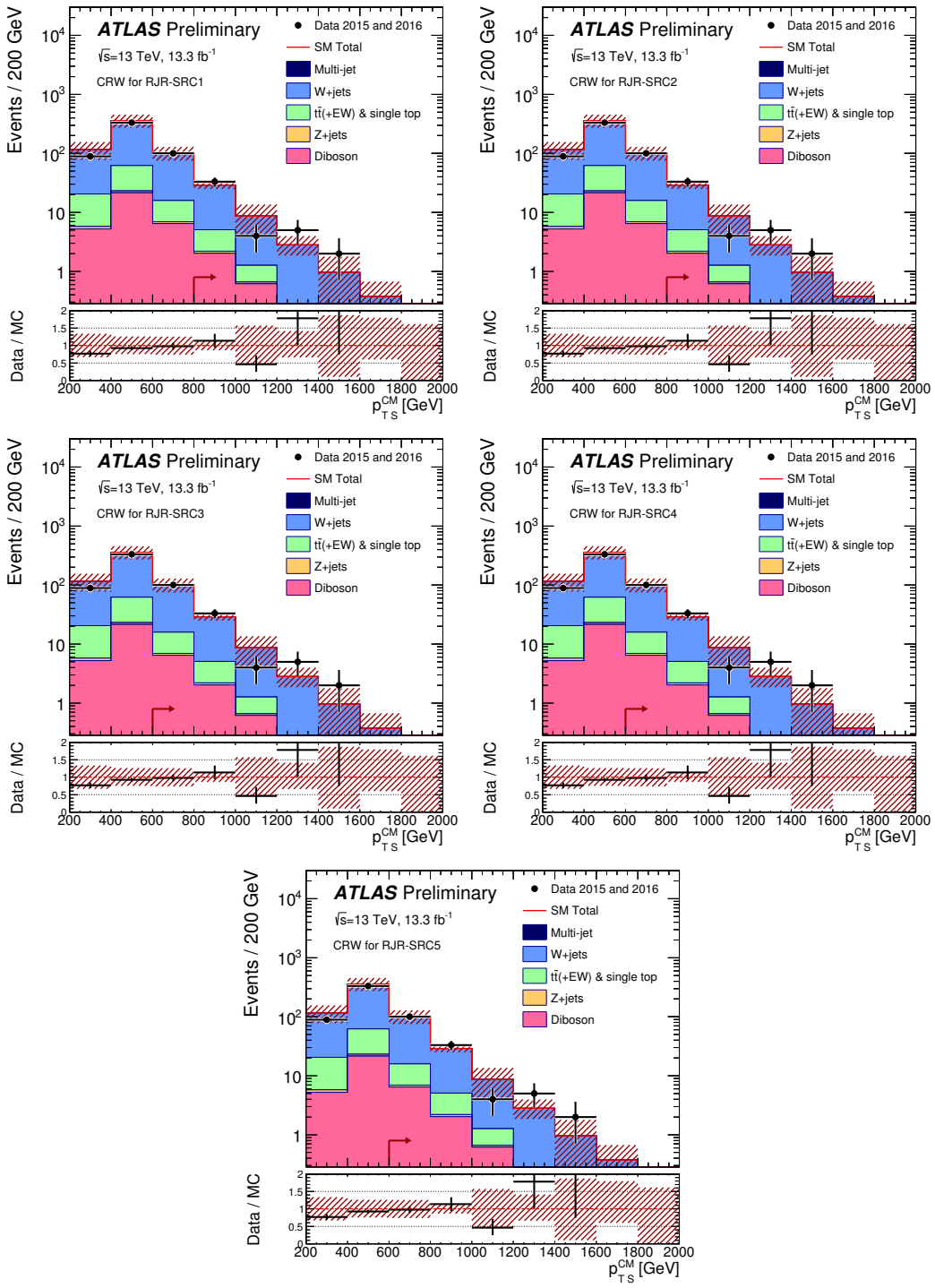


Figure 8.7: Scale variable distributions for the compressed CRW regions.

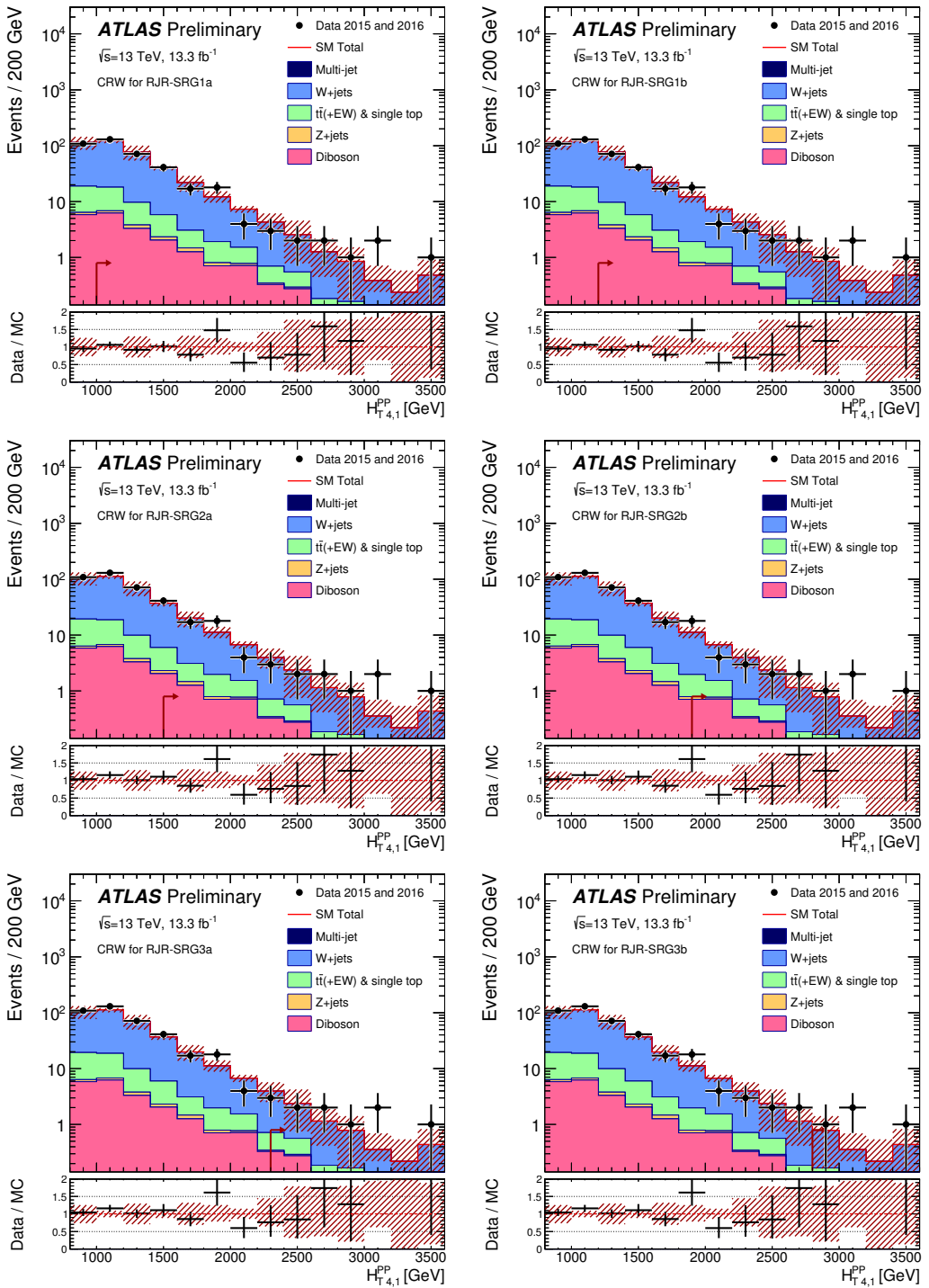


Figure 8.8: Scale variable distributions for the gluino CRW regions.

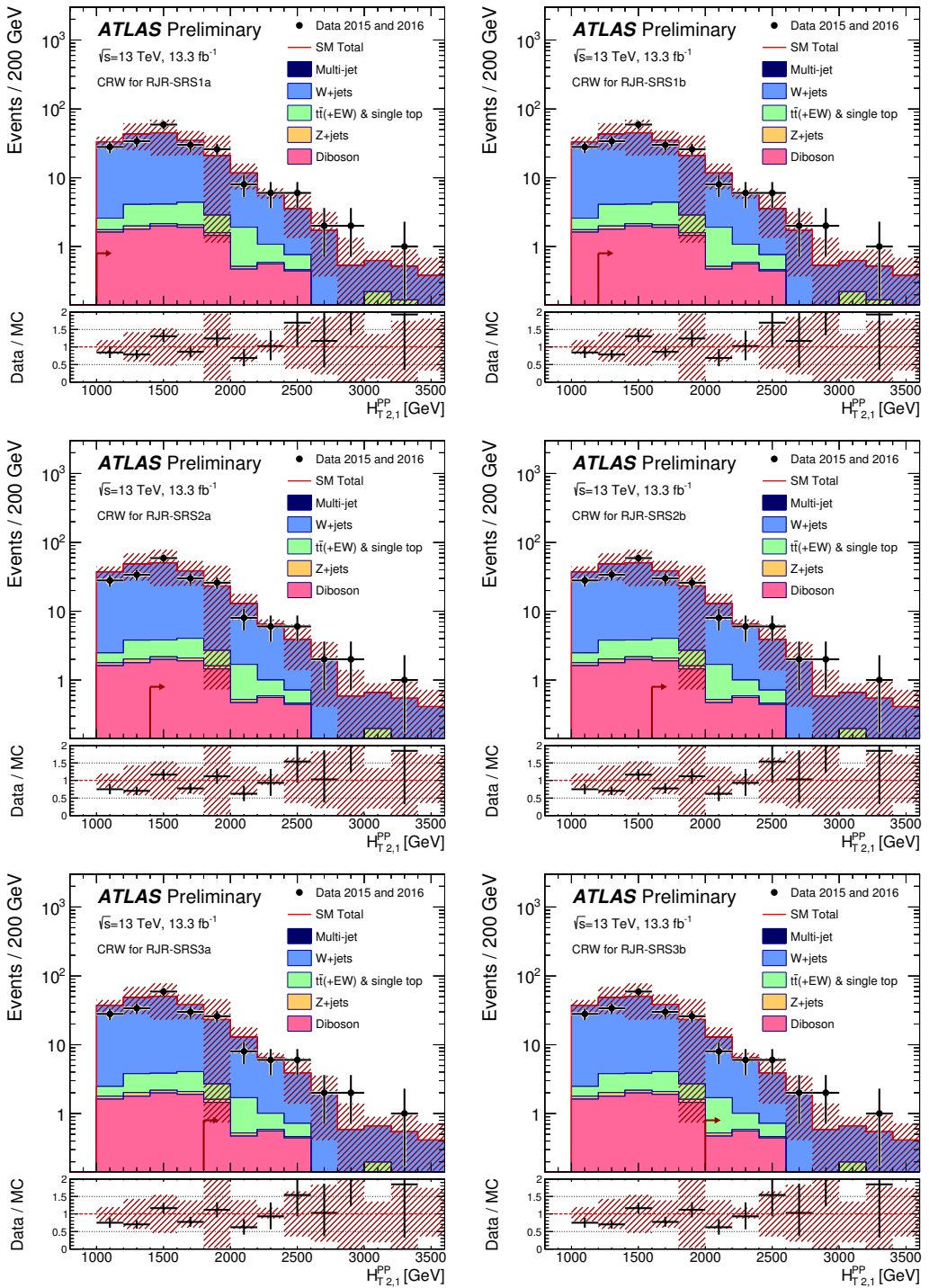


Figure 8.9: Scale variable distributions for the squark CRW regions.

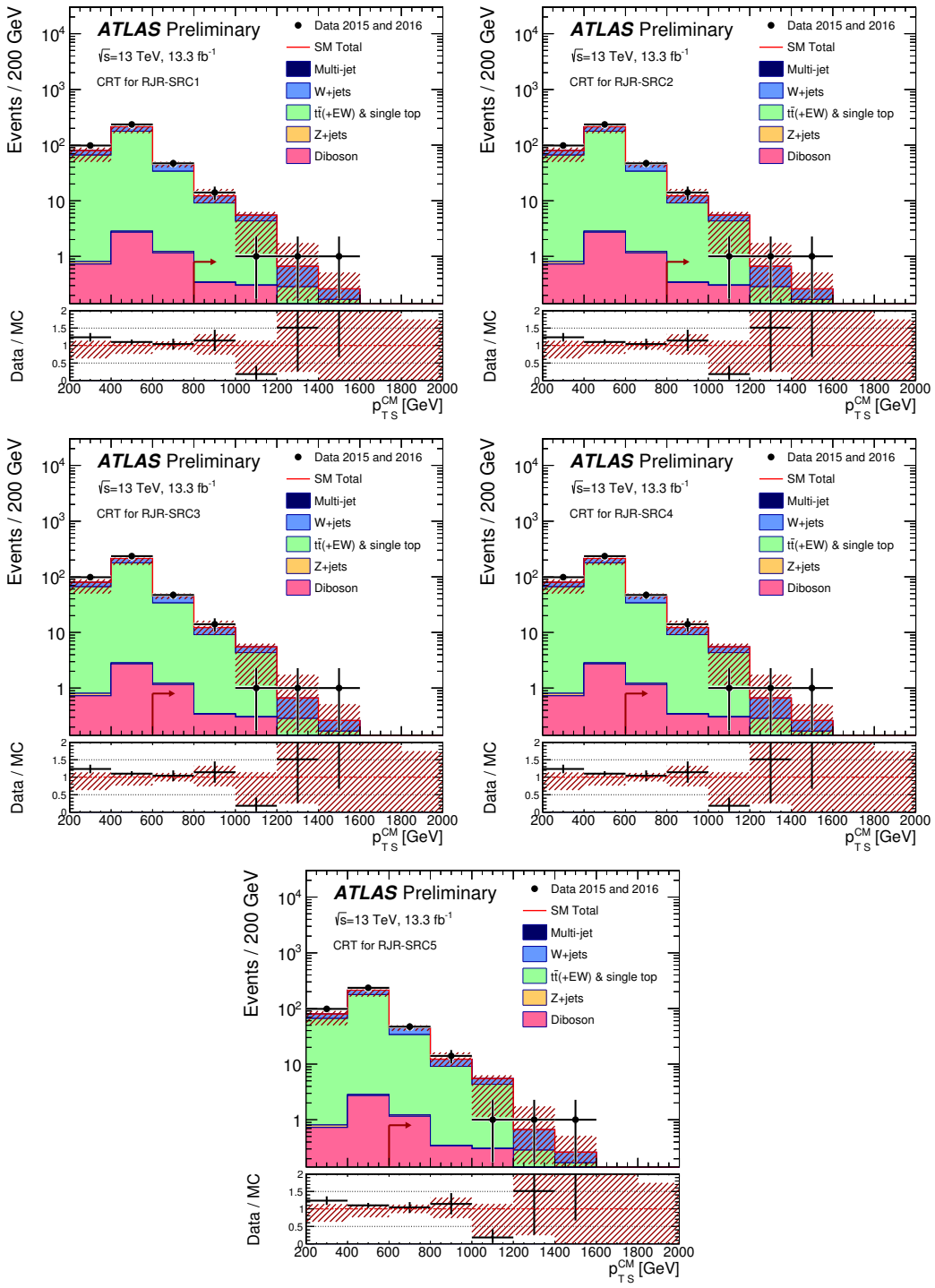


Figure 8.10: Scale variable distributions for the compressed CRT regions.

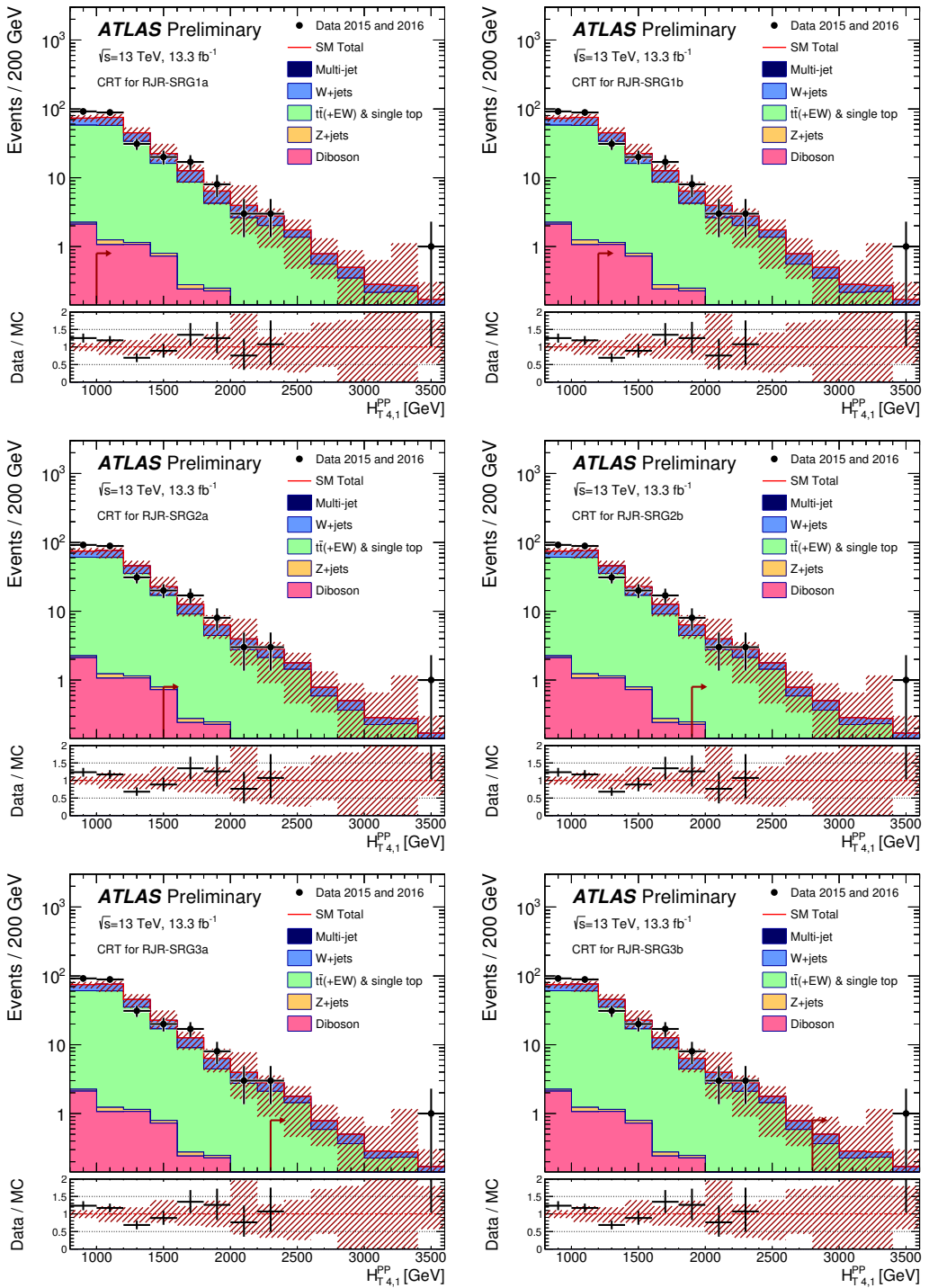


Figure 8.11: Scale variable distributions for the gluino CRT regions.

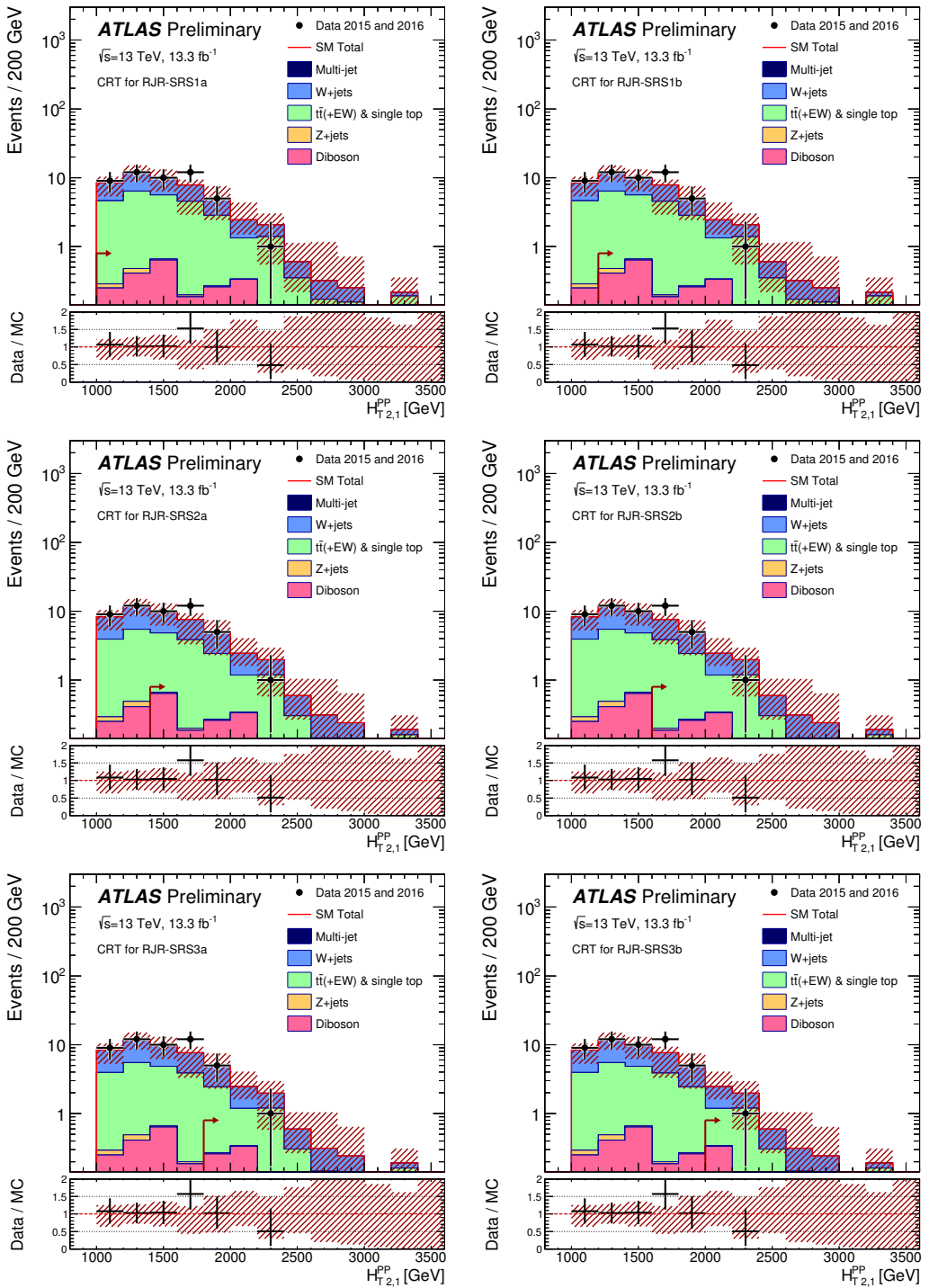


Figure 8.12: Scale variable distributions for the squark CRT regions.

1967 **Validation Regions**

1968 As discussed in general terms above, we define a set of validation regions to ensure
1969 we can properly model the particular backgrounds as we move closer to the SRs in
1970 phase space. We define at least one validation region for each major background.

1971 For the most important background $Z \rightarrow \nu\nu$, we use a series of validation regions.
1972 The primary validation region, which we label as VRZ, is defined by selecting lepton
1973 pairs of opposite sign and identical flavor which lie within $\pm 25\text{ GeV}$ of the Z boson mass.
1974 This selection has high purity for $Z \rightarrow \ell\ell$ events as seen in simulation. We treat the
1975 two leptons as contributions to the E_T^{miss} (as we did with the photon in CRY). This
1976 selection uses the same kinematic cuts as the signal region. We also define two VRs
1977 using the same event selection but looser kinematic cuts, which we label VRZa and
1978 VRZb. VRZa has a loosened selection on $H_{1,1}^{PP}$, again to the loosest value among the
1979 signal regions, as was done for CRW and CRt. VRZa has a loosened selection on
1980 the primary scaleful variable ($H_{T,2,1}^{PP}$ or $H_{T,4,1}^{PP}$), again to the loosest value among the
1981 signal regions, as was done for CRW and CRT. These two validation regions allow us
1982 to test the modeling of each of these variables individually, as well as allowing more
1983 validation region statistics in the signal regions with tighter cuts on these variables.

1984 For the compressed regions, these Z validation region were found lacking. The
1985 leptons are highly boosted in the compressed case, and the lepton acceptance was
1986 quite low due to lepton isolation requirements in ΔR . Instead, two fully hadronic
1987 validation region were developed for the compressed regions. The first, VRZc has
1988 identical requirements to the signal regions with an inverted requirement on $\Delta\phi_{ISR,I}$.
1989 From simulation, this region was found to be at least 50% pure in Z events, which
1990 was considered enough to validate this background in this extreme portion of phase
1991 space. For additional validation region statistics, we also developed VRZca, which
1992 takes again uses the loosest set of cuts from each signal region. Note this means that
1993 each compressed signal region has an identical VRZca.

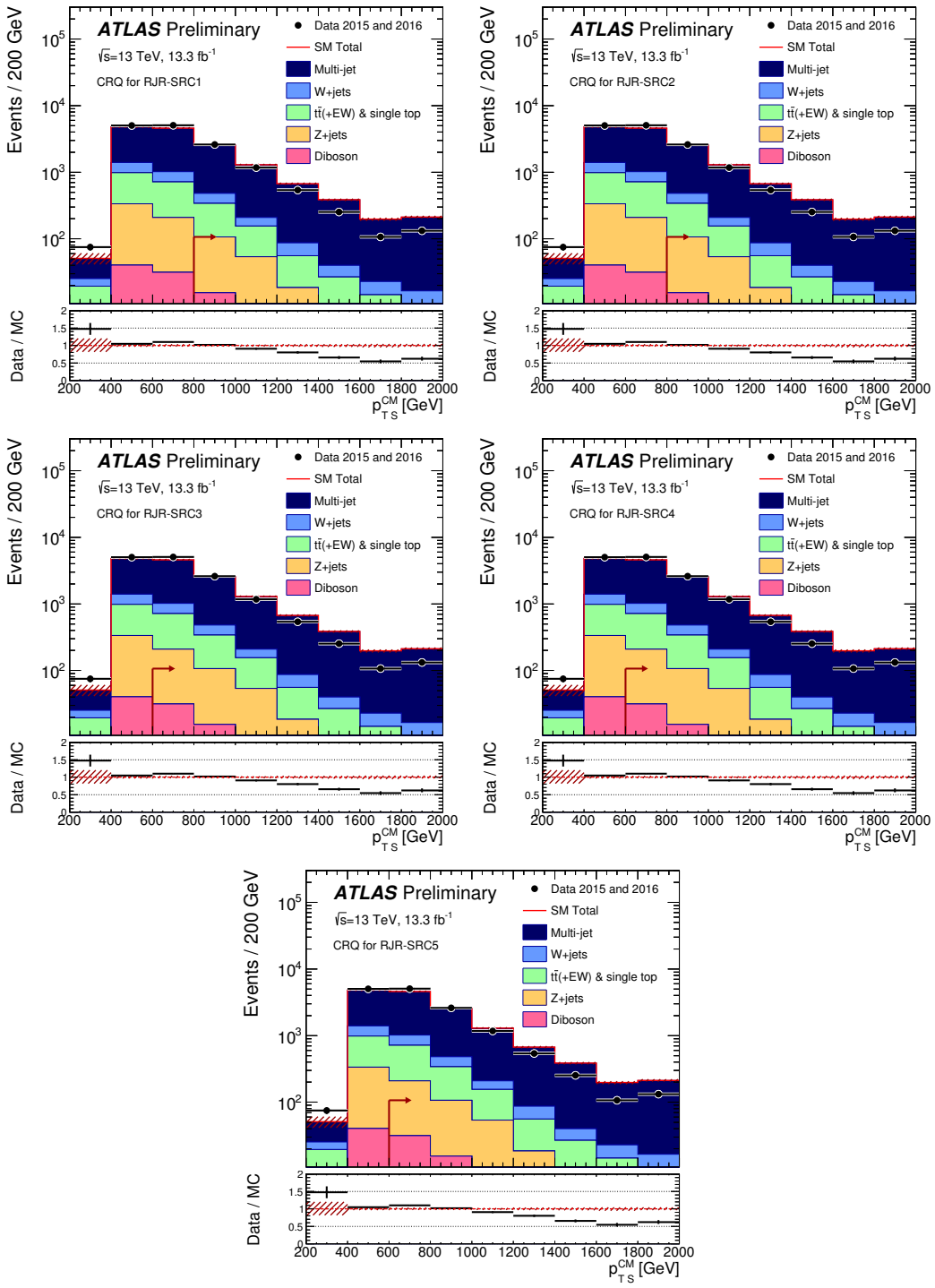


Figure 8.13: Scale variable distributions for the compressed CRQ regions.

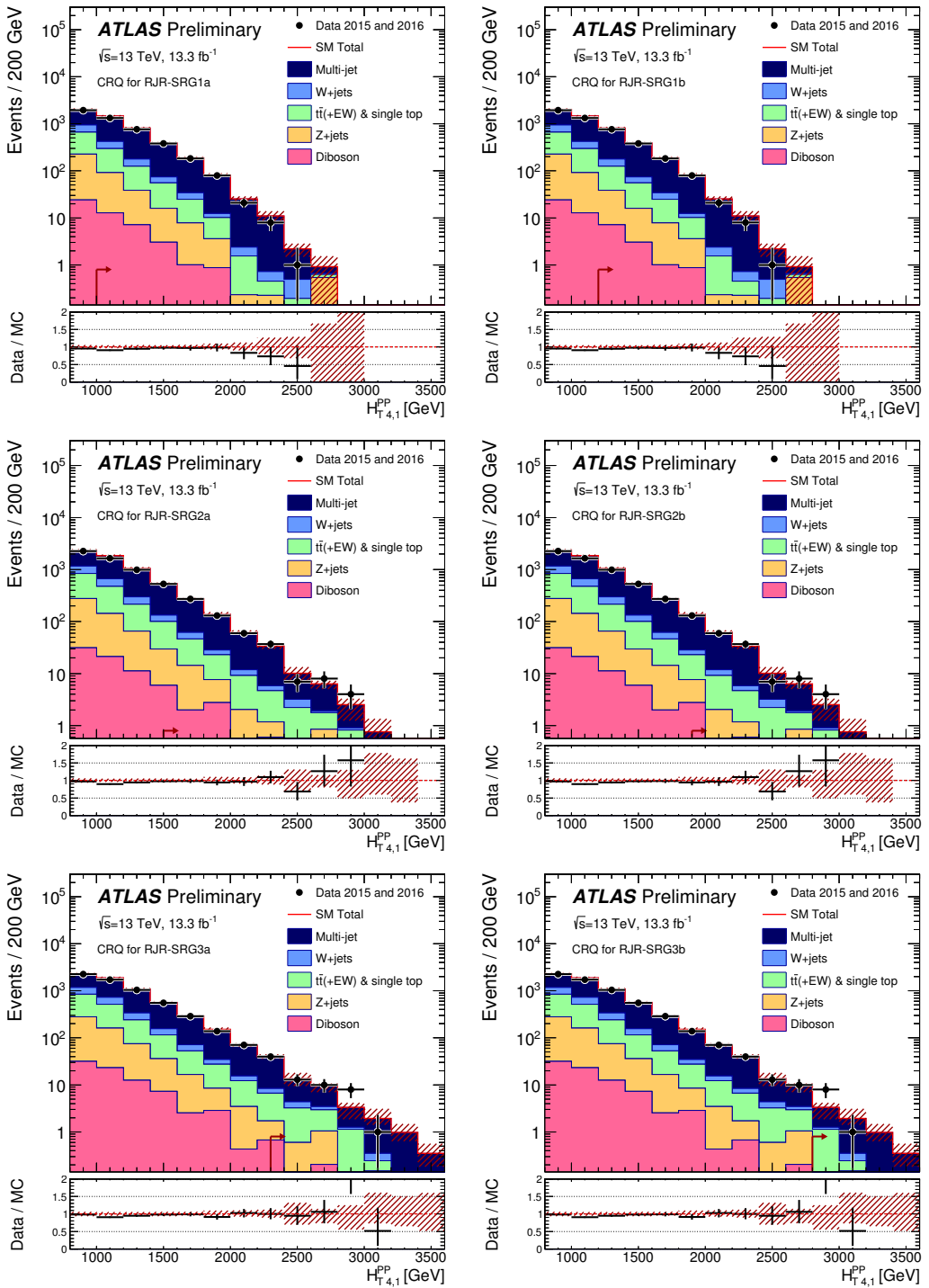


Figure 8.14: Scale variable distributions for the gluino CRQ regions.

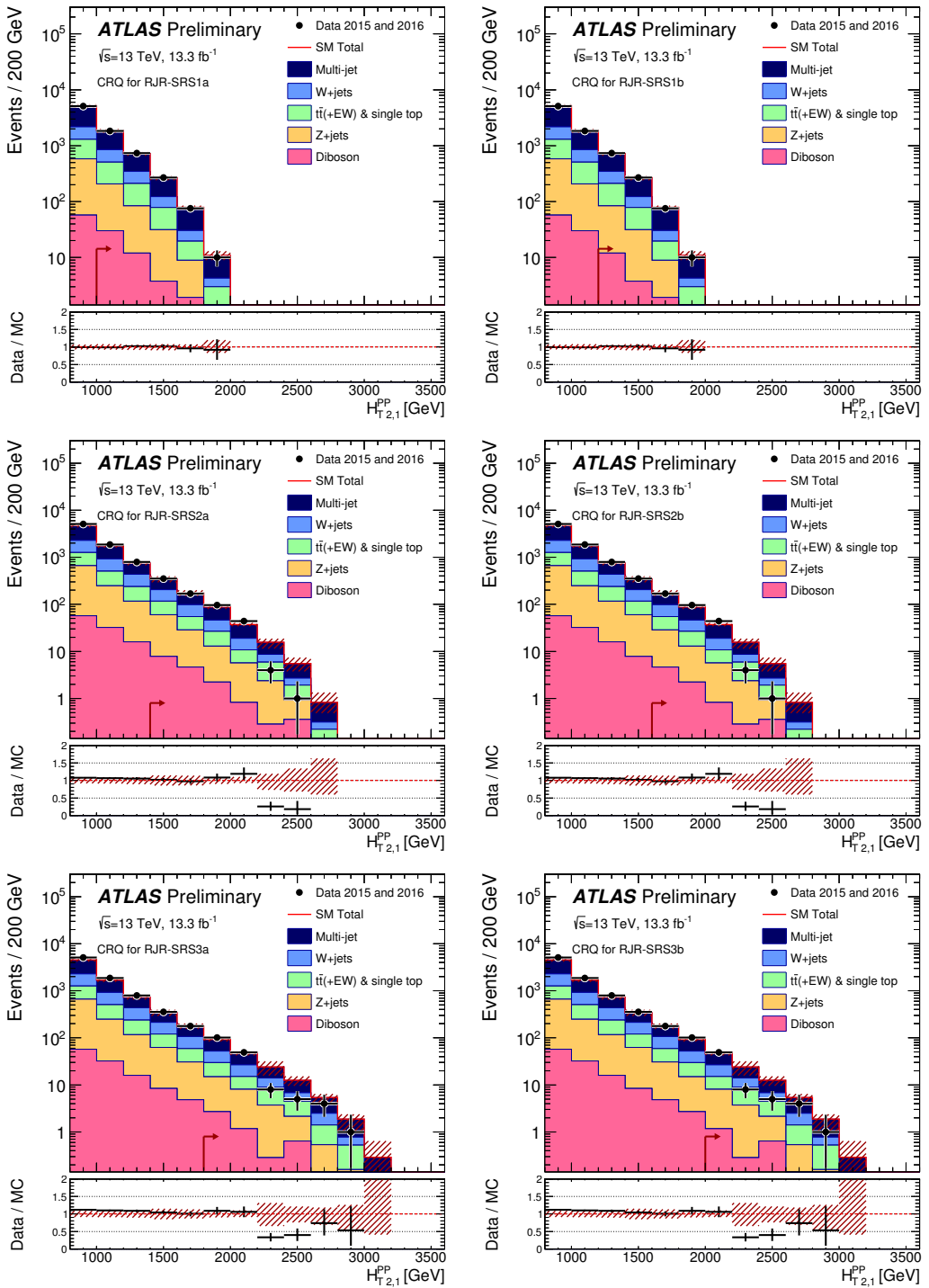


Figure 8.15: Scale variable distributions for the squark CRQ regions.

1994 The top and W validation regions use the same event selection as the correspond-
 1995 ing control regions, as described above. However, unlike the control regions, these
 1996 validation regions reimpose the SR scaleful variable selections, to be closer in phase
 1997 space to the hadronic signal regions. In the same way as we did for VRZa and
 1998 VRZb, we also define auxiliary VRs which loosen the cuts on the scale variables. We
 1999 define VRTa (VRWa) as VRT (VRW) with the same loosened cut on $H_{1,1}^{PP}$ and VRTb
 2000 (VRWb) as VRT (VRW) with the same loosened cut on the primary scale variable.

2001 The final set of validation regions are those defined to check the estimation of
 2002 the QCD background. VRQ is defined to be identical to the corresponding CRQ,
 2003 but again we use the full SR region cuts for the scaleful variables. This selection is
 2004 then closer to the corresponding signal region to validate the CRQ estimate. We also
 2005 define the auxiliary validation regions VRQa and VRQb for the noncompressed signal
 2006 regions. In this case, we reimpose one of the two inverted cuts in CRQ with respect
 2007 to the signal regions, to make each one even closer to the SRs. In CRQa (CRQb), we
 2008 reimpose the $H_{1,1}^{PP}$ (Δ_{QCD}).

2009 For the compressed case, we again define a separate validation region, due to
 2010 the special kinematics probed. We construct a validation region which is the same
 2011 as CRQ, with $.5 < R_{\text{ISR}} < R_{\text{ISR, SR}}$, where $R_{\text{ISR, SR}}$ is the cut on R_{ISR} in the
 2012 corresponding SR. Again, this can be seen as probing “in between” the CR and
 2013 SR in phase space.

The results of this validation can be seen in Fig. 8.16. Each bin is *pull* of the
 validation region corresponding to a particular signal region. This is defined

$$\text{Pull} = \frac{N_{\text{obs}} - N_{\text{pred}}}{\sigma_{\text{tot}}}.$$
 (8.4)

2014 where σ_{tot} is the total uncertainty folding in all systematic uncertainties, which we
 2015 will describe later. Assuming we have well-measured our backgrounds, we expect a
 2016 Gaussian distribution of the pulls around 0, with a standard deviation of 1, as this
 2017 is measuring the number of standard deviations around the mean. We can see there

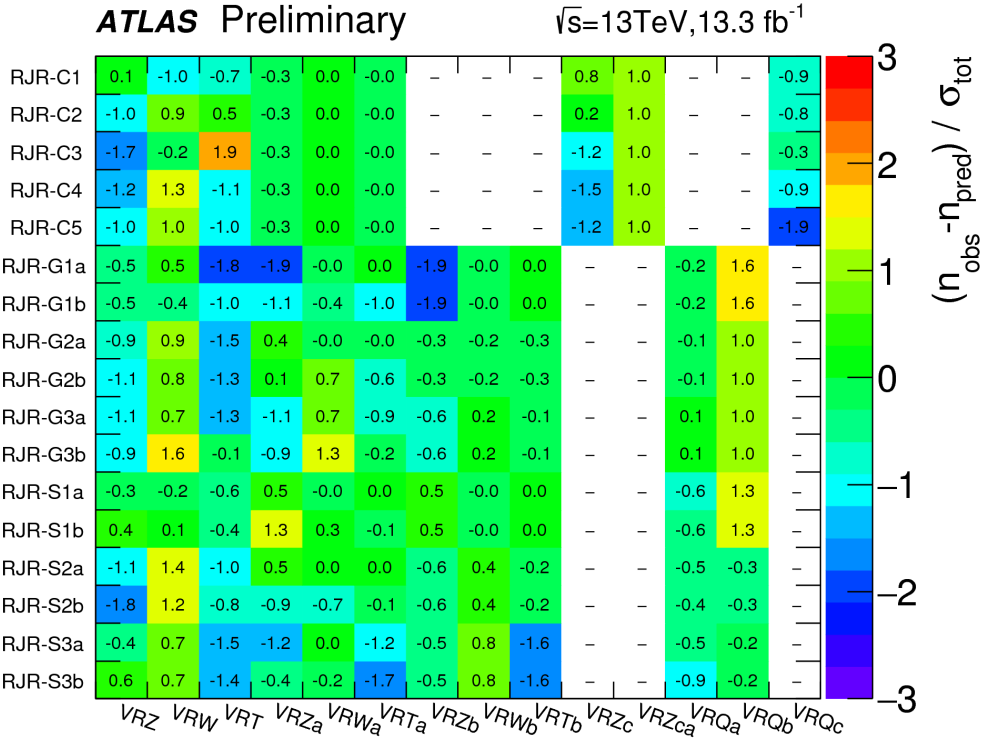


Figure 8.16: Summary of the validation region pulls

2018 are few positive pulls (indicating an underestimation of the background), indicating
 2019 we have conservatively measured the Standard Model backgrounds with our control
 2020 regions.

2021 Systematic Uncertainties

2022 In this section, we discuss the uncertainties considered. These generally fall into
 2023 four categories: theoretical generator uncertainties, uncertainties on the CR to SR
 2024 extrapolations, uncertainties on the data-driven transfer factor corrections, and object
 2025 reconstruction uncertainties. We discuss each of these categories here. A table
 2026 summarizing this section is in Tab. 8.5

Systematic	Uncertainty Description
alpha_GeneratorZ	Theoretical on Z cross-section
alpha_generatorW	Theoretical on W cross-section
alpha_generatorTop	Theoretical on t cross-section
alpha_radiationTop	Theoretical on t radiation tune
alpha_Pythia8Top	Theoretical on t fragmentation tune
alpha_FlatDiboson	Flat on diboson cross-section
mu_Zjets	CRY extrapolation to SR
mu_Wjets	CRW extrapolation to SR
mu_Top	CRT extrapolation to SR
mu_Multijets	CRQ extrapolation to SR
alpha_Kappa	κ factor
alpha_QCDError	Jet smearing
alpha_JET_GroupedNP_1	JES NP group 1
alpha_JET_GroupedNP_2	JES NP group 2
alpha_JET_GroupedNP_3	JES NP group 3
alpha_JER	JER
alpha_MET_SoftTrk_ResoPerp	Soft E_T^{miss} resolution perpendicular to hard object system
alpha_MET_SoftTrk_ResoPara	Soft E_T^{miss} resolution parallel to hard object system
alpha_MET_SoftTrk_Scale	Soft E_T^{miss} scale

Table 8.5: Description of the systematic uncertainties in the analysis.

2027 The theoretical generator uncertainties are evaluated by using alternative sim-
 2028 ulation samples or varying scale uncertainties. In the case of the $Z+jets$ and
 2029 $W+jets$ backgrounds, the related theoretical uncertainties are estimated by varying
 2030 the renormalization, factorization, and resummation scales by two, and decreasing
 2031 the nominal CKKW matching scale by 5 GeV and 10 GeV respectively. In
 2032 the case of $t\bar{t}$ production, we compare the nominal POWHEG-Box generator with
 2033 MG5_aMC@NLO, as well as comparing different radiation and generator tunes. As
 2034 stated above, we account for the uncertainty on the small diboson background by
 2035 imposition of a flat 50% uncertainty.

2036 The CR to SR extrapolation uncertainties, or what could be called the transfer

2037 factor uncertainties, are listed in Tab. 8.5 as $\mu_{\text{--}}$. There is one normalization factor μ
2038 for each major background, and their uncertainties, especially μ_Z , are often dominant
2039 for the measurement in many signal regions. This uncertainty is generally dominated
2040 by the statistical uncertainty in the CR.

2041 There are two uncertainties from the data-driven corrections to the transfer
2042 factors. The first is the uncertainty on κ , which is measured using an auxiliary $Z \rightarrow \ell\ell$
2043 control region. This is labeled alpha_Kappa. The other is the uncertainty is that
2044 assigned to the jet smearing method, which is seen in the table as alpha_QCDError.

2045 The final set of uncertainties are those related to object reconstruction. In the
2046 case of the hadronic search presented, the important uncertainties are those assigned
2047 to the jet energy and E_T^{miss} . The uncertainties on the lepton reconstruction and
2048 b -tagging uncertainties were found to be negligible in all SRs. The measurement
2049 of the jet energy scale (JES) uncertainty is quite complicated, and described in
2050 [138–140]. After a complicated procedure to decorrelate the various components
2051 of the JES uncertainty, there are three components which remain, which are labeled
2052 as alpha_JET_GroupedNP_1,2,3. The jet energy resolution uncertainty is estimated
2053 using the methods discussed in Refs. [140, 141], and is labeled alpha_JER.

2054 The E_T^{miss} soft term uncertainties are described in [117, 118, 142]. The
2055 uncertainty on the E_T^{miss} soft term resolution is parameterized into a component
2056 parallel to direction of the rest of the event (the sum of the hard objects p_T)
2057 and a component perpendicular to this direction. There is also an uncertainty
2058 on the E_T^{miss} soft term scale. These are labeled as alpha_MET_SoftTrk_ResoPara,
2059 alpha_MET_SoftTrk_ResoPerp, and alpha_MET_SoftTrk_Scale.

2060 Fitting procedure

2061 This section describes the fitting procedure to properly account for the correlations
2062 between the various uncertainties and the simultaneous fitting of the control and

2063 signal regions.

2064 Maximum likelihood fit

2065 To properly account for the systematic uncertainties and simultaneously fit the control
2066 regions, we employ a maximum-likelihood fit as described in [125]. The likelihood
2067 function \mathcal{L} is the product of the Poisson distributions governing the likelihood in each
2068 of the signal regions and the corresponding control regions: We begin by considering
2069 our event counts \mathbf{b} in a signal region with its corresponding signal regions. The
2070 systematic uncertainties are included as a set of nuisance parameters $\boldsymbol{\theta}$.

The full likelihood function can be written [125]:

$$\mathcal{L}(n|\mu, \mathbf{b}) = P_{\text{SR}} \times P_{\text{CR}} \times C_{\text{syst}} \quad (8.5)$$

$$= P(n_S|\lambda_S(\mu_S, \mathbf{b}, \boldsymbol{\theta})) \times \prod_{i \in \text{CR}} P(n_i|\lambda_i(\mu_b, \mathbf{b}, \boldsymbol{\theta})) \times C_{\text{syst}}(\boldsymbol{\theta}^0, \boldsymbol{\theta}) \quad (8.6)$$

where $P(n_i|\lambda_i(\mu, \mathbf{b}, \boldsymbol{\theta}))$ is a Poisson distribution conditioned on the event counts n_i in
the i -th CR with mean parameter $\lambda_i(\mu, \mathbf{b}, \boldsymbol{\theta})$. The term $C_{\text{syst}}(\boldsymbol{\theta}^0, \boldsymbol{\theta})$ is the probability
density function with central values $\boldsymbol{\theta}^0$ which are varied with the nuisance parameters
 $\boldsymbol{\theta}$. We model these as Gaussian distributions with unit width and mean zero:

$$C_{\text{syst}}(\boldsymbol{\theta}^0, \boldsymbol{\theta}) = \prod_{s \in S} G(\mu = \theta_s, \sigma = 1), \quad (8.7)$$

2071 where S is the set of systematic uncertainties considered in the analysis.

The terms λ_j for any region j can be expressed as

$$\lambda_j(\mu, \mathbf{b}, \boldsymbol{\theta}) = \sum_b \mu_b b_j \prod_{s \in S} (1 + \Delta_{j,b,s} \theta_s) \quad (8.8)$$

2072 The term μ_b is the normalization factor associated to the background b with event
2073 count b_j in the region j . The terms Δ inside the product represent scale factors
2074 freeing the model to account for the systematic uncertainties θ_s .

2075 The process now is to maximize this likelihood function, given the free parameters
2076 μ_b and the parameters Δ associated to the systematics as nuisance parameters. This

2077 is done using the HISTFITTER package [125]. The normalization parameters μ_b are
2078 the primary output of this maximization, and are in fact the control regions' raison
2079 d'être. This allows the magnitudes of each background process to be maximized *given*
2080 *the actual control region event counts*. We can say the normalization parameters
2081 are found such that the likelihood is maximized. The nuisance parameters are also
2082 determined by this procedure, but do not have a straightforward

The final expected background prediction in each fit by region r_s is then given by

$$N_{\text{total background}} = \sum_b \mu_b N_{b,\text{MC}} \quad (8.9)$$

2083 **Background-only fit, model-independent fit, and**
2084 **model-dependent fit**

2085 The maximum likelihood fit described above can be used with a variety of event count
2086 inputs. We use three separate fit classes, which we call *background-only*, *model-*
2087 *independent*, and *model-dependent* fits. In terms of the likelihood function inputs,
2088 these can be seen as including a different list of event counts \mathbf{b}

2089 In this section, we describe the fitting procedure employed, which properly
2090 accounts for the correlations between the uncertainties through the use of a likelihood
2091 fit as described in [125]. We use three classes of likelihood fits: *background-only*,
2092 *model-independent*, and *model-dependent* fits. The background-only fits estimate the
2093 background yields in each signal region. These fits use only the control region event
2094 yields as inputs; they do not include the information from the signal regions besides
2095 the simulation event yield. The cross-contamination between CRs is also fit by this
2096 procedure. The systematic uncertainties described in the previous section are used as
2097 nuisance parameters. This background only fit also estimates the background event
2098 yields in the validation regions. When designing the analysis (before unblinding
2099 the signal regions), checking the validation region agreement is the primary way to

2100 validate the consistency and accuracy of the background estimation procedure.

2101 In the case no excess is observed, we use a model-independent fit to set upper limits
2102 on the possible number of possible beyond the Standard Model events in each SR.
2103 These limits are derived using the same procedure as the background-only fit, with
2104 two additional pieces of information included in the fitting procedure. We include
2105 the SR event count, and a parameter known as the *signal strength*, defined as $\mu =$
2106 $\sigma/\sigma_{\text{BG}}$. Using the CL_s procedure [143] and neglecting the possible (small) signal
2107 contamination in control regions, we derive the the observed and expected limits on
2108 the number of events from BSM phenomena in each signal region.

2109 Model-dependent fits are used to set exclusion limits on the specific SUSY
2110 models considered in this thesis, particular the gluino or squark pair production
2111 with various mass splittings. This can be seen as identical to the background-only
2112 fit with an additional simulation input from the particular model of interest, with its
2113 corresponding systematic uncertainties from detector effects accounted for as in the
2114 background-only fit. As noted when we introduced Fig. 8.1, the exclusion contours
2115 from previous model-dependent fits are the primary motivating factor in the design
2116 of our signal regions. If no excess is found, we set limits on each of the simplified
2117 signal models with various mass splittings.

2118

Chapter 9

2119

Results

2120 This chapter presents the results of the analysis presented in the previous chapter.
2121 We present the full set of signal region distributions after applying the μ factors
2122 derived from the fitting procedure. We also present the systematic uncertainties in
2123 each signal region properly accounting for the correlations of the uncertainties. As
2124 no excess is observed, we show exclusion limits in the sparticle- $\tilde{\chi}_1^0$ plane based on
2125 the results of the model-dependent fits and present the model-independent limits.

2126

9.1 Signal region distributions

2127 In Figs. 9.1 to 9.3, we can see the unblinded distributions of the last scale cut used
2128 for each signal region. These distributions include the μ normalization scale factors
2129 derived from the fitting procedure. The systematic uncertainties are also shown.
2130 Each plot shows the distribution from a signal model which is targetted by the given
2131 signal region.

2132 These distributions have all cuts applied except for the cut on this scale variable,
2133 which allows us to see the additional discrimination provided by the given variable.
2134 Since signal regions with the same numeral have identical cuts except for that on the
2135 main scale variable, we show (a) and (b) on the same figure. The left-most (right-
2136 most) arrow shown is the location of the a (b) cut applied in the analysis. We call
2137 these plot $N - 1$ plots, where N refers to the number of cuts applied in the analysis.
2138 The full set of $N - 1$ plots in the signal regions for the other variables used in the

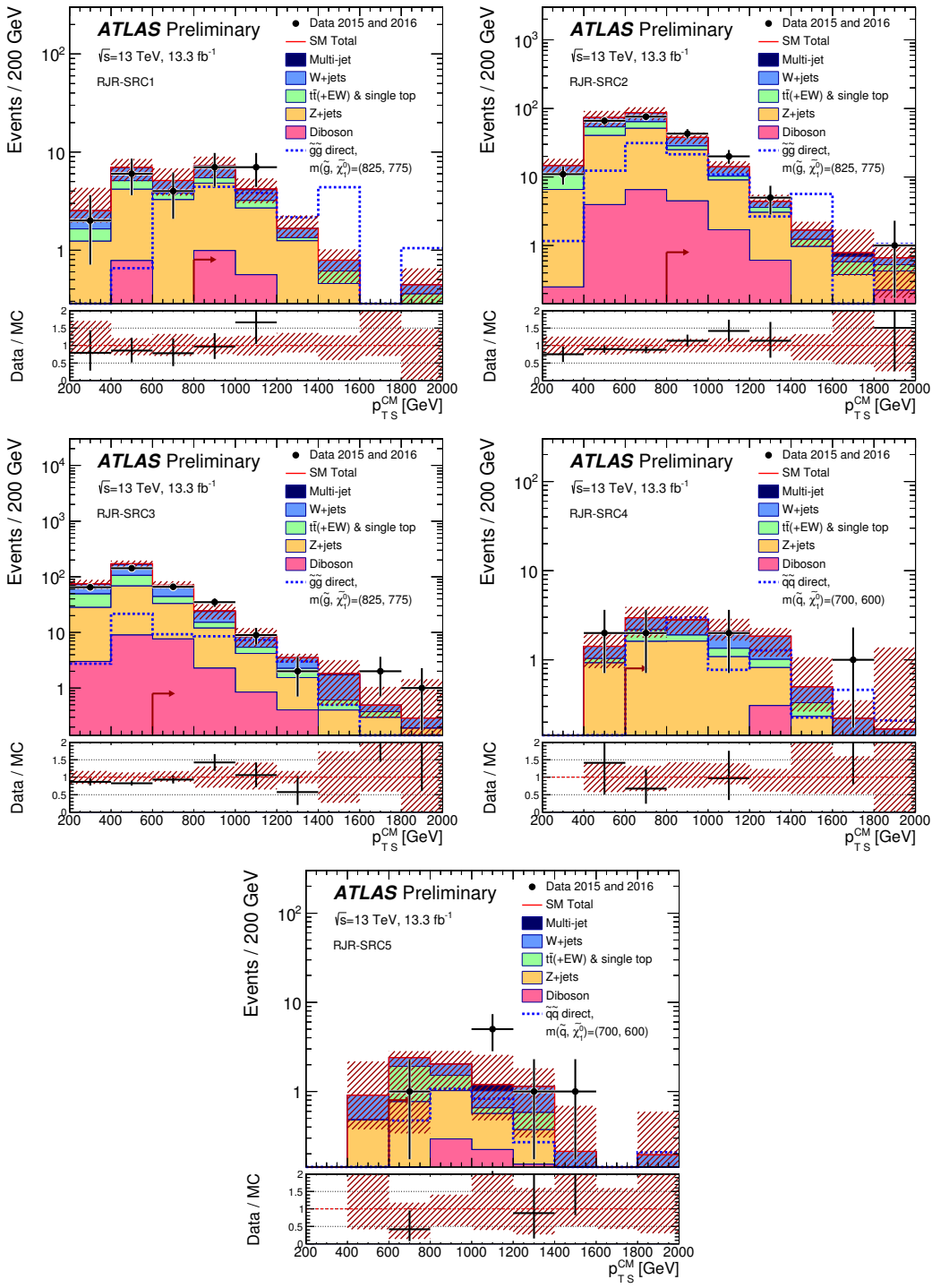


Figure 9.1: Scale variable distributions for the compressed signal regions.

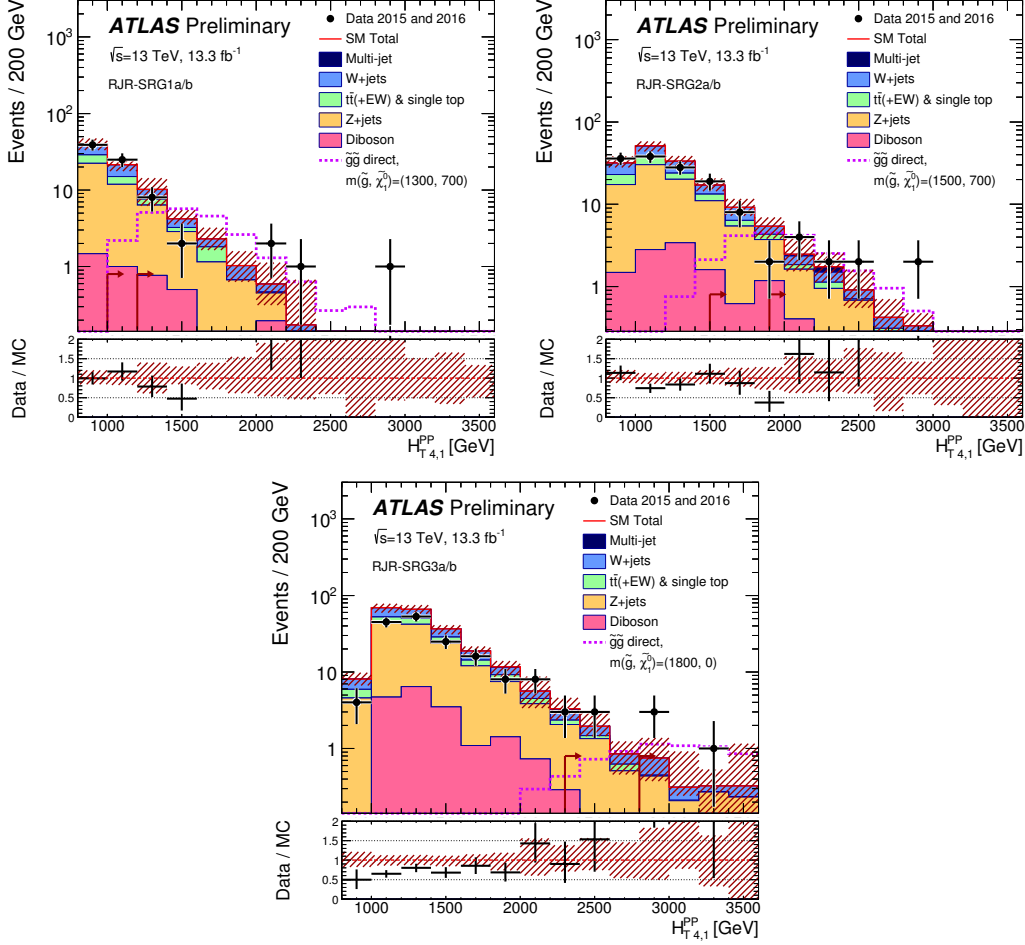


Figure 9.2: Scale variable distributions for the gluino signal regions.

analysis are shown in Sec. 9.4.

A figure showing a summary of the pulls in all of the SRs is shown in Fig. 9.4. This figure shows the integrated data and simulation values above the cut values in the N-1 plots, with the corresponding statistical and systematic uncertainties, for all signal regions simultaneously. The systematic uncertainties will be discussed in the next section. From this plot, we can see there is no significant excess of events over the Standard Model background.

This information is also presented in Tab. 9.2. The table includes the expectations from simulation before applying the μ normalization factor, as well as the model-independent limits we will discuss later.

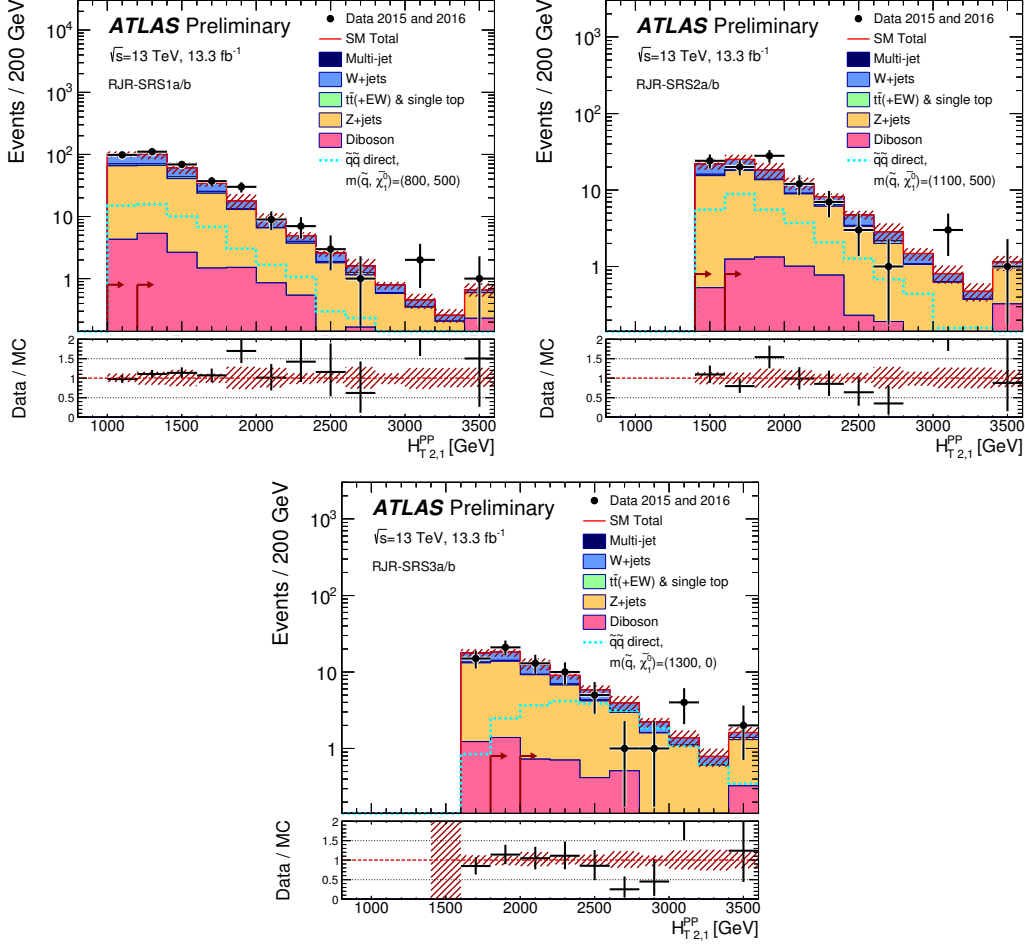


Figure 9.3: Scale variable distributions for the squark signal regions.

2149 We now consider the final values of the systematic uncertainties.

2150 9.2 Systematic Uncertainties

2151 This section considers the results of Tab. 9.1. This table is a summary of the resulting
 2152 systematic uncertainties on the background estimation in each signal region, properly
 2153 accounting for systematic uncertainties. These uncertainties are expressed both as a
 2154 relative uncertainty and absolute uncertainty. As correlations are properly treated,
 2155 the absolute uncertainties do not add in quadrature, although most uncertainties are
 2156 relatively uncorrelated. We discuss the general trends in the systematic uncertainties

2157 for each type of signal region.

2158 In the squark regions, the total uncertainties range from 10% to 11%. We note
2159 that the uncertainties on the Z , both theoretical and $\Delta_{\mu, Z+\text{jets}}$ account for the largest
2160 on the background estimate in each signal region. The κ factor uncertainty, which is
2161 also an uncertainty on the Z estimate, is also significant at 4% in each region. The
2162 $Z \rightarrow \nu\nu$ contribution to the squark regions is the primary irreducible background, so
2163 even when relatively well-measured, the uncertainty on its event yield dominates the
2164 overall uncertainty. There are also significant uncertainties from the W , top, and flat
2165 diboson uncertainties, although these are subdominant. We note that the uncertainty
2166 due to statistics of the MC simulation samples are very small for the squark case; this
2167 is a reflection of the “looseness” of these regions, as the MC statistics are sufficient
2168 for all of the major backgrounds.

2169 The gluino regions have overall larger uncertainties than the squark regions,
2170 between 10% and 25%, due to a multitude of factors. The Z related uncertainties
2171 all contribute significantly to the final background yield uncertainties. These
2172 are relatively similar to the squark Z uncertainties. The W , top, and diboson
2173 uncertainties are all significantly more important than in the squark case however. In
2174 the gluino case, we also see that the limited simulation statistics begin to significantly
2175 affect the measurement of the Standard Model background. These are all reflections
2176 of the overall “tighter” quality of the gluino regions, as indicated by the event yields.
2177 The Δ_μ uncertainties are affected by this due to the need to use overall looser
2178 control regions, while the theory uncertainties are more affected by small statistical
2179 fluctuations between different generators. The low statistics is particularly clear in
2180 SRG3b, where the simulation statistics account for a very large 14% uncertainty.

2181 The compressed regions have systematic uncertainties ranging from 10% to 19%.
2182 For the tighter regions, SRC1, SRC4, and SRC5, we see a large contribution from
2183 the lack of MC statistics. SRC1 and SRC4 should a large value for the W theory

2184 uncertainty, while all compressed regions show a large uncertainty on the Z estimate.
2185 These large uncertainties result from the fact that we are probing extreme phase
2186 space in boson p_T with the compressed regions. SRC5 shows large top and jet/ E_T^{miss}
2187 uncertainties; these uncertainties are more pronounced in this region than the other
2188 compressed region due to the $N_{\text{jet}}^V > 3$ cut, and thus the uncertainty in this region is
2189 quite affected by fluctuations in the top, jet, or E_T^{miss} uncertainties.

2190 9.3 Limits and Model-dependent Exclusions

2191 In Tab. 9.1, we show the statistical significance Z for each signal region. We calculate
2192 this using the fitted simulation mean compared with the observed event counts in
2193 each region. There is no significant excess in each region; the highest excess is in
2194 SRG3b, which is only $Z_{\text{SRG3b}} = 1.55$. This information is summarized in Fig. 9.4.
2195 We thus set model-independent and model-dependent limits.

2196 As no significant excess is observed in any of the signal regions of this analysis
2197 after estimating the background using the background-only fit, we set limits on the
2198 model-independent and model-dependent cross sections.

2199 The model-independent limits are shown in Tab. 9.1. We present the limits on
2200 the new physics cross section in each SR. The observed and expected limits S_{obs}^{95} and
2201 S_{exp}^{95} are reported for the potential contribution from new physics in each region.
2202 Including the acceptance ϵ , the model-independent limits in most signal regions are
2203 of $\sim 1 - 2$ fb. One should note that the (b) version of each signal region is strictly
2204 tighter in the primary scale cut, and thus provides a stronger limit when we observe
2205 no excess, as seen here.

2206 Additionally, we derive exclusion limits for the simplified models considered in this
2207 thesis. These are the models with pair-production of squark pairs with inaccessible
2208 gluinos, and gluino pairs with inaccessible squarks. They correspond directly to the

Channel	RJR-S1a	RJR-S1b	RJR-S2a	RJR-S2b	RJR-S3a	RJR-S3b
Total bkg	334	233	96	75	56	37
Total bkg unc.	± 35 [10%]	± 25 [11%]	± 10 [10%]	± 8 [11%]	± 6 [11%]	± 4 [11%]
MC statistics	—	± 2.6 [1%]	± 1.5 [2%]	± 1.3 [2%]	± 1.0 [2%]	± 0.7 [2%]
$\Delta\mu_{Z,+jets}$	± 20 [6%]	± 14 [6%]	± 4 [4%]	± 2.9 [4%]	± 2.2 [4%]	± 1.5 [4%]
$\Delta\mu_{W,+jets}$	± 10 [3%]	± 7 [3%]	± 3.1 [3%]	± 2.3 [3%]	± 1.6 [3%]	± 1.1 [3%]
$\Delta\mu_{Top}$	± 6 [2%]	± 4 [2%]	± 1.5 [2%]	± 1.1 [1%]	± 0.9 [2%]	± 0.6 [2%]
$\Delta\mu_{Multijet}$	± 0.09 [0%]	± 0.05 [0%]	± 0.02 [0%]	—	—	—
CR γ corr. factor	± 12 [4%]	± 8 [3%]	± 4 [4%]	± 2.9 [4%]	± 2.2 [4%]	± 1.4 [4%]
Theory Z	± 23 [7%]	± 16 [7%]	± 7 [7%]	± 6 [8%]	± 4 [7%]	± 2.8 [8%]
Theory W	± 4 [1%]	± 5 [2%]	± 0.4 [0%]	± 0.11 [0%]	± 1.5 [3%]	± 1.2 [3%]
Theory Top	± 4 [1%]	± 2.7 [1%]	± 0.8 [1%]	± 0.7 [1%]	± 0.6 [1%]	± 0.4 [1%]
Theory Diboson	± 9 [3%]	± 6 [3%]	± 2.8 [3%]	± 2.6 [3%]	± 2.1 [4%]	± 1.4 [4%]
Jet/MET	± 3.3 [1%]	± 1.5 [1%]	± 0.6 [1%]	± 0.6 [1%]	± 1.2 [2%]	± 1.0 [3%]
Multijet method	± 0.7 [0%]	± 0.4 [0%]	± 0.08 [0%]	—	—	—
Channel	RJR-G1a	RJR-G1b	RJR-G2a	RJR-G2b	RJR-G3a	RJR-G3b
Total bkg	40	18.8	27.8	8.5	5.8	1.7
Total bkg unc.	± 4 [10%]	± 2.5 [13%]	± 3.4 [12%]	± 1.4 [16%]	± 1.1 [19%]	± 0.4 [24%]
MC statistics	± 1.6 [4%]	± 1.0 [5%]	± 1.2 [4%]	± 0.6 [7%]	± 0.4 [7%]	± 0.23 [14%]
$\Delta\mu_{Z,+jets}$	± 1.5 [4%]	± 0.7 [4%]	± 1.6 [6%]	± 0.5 [6%]	± 0.4 [7%]	± 0.1 [6%]
$\Delta\mu_{W,+jets}$	± 0.9 [2%]	± 0.4 [2%]	± 1.2 [4%]	± 0.31 [4%]	± 0.28 [5%]	± 0.1 [6%]
$\Delta\mu_{Top}$	± 0.8 [2%]	± 0.33 [2%]	± 0.9 [3%]	± 0.23 [3%]	± 0.07 [1%]	± 0.1 [6%]
$\Delta\mu_{Multijet}$	± 0.1 [0%]	—	± 0.03 [0%]	± 0.02 [0%]	—	—
CR γ corr. factor	± 1.2 [3%]	± 0.6 [3%]	± 0.8 [3%]	± 0.26 [3%]	± 0.19 [3%]	± 0.05 [3%]
Theory Z	± 2.3 [6%]	± 1.1 [6%]	± 1.6 [6%]	± 0.5 [6%]	± 0.4 [7%]	± 0.1 [6%]
Theory W	± 1.1 [3%]	± 1.3 [7%]	± 0.3 [1%]	± 0.7 [8%]	± 0.6 [10%]	± 0.16 [9%]
Theory Top	± 1.2 [3%]	± 0.7 [4%]	± 1.0 [4%]	± 0.4 [5%]	± 0.4 [7%]	± 0.26 [15%]
Theory Diboson	± 1.3 [3%]	± 0.8 [4%]	± 1.5 [5%]	± 0.6 [7%]	± 0.31 [5%]	± 0.13 [8%]
Jet/MET	± 1.0 [3%]	± 0.6 [3%]	± 0.4 [1%]	± 0.17 [2%]	± 0.22 [4%]	± 0.05 [3%]
Multijet method	± 0.24 [1%]	± 0.12 [1%]	± 0.5 [2%]	± 0.4 [5%]	—	—
Channel	RJR-C1	RJR-C2	RJR-C3	RJR-C4	RJR-C5	
Total bkg	14.5	59	110	10.5	7.3	
Total bkg unc.	± 2.2 [15%]	± 6 [10%]	± 11 [10%]	± 1.5 [14%]	± 1.4 [19%]	
MC statistics	± 0.7 [5%]	± 1.7 [3%]	± 2.4 [2%]	± 0.6 [6%]	± 0.6 [8%]	
$\Delta\mu_{Z,+jets}$	± 0.5 [3%]	± 1.9 [3%]	± 2.5 [2%]	± 0.31 [3%]	± 0.13 [2%]	
$\Delta\mu_{W,+jets}$	± 0.4 [3%]	± 1.7 [3%]	± 5 [5%]	± 0.4 [4%]	± 0.25 [3%]	
$\Delta\mu_{Top}$	± 0.33 [2%]	± 1.3 [2%]	± 4 [4%]	± 0.31 [3%]	± 0.4 [5%]	
$\Delta\mu_{Multijet m}$	—	± 0.1 [0%]	± 0.06 [0%]	—	± 0.1 [1%]	
CR γ corr. factor	± 0.5 [3%]	± 1.8 [3%]	± 2.3 [2%]	± 0.29 [3%]	± 0.13 [2%]	
Theory Z	± 0.8 [6%]	± 3.5 [6%]	± 4 [4%]	± 0.6 [6%]	± 0.24 [3%]	
Theory W	± 1.3 [9%]	± 0.03 [0%]	± 2.0 [2%]	± 1.0 [10%]	± 0.13 [2%]	
Theory Top	± 0.5 [3%]	± 1.3 [2%]	± 3.2 [3%]	± 0.6 [6%]	± 0.9 [12%]	
Theory Diboson	± 1.0 [7%]	± 4 [7%]	± 6 [5%]	± 0.27 [3%]	± 0.4 [5%]	
Jet/MET	± 0.5 [3%]	± 1.5 [3%]	± 3.1 [3%]	± 0.24 [2%]	± 0.5 [7%]	
Multijet method	± 0.09 [1%]	± 0.4 [1%]	± 2.1 [2%]	—	± 0.18 [2%]	

Table 9.1: Breakdown of the dominant systematic uncertainties in the background estimates for the RJR-based search. The individual uncertainties can be correlated, and do not necessarily add in quadrature to the total background uncertainty. Δ_μ uncertainties are the result of the control region statistical uncertainties and the systematic uncertainties entering a specific control region. In brackets, uncertainties are given relative to the expected total background yield, also presented in the Table. Empty cells (indicated by a ‘-’) correspond to uncertainties $< 0.1\%$.

Signal Region	RJR-S1a	RJR-S1b	RJR-S2a	RJR-S2b	RJR-S3a	RJR-S3b
MC expected events						
Diboson	17	13	5.6	5.1	4.2	2.8
Z/ γ^* +jets	231	163	63	48	36	24
W+jets	97	66	22	16	11	7.8
$t\bar{t}$ (+EW) + single top	15	10	2.9	2.1	1.7	1.1
Fitted background events						
Diboson	17 ± 9	13 ± 7	5.6 ± 2.8	5.1 ± 2.6	4.2 ± 2.1	2.8 ± 1.4
Z/ γ^* +jets	207 ± 33	146 ± 23	65 ± 9	50 ± 7	37 ± 5	25.0 ± 3.5
W+jets	95 ± 9	65 ± 7	24.1 ± 2.9	18.3 ± 2.3	12.8 ± 2.8	8.7 ± 2.0
$t\bar{t}$ (+EW) + single top	14 ± 7	9 ± 5	2.1 ± 1.7	1.6 ± 1.3	1.3 ± 1.0	0.8 ± 0.7
Multi-jet	$0.71^{+0.71}_{-0.71}$	$0.41^{+0.41}_{-0.41}$	$0.08^{+0.09}_{-0.08}$	—	—	—
Total Expected MC	362	253	93	72	53	36
Total Fitted bkg	334 ± 35	233 ± 25	96 ± 10	75 ± 8	56 ± 6	37 ± 4
Observed	368	270	99	75	57	36
$\langle\epsilon\sigma\rangle_{\text{obs}}^{95}$ [fb]	7.6	6.5	2.2	1.7	1.6	1.1
S_{obs}^{95}	101	86	29	23	22	15
S_{exp}^{95}	78^{+27}_{-21}	61^{+22}_{-16}	28^{+11}_{-8}	23^{+9}_{-7}	20^{+8}_{-6}	16^{+7}_{-5}
p_0 (Z)	0.20 (0.84)	0.12 (1.17)	0.44 (0.15)	0.50 (0.00)	0.44 (0.14)	0.50 (0.00)
Signal Region	RJR-G1a	RJR-G1b	RJR-G2a	RJR-G2b	RJR-G3a	RJR-G3b
MC expected events						
Diboson	2.6	1.6	2.9	1.1	0.62	0.26
Z/ γ^* +jets	18	8.8	13	4.2	3.1	0.83
W+jets	11	4.7	7.7	2.0	1.9	0.63
$t\bar{t}$ (+EW) + single top	7.4	3.1	4.4	1.1	0.34	0.03
Fitted background events						
Diboson	2.6 ± 1.3	1.6 ± 0.8	2.9 ± 1.5	1.1 ± 0.6	0.6 ± 0.4	0.26 ± 0.14
Z/ γ^* +jets	21.1 ± 3.1	10.2 ± 1.6	14.3 ± 2.5	4.5 ± 0.8	3.3 ± 0.6	0.88 ± 0.19
W+jets	10.8 ± 1.7	4.6 ± 1.4	6.7 ± 1.3	1.7 ± 0.7	1.6 ± 0.7	0.55 ± 0.2
$t\bar{t}$ (+EW) + single top	5.4 ± 1.6	2.3 ± 0.9	3.4 ± 1.4	0.8 ± 0.5	$0.26^{+0.45}_{-0.26}$	$0.02^{+0.26}_{-0.02}$
Multi-jet	0.24 ± 0.24	0.12 ± 0.12	0.5 ± 0.5	0.4 ± 0.4	—	—
Total Expected MC	39	18	29	8.7	5.9	1.7
Total Fitted bkg	40 ± 4	18.8 ± 2.5	27.8 ± 3.4	8.5 ± 1.4	5.8 ± 1.1	1.7 ± 0.4
Observed	39	14	30	10	8	4
$\langle\epsilon\sigma\rangle_{\text{obs}}^{95}$ [fb]	1.1	0.56	1.1	0.71	0.64	0.55
S_{obs}^{95}	15	7.5	15	9.4	8.5	7.3
S_{exp}^{95}	16^{+7}_{-4}	10^{+5}_{-3}	14^{+6}_{-4}	$7.6^{+3.5}_{-2.0}$	$7.0^{+2.5}_{-2.1}$	$4.2^{+1.9}_{-0.5}$
p_0 (Z)	0.50 (0.00)	0.50 (0.00)	0.36 (0.35)	0.31 (0.50)	0.21 (0.81)	0.06 (1.55)
Signal Region	RJR-C1	RJR-C2	RJR-C3	RJR-C4	RJR-C5	
MC expected events						
Diboson	1.9	7.1	11	0.54	0.75	
Z/ γ^* +jets	8.8	36	46	5.8	2.5	
W+jets	3.5	16	43	3.8	2.3	
$t\bar{t}$ (+EW) + single top	1.9	7.2	20	1.7	2.5	
Fitted background events						
Diboson	1.9 ± 1.0	7 ± 4	11 ± 6	0.54 ± 0.29	0.8 ± 0.5	
Z/ γ^* +jets	7.7 ± 1.1	32 ± 5	40 ± 6	5.0 ± 0.8	2.2 ± 0.4	
W+jets	3.3 ± 1.4	14.5 ± 1.7	40 ± 5	3.56 ± 1.0	2.14 ± 0.35	
$t\bar{t}$ (+EW) + single top	1.5 ± 0.6	5.8 ± 1.8	16 ± 5	1.4 ± 0.7	2.0 ± 1.1	
Multi-jet	0.09 ± 0.09	0.4 ± 0.4	2.1 ± 2.1	—	0.18 ± 0.18	
Total Expected MC	16	67	124	12	8.3	
Total Fitted bkg	14.5 ± 2.2	59 ± 6	110 ± 11	10.5 ± 1.5	7.3 ± 1.4	
Observed	14	69	115	5	8	
$\langle\epsilon\sigma\rangle_{\text{obs}}^{95}$ [fb]	0.76	2.2	2.5	0.35	0.61	
S_{obs}^{95}	10	29	34	4.7	8.1	
S_{exp}^{95}	11^{+5}_{-3}	21^{+9}_{-6}	30^{+12}_{-8}	$8.1^{+3.0}_{-2.3}$	$7.4^{+2.9}_{-1.8}$	
p_0 (Z)	0.50 (0.00)	0.18 (0.92)	0.37 (0.32)	0.50 (0.00)	0.39 (0.30)	

Table 9.2: Numbers of events observed in the signal regions used in the RJR-based analysis compared with background expectations obtained from the fits described in the text. Empty cells (indicated by a ‘-’) correspond to estimates lower than 0.01. The p-values (p_0) give the probabilities of the observations being consistent with the estimated backgrounds. For an observed number of events lower than expected, the p-value is truncated at 0.5. Between parentheses, p -values are also given as the number of equivalent Gaussian standard deviations (Z). Also shown are 95% CL upper limits on the visible cross-section ($\langle\epsilon\sigma\rangle_{\text{obs}}^{95}$), the visible number of signal events (S_{obs}^{95}) and the number of signal events (S_{exp}^{95}) given the expected number of background events (and $\pm 1\sigma$ excursions of the expectation).

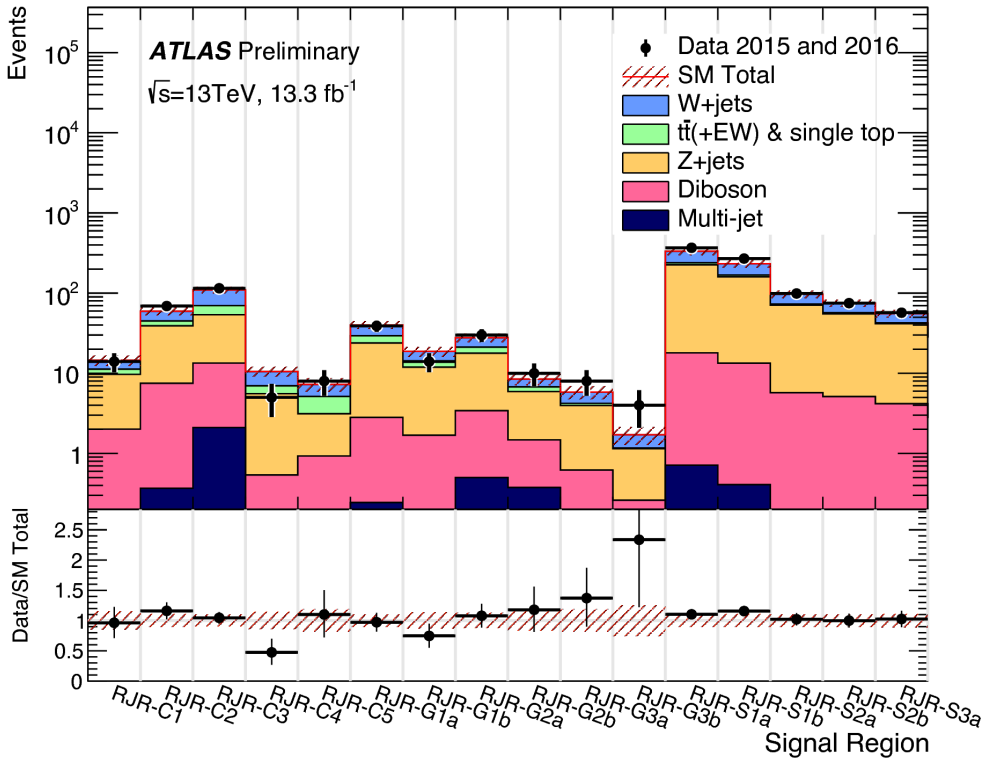


Figure 9.4: Summary of the signal region pulls

2209 Feynman diagrams shown previously. The free parameters of these simplified models
 2210 are the relevant sparticle mass and the mass of the LSP $\tilde{\chi}_1^0$. We set limits in a plane
 2211 of these free parameters.

2212 The exclusion limits are shown in Fig. 9.5. Gray text is imposed on the plane at the
 2213 point of each simplified model with masses $(m_{\text{sparticle}}, m_{\tilde{\chi}_1^0})$. This gray text indicates
 2214 the signal region which provided the best sensitivity at that point, as measured by the
 2215 background-only fit. For each simplified signal model, we run the model-dependent fit
 2216 described in the last chapter, where the signal model signal strength μ_{sig} is included
 2217 as an additional free parameter. The signal sample is also allowed to freely contribute
 2218 to the control regions due to signal contamination. This produces a CL_s p -value for
 2219 each signal model in the plane, and we can find those with $p = 0.05$ to set a 95%
 2220 exclusion limit.

2221 In the squark- $\tilde{\chi}_1^0$ plane, we observe that the limits from the 2015 dataset are far
2222 extended in all directions. The expected and observed exclusions are similar, which
2223 is a reflection of the compatibility of the expected Standard Model event counts and
2224 observed event counts in the squark regions. A squark with mass of 1350 GeV or less
2225 is excluded by the analysis in direct decays to a quark and LSP. In the compressed
2226 spectra, we have extended limits significantly over the 2015 result in the region of 600-
2227 700 GeV in squark mass with an LSP of 450 GeV to 600 GeV. We note that directly
2228 along the kinematically-forbidden diagonal, the shape of the exclusions is affected
2229 by the interpolation between the signal models considered. This could be rectified
2230 by inclusion of additional compressed signal models. The limits in the intermediate
2231 with an LSP of \sim 450-500 GeV are not far extended beyond the previous dataset. We
2232 also note that every signal region designed to provide sensitivity to this simplified
2233 model (all SRS regions and SRC1-4) is chosen as the best region at least once in
2234 the plane, indicating that each signal region provided additional sensitivity to squark
2235 phenomena.

2236 Another curiosity is the fact that a gluino region, SRG2a is chosen as the optimal
2237 region in the squark- $\tilde{\chi}_1^0$ plane, when the squark mass is \sim 700 GeV. Generally, the
2238 squark regions are looser than the gluino regions, as seen in their overall event counts.
2239 One could see this as an indication that the next iteration of the analysis should have
2240 an additional tight squark region here. Another possibility is that this region also
2241 benefits from the compressed region strategy of using an ISR jet. As the gluino
2242 regions require four jets from the imposition of the gluino decay tree, these could be
2243 capturing events where a two jet ISR system recoils off the disquark system.

2244 In the gluino- $\tilde{\chi}_1^0$ plane, the limits on gluino masses in the simplified model where
2245 gluinos decay to two jets and an $\tilde{\chi}_1^0$ are again far extended beyond the 2015 dataset.
2246 We note in most of the plane, the expected limit is significantly stronger than the
2247 observed limit; for example, the gluino mass limit is more than 50 GeV stronger in

2248 the case of a massless $\tilde{\chi}_1^0$. As much of the phase space is covered by SRG3a and
2249 SRG3b, this results from the small statistical fluctuation upward in these regions.
2250 Again, we note that every gluino signal region is the best choice at some point in this
2251 plane. This is an indication of the utility of the signal region strategy employed in
2252 this thesis, as each point provides additional sensitivity to new SUSY models.

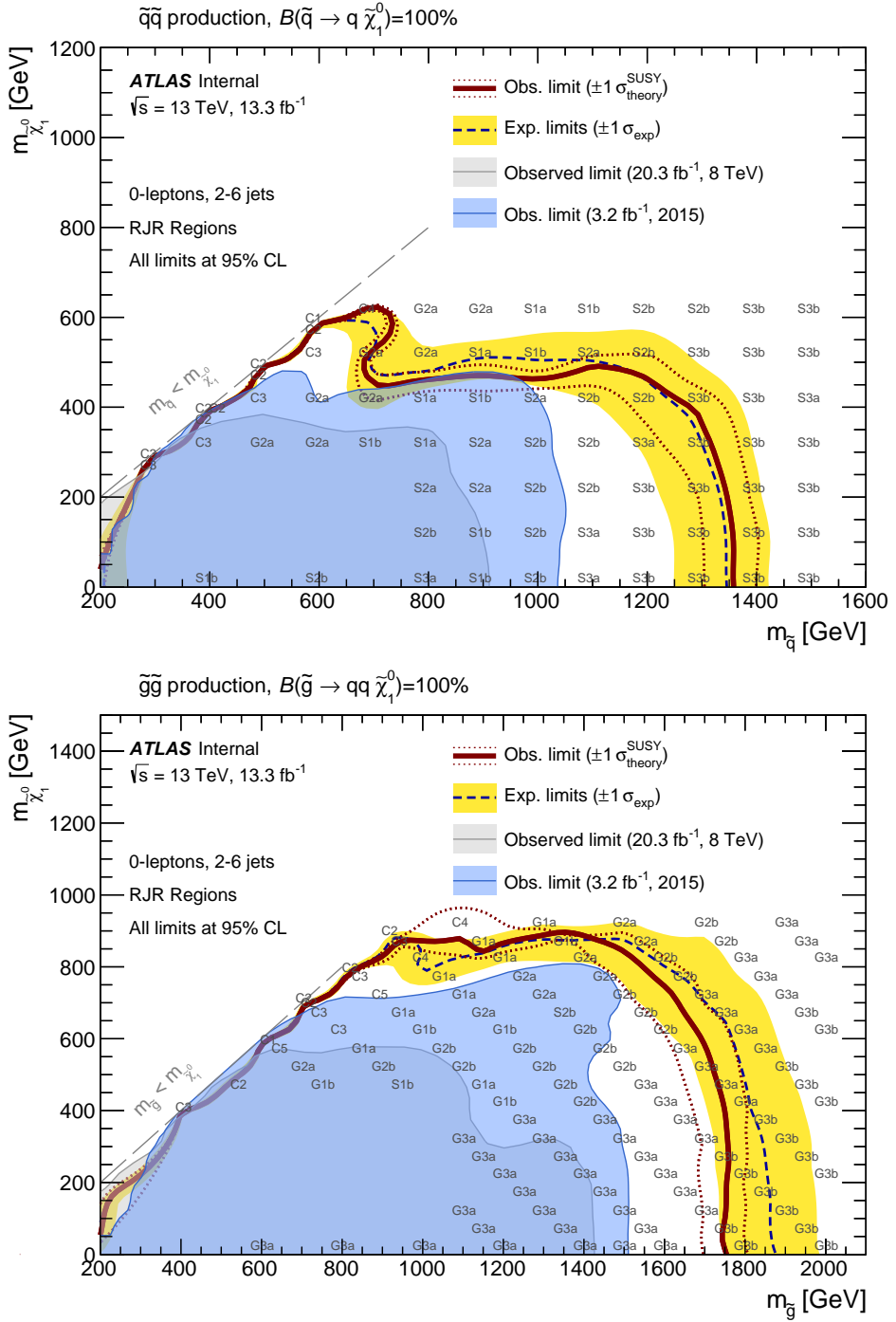


Figure 9.5: Exclusion limits for direct production of (a) light-flavour squark pairs with decoupled gluinos and (b) gluino pairs with decoupled squarks. Exclusion limits are obtained by using the signal region with the best expected sensitivity at each point. The blue dashed lines show the expected limits at 95% CL, with the yellow bands indicating the 1σ excursions due to experimental and background-only theoretical uncertainties. Observed limits are indicated by maroon curves where the solid contour represents the nominal limit, and the dotted lines are obtained by varying the signal cross-section by the renormalization and factorization scale and PDF uncertainties. Results are compared with the observed limits obtained by the previous ATLAS searches with no leptons, jets and missing transverse momentum [135, 144].

2253

Conclusion

2254 Here you can write some introductory remarks about your chapter. I like to give each
2255 sentence its own line.
2256 When you need a new paragraph, just skip an extra line.

2257 **9.4 New Section**

2258 By using the asterisk to start a new section, I keep the section from appearing in the
2259 table of contents. If you want your sections to be numbered and to appear in the
2260 table of contents, remove the asterisk.

2261

Bibliography

- 2262 [1] O. Perdereau, *Planck 2015 cosmological results*,
2263 AIP Conf. Proc. **1743** (2016) p. 050014.
- 2264 [2] N. Aghanim et al.,
2265 *Planck 2016 intermediate results. LI. Features in the cosmic microwave*
2266 *background temperature power spectrum and shifts in cosmological parameters*
2267 (2016), arXiv: [1608.02487 \[astro-ph.CO\]](https://arxiv.org/abs/1608.02487).
- 2268 [3] J. S. Schwinger,
2269 *On Quantum electrodynamics and the magnetic moment of the electron*,
2270 Phys. Rev. **73** (1948) p. 416.
- 2271 [4] S. Laporta and E. Remiddi,
2272 *The Analytical value of the electron (g-2) at order alpha**3 in QED*,
2273 Phys. Lett. **B379** (1996) p. 283, arXiv: [hep-ph/9602417 \[hep-ph\]](https://arxiv.org/abs/hep-ph/9602417).
- 2274 [5] S. Schael et al., *Precision electroweak measurements on the Z resonance*,
2275 Phys. Rept. **427** (2006) p. 257, arXiv: [hep-ex/0509008 \[hep-ex\]](https://arxiv.org/abs/hep-ex/0509008).
- 2276 [6] S. L. Glashow, *Partial Symmetries of Weak Interactions*,
2277 Nucl. Phys. **22** (1961) p. 579.
- 2278 [7] S. Weinberg, *A Model of Leptons*, Phys. Rev. Lett. **19** (1967) p. 1264.
- 2279 [8] A. Salam, *Weak and Electromagnetic Interactions*,
2280 Conf. Proc. **C680519** (1968) p. 367.
- 2281 [9] M. Gell-Mann, *A Schematic Model of Baryons and Mesons*,
2282 Phys. Lett. **8** (1964) p. 214.
- 2283 [10] G. Zweig, “An SU(3) model for strong interaction symmetry and its
2284 breaking. Version 2,” *DEVELOPMENTS IN THE QUARK THEORY OF*
2285 *HADRONS. VOL. 1. 1964 - 1978*, ed. by D. Lichtenberg and S. P. Rosen,
2286 1964 p. 22,
2287 URL: <http://inspirehep.net/record/4674/files/cern-th-412.pdf>.

- 2288 [11] S. Weinberg, *Implications of Dynamical Symmetry Breaking*,
2289 Phys. Rev. **D13** (1976) p. 974.
- 2290 [12] S. Weinberg, *Implications of Dynamical Symmetry Breaking: An Addendum*,
2291 Phys. Rev. **D19** (1979) p. 1277.
- 2292 [13] E. Gildener, *Gauge Symmetry Hierarchies*, Phys. Rev. **D14** (1976) p. 1667.
- 2293 [14] L. Susskind, *Dynamics of Spontaneous Symmetry Breaking in the*
2294 *Weinberg-Salam Theory*, Phys. Rev. **D20** (1979) p. 2619.
- 2295 [15] S. P. Martin, “A Supersymmetry Primer,” 1997,
2296 eprint: [arXiv:hep-ph/9709356](https://arxiv.org/abs/hep-ph/9709356).
- 2297 [16] V. C. Rubin and W. K. Ford Jr., *Rotation of the Andromeda Nebula from a*
2298 *Spectroscopic Survey of Emission Regions*, Astrophys. J. **159** (1970) p. 379.
- 2299 [17] M. S. Roberts and R. N. Whitehurst,
2300 “*The rotation curve and geometry of M31 at large galactocentric distances*,
2301 Astrophys. J. **201** (1970) p. 327.
- 2302 [18] V. C. Rubin, N. Thonnard, and W. K. Ford Jr.,
2303 *Rotational properties of 21 SC galaxies with a large range of luminosities and*
2304 *radii, from NGC 4605 /R = 4kpc/ to UGC 2885 /R = 122 kpc/*,
2305 Astrophys. J. **238** (1980) p. 471.
- 2306 [19] V. C. Rubin et al., *Rotation velocities of 16 SA galaxies and a comparison of*
2307 *Sa, Sb, and SC rotation properties*, Astrophys. J. **289** (1985) p. 81.
- 2308 [20] A. Bosma,
2309 *21-cm line studies of spiral galaxies. 2. The distribution and kinematics of*
2310 *neutral hydrogen in spiral galaxies of various morphological types.*,
2311 Astron. J. **86** (1981) p. 1825.
- 2312 [21] M. Persic, P. Salucci, and F. Stel, *The Universal rotation curve of spiral*
2313 *galaxies: 1. The Dark matter connection*,
2314 Mon. Not. Roy. Astron. Soc. **281** (1996) p. 27,
2315 arXiv: [astro-ph/9506004](https://arxiv.org/abs/astro-ph/9506004) [astro-ph].
- 2316 [22] M. Lisanti, “Lectures on Dark Matter Physics,” 2016,
2317 eprint: [arXiv:1603.03797](https://arxiv.org/abs/1603.03797).
- 2318 [23] H. Miyazawa, *Baryon Number Changing Currents*,
2319 Prog. Theor. Phys. **36** (1966) p. 1266.

- 2320 [24] J.-L. Gervais and B. Sakita, *Generalizations of dual models*,
 2321 *Nucl. Phys.* **B34** (1971) p. 477.
- 2322 [25] J. Gervais and B. Sakita,
 2323 *Field theory interpretation of supergauges in dual models*,
 2324 *Nucl. Phys. B* **34** (1971) p. 632.
- 2325 [26] Y. A. Golfand and E. P. Likhtman, *Extension of the Algebra of Poincare
 2326 Group Generators and Violation of p Invariance*,
 2327 *JETP Lett.* **13** (1971) p. 323, [*Pisma Zh.Eksp.Teor.Fiz.*13:452-455,1971].
- 2328 [27] A. Neveu and J. H. Schwarz, *Factorizable dual model of pions*,
 2329 *Nucl. Phys. B* **31** (1971) p. 86.
- 2330 [28] A. Neveu and J. H. Schwarz, *Quark Model of Dual Pions*,
 2331 *Phys. Rev. D* **4** (1971) p. 1109.
- 2332 [29] D. V. Volkov and V. P. Akulov, *Is the Neutrino a Goldstone Particle?*
 2333 *Phys. Lett. B* **46** (1973) p. 109.
- 2334 [30] J. Wess and B. Zumino,
 2335 *A Lagrangian Model Invariant Under Supergauge Transformations*,
 2336 *Phys. Lett. B* **49** (1974) p. 52.
- 2337 [31] A. Salam and J. A. Strathdee, *Supersymmetry and Nonabelian Gauges*,
 2338 *Phys. Lett. B* **51** (1974) p. 353.
- 2339 [32] S. Ferrara, J. Wess, and B. Zumino, *Supergauge Multiplets and Superfields*,
 2340 *Phys. Lett. B* **51** (1974) p. 239.
- 2341 [33] J. Wess and B. Zumino, *Supergauge Transformations in Four-Dimensions*,
 2342 *Nucl. Phys. B* **70** (1974) p. 39.
- 2343 [34] J. D. Lykken, “Introduction to supersymmetry,” *Fields, strings and duality. Proceedings, Summer School, Theoretical Advanced Study Institute in Elementary Particle Physics, TASI’96, Boulder, USA, June 2-28, 1996*, 1996
 2344 p. 85, arXiv: [hep-th/9612114](https://arxiv.org/abs/hep-th/9612114) [hep-th],
 2345 URL: http://lss.fnal.gov/cgi-bin/find_paper.pl?pub=96-445-T.
- 2346 [35] A. Kobakhidze, “Intro to SUSY,” 2016, URL: <https://indico.cern.ch/event/443176/page/5225-pre-susy-programme>.
- 2347 [36] G. R. Farrar and P. Fayet, *Phenomenology of the Production, Decay, and Detection of New Hadronic States Associated with Supersymmetry*,
 2348 *Phys. Lett. B* **76** (1978) p. 575.

- 2353 [37] ATLAS Collaboration,
 2354 *Search for the electroweak production of supersymmetric particles in*
 2355 $\sqrt{s} = 8 \text{ TeV}$ *pp collisions with the ATLAS detector,*
 2356 *Phys. Rev. D* **93** (2016) p. 052002, arXiv: [1509.07152 \[hep-ex\]](#).
- 2357 [38] ATLAS Collaboration, *Summary of the searches for squarks and gluinos*
 2358 *using $\sqrt{s} = 8 \text{ TeV}$ pp collisions with the ATLAS experiment at the LHC,*
 2359 *JHEP* **10** (2015) p. 054, arXiv: [1507.05525 \[hep-ex\]](#).
- 2360 [39] ATLAS Collaboration, *ATLAS Run 1 searches for direct pair production of*
 2361 *third-generation squarks at the Large Hadron Collider,*
 2362 *Eur. Phys. J. C* **75** (2015) p. 510, arXiv: [1506.08616 \[hep-ex\]](#).
- 2363 [40] CMS Collaboration, *Search for supersymmetry with razor variables in pp*
 2364 *collisions at $\sqrt{s} = 7 \text{ TeV}$, Phys. Rev. D* **90** (2014) p. 112001,
 2365 arXiv: [1405.3961 \[hep-ex\]](#).
- 2366 [41] CMS Collaboration, *Inclusive search for supersymmetry using razor variables*
 2367 *in pp collisions at $\sqrt{s} = 7 \text{ TeV}$, Phys. Rev. Lett.* **111** (2013) p. 081802,
 2368 arXiv: [1212.6961 \[hep-ex\]](#).
- 2369 [42] CMS Collaboration, *Search for Supersymmetry in pp Collisions at 7 TeV in*
 2370 *Events with Jets and Missing Transverse Energy,*
 2371 *Phys. Lett. B* **698** (2011) p. 196, arXiv: [1101.1628 \[hep-ex\]](#).
- 2372 [43] CMS Collaboration, *Search for Supersymmetry at the LHC in Events with*
 2373 *Jets and Missing Transverse Energy, Phys. Rev. Lett.* **107** (2011) p. 221804,
 2374 arXiv: [1109.2352 \[hep-ex\]](#).
- 2375 [44] CMS Collaboration, *Search for supersymmetry in hadronic final states using*
 2376 *M_{T2} in pp collisions at $\sqrt{s} = 7 \text{ TeV}$, JHEP* **10** (2012) p. 018,
 2377 arXiv: [1207.1798 \[hep-ex\]](#).
- 2378 [45] CMS Collaboration, *Searches for supersymmetry using the M_{T2} variable in*
 2379 *hadronic events produced in pp collisions at 8 TeV, JHEP* **05** (2015) p. 078,
 2380 arXiv: [1502.04358 \[hep-ex\]](#).
- 2381 [46] CMS Collaboration, *Search for new physics with the M_{T2} variable in all-jets*
 2382 *final states produced in pp collisions at $\sqrt{s} = 13 \text{ TeV}$, JHEP* (2016),
 2383 arXiv: [1603.04053 \[hep-ex\]](#).
- 2384 [47] ATLAS Collaboration, *Multi-channel search for squarks and gluinos in*
 2385 $\sqrt{s} = 7 \text{ TeV}$ *pp collisions with the ATLAS detector at the LHC,*
 2386 *Eur. Phys. J. C* **73** (2013) p. 2362, arXiv: [1212.6149 \[hep-ex\]](#).

- 2387 [48] Y. Grossman, “Introduction to the SM,” 2016, URL: <https://indico.fnal.gov/sessionDisplay.py?sessionId=3&confId=11505#20160811>.
- 2388
- 2389 [49] W Buchmuller and C Ludeling, *Field Theory and Standard Model* (Sept. 2006) p. 70, URL: <https://cds.cern.ch/record/984122>.
- 2390
- 2391 [50] P. W. Higgs, *Broken Symmetries and the Masses of Gauge Bosons*,
2392 Phys. Rev. Lett. **13** (1964) p. 508.
- 2393 [51] ATLAS Collaboration, *Observation of a new particle in the search for the*
2394 *Standard Model Higgs boson with the ATLAS detector at the LHC*,
2395 Phys. Lett. B **716** (2012) p. 1, arXiv: [1207.7214 \[hep-ex\]](https://arxiv.org/abs/1207.7214).
- 2396 [52] CMS Collaboration, *Observation of a new boson at a mass of 125 GeV with*
2397 *the CMS experiment at the LHC*, Phys. Lett. B **716** (2012) p. 30,
2398 arXiv: [1207.7235 \[hep-ex\]](https://arxiv.org/abs/1207.7235).
- 2399 [53] A. Chodos et al., *A New Extended Model of Hadrons*,
2400 Phys. Rev. **D9** (1974) p. 3471.
- 2401 [54] A. Chodos et al., *Baryon Structure in the Bag Theory*,
2402 Phys. Rev. **D10** (1974) p. 2599.
- 2403 [55] J. C. Collins, D. E. Soper, and G. F. Sterman,
2404 *Factorization of Hard Processes in QCD*,
2405 *Adv. Ser. Direct. High Energy Phys.* **5** (1989) p. 1,
2406 arXiv: [hep-ph/0409313 \[hep-ph\]](https://arxiv.org/abs/hep-ph/0409313).
- 2407 [56] K. A. Olive et al., *Review of Particle Physics*,
2408 Chin. Phys. **C38** (2014) p. 090001.
- 2409 [57] N. Cabibbo, *Unitary Symmetry and Leptonic Decays*,
2410 Phys. Rev. Lett. **10** (1963) p. 531, [[648\(1963\)](#)].
- 2411 [58] M. Kobayashi and T. Maskawa,
2412 *CP Violation in the Renormalizable Theory of Weak Interaction*,
2413 Prog. Theor. Phys. **49** (1973) p. 652.
- 2414 [59] W. F. L. Hollik, *Radiative Corrections in the Standard Model and their Role*
2415 *for Precision Tests of the Electroweak Theory*,
2416 Fortsch. Phys. **38** (1990) p. 165.
- 2417 [60] D. Yu. Bardin et al.,
2418 *ELECTROWEAK RADIATIVE CORRECTIONS TO DEEP INELASTIC*

- 2419 *SCATTERING AT HERA! CHARGED CURRENT SCATTERING,*
 2420 *Z. Phys. C***44** (1989) p. 149.
- 2421 [61] D. C. Kennedy et al.,
 2422 *Electroweak Cross-Sections and Asymmetries at the Z0,*
 2423 *Nucl. Phys. B***321** (1989) p. 83.
- 2424 [62] A. Sirlin, *Radiative Corrections in the SU(2)-L x U(1) Theory: A Simple*
 2425 *Renormalization Framework*, *Phys. Rev. D***22** (1980) p. 971.
- 2426 [63] S. Fanchiotti, B. A. Kniehl, and A. Sirlin,
 2427 *Incorporation of QCD effects in basic corrections of the electroweak theory*,
 2428 *Phys. Rev. D***48** (1993) p. 307, arXiv: [hep-ph/9212285 \[hep-ph\]](#).
- 2429 [64] C. Quigg, “Cosmic Neutrinos,” *Proceedings, 35th SLAC Summer Institute on*
 2430 *Particle Physics: Dark matter: From the cosmos to the Laboratory (SSI*
 2431 *2007): Menlo Park, California, July 30- August 10, 2007*, 2008,
 2432 arXiv: [0802.0013 \[hep-ph\]](#),
 2433 URL: http://lss.fnal.gov/cgi-bin/find_paper.pl?conf-07-417.
- 2434 [65] S. R. Coleman and J. Mandula, *All Possible Symmetries of the S Matrix*,
 2435 *Phys. Rev. 159* (1967) p. 1251.
- 2436 [66] R. Haag, J. T. Lopuszanski, and M. Sohnius,
 2437 *All Possible Generators of Supersymmetries of the s Matrix*,
 2438 *Nucl. Phys. B***88** (1975) p. 257.
- 2439 [67] A. Salam and J. A. Strathdee, *On Superfields and Fermi-Bose Symmetry*,
 2440 *Phys. Rev. D***11** (1975) p. 1521.
- 2441 [68] S. Dimopoulos and H. Georgi, *Softly Broken Supersymmetry and SU(5)*,
 2442 *Nucl. Phys. B***193** (1981) p. 150.
- 2443 [69] S. Dimopoulos, S. Raby, and F. Wilczek,
 2444 *Supersymmetry and the Scale of Unification*, *Phys. Rev. D***24** (1981) p. 1681.
- 2445 [70] L. E. Ibanez and G. G. Ross,
 2446 *Low-Energy Predictions in Supersymmetric Grand Unified Theories*,
 2447 *Phys. Lett. B***105** (1981) p. 439.
- 2448 [71] W. J. Marciano and G. Senjanovic,
 2449 *Predictions of Supersymmetric Grand Unified Theories*,
 2450 *Phys. Rev. D***25** (1982) p. 3092.

- 2451 [72] L. Girardello and M. T. Grisaru, *Soft Breaking of Supersymmetry*,
 2452 *Nucl. Phys.* **B194** (1982) p. 65.
- 2453 [73] D. J. H. Chung et al.,
 2454 *The Soft supersymmetry breaking Lagrangian: Theory and applications*,
 2455 *Phys. Rept.* **407** (2005) p. 1, arXiv: [hep-ph/0312378 \[hep-ph\]](#).
- 2456 [74] J. Hisano et al., *Lepton flavor violation in the supersymmetric standard*
 2457 *model with seesaw induced neutrino masses*, *Phys. Lett.* **B357** (1995) p. 579,
 2458 arXiv: [hep-ph/9501407 \[hep-ph\]](#).
- 2459 [75] F. Gabbiani et al., *A Complete analysis of FCNC and CP constraints in*
 2460 *general SUSY extensions of the standard model*,
 2461 *Nucl. Phys.* **B477** (1996) p. 321, arXiv: [hep-ph/9604387 \[hep-ph\]](#).
- 2462 [76] F. Gabbiani and A. Masiero,
 2463 *FCNC in Generalized Supersymmetric Theories*,
 2464 *Nucl. Phys.* **B322** (1989) p. 235.
- 2465 [77] J. S. Hagelin, S. Kelley, and T. Tanaka, *Supersymmetric flavor changing*
 2466 *neutral currents: Exact amplitudes and phenomenological analysis*,
 2467 *Nucl. Phys.* **B415** (1994) p. 293.
- 2468 [78] J. S. Hagelin, S. Kelley, and V. Ziegler, *Using gauge coupling unification and*
 2469 *proton decay to test minimal supersymmetric SU(5)*,
 2470 *Phys. Lett.* **B342** (1995) p. 145, arXiv: [hep-ph/9406366 \[hep-ph\]](#).
- 2471 [79] D. Choudhury et al.,
 2472 *Constraints on nonuniversal soft terms from flavor changing neutral currents*,
 2473 *Phys. Lett.* **B342** (1995) p. 180, arXiv: [hep-ph/9408275 \[hep-ph\]](#).
- 2474 [80] R. Barbieri and L. J. Hall, *Signals for supersymmetric unification*,
 2475 *Phys. Lett.* **B338** (1994) p. 212, arXiv: [hep-ph/9408406 \[hep-ph\]](#).
- 2476 [81] B. de Carlos, J. A. Casas, and J. M. Moreno,
 2477 *Constraints on supersymmetric theories from mu —> e gamma*,
 2478 *Phys. Rev.* **D53** (1996) p. 6398, arXiv: [hep-ph/9507377 \[hep-ph\]](#).
- 2479 [82] J. A. Casas and S. Dimopoulos,
 2480 *Stability bounds on flavor violating trilinear soft terms in the MSSM*,
 2481 *Phys. Lett.* **B387** (1996) p. 107, arXiv: [hep-ph/9606237 \[hep-ph\]](#).
- 2482 [83] C. Borschensky et al., *Squark and gluino production cross sections in pp*
 2483 *collisions at $\sqrt{s} = 13, 14, 33$ and 100 TeV*,
 2484 *Eur. Phys. J.* **C74** (2014) p. 3174, arXiv: [1407.5066 \[hep-ph\]](#).

- 2485 [84] M. Klasen, M. Pohl, and G. Sigl, *Indirect and direct search for dark matter*,
2486 Prog. Part. Nucl. Phys. **85** (2015) p. 1, arXiv: [1507.03800](https://arxiv.org/abs/1507.03800) [hep-ph].
- 2487 [85] L. Evans and P. Bryant, *LHC Machine*, JINST **3** (2008) S08001.
- 2488 [86] Vladimir Shiltsev, “Accelerator Physics and Technology,” Aug. 2016,
2489 URL: [https://indico.fnal.gov/sessionDisplay.py?sessionId=3&](https://indico.fnal.gov/sessionDisplay.py?sessionId=3&confId=11505#20160811)
2490 [confId=11505#20160811](https://indico.fnal.gov/sessionDisplay.py?sessionId=3&confId=11505#20160811).
- 2491 [87] *LEP design report*, Copies shelved as reports in LEP, PS and SPS libraries,
2492 Geneva: CERN, 1984, URL: <https://cds.cern.ch/record/102083>.
- 2493 [88] ATLAS Collaboration,
2494 *The ATLAS Experiment at the CERN Large Hadron Collider*,
2495 JINST **3** (2008) S08003.
- 2496 [89] G. Aad et al., *ATLAS pixel detector electronics and sensors*,
2497 JINST **3** (2008) P07007.
- 2498 [90] ATLAS Collaboration, *ATLAS Insertable B-Layer Technical Design Report*,
2499 ATLAS-TDR-19 (2010), URL: <http://cdsweb.cern.ch/record/1291633>.
- 2500 [91] ATLAS Collaboration,
2501 *Operation and performance of the ATLAS semiconductor tracker*,
2502 JINST **9** (2014) P08009, arXiv: [1404.7473](https://arxiv.org/abs/1404.7473) [hep-ex].
- 2503 [92] ATLAS Collaboration, *2015 start-up trigger menu and initial performance*
2504 *assessment of the ATLAS trigger using Run-2 data*,
2505 ATL-DAQ-PUB-2016-001 (2016),
2506 URL: <https://cds.cern.ch/record/2104298>.
- 2507 [93] ATLAS Collaboration, *Performance of the ATLAS Inner Detector Track and*
2508 *Vertex Reconstruction in High Pile-Up LHC Environment*,
2509 ATLAS-CONF-2012-042, 2012,
2510 URL: <https://cds.cern.ch/record/1435196>.
- 2511 [94] ATLAS Collaboration, *Early Inner Detector Tracking Performance in the*
2512 *2015 Data at $\sqrt{s} = 13$ TeV*, ATL-PHYS-PUB-2015-051, 2015,
2513 URL: <https://cds.cern.ch/record/2110140>.
- 2514 [95] K Hamano, A Morley, and A Salzburger,
2515 “Track Reconstruction Performance and Efficiency Estimation using different
2516 ID geometry samples,” tech. rep. ATL-COM-PHYS-2012-1541,
2517 plots for a poster at HCP: CERN, Oct. 2012,
2518 URL: <https://cds.cern.ch/record/1489674>.

- 2519 [96] ATLAS Collaboration,
 2520 *Electron reconstruction and identification efficiency measurements with the*
 2521 *ATLAS detector using the 2011 LHC proton–proton collision data,*
 2522 *Eur. Phys. J. C* **74** (2014) p. 2941, arXiv: [1404.2240 \[hep-ex\]](#).
- 2523 [97] ATLAS Collaboration, *Topological cell clustering in the ATLAS calorimeters*
 2524 *and its performance in LHC Run 1* (2016), arXiv: [1603.02934 \[hep-ex\]](#).
- 2525 [98] ATLAS Collaboration, *Jet energy resolution in proton–proton collisions at*
 2526 $\sqrt{s} = 7 \text{ TeV}$ *recorded in 2010 with the ATLAS detector,*
 2527 *Eur. Phys. J. C* **73** (2013) p. 2306, arXiv: [1210.6210 \[hep-ex\]](#).
- 2528 [99] ATLAS Collaboration, *Electron performance measurements with the ATLAS*
 2529 *detector using the 2010 LHC proton–proton collision data,*
 2530 *Eur. Phys. J. C* **72** (2012) p. 1909, arXiv: [1110.3174 \[hep-ex\]](#).
- 2531 [100] M. Aaboud et al., *Measurement of the photon identification efficiencies with*
 2532 *the ATLAS detector using LHC Run-1 data* (2016),
 2533 arXiv: [1606.01813 \[hep-ex\]](#).
- 2534 [101] ATLAS Collaboration, *Electron and photon energy calibration with the*
 2535 *ATLAS detector using LHC Run 1 data*, *Eur. Phys. J. C* **74** (2014) p. 3071,
 2536 arXiv: [1407.5063 \[hep-ex\]](#).
- 2537 [102] “Electron and photon energy calibration with the ATLAS detector using
 2538 data collected in 2015 at $\sqrt{s} = 13 \text{ TeV}$,”
 2539 tech. rep. ATL-PHYS-PUB-2016-015, CERN, Aug. 2016,
 2540 URL: <https://cds.cern.ch/record/2203514>.
- 2541 [103] ATLAS Collaboration, *Muon reconstruction performance of the ATLAS*
 2542 *detector in proton–proton collision data at $\sqrt{s} = 13 \text{ TeV}$,*
 2543 *Eur. Phys. J. C* **76** (2016) p. 292, arXiv: [1603.05598 \[hep-ex\]](#).
- 2544 [104] ATLAS Collaboration, *Jet energy measurement with the ATLAS detector in*
 2545 *proton–proton collisions at $\sqrt{s} = 7 \text{ TeV}$* , *Eur. Phys. J. C* **73** (2013) p. 2304,
 2546 arXiv: [1112.6426 \[hep-ex\]](#).
- 2547 [105] ATLAS Collaboration,
 2548 *Jet energy measurement and its systematic uncertainty in proton–proton*
 2549 *collisions at $\sqrt{s} = 7 \text{ TeV}$ with the ATLAS detector,*
 2550 *Eur. Phys. J. C* **75** (2015) p. 17, arXiv: [1406.0076 \[hep-ex\]](#).
- 2551 [106] S. D. Ellis and D. E. Soper,
 2552 *Successive combination jet algorithm for hadron collisions,*
 2553 *Phys. Rev. D* **48** (1993) p. 3160, arXiv: [hep-ph/9305266 \[hep-ph\]](#).

- 2554 [107] M. Cacciari and G. P. Salam, *Dispelling the N^3 myth for the k_t jet-finder*,
2555 Phys. Lett. B **641** (2006) p. 57, arXiv: [hep-ph/0512210](#).
- 2556 [108] M. Cacciari, G. P. Salam, and G. Soyez, *The anti- k_t jet clustering algorithm*,
2557 JHEP **04** (2008) p. 063, arXiv: [0802.1189 \[hep-ph\]](#).
- 2558 [109] *Particle-Flow Event Reconstruction in CMS and Performance for Jets, Taus,
2559 and MET* (2009).
- 2560 [110] ATLAS Collaboration,
2561 *Tagging and suppression of pileup jets with the ATLAS detector*,
2562 ATLAS-CONF-2014-018, 2014,
2563 URL: <https://cds.cern.ch/record/1700870>.
- 2564 [111] M. Cacciari, G. P. Salam, and G. Soyez, *The Catchment Area of Jets*,
2565 JHEP **04** (2008) p. 005, arXiv: [0802.1188 \[hep-ph\]](#).
- 2566 [112] G. Aad et al., *Performance of b-Jet Identification in the ATLAS Experiment*,
2567 JINST **11** (2016) P04008, arXiv: [1512.01094 \[hep-ex\]](#).
- 2568 [113] ATLAS Collaboration,
2569 *Optimisation of the ATLAS b-tagging performance for the 2016 LHC Run*,
2570 ATL-PHYS-PUB-2016-012 (2016),
2571 URL: <https://cds.cern.ch/record/2160731>.
- 2572 [114] G. Aad et al., *Performance of algorithms that reconstruct missing transverse
2573 momentum in $\sqrt{s} = 8$ TeV proton-proton collisions in the ATLAS detector*
2574 (2016), arXiv: [1609.09324 \[hep-ex\]](#).
- 2575 [115] ATLAS Collaboration,
2576 *Prospects for Supersymmetry discovery based on inclusive searches at a*
2577 *7 TeV centre-of-mass energy with the ATLAS detector*,
2578 ATL-PHYS-PUB-2010-010, 2010,
2579 URL: <https://cds.cern.ch/record/1278474>.
- 2580 [116] ATLAS Collaboration,
2581 *Expected sensitivity studies for gluino and squark searches using the early*
2582 *LHC 13 TeV Run-2 dataset with the ATLAS experiment*,
2583 ATL-PHYS-PUB-2015-005, 2015, URL:
2584 <https://atlas.web.cern.ch/Atlas/GROUPS/PHYSICS/PUBNOTES/ATL-PHYS-PUB-2015-005>.
- 2586 [117] ATLAS Collaboration, *Expected performance of missing transverse
2587 momentum reconstruction for the ATLAS detector at $\sqrt{s} = 13$ TeV*,

- 2588 ATL-PHYS-PUB-2015-023, 2015,
 2589 URL: <https://cds.cern.ch/record/2037700>.
- 2590 [118] ATLAS Collaboration,
 2591 *Performance of missing transverse momentum reconstruction with the*
 2592 *ATLAS detector in the first proton–proton collisions at $\sqrt{s} = 13$ TeV,*
 2593 ATL-PHYS-PUB-2015-027, 2015,
 2594 URL: <https://cds.cern.ch/record/2037904>.
- 2595 [119] P. Jackson, C. Rogan and M. Santoni, *Sparticles in Motion - getting to the*
 2596 *line in compressed scenarios with the Recursive Jigsaw Reconstruction*
 2597 (2016), arXiv: [1607.08307 \[hep-ph\]](https://arxiv.org/abs/1607.08307).
- 2598 [120] ATLAS Collaboration,
 2599 *Further searches for squarks and gluinos in final states with jets and missing*
 2600 *transverse momentum at $\sqrt{s} = 13$ TeV with the ATLAS detector,*
 2601 ATLAS-CONF-2016-078, 2016,
 2602 URL: <https://cds.cern.ch/record/2206252>.
- 2603 [121] C. Rogan, *Kinematical variables towards new dynamics at the LHC* (2010),
 2604 arXiv: [1006.2727 \[hep-ph\]](https://arxiv.org/abs/1006.2727).
- 2605 [122] M. R. Buckley et al.,
 2606 *Super-Razor and Searches for Sleptons and Charginos at the LHC*,
 2607 Phys. Rev. **D89** (2014) p. 055020, arXiv: [1310.4827 \[hep-ph\]](https://arxiv.org/abs/1310.4827).
- 2608 [123] CMS Collaboration, *Search for supersymmetry using razor variables in*
 2609 *events with b-tagged jets in pp collisions at $\sqrt{s} = 8$ TeV,*
 2610 Phys. Rev. D **91** (2015) p. 052018, arXiv: [1502.00300 \[hep-ex\]](https://arxiv.org/abs/1502.00300).
- 2611 [124] Chris Rogan, “RestFrames,” URL: <http://restframes.com>.
- 2612 [125] M. Baak et al., *HistFitter software framework for statistical data analysis*,
 2613 Eur. Phys. J. **C75** (2015) p. 153, arXiv: [1410.1280 \[hep-ex\]](https://arxiv.org/abs/1410.1280).
- 2614 [126] M. L. Mangano et al., *Matching matrix elements and shower evolution for*
 2615 *top-quark production in hadronic collisions*, JHEP **01** (2007) p. 013,
 2616 arXiv: [hep-ph/0611129 \[hep-ph\]](https://arxiv.org/abs/hep-ph/0611129).
- 2617 [127] T. Gleisberg et al., *Event generation with SHERPA 1.1*,
 2618 JHEP **02** (2009) p. 007, arXiv: [0811.4622 \[hep-ph\]](https://arxiv.org/abs/0811.4622).
- 2619 [128] S. Schumann and F. Krauss,
 2620 *A Parton shower algorithm based on Catani-Seymour dipole factorisation*,
 2621 JHEP **03** (2008) p. 038, arXiv: [0709.1027 \[hep-ph\]](https://arxiv.org/abs/0709.1027).

- 2622 [129] F. Maltoni and T. Stelzer,
 2623 *MadEvent: Automatic event generation with MadGraph*,
 2624 *JHEP* **02** (2003) p. 027, arXiv: [hep-ph/0208156 \[hep-ph\]](#).
- 2625 [130] T. Sjöstrand et al., *An Introduction to PYTHIA 8.2*,
 2626 *Comput. Phys. Commun.* **191** (2015) p. 159, arXiv: [1410.3012 \[hep-ph\]](#).
- 2627 [131] S. Alioli et al., *A general framework for implementing NLO calculations in shower Monte Carlo programs: the POWHEG BOX*, *JHEP* **06** (2010) p. 043,
 2628 arXiv: [1002.2581 \[hep-ph\]](#).
- 2630 [132] J. Alwall, R. Frederix, S. Frixione, V. Hirschi, F. Maltoni, O. Mattelaer, H.
 2631 -S. Shao, T. Stelzer, P. Torrielli, M. Zaro,
 2632 *The automated computation of tree-level and next-to-leading order differential*
 2633 *cross sections, and their matching to parton shower simulations*,
 2634 *JHEP* **07** (2014) p. 079, arXiv: [1405.0301 \[hep-ph\]](#).
- 2635 [133] S. Frixione et al., *NLO QCD corrections in Herwig++ with MC@NLO*,
 2636 *JHEP* **01** (2011) p. 053, arXiv: [1010.0568 \[hep-ph\]](#).
- 2637 [134] S. Agostinelli et al., *GEANT4: A simulation toolkit*,
 2638 *Nucl. Instrum. Meth. A* **506** (2003) p. 250.
- 2639 [135] ATLAS Collaboration,
 2640 *Search for squarks and gluinos in final states with jets and missing transverse*
 2641 *momentum at $\sqrt{s} = 13$ TeV with the ATLAS detector*,
 2642 *Eur. Phys. J. C* **76** (2016) p. 392, arXiv: [1605.03814 \[hep-ex\]](#).
- 2643 [136] R. D. Cousins, J. T. Linnemann, and J. Tucker,
 2644 *Evaluation of three methods for calculating statistical significance when*
 2645 *incorporating a systematic uncertainty into a test of the background-only*
 2646 *hypothesis for a Poisson process*, *Nucl. Instrum. Meth. A* **595** (2008) p. 480.
- 2647 [137] ATLAS Collaboration, *Search for squarks and gluinos with the ATLAS*
 2648 *detector in final states with jets and missing transverse momentum using*
 2649 *4.7 fb^{-1} of $\sqrt{s} = 7$ TeV proton-proton collision data*,
 2650 *Phys. Rev. D* **87** (2013) p. 012008, arXiv: [1208.0949 \[hep-ex\]](#).
- 2651 [138] ATLAS Collaboration, *Jet energy measurement with the ATLAS detector in*
 2652 *proton-proton collisions at $\sqrt{s} = 7$ TeV*, *Eur. Phys. J. C* **73** (2013) p. 2304,
 2653 arXiv: [1112.6426 \[hep-ex\]](#).
- 2654 [139] ATLAS Collaboration, *Single hadron response measurement and calorimeter*
 2655 *jet energy scale uncertainty with the ATLAS detector at the LHC*,
 2656 *Eur. Phys. J. C* **73** (2013) p. 2305, arXiv: [1203.1302 \[hep-ex\]](#).

- 2657 [140] ATLAS Collaboration, *Jet Calibration and Systematic Uncertainties for Jets*
2658 *Reconstructed in the ATLAS Detector at $\sqrt{s} = 13 \text{ TeV}$,*
2659 ATL-PHYS-PUB-2015-015, 2015,
2660 URL: <https://cds.cern.ch/record/2037613>.
- 2661 [141] ATLAS Collaboration, *Jet energy resolution in proton-proton collisions at*
2662 *$\sqrt{s} = 7 \text{ TeV}$ recorded in 2010 with the ATLAS detector,*
2663 *Eur. Phys. J. C* **73** (2013) p. 2306, arXiv: [1210.6210 \[hep-ex\]](https://arxiv.org/abs/1210.6210).
- 2664 [142] ATLAS Collaboration,
2665 *Performance of algorithms that reconstruct missing transverse momentum in*
2666 *$\sqrt{s} = 8 \text{ TeV}$ proton–proton collisions in the ATLAS detector* (2016),
2667 arXiv: [1609.09324 \[hep-ex\]](https://arxiv.org/abs/1609.09324).
- 2668 [143] G. J. Feldman and R. D. Cousins,
2669 *A Unified approach to the classical statistical analysis of small signals*,
2670 *Phys. Rev. D* **57** (1998) p. 3873,
2671 arXiv: [physics/9711021 \[physics.data-an\]](https://arxiv.org/abs/physics/9711021).
- 2672 [144] ATLAS Collaboration, *Search for squarks and gluinos with the ATLAS*
2673 *detector in final states with jets and missing transverse momentum using*
2674 *$\sqrt{s} = 8 \text{ TeV}$ proton–proton collision data*, *JHEP* **09** (2014) p. 176,
2675 arXiv: [1405.7875 \[hep-ex\]](https://arxiv.org/abs/1405.7875).

2676

The Standard Model

2677

2678 **Compressed region N-1 plots**

add some
text or cut
this

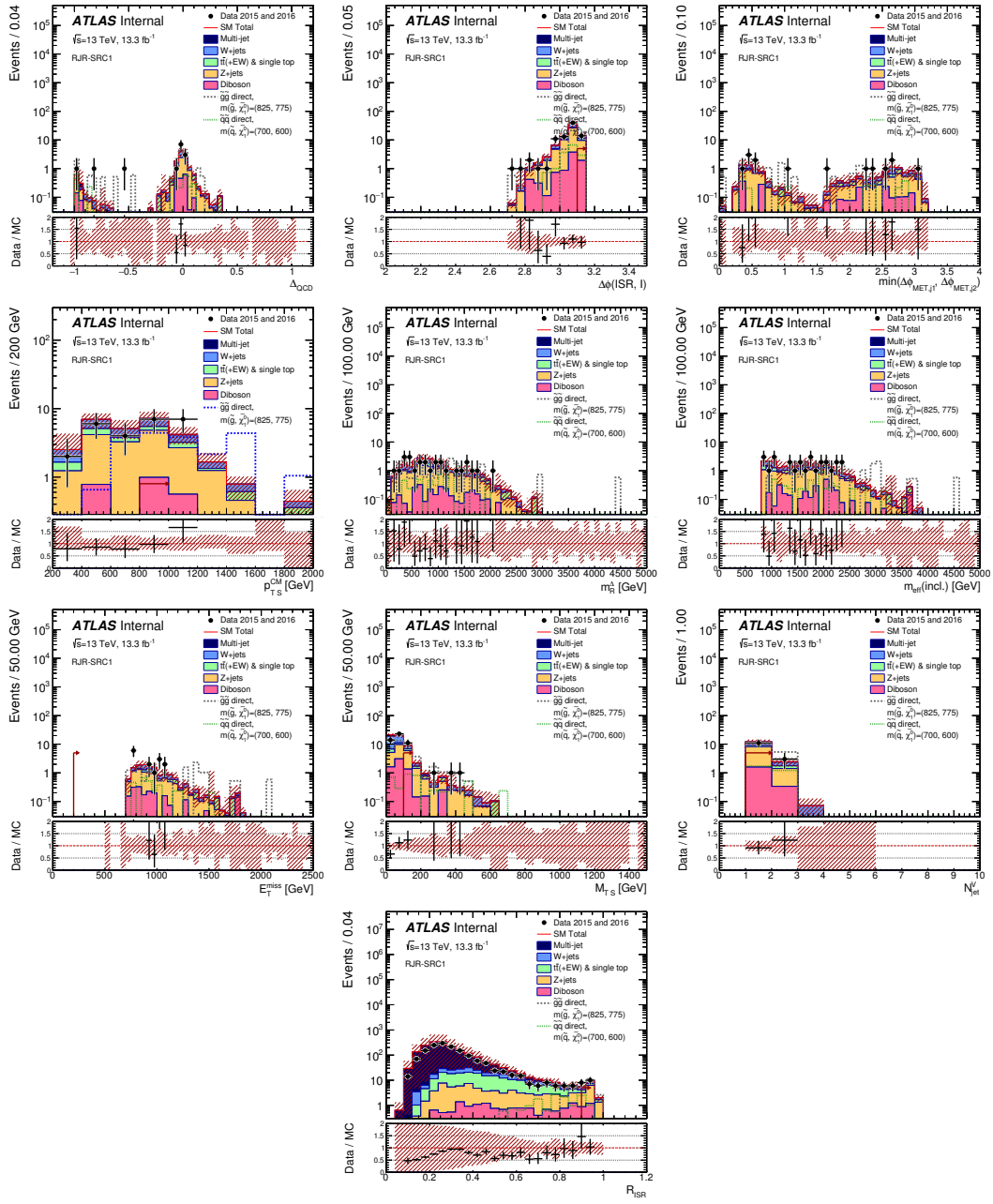


Figure 1

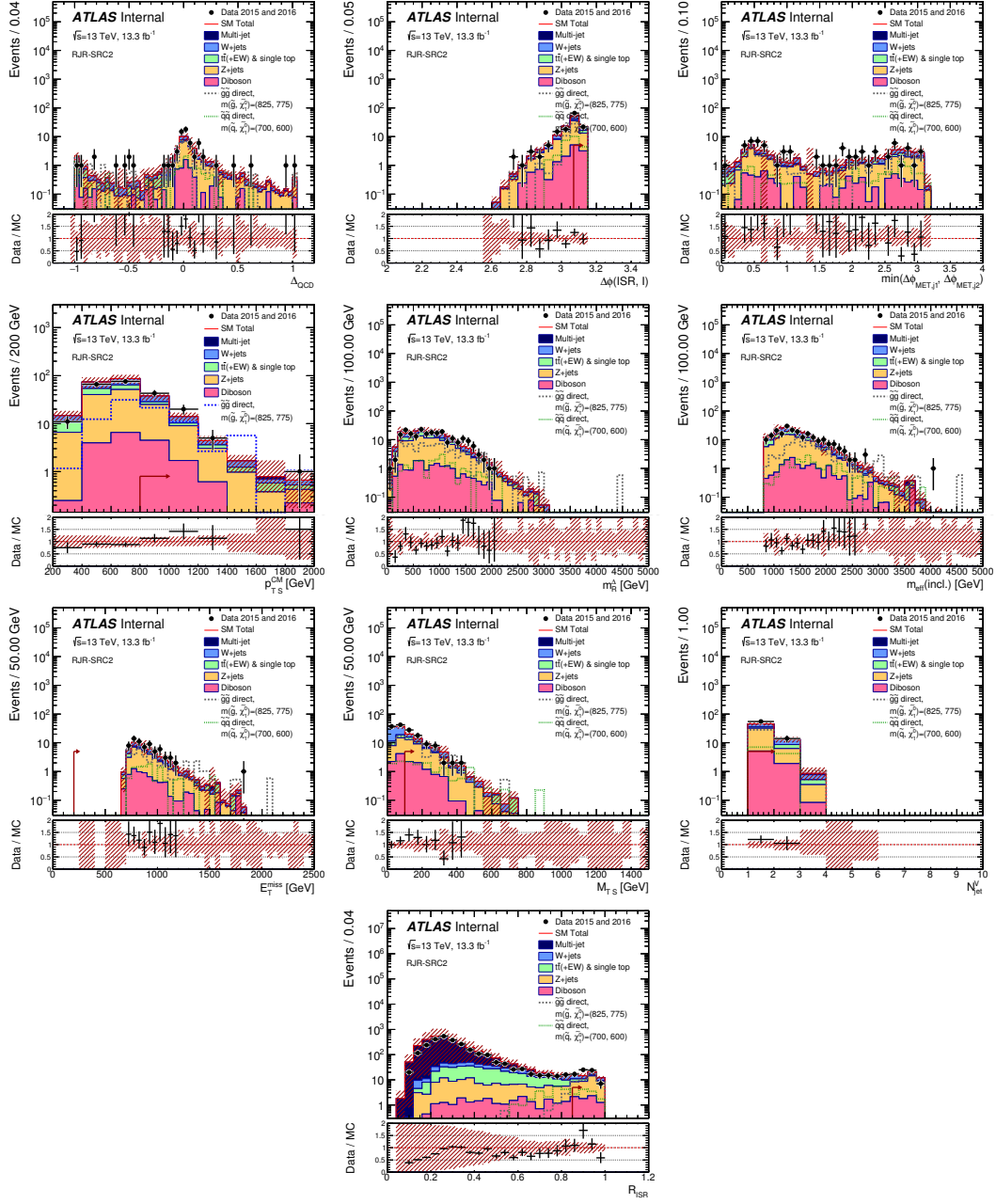


Figure 2

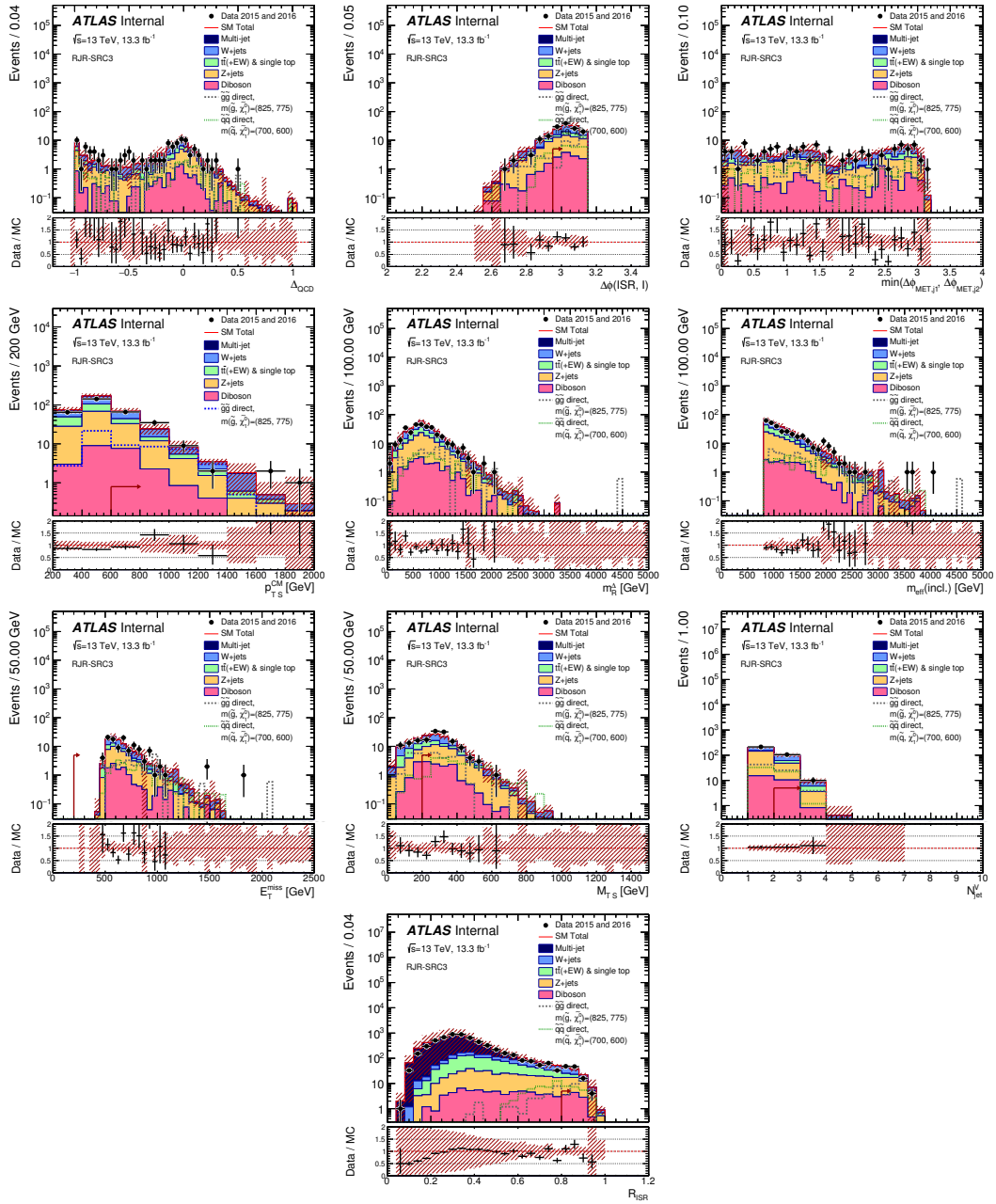


Figure 3

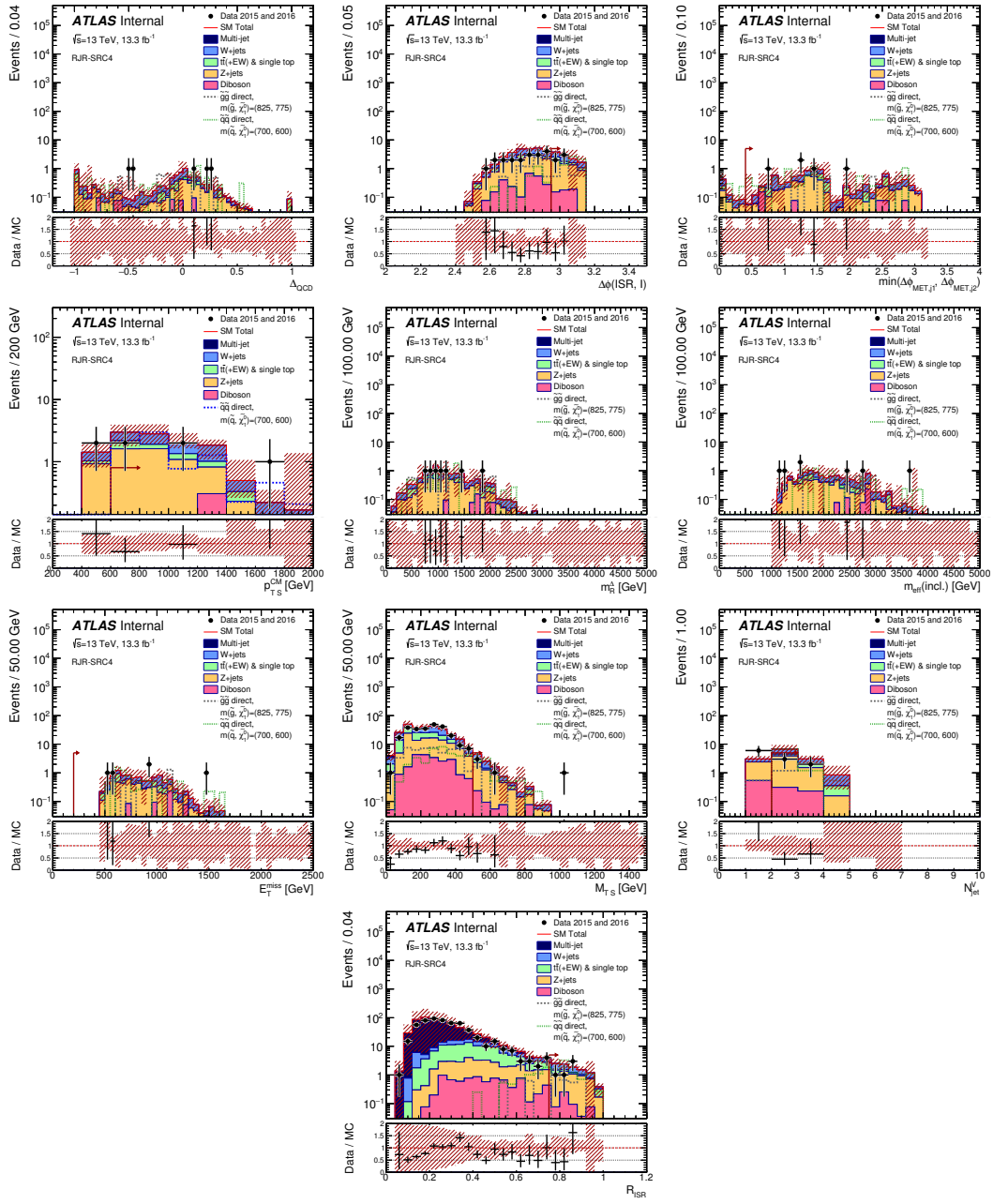


Figure 4

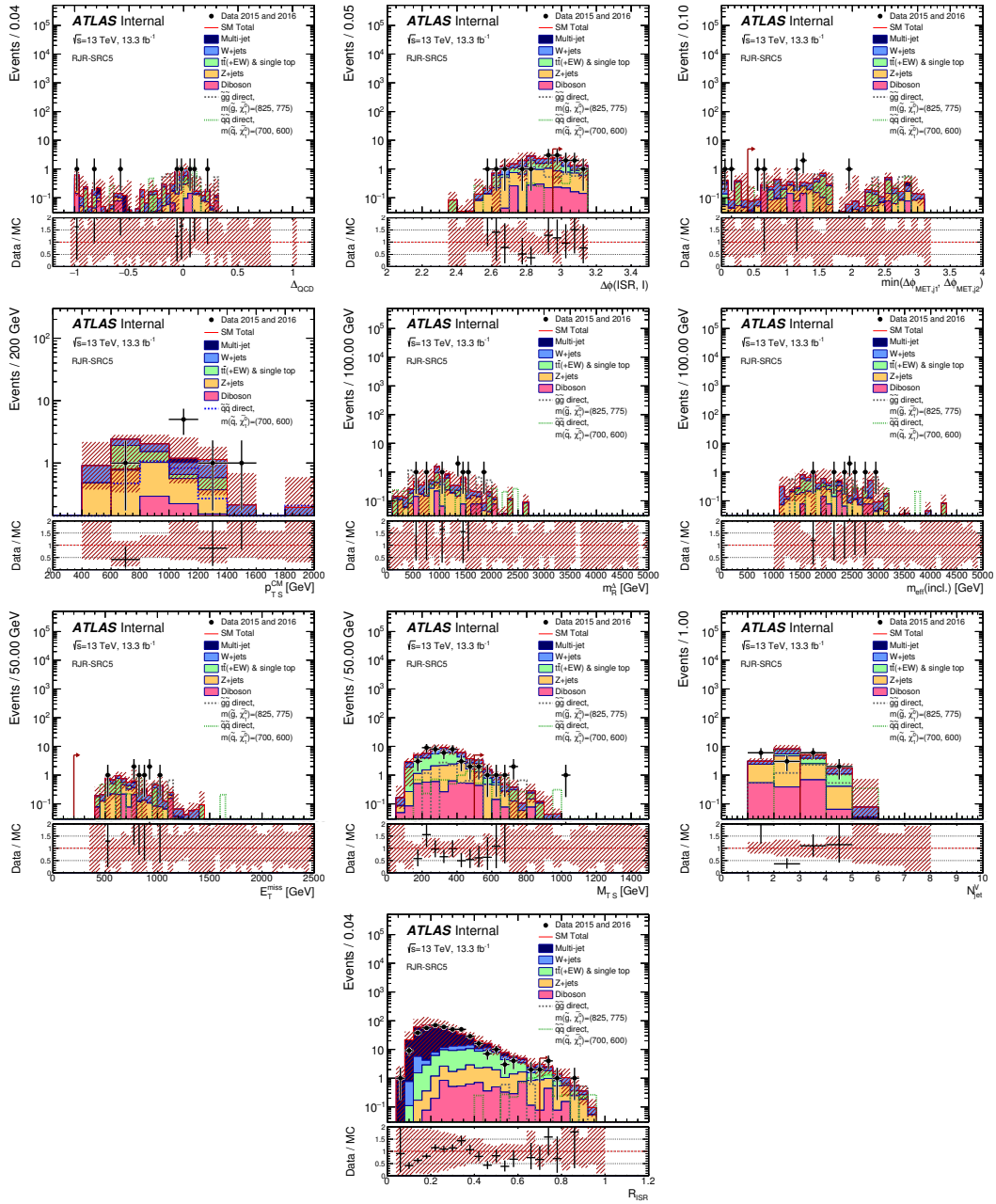


Figure 5

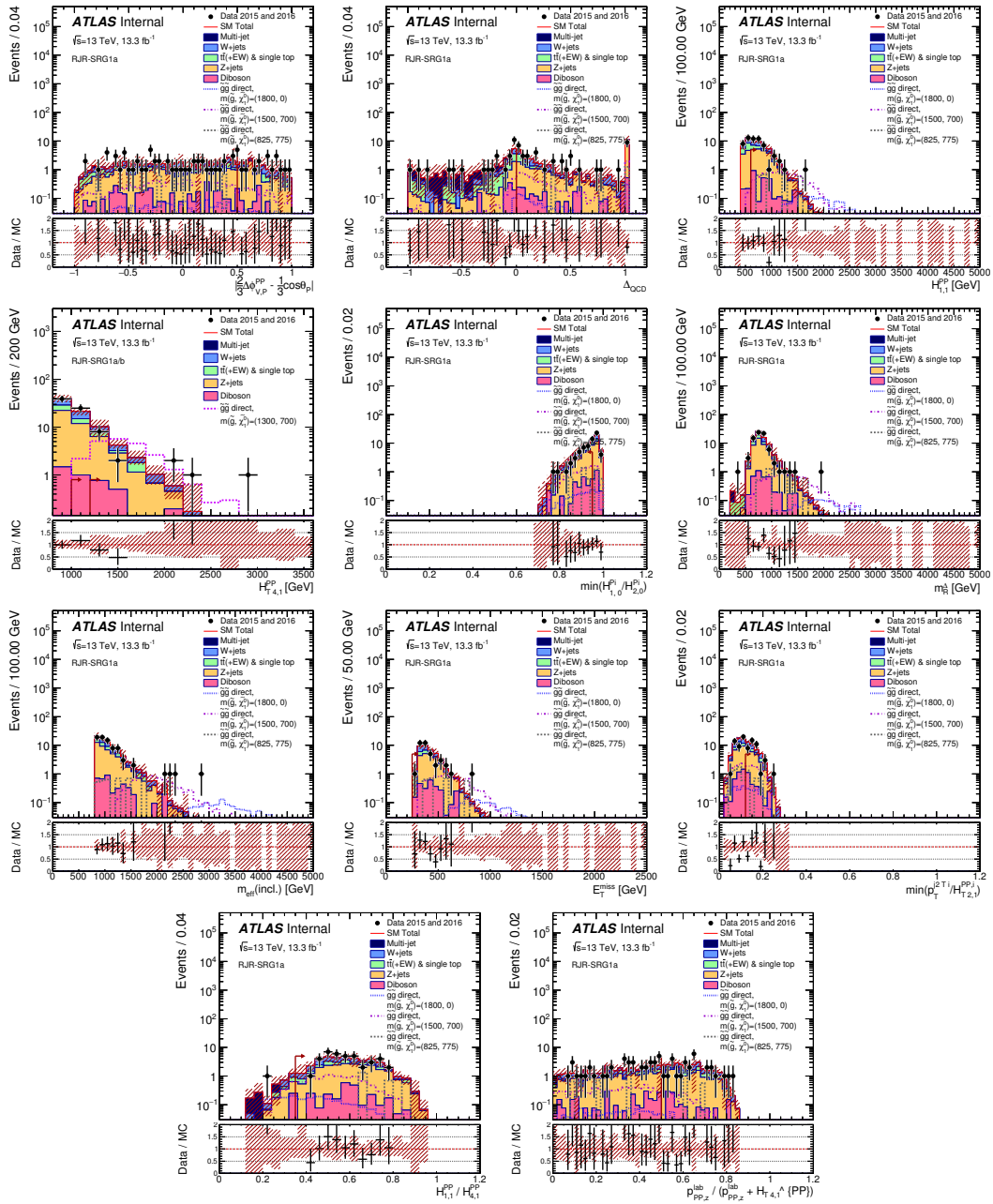


Figure 6

Figure 7

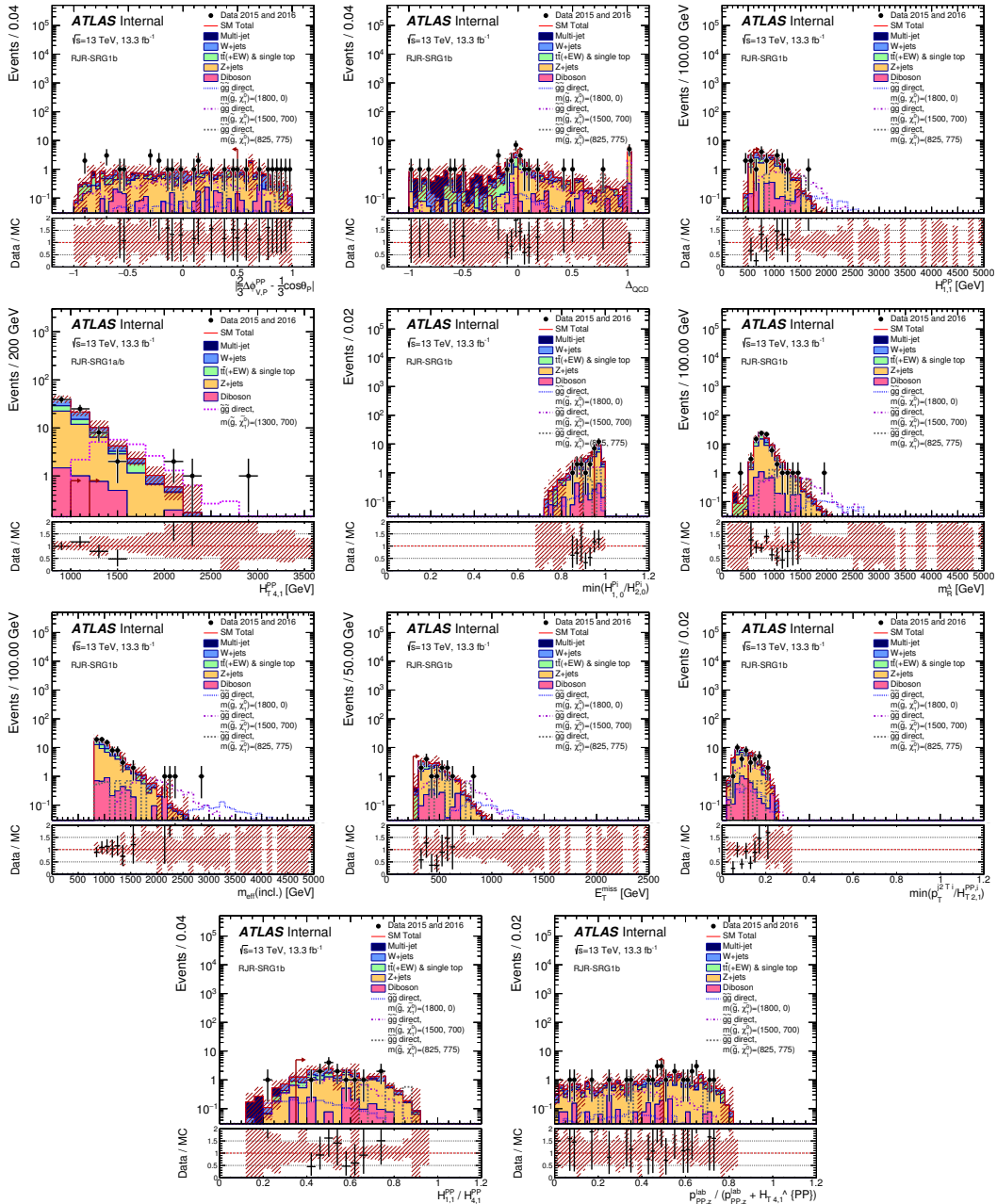


Figure 8

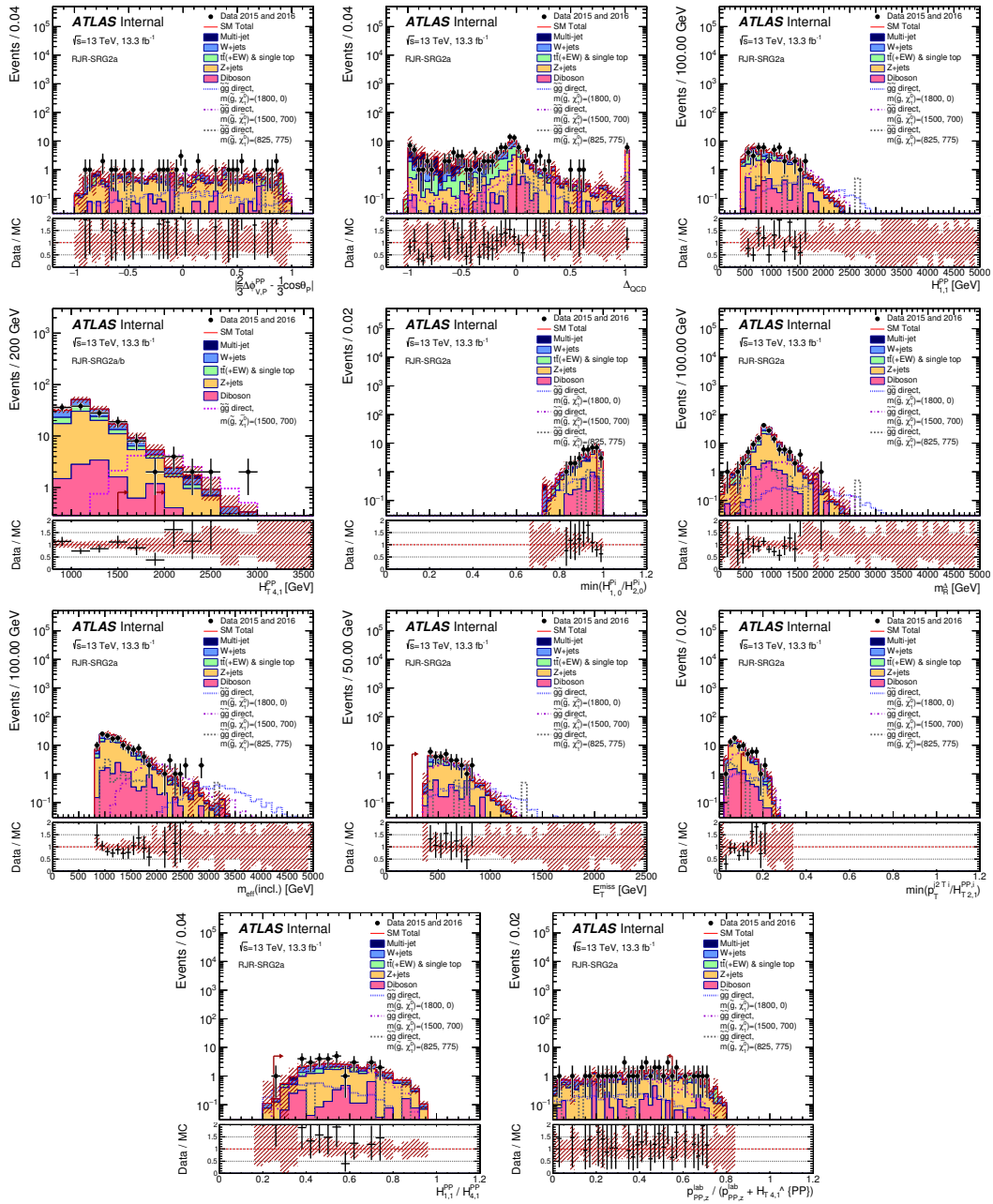


Figure 9

Figure 10

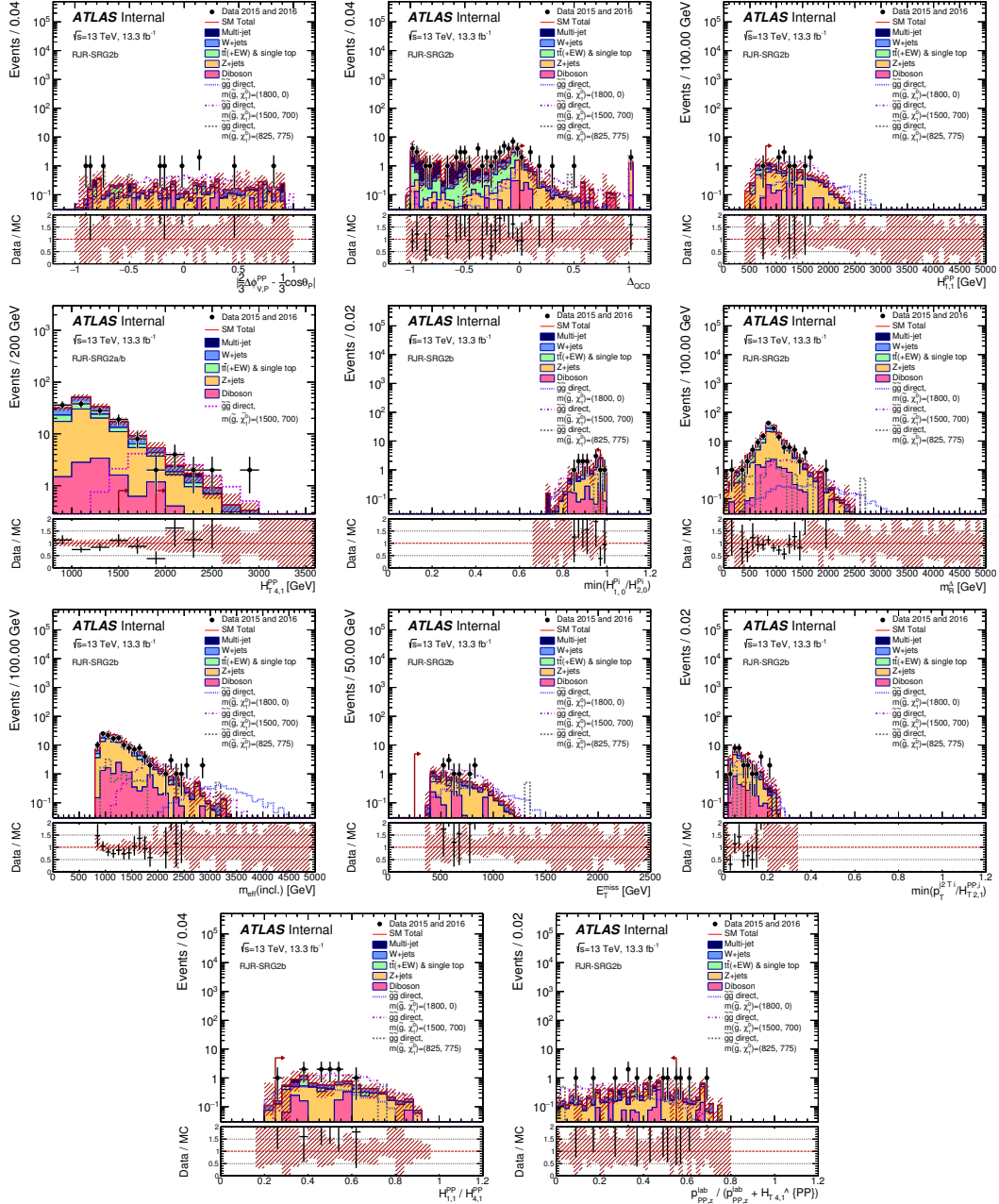


Figure 11

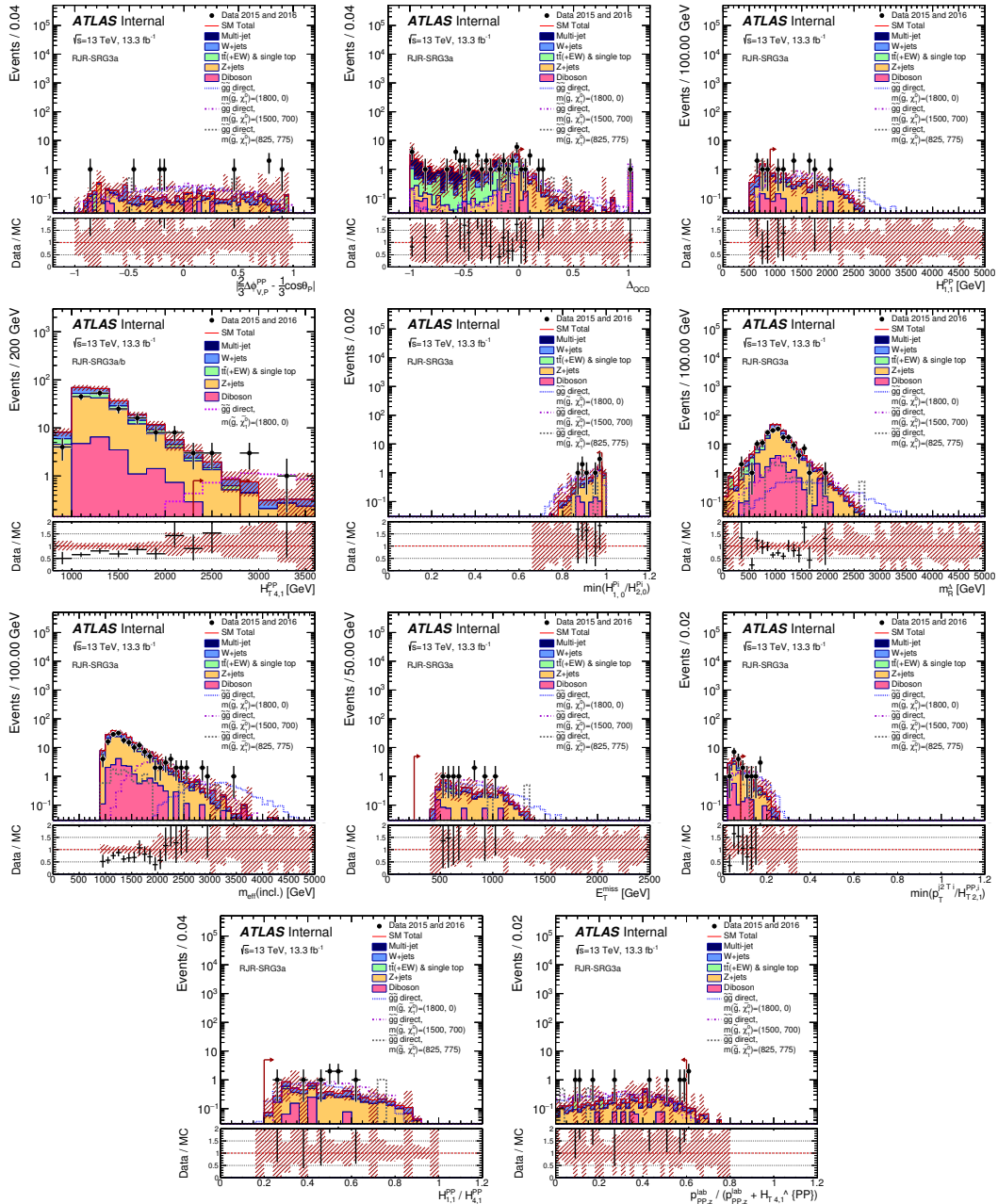


Figure 12

Figure 13

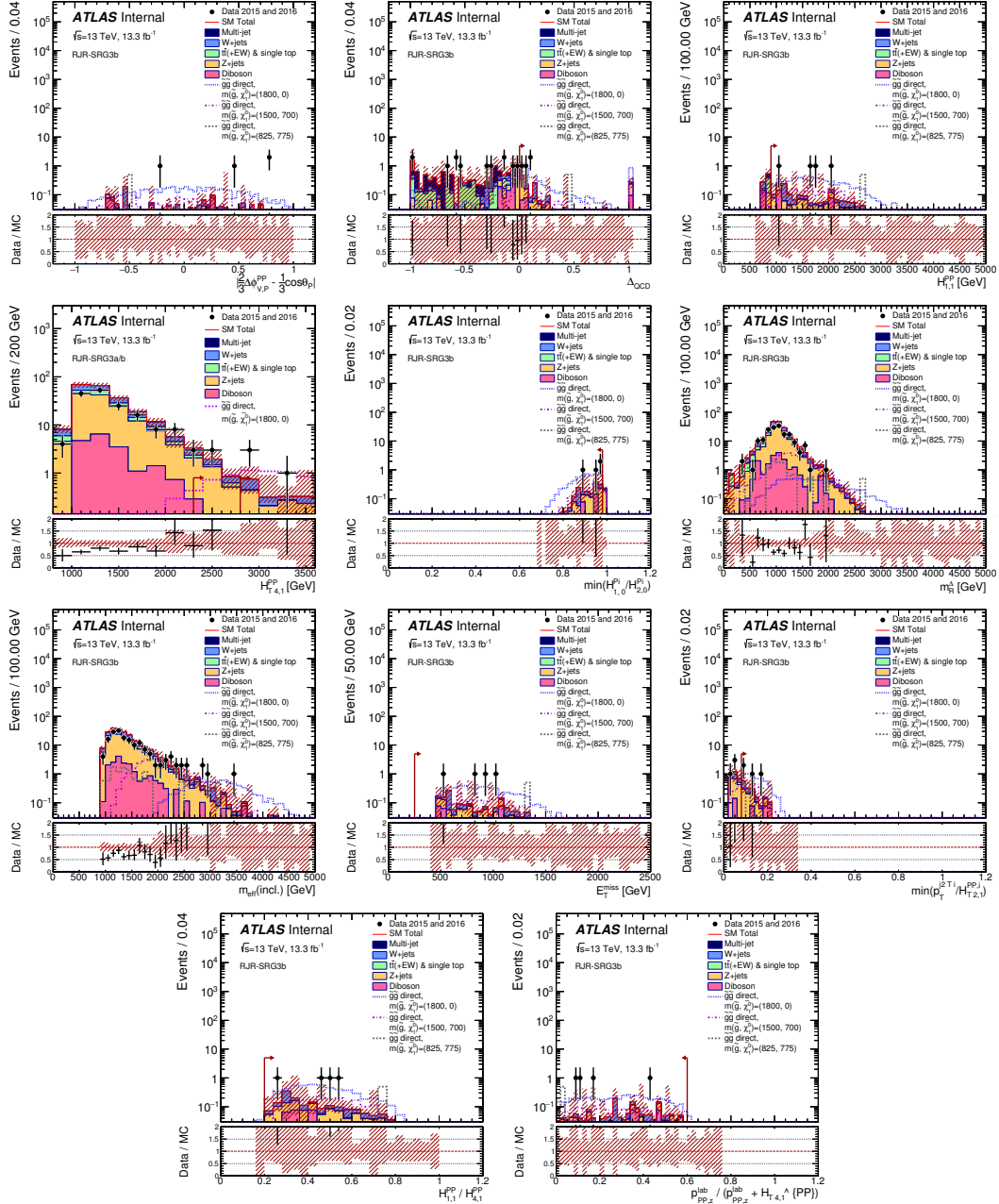


Figure 14

Figure 15

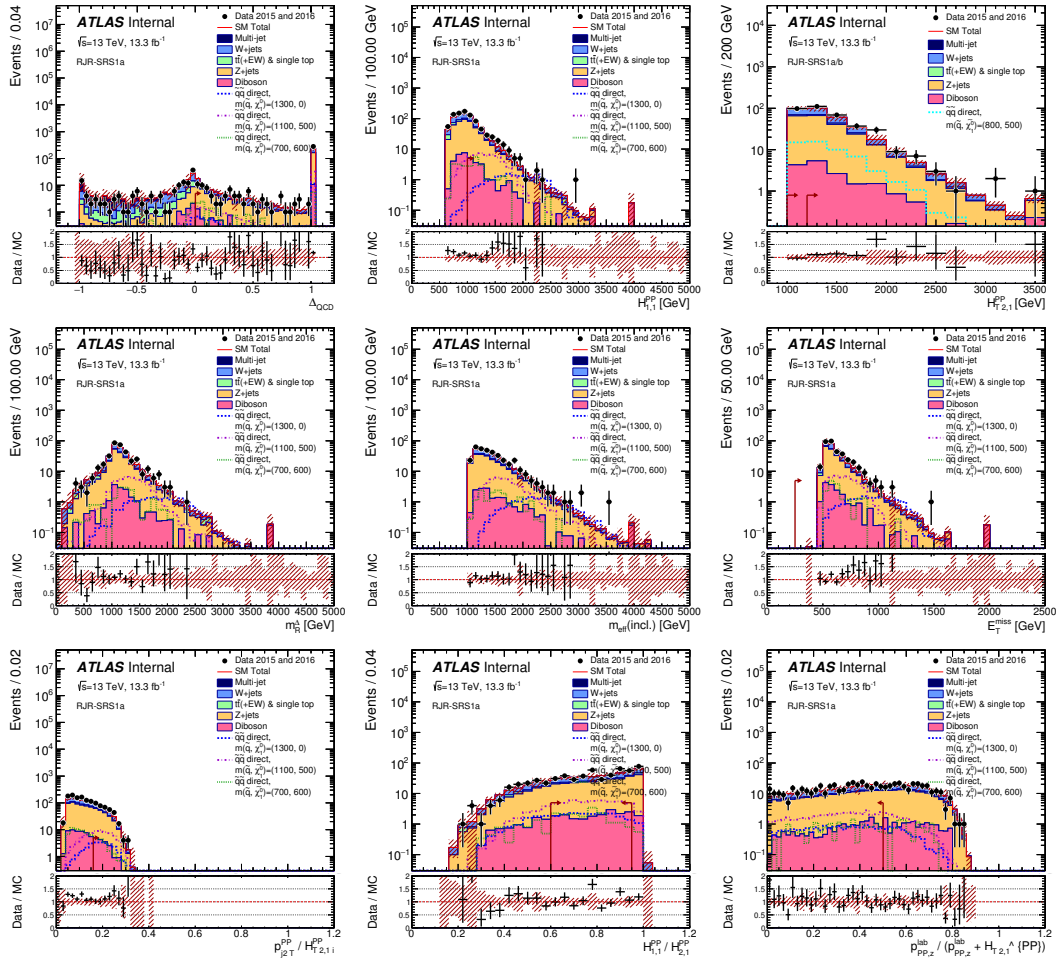


Figure 16

Figure 17

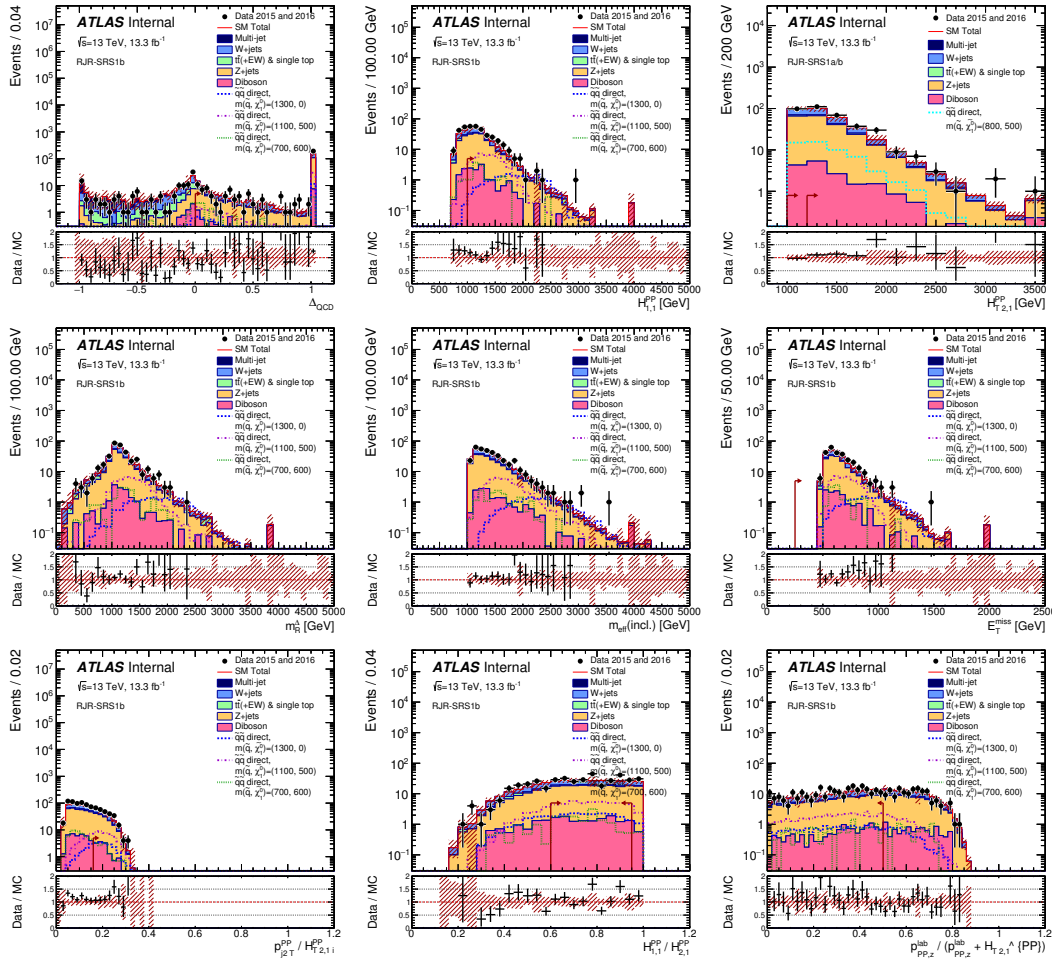


Figure 18

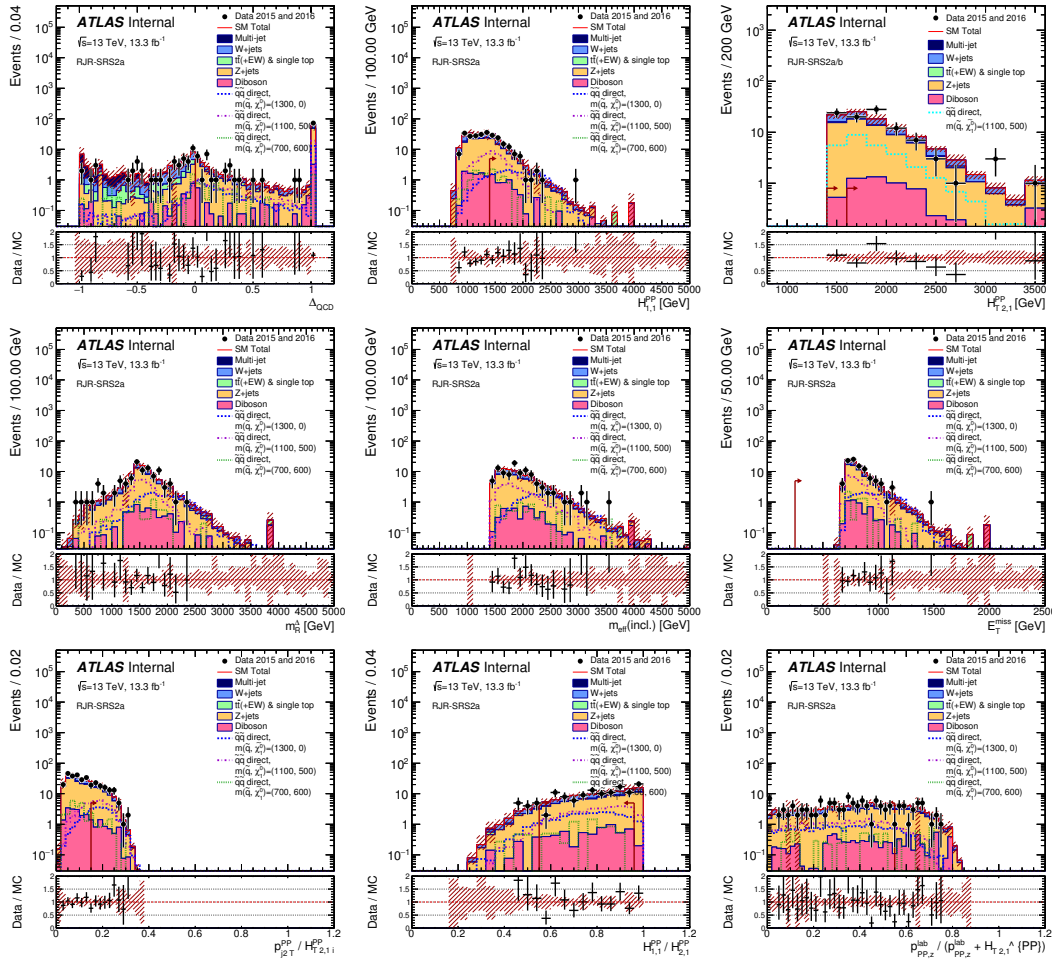


Figure 19

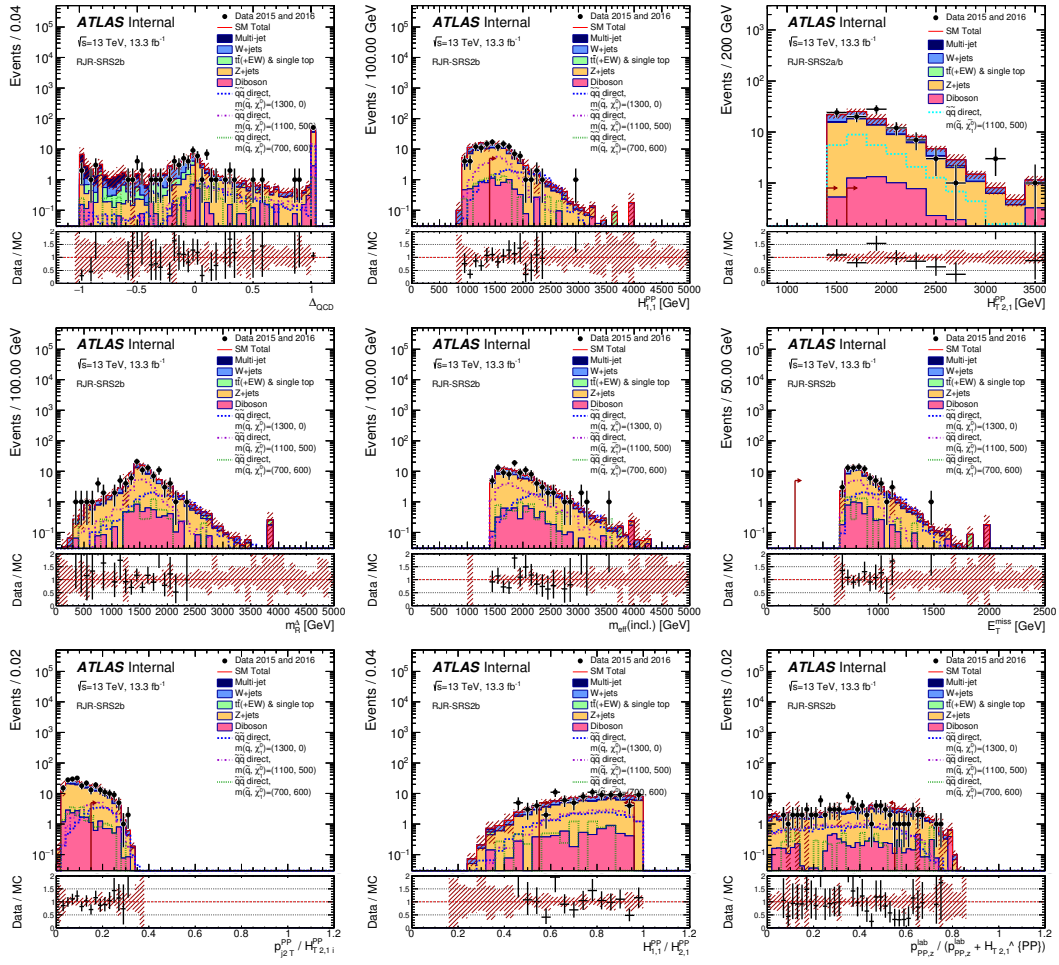


Figure 20

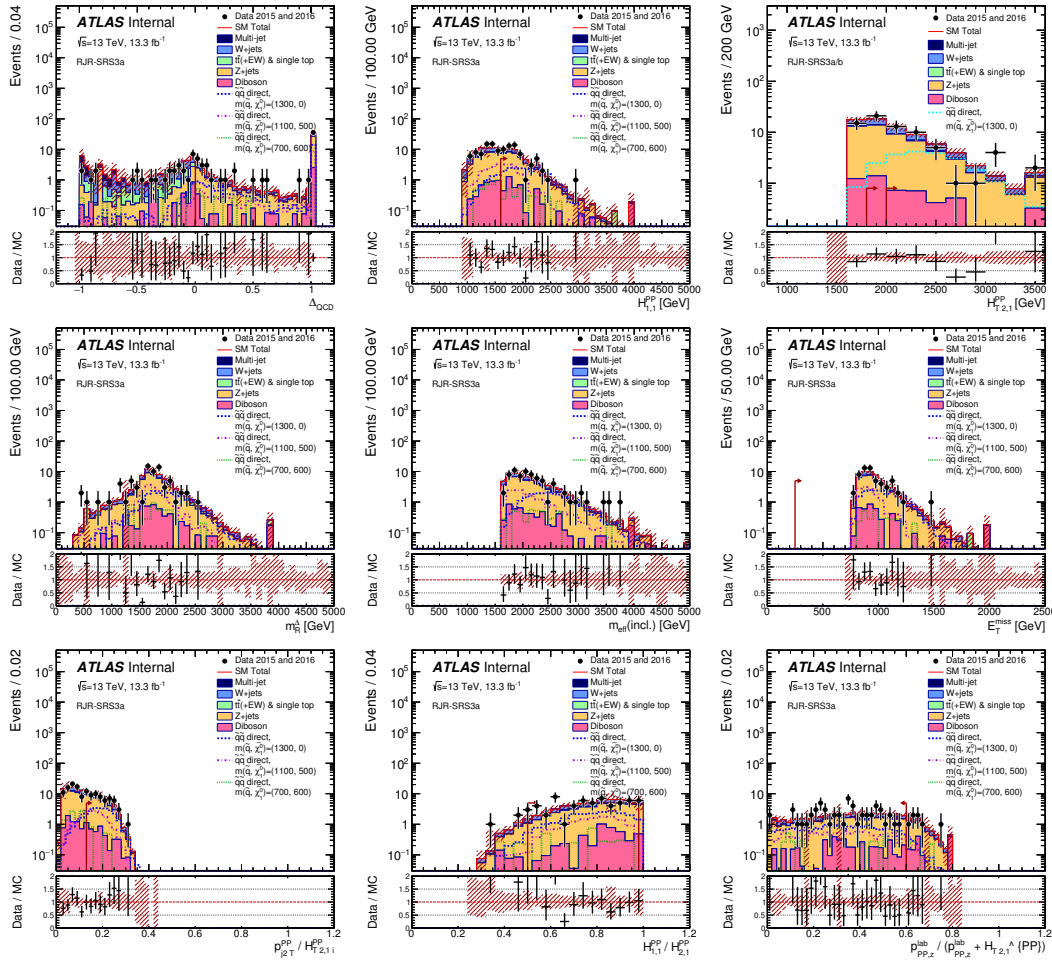


Figure 21

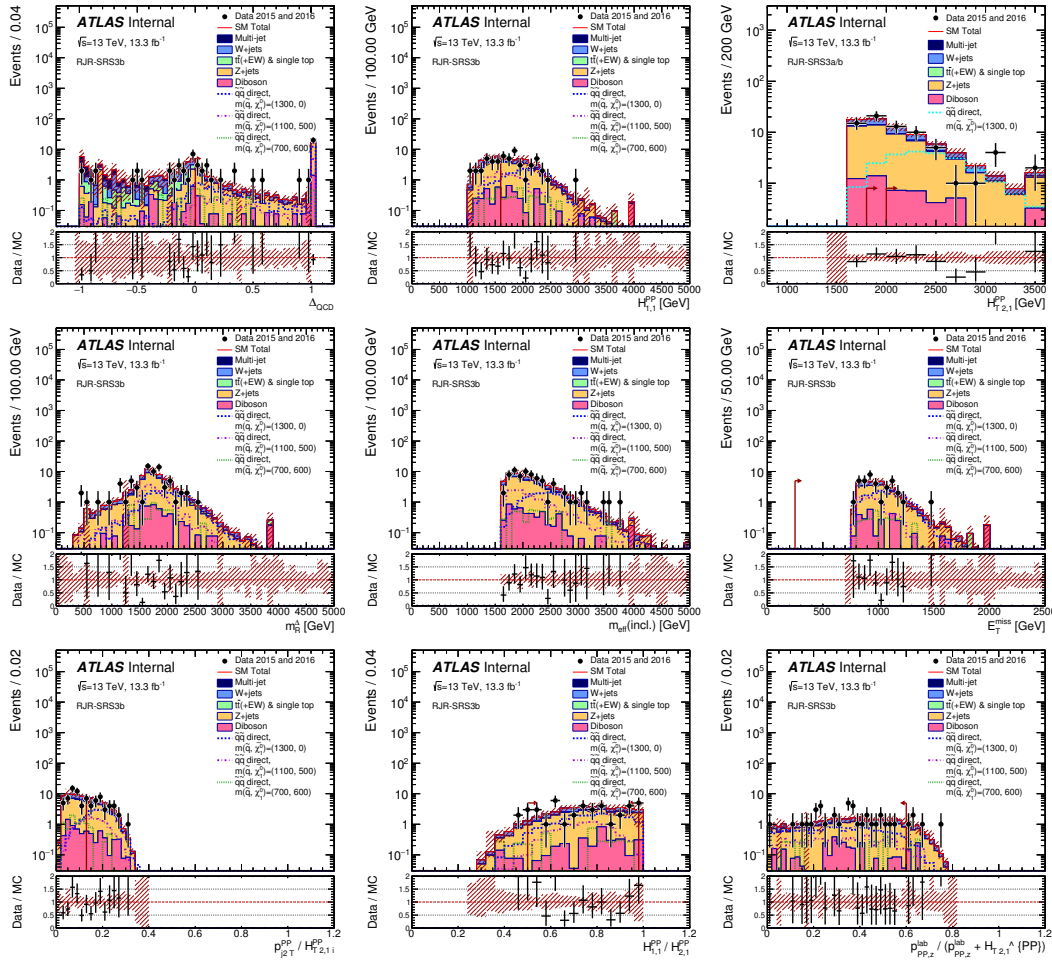


Figure 22